Bond Behaviour of Recycled Coarse Aggregate Concrete Beam-Ends under Monotonic and Cyclic Loading for Seismic Applications

by

Pablo Aguilera Clouet

A Thesis Submitted to the University of Ottawa

in Partial Fulfillment of the Requirements for the

Degree of Master of Applied Science (MASc.) in Civil Engineering

Department of Civil Engineering

Faculty of Engineering

University of Ottawa

i. Abstract

In pursuit of reducing the carbon footprint and improve the efficiency of the concrete industry, the use of recycled concrete aggregates (RCA) has been proposed and researched as possible solution. However, their reputation has been hampered by the low workability and performance of new RCA concrete mixes. The development of the Equivalent Mortar Volume (EMV) Method in the past decade allowed a better understanding of RCA characteristics and provided way to produce reliable and consistent concrete with properties like those of conventional concrete.

This project continues the development path of the EMV Method by studying its influence on the bond behaviour of small-scale structural specimens subjected to cyclic loads to assess the possible use of structural concrete containing RCA in seismic applications. The first stage was dedicated to the development of an EMV mix with a characteristic compressive strength of 35 MPa and a water-to-cement ratio of 0.40. These parameters resulted in a cement mass reduction of 28% and an RCA replacement ratio of 74% when compared to a reference mix without RCA.

The second stage of the project focused on 18 beam-end tests with three bar size – embedment length configurations, namely 15M – 170 mm, 15M – 320 mm, and 25M – 320 mm. Half of the specimens were subjected to monotonic loading and the other half to tension cyclic loading. The chosen combinations allowed the study of different failure mechanisms, such as splitting/pullout failure, bar rupture, and splitting failure, respectively.

The results of the bond tests indicate the EMV mixes were able to follow the performance of the conventional concrete during the cyclic tests across all combinations, closely matching the failure mechanisms, peak loads, and ultimate displacements; thus, following the same trends observed during previous monotonic studies. It is also proved that the current Canadian provisions for conventional concrete could be potentially applied for RCA concrete made with the EMV Method.

ii. Table of Contents

iii. List of Tables

iv. List of Figures

v. Notation

Subscripts obtained by abbreviation:

- AAM: Alkali-activated materials
- ACI: American Concrete Institute
- AE: Air-entrainer admixture
- BYF: Belite-ye'elimite-ferrite clinkers
- CCSC: Carbonatable calcium silicate clinkers
- CSA: Canadian Standards Association
- CSAs: Calcium sulfoaluminates
- C&D: Construction and demolition waste
- DFOS: Distributed fibre optical sensing
- DIF: Dynamic increasing factors
- DRM: Direct replacement method
- EMV: Equivalent mortar volume
- EMVc: Equivalent mortar volume with an alternative binder
- EV: Equivalent volume
- FRP: Fibre-reinforced polymers
- GGBFS: Ground granulated blast furnace slag
- GHG: Greenhouse gas
- GU: General use Portland cement
- GUL: General use Portland limestone cement
- HE: High-early-strength Portland cement
- HEL: High-early-strength Portland limestone cement
- HRWR: High-range-water-reducer admixture
- HS: High-sulphate-resistant Portland cement
- HSL: High-sulphate-resistant Portland limestone cement
- ITZ: Interfacial transition zone
- LC^3: Calcined clay limestone cements

- MOMS: Magnesium oxides derived from magnesium silicates
- MS: Moderate-sulphate-resistant Portland cement
- MSL: Moderate-sulphate-resistant Portland limestone cement
- NAC: Natural aggregate concrete
- New-NA: New natural coarse aggregate source
- OD: Oven-dry
- Old-NA: Old natural aggregate source
- OVA: Original virgin aggregates
- PC: Portland cement
- PCE: Polycarboxylates-based chemical admixtures
- PLC: Portland limestone cement
- PSD: Particle size distribution
- RBPC: Belite-rich Portland cement
- RC: Reinforced concrete
- RCA: Recycled concrete aggregates
- RCM: Reclaimed concrete material
- RHC: Returned hardened concrete
- RM: Residual mortar
- RMC: Residual mortar content
- RUC: Returned unused concrete
- SAP: Super absorbent polymers
- SCM: Supplementary cementitious material
- SSD: Surface-saturated-dry
- TSMA: Two-stage-mixing-approach
- W/C: Water-to-cement ratio
- WRA: Water reducing admixture
- WS: Water glass or sodium metasilicates

Notation starting with Roman upper-case letters:

- A_b: Bar area
- A_{tr}: Area of each stirrup or tie crossing the potential splitting plane
- CO_2: Carbon dioxide
- E_c: Elastic modulus of concrete
- F: Splitting tensile force; force; load
- F_p: Steel peak load
- $F_{p,s}$: Scaled steel peak load
- F_u: Steel ultimate force
- F_{uc}: Ultimate force of the steel coupon
- F_y: Steel yielding force
- F_{yc}: Yielding force of the steel coupon
- K_{tr}: Transverse confinement index
- L: Cylinder length
- MgO: Magnesium oxide
- N: Number of transverse stirrups, or ties, within the development or splice length
- $NaOH$: Sodium hydroxide
- P: Force; load
- P_c: Cracking load
- P_m: Peak load
- P_u: Ultimate load
- P_y: Yielding load
- $P-\Delta$: P-delta effect
- R: Natural coarse aggregate replacement ratio in EMV mixes
- R_{min}: Minimum coarse aggregate replacement in RCA concrete mix.
- RMC_{max}: Maximum residual mortar content for a particular RCA source
- S^{-3}: Tri-sulfur radical anion

- SG_b^{NA}: Specific gravity of natural coarse aggregate
- SG_b^{OVA}: Specific gravity of original coarse virgin aggregate
- SG_b^{RCA}: Specific gravity of RCA
- T: Force; load
- T_b: Total bond force of a developed or spliced bar
- $T_{b,ACI}$: Predicted bond force by ACI 408
- $T_{b,ex}$: Experimental bond force of ACI 408 database
- T_c: Concrete contribution to total bond force
- T_s: Steel contribution to total bond force
- V_{DR-NA}^{NAC}: Dry-rodded volume of fresh coarse aggregate in conventional concrete mix
- V_M^{NAC}: Mortar volume in conventional concrete mix
- V_{NA}^{NAC}: Volume of fresh new coarse aggregates in a conventional concrete mix
- V_{NA}^{RCA-C}: Volume of fresh new coarse aggregates in an RCA concrete mix
- V_{NM}^{RCA-C}: Fresh mortar volume in RCA concrete mix
- V_{OVA}^{RCA-C}: Original virgin coarse aggregate volume in RCA concrete mix
- V_{RCA}^{RCA-C}: Volume of RCA in RCA concrete mix
- V_{RM}^{RCA-C}: Residual mortar volume in RCA concrete mix
- V_{TM}^{RCA-C}: Total mortar volume in RCA concrete mix
- V_{TNA}^{RCA-C}: Total coarse aggregate volume in RCA concrete mix
- W_{OVA}: Oven-dry mass of the original natural coarse aggregate
- W_{RCA}: Oven-dry mass of the RCA

Notation starting with Roman lower-case letters:

- a: Coefficient that accounts for the steel strain
- a/d: Shear span-to-depth ratio
- b: Coefficient that accounts for the steel stress
- c_b: Bottom cover of the rebar
- c_{max}: Maximum combination between cover and bar spacing

- c_{min}: Minimum combination between cover and bar spacing
- c/d_b: Cover-to-bar diameter ratio
- d: Depth of member or size effect; cylinder diameter
- d_b: Bar diameter
- d_{cs}: Smaller between minimum concrete cover to the bar centre, and two-thirds of the centre-to-centre spacing of the bars being developed
- f_c': Specified compressive strength of concrete
- f_s: Steel stress; steel stress being evaluated
- f_{spt}: Splitting tensile stress
- f_u: Steel ultimate stress
- $f_{u,max}$: Maximum steel ultimate stress
- $f_{u,min}$: Minimum steel ultimate stress
- f_y: Steel yielding stress
- $f_{y,max}$: Maximum steel yielding stress
- $f_{y,min}$: Minimum steel yielding stress
- f_{yg}: Minimum yielding strength as defined in the applicable material standard for the specified grade of reinforcing steel
- h_L: Rebar lug height
- k_c: Bar coating factor
- k_d: Concrete density factor
- k_g: Reinforcement grade factor
- k_l: Bar location factor
- k_s: Bar size factor
- l_d: Embedment length
- l_{dc}: Development length of bar in compression (mm)
- n: Number of bars being developed or spliced
- s: Spacing of transverse reinforcement
- s_L: Rebar lug spacing

- s_s: Bond slip
- s_1: Bond slip at the beginning of the bond peak
- s_2: Bond slip at the end of the bond peak
- s_3: Bond slip at the beginning of the ultimate bond
- t_d: Effect of bar size on steel contribution to total bond force
- t_r: Effect of relative rib area on steel contribution to total bond force
- u: Bond stress
- u_f: Final bond stress
- u_u: Ultimate bond stress

Notation starting with Greek upper-case letters:

- Δ: Displacement; deformation limits
- Δ_c: Cracking deformation
- Δ_m: Peak deformation
- Δ_u: Ultimate deformation
- Δ_y: Yielding deformation
- $\dot{\Delta}$: Displacement rate
- Φ: Deformation step
- Ψ_e: Epoxy coating factor
- Ψ_g: Reinforcement grade factor
- Ψ_s: Bar size factor
- Ψ_t: Bar casting position factor
- Ω_y: Strain-calibrated factor to account for the yielding effects

Notation starting with Greek lower-case letters:

- α: Coefficient for bond stress development
- δ_s: Bond slip
- δ_{s1}: Bond slip at the beginning of the bond peak
- δ_{s2}: Bond slip at the end of bond the peak

- δ_{s3}: Bond slip at the beginning of the ultimate bond
- ε: Strain
- ε_m: Strain at the maximum elongation point before failure
- ε_s: Steel strain; steel strain being evaluated
- ε_{sh}: Strain at the beginning of the strain hardening region
- ε_u: Strain at the ultimate peak stress; steel ultimate strain
- ε_y: Yielding strain, steel yielding strain
- ε_{yp}: Strain at the beginning of the yielding plateau
- $\dot{\varepsilon}$: Strain rate
- η_2: Coefficient to account for the effect of the bond conditions
- λ: Lightweight aggregate concrete factor
- μ: Structural ductility; ductility ratio
- ρ: Longitudinal reinforcement ratio
- σ: Stress
- σ_m: Stress at the maximum elongation point before failure
- σ_{sh}: Stress at the beginning of the strain hardening region
- σ_u: Stress at the ultimate peak stress
- σ_y: Yielding stress
- σ_{yp}: Stress at the beginning of the yielding plateau
- τ_f: Residual bond stress
- τ_{max}: Peak bond stress; peak bond stress for pullout failure
- $\tau_{max,y}$: Scaled maximum bond stress due to steel yielding
- τ_o: Bond stress
- τ_{split}: Peak bond stress for splitting failure
- ϕ_b: Bar diameter

Mathematical symbols

- $\forall$: For all

vi. Acknowledgments

The development of this research project as part of my MASc. program was the exact definition of running a marathon, the goal was clear at the beginning, but 42.175 km (or 26.2 miles as you might prefer) had to be completed first, and no one is going to run them for you, you have to earn your medal. This road has been an experience of a lifetime, it has (literally) taken me to places where I never thought I would be, and most importantly, it has allowed me to grow both as an individual and as a professional.

I would like to start by thanking my Supervisors, Dr. Martin Noël from the University of Ottawa, Dr. Reza Fathi-Fazl and Dr. Farrokh Fazileh, both from the National Research Council Canada, for giving me the opportunity to develop this project, for trusting in my abilities from our very first meeting, and for your continued support and mentoring as the project progressed towards our final goal. You have pushed my limits in ways I did not think were possible, and I will be forever grateful for giving me the chance to develop new tools and skills that will be of great value in my future life.

I would also like to acknowledge Dr. Adeyemi Adesina from the University of Windsor and Dr. Terry YP Yuen from the National Yang Ming Chiao Tung University of Taiwan, for their advice and collaboration in the design and testing of the concrete mixes, and test specimen modelling, respectively. Your contribution was key for the optimization of my learning curve process. I also have to thank Dr. Yuen for being my supervisor and an amazing host while I was doing my 4-week internship in Taiwan.

To my dear friends, Emre Insel and Felipe Sáez, thank you for helping me every time I needed extra hands and brains. Emre, I will never forget your motivation and kindness, getting to know you at the university has been one of the best gifts of this project. You were always there to listen and help in every stage of this project, something I will be forever grateful for. Felipe, despite the physical distance of the last few years, you were always

there, and your help was invaluable during the data analysis and writing stages. I owe you the development of my coding skills.

At the University of Ottawa, I have to extend my sincere appreciation to Dr. Muslim Majeed, Dr. Gamal Elnabelsya, Jacques Audet, James Kent, and Luc Cloutier for their invaluable knowledge, skills and time. This project was complex from the very beginning, and its implementation demanded specific materials, machining processes, instrumentation and testing skills. Luckily, you were there to give me a hand every time, and I sincerely thank you for your patience and insights throughout the project.

I would also like to acknowledge my task force, Dario Ramírez, Hiba Dahrabou, and Sarthak Rathi. You were instrumental and the muscles of the batching and casting stages that lasted for weeks. I know it was hard, and I demanded a lot from you, but you gave your best and were the best team I could have asked for. I really enjoyed our time together.

To my fellow colleagues from the Noël Research Group, Alejandro Ríos, Luis Soto, Issa Fowai, Abdulla Zahmak, Seyed Alireza Alavi, Osamah Mahmood, Mohammed Skalli, and Magd Abdelmelek, thank you for your help every time I needed it. Likewise, I extend my gratitude to my colleagues from other research groups, Antoine Bérubé, Kamesh Solaiappan, Fernanda Scussiato Lago, Dana Tawil, Claude Xia, and Leah Kristufek, who were there as well every time I needed extra hands or advice.

At the National Research Council Canada, I would like to recognize the help from Ken Trischuk, Dennys Krys, Roger Smith, Alex Wang, Antal Prigli, Kerri Henriques, Olga Naboka, Joe Hum, Bruce Baldock, Skylar Manitowabi, and Patrick Reid. When I started this program, I never considered the technical knowledge and skills I would gain. I thank you for guiding me through the details, hands-on, and practical processes. Many times, we engineers think about theories and models, but things need to be implemented in real-life, and that transition from the virtual to the real world is something I learned from you.

Finally, and not less important, I would like to express my love and utmost respect for my dear mother, father, and sister, the core of my family. You better than no one know the ups and downs I had to endure during these past few years, but you were always there to have my back and remind me that I could always push myself and give a little more, because you trusted in my abilities. The result of this project is yours as well.

This marathon was one for the ages, but thanks to everyone that was supporting me along the way, I was able to not only finish it but to enjoy the ride even when the course got harder. At the end of the day, the goal was achieved, and I leave with a smile on my face, but the sweetest taste does not come from the medal or final time, but from the lessons I gained during the entire process. This project, as well as with many things in life, is a living proof that hard work always pays off.

Industry partners recognition

The authors would like to thank Amrize (formerly known as Lafarge Canada) and Tomlinson Group for the donation of the cement, concrete admixtures, and the recycled concrete aggregates used for this project. Their contribution is greatly appreciated in the pursuit of expanding concrete's knowledge.

1. Introduction

1.1. General overview

Concrete is the most used construction material worldwide; it is trusted by structural engineers as a key component in the design of structures that need to be safe and serve various purposes, as well as by construction engineers who oversee bringing those designs to life. In its most basic composition, concrete is an artificial grey stone formed by mixing cement, water, coarse aggregates, and fine aggregates.

The cement is a dry powder that develops binding properties when mixed with water, a product known as cement paste. If the reactions are stable it is known as a hydraulic cement, of which Portland cement is the most common type. The aggregates are granular materials that form a skeleton structure and are classified as coarse or fine depending on their size. Coarse aggregates are traditionally gravels or crushed stones with particles larger than 4.75 mm, while fine aggregates are usually sands with particles larger than 80 μm and smaller than 4.75 mm (Mehta & Monteiro, 2014).

Another important component in modern-day concretes are the so-called concrete admixtures, which were developed with the intention of modifying one or more concrete properties. These are chemical products that are added to the mix (in liquid or solid states) in quantities no larger than 5% of cement mass (Neville, 2011).

Concrete is a versatile material because it has two distinctive phases with unique characteristics. The first phase is known as the fresh state, which starts as soon as the main ingredients are mixed. Once the cement meets water, it reacts and starts forming the hydration products that are responsible for giving concrete its strength. These reactions take a while to manifest, hence concrete's low viscosity and fluid-like behaviour. It is during this phase that the pouring takes place since concrete is workable and it can be formed into

any shape. The end of this phase is usually associated with a phenomenon known as setting, which is when the cement paste begins its solidification.

The setting of the cement paste can be characterized by an initial and a final set. The initial set marks the beginning of the solidification, and it translates into a workability loss (or as a slump loss as it is typically known in the field). The final set, on the other hand, marks the end of the cement paste solidification, and it occurs when the paste becomes fully rigid. Setting times can vary upon the mix formulation and employed admixtures, but usually it takes approximately 6 – 10 hours (Mehta & Monteiro, 2014).

The second phase, or hardened state, begins with the cement paste setting. It is in this phase where concrete develops its strength and stiffness (properties required for different structural applications), and where it effectively becomes a grey composite stone. This phase is also concrete's final state, and with proper care it can deliver a waterproof material that can last for many years. For normal applications, concrete has a density that ranges from approximately 2200 – 2400 kg/m^3, and compression strengths between 25 – 55 MPa. Conversely, concrete's tensile properties are typically only 8 – 15% of its compressive strength (Wight, 2021). To compensate for the low tensile strength of concrete, deformed steel bars that can bear the tensile stresses are employed as internal reinforcement. This composite system is known as reinforced concrete (RC).

Thanks to its structural properties, relatively low cost, and local availability (Mehta & Monteiro, 2014), RC is an ideal solution for many structural applications, such as residential buildings, skyscrapers, dams, and nuclear power stations, among others. Its versatility and durability have been proven over the last century and positioned RC alongside structural steel and timber as one of the default materials in the construction industry.

1.2. Environmental challenges of the cement and concrete industry

Despite the mentioned benefits, concrete has downsides that have attracted increasing public attention in recent years. Its carbon footprint is high due to cement production and raw materials extraction, which is in addition to its energy demand and consumption. When considering current initiatives that promote cleaner and more sustainable industries, like the Canada action plan to reach net-zero emissions by 2050, it becomes imperative to develop eco-friendly solutions that can be feasibly adopted at scale by existing cement and concrete industries over the medium and long term.

As is to be expected, the cement and concrete industries are closely related, as the former produces the hydraulic cement that is essential for concrete production. Cement is an artificial product obtained through the calcination of limestone, clay, and other mineral fractions at very high temperatures, usually around 1450°C (Neville, 2011). This stage is highly pollutant due to the chemical decomposition of the raw materials (which releases carbon dioxide) and the fuel required to operate the kiln. Once this process is complete, the result is a stone known as clinker, which is ground and mixed with gypsum to form the final cement powder, better known as Portland cement.

The global annual cement production in 2022 was around 4.1 billion tons (U.S. Geological Survey, 2023). It is estimated that the production of 1 ton of cement generates 1 ton of carbon dioxide (CO_2), and its production contributes 8% of the worldwide green house gas (GHG) emissions and 3% of the global energy demand (Monteiro et al., 2017). Considering that cement accounts for 8 – 15% concrete's composition by mass, or 10 – 20% by volume, and that per year almost 33 billion concrete tons are produced, the impact of these two industries on air pollution and global warming is significant.

Aside from cement, aggregate production also plays a major role in the concrete industry's environmental footprint. Coarse and fine aggregates collectively account for 60 – 75% of concrete's volume. These materials are traditionally obtained through the

exploitation of natural sources (like riverbeds or sand banks) and quarries that are locally available but are being depleted at an accelerating rate due to the increased demand. It is estimated that the current yearly demand of natural aggregates that are used for concrete production is close to 25 – 30 gigatons (Coffetti et al., 2022).

This situation has led to two issues, namely supply and logistics. The supply issue arises from the depletion of the current sources, which makes the exploration and exploitation of new sources with the required quality a necessity. Besides that, the current extraction processes are being questioned due to their pollution and environmental impact. Most likely, the new sources will be located far from urban centres, as the current sources are the ones closer to them. Therefore, delivery times, transportation costs, and emissions are expected to increase due to the geographical factor (Abbas et al., 2006).

Projections indicate that the use of concrete will keep growing over the coming years, as the human population could potentially reach 10 billion by 2050 (Coffetti et al., 2022). This will impose a great challenge for the industry, especially considering the current decarbonization goals that aim to tackle global warming and climate change. The goals established by the Canadian Federal Government target an emissions reduction of 40% below 2005 levels by 2030, and total carbon neutrality by 2050 (Government of Canada, 2022). Therefore, to meet these goals, newer alternatives are required.

1.3. Research contribution

Although there is general agreement on the challenges the industry faces, a lack of consensus remains on how to solve them. Among the pool of options is the use of recycled concrete aggregates, or RCA, as a step towards a circular economy. This material is primarily classified upon its source origin, being either construction and demolition waste (C&D) or returned unused concrete (i.e., concrete that is brought back to the plant after not being poured in its original destination).

The first family can vary depending on the quality, age, and function of the parent structures that were demolished, while the second generally presents more uniformity in its properties and quality, thus making it easier to characterize. Both RCA sources not only present the advantage of reducing the required amount of fresh new aggregates for new concrete mixes (which by itself already helps to curb the carbon footprint), but they can also give a second life to materials that are usually seen as waste or low-quality products that would otherwise be disposed of in landfills.

The composition of RCA is highly variable depending on the parent concrete, but it can generally be considered as a mix between virgin aggregates, attached mortar (or residual mortar), and impurities. The use of RCA is not a new concept; it has been studied over the past decades but mainly by incorporating them via direct coarse or fine aggregate replacement, which can be by volume or mass. Nevertheless, this simple and common method does not account for the extra mortar content that is being incorporated into the concrete; thus, lower mechanical properties can be expected since the proportions and characteristics of the components in the resulting concrete are not the same. Hence, the use of RCA concrete for structural applications is still an area of debate, since there is a lack of consensus regarding the safety and quality of concrete structures made with recycled materials (Coppola et al., 2019).

To account for this difference, the Equivalent Mortar Volume Method, or EMV, was developed. This method acknowledges the RCA nature and uses the residual mortar as a key parameter to allow the designer to rebalance the proportions of the different concrete ingredients, thus allowing the design of a mix that can effectively incorporate RCA and match the original proportions of a mix made with fresh new aggregates (Fathifazl et al., 2009a). The advantage of the EMV Method relies on its applicability to different RCA sources, and on its ability to produce concrete with similar mechanical properties to reference mixes made with natural aggregates only.

This work aims to contribute to the advancement of knowledge and practice by extending research on the EMV Method to an area that has not yet been fully investigated, which is the bond behaviour of steel-reinforced RCA concrete samples that are subjected to cyclic loading. This research aims to achieve three primary objectives:

1) Understand the impact of the EMV Method on the design and performance of new concrete mixes using coarse RCA at high replacement levels.
2) Analyze the bond behaviour between steel and EMV-mixed RCA concrete under monotonic and cyclic loading based on the current Canadian provisions for structural applications (CSA A23.3).
3) Based on the performance of EMV-mixed RCA concrete, determine if the current Canadian provisions can be applied for structural applications involving the use of coarse RCA and the EMV Method.

It is expected that the results of this research project can help orient future full-scale tests to determine whether EMV-mixed RCA concrete can be safely used for structural seismic applications.

1.4. Thesis organization

This thesis comprises four chapters that detail the materials and methods employed to fulfill the research objectives. A brief description of each is presented below:

- Chapter 2 – Literature review and current state-of-the-art, will focus on the up-to-date knowledge, practices, and trends involved in the development of the cement and concrete industries. The first part will introduce general concepts and the challenges faced by these industries. Meanwhile, the second part will be based on the use of RCA, the EMV Method, and their potential for structural applications. Finally, the third part will be dedicated to bond behaviour of steel reinforcing bars in concrete, current testing procedures, and their relevance for seismic applications.

- Chapter 3 – Concrete mix design, will focus on the materials science component of the project, which involved the development of four concrete mixes with the same water-to-cement (W/C) ratio and produced with different mix design techniques, binder type, nature and quantity of coarse aggregates.
- Chapter 4 – Bond behaviour of steel-reinforced RCA beam-ends, will introduce the structural testing portion of this project that focused on the cyclic bond behaviour of RCA concrete specimens proportioned by the EMV Method. The first part will describe the development of the test specimen, testing apparatus, and loading protocol. In contrast, the second part will concentrate on the data analysis and understanding of the test results.
- Chapter 5 – Conclusions and recommendations, will be centered on the main outcomes of the research, their implications and contribution to the academic world and industry. Likewise, considerations and recommendations for future work will be outlined based on the gathered experience.

2. Literature review and current state-of-the-art

2.1. General considerations

This research can be considered as a two-stage project, since the implementation of RCA in new concrete mixes for structural seismic applications has two key components: one related to material science, and another one related to structural performance. The former aims to demonstrate that effective mix proportioning (with some iteration) yields a quality and reliable product, while the latter focuses on a structural testing program to evaluate the bond performance for the desired seismic applications.

Therefore, this chapter will focus on the current state-of-the-art of both stages with the use of RCA as the main driver. The chapter is organized in five subsections, which will cover the main practices, regulations, and challenges, and a final summary subsection highlighting identified research gaps that will help define the experimental phase of the program.

2.2. Cement and concrete industry

2.2.1. Basic components and current regulations

Even though the use of cement and concrete is a worldwide practice, every country has a set of regulations that dictate the parameters under which they must be implemented. In the case of Canada, hydraulic cements must comply with the guidelines established in *CSA A3000:23 – Cementitious materials compendium* (CSA Group, 2023). Here, different binders are classified based on their intended use and/or chemical composition, divided into four main types:

- General use hydraulic cement.
- High-early-strength hydraulic cement.
- Moderate sulphate-resistant hydraulic cement.
- High sulphate-resistant hydraulic cement.

When using Portland cement (PC), the nomenclature for these types becomes GU, HE, MS, and HS, respectively. Additionally, in the last couple of years, blends of PC and limestone filler, or Portland-limestone cement (PLC), have been approved for use under the same categories but with a different nomenclature, namely GUL, HEL, MSL, and HSL, respectively. These variations currently represent most of the market offering.

The use of limestone filler has primarily been driven by an effort to reduce the carbon footprint and energy demand of cement production (Voglis et al., 2005). The replacement limits have different tolerances and vary per country or territory. In Canada, PLCs can contain up to 15% of limestone filler, as the established limit provides a safety margin to keep the binder's performance in terms of strength and durability, but at the same time benefiting from the emissions reduction, which in Canada is estimated to be close to 10% (Cement Association of Canada, 2023). In the United States, the same 15% limit is mandated by *ASTM C595 – Specification for Blended Hydraulic Cements* (ASTM, 2024e); while in Europe, the allowance is significantly higher as stated in the *EN 197-1 - Cement - Part 1: Composition, specifications and conformity criteria for common cements* (CEN, 2011), with a ceiling of up to 35%.

Concrete, on the other hand, when used in Canada shall conform to the requirements of *CSA A23.1:24 – Concrete materials and methods of concrete construction*, and *CSA A23.2:24 – Test Methods and Standard Practices for concrete* (CSA Group, 2024a). Apart from cement, requirements are also outlined for other concrete constituents to achieve consistent properties and quality control. Reinforced concrete containing deformed steel bars for structural applications must comply with the requirements of *CSA A23.3:24 – Design of concrete structures* (CSA Group, 2024b).

The main requirement for the mixing water in concrete is to be potable (to avoid any pathogens that can damage concrete), otherwise it must be tested. For aggregates, CSA A23.1:24 sets the parameters that control the grading and particle shape of both fine and

coarse aggregates. For most applications, normal-density aggregates are used; gravels or crushed stones comprise the coarser fraction, while natural or manufactured sand are considered as fine aggregates.

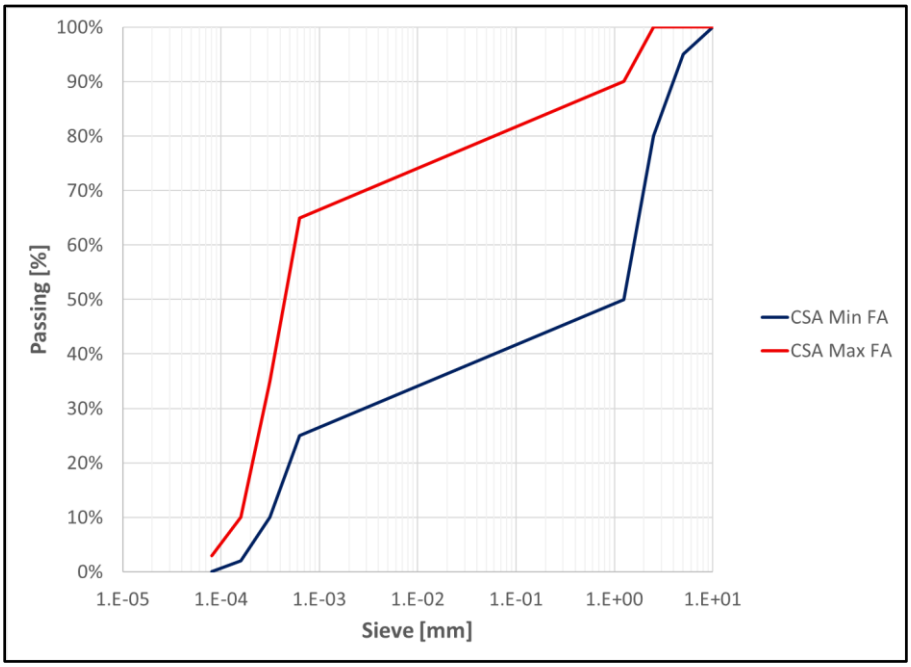

Figure 2-1: Grading limits for class FA1 fine aggregates (CSA Group, 2024a).

Grading is evaluated by a sieve analysis and pre-defined particle size distribution (PSD) curves with different tolerances based on the maximum nominal sizes of the fine and coarse aggregates (as seen in Figure 2-1 and Figure 2-2, respectively). On the other hand, particle shape mostly depends on the source origin of the material: when coming from riverbeds, shapes tend to be round, whereas, when coming from quarries or pits, shapes are angular due to the crushing process.

Concrete properties can generally be classified according to the phase in which they are measured: fresh state or hardened state. These properties are tested to guarantee a concrete that meets workability, strength, and durability requirements. Since concrete's microstructure is not uniform like steel, it is highly dependent on the proportions of its components, mix design, and batching techniques.

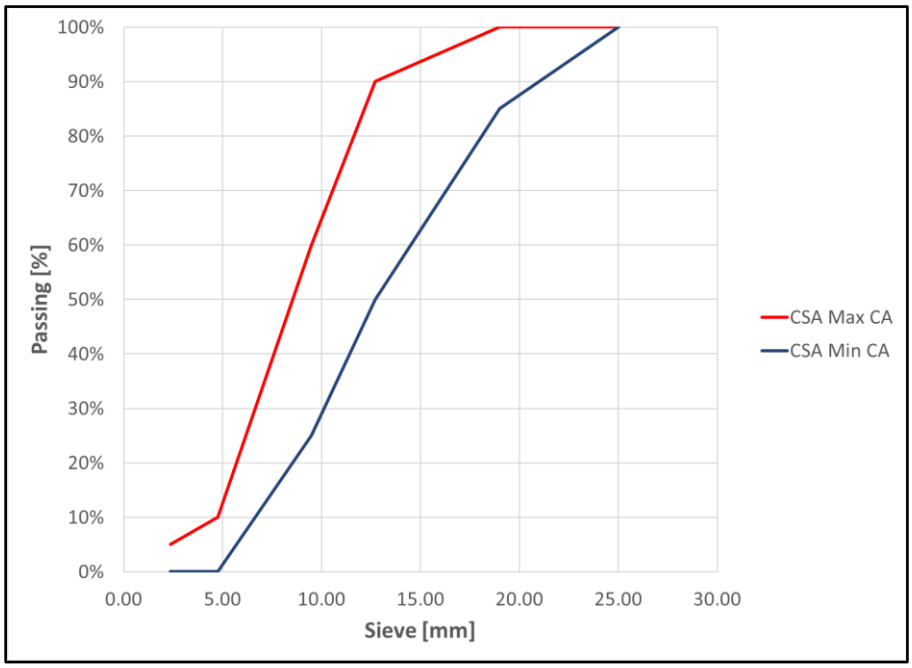

Figure 2-2: Grading limits for Group I, 20 – 5 mm coarse aggregates (CSA Group, 2024a).

In the Canadian practice, CSA A23.1 establishes different classes of exposures, which are defined based on combinations of applications (including those for reinforced concrete) and exposure conditions. A class can be divided into different subcategories for more specificity, and requirements are outlined for the following parameters:

- Maximum water-to-cement (W/C) ratio.
- Minimum specified compressive strength (f_c') in megapascals (MPa), and age at test in days.
- Air content category.
- Curing type.
- Resistance to chloride ion penetration.
- Additional requirements for sulphate attack if needed.

These requirements directly impact the mix proportioning of the concrete, which in Canada is based on the guidelines provided by *ACI 211.1 - Selecting Proportions for Normal-Density and High-Density Concrete—Guide* (ACI, 2022), or by the *Design and Control of*

Concrete Mixtures (EB101) (Cement Association of Canada, 2022). It is important to highlight that most of the available data on these guidelines was empirically obtained; therefore, the provided tables and graphs should be used as a reference when selecting the values, which later will need to be tested and updated in a series of trial batches before going into full production (Hover, 1995).

In the design, the intended concrete application sets the workability requirements, which limits the nominal maximum size of the aggregates (to avoid issues in congested zones as when working with steel reinforcement) and the desired slump target (how flowable the fresh concrete must be). Durability is commonly related to the minimum cement and air contents, where the latter can be entrapped (as a natural mix design result) or entrained (artificially incorporated).

These requirements are based on the selected class of exposure, which will also set a maximum W/C ratio, a minimum compressive strength target at a determined age (i.e. 28 or 56 days), and the curing type. Curing focuses on providing adequate moisture and temperature levels after the concrete is placed and maintaining them for a finite period to guarantee the development of the desired properties like compressive strength.

The strength estimation is derived from Abrams' Law, which defines that concrete's strength is inversely proportional to the W/C ratio (Neville, 2011). In other words, concrete applications that require higher strengths will need to have lower W/C ratios, which translates into more cement for a given amount of mixing water. Since the water content is given by the slump target, the estimated cement content can be computed using this arithmetic relationship.

Finally, the aggregates proportioning is based on a unit volume, traditionally one cubic metre (1 m^3). The coarse aggregate volume is determined by its nominal maximum size, dry-rodded density, and the fineness modulus of the fine aggregate. On the other hand, the

volume of fine aggregates is computed at the end by volumetric differences since the values of the water, concrete, air, and coarse aggregates volumes are known.

When referring to the batching techniques, they are mainly divided according to the size of the intended concrete volume production. For most applications, ready-mix concrete is the default option since larger amounts of concrete are required. Ready-mix refers to concrete made in a special facility off-site and that is delivered to the place where the construction is taking place. CSA A23.1 establishes a maximum time of 120 minutes for the delivery, and the number of revolutions of the equipment used for the mixing is left to the manufacturer's criteria.

Concrete mixed on-site is employed when ready-mix concrete is not a viable option, which can be due to size, cost, or location factors. This alternative is also used for small-scale applications, such as concrete made in a laboratory, where the main difference is that the mixing process is less industrialized. For such applications, the mixing process, which includes the apparatus and mixing time, is ruled by the Standard Practice A23.2-2C of CSA A23.2, or by its American counterpart *ASTM C192 - Standard Practice for Making and Curing Concrete Test Specimens in the Laboratory* (ASTM, 2019).

Finally, quality control refers to all the tests and requirements that must be met to guarantee that the final product will meet the design goals. In the fresh state, properties like air content, fresh density, and slump measurements are among the ones that must be controlled. CSA A23.2 contains the details that regulate the tests that need to be applied in the Standard Practices A23.2-4C, A23.2-5C, and A23.2-6C, respectively. In the case of the hardened state, one of the critical parameters to determine concrete's quality is the measurement of the compressive strength, which is made via standard-cured cylinders that must come from the same batch that was placed in the field and be tested at specific ages, and whose requirements are established in the Standard Practice A23.2-9C.

2.2.2. Additional features of modern-day concrete

Besides the traditional constituents of a concrete mix design, two additional elements are relevant for the modern-day formulation and production of concrete: supplementary cementitious materials (SCMs) and admixtures.

According to the definition provided by *ASTM C125-25a - Standard Terminology Relating to Concrete and Concrete Aggregates* (ASTM, 2025), an SCM is an inorganic material that contributes to the properties of a cementitious mixture through hydraulic or pozzolanic activity, or both. Examples include fly ash, silica fume, and slag cement, among others. When referring to the activity of an SCM, hydraulic refers to the same behaviour as with PC or PLC, meaning that the material reacts in the presence of water and starts developing hydration products. In contrast, pozzolanic activity means that the material does not directly react in the presence of water, but it will once the initial cementitious hydration products coming from PC or PLC start to take place.

SCMs come from natural sources, like volcanic pozzolans, or as byproducts of other industrial processes, like ground granulated blast furnace slag (GGBFS) or fly ash. SCMs are used in combination with PC or PLC; consequently, CSA A23.1 employs the term “blended hydraulic cement”. As with regular cement, there are different blends based on the intended application, as well as limits in the number of SCMs and in the respective amount that can be incorporated, also known as clinker replacement ratio.

The use of SCMs has been a way to reduce the environmental and economical impact of PC, not only due to the PC replacement levels, but also because of the recycling of products that are residues of other industries (Liew et al., 2017). Moreover, the chemical compatibility of SCMs and PC further enhances their use, since minimal changes to the mix design need to be adopted while gaining improvements in areas such as workability, thermal cracking, and sulphate attacks (Mehta & Monteiro, 2014). Such benefits have created the desire of trying to increase the clinker replacement ratio, but there is still a

debate on how to predict the mechanical properties and durability, especially at early stages (Juenger & Siddique, 2015).

Nevertheless, two major concerns affect the use of SCMs. The first one is the geographical location of the source, which limits the availability of a specific blend and increases the transportation costs, and by consequence, the associated GHG emissions (Miller, 2018). The second concern is regarding their medium- and long-term supply. Since SCMs either come from natural limited deposits, or from industries that are trying to reduce their emissions and waste, or directly expected to be decommissioned in the next decades as in the case of coal power plants, the use of SCMs might become more strategic while newer alternatives are explored (Diaz-Loya et al., 2019; Scrivener et al., 2018).

The second element of modern-day concrete that requires attention is the use of admixtures. These are materials other than water, aggregates, cementitious materials, and fibre reinforcement that are used as an ingredient of a cementitious mixture to modify its freshly mixed, setting, or hardened properties, and that are added to the batch before or during its mixing (ASTM C125-25). Furthermore, another characteristic is that they are added to the mix in small quantities, commonly a fraction of the required cement mass.

CSA A23.1:24 splits the requirements into three categories: air-entraining admixtures, chemical admixtures, and powdered admixtures. The first category shall comply with the requirements of *ASTM C260 – Specification for Air-Entraining Admixtures for Concrete* (ASTM, 2024c). The second category, which includes admixtures such as high-water-reducers or superplasticizers, shall conform to the requirements of *ASTM C494 – Specification for Chemical Admixtures for Concrete* (ASTM, 2024d). Finally, powdered admixtures are left to the manufacturer's recommendations.

The current concrete admixtures offering is wide since they are developed to modify specific properties upon the intended use, thus their development and testing is costly

given the chemical complexity of their formulation (Hanehara & Yamada, 1999). Even though they are an intrinsic component of modern concrete, it is easy to misuse them as they might not be compatible with certain cement compositions or with another admixture used for the same mix, hence the relevance of trial batches. Additionally, they will not compensate for a lack of quality materials or mixing processes (Mehta & Monteiro, 2014). For the purposes of this research, two types are of particular interest: air-entrainers (AE) and high-range-water-reducers (HRWR).

Air-entraining agents are primarily designed to avoid the negative impact of freeze-and-thaw cycles or, in other words, the damage caused in the concrete microstructure due to expansion and diffusion of the capillary water. This phenomenon is recurrent in countries with cold climates like Canada. Thus, the concept of air entrainment is to provide a way for that water to escape and avoid the mentioned damage. This effect is achieved by intentionally incorporating air bubbles to the mix via a suitable agent (Neville, 2011).

Air will always be present in a concrete mix; therefore, it is important to distinguish the two types to avoid confusion. Entrapped air occurs naturally during mixing and ASTM C125 defines it as voids with a size of 1 mm or larger, and of irregular shape. In contrast, the voids of entrained air have a size in between 10 – 1000 μm (1 mm), and with a near perfect spherical shape (ASTM, 2025). The use of entrained air is an effective way to enhance concrete's durability in cold climates, but it also decreases its density and compressive strength, which is reflected in the mix design guideline curves.

Water-reducer agents, also known as plasticizers, are one of the most known and used admixtures. They control the rheological properties of concrete, such as the plastic yield stress and plastic viscosity (Marchon et al., 2018). Their actions usually take place at early stages once initiated during the mixing process and translate into benefits such as a reduction in the amount of mixing water (and consequently lowering the W/C ratio), and improvements in the workability of the mix (higher slumps and better mix homogeneity).

Due to their formulation, these chemical admixtures are conceived to act based on the different stages of cement hydration, which is a combination of solution processes, interfacial phenomena and solid-state reactions. They present an affinity towards the surface of the cement hydration products, resulting in high adsorption levels and in the alteration of the surface properties of the cement particle and its interaction with the solution phase; this is why these admixtures can modify specific properties by enhancing dispersion and reducing nucleation (Jolicoeur & Simard, 1998).

Dispersion, also known as Van der Waals forces, is based in local polarization fluctuation between particles; this change in polarity modifies the traditional particle affinity and results in electrostatic repulsion (Gelardi & Flatt, 2016). Nucleation, on the other hand, refers to the formation of any solid hydration products, which can be homogeneous in a solution phase, and heterogeneous in a solid-solution interphase (Jolicoeur & Simard, 1998). Besides these concepts, the differentiation between plasticizers and superplasticizers is relevant. According to *ASTM C494 – Standard Specification for Chemical Admixtures in Concrete* (ASTM, 2024d), a superplasticizer or high-water-reducer-agent, has the same effects of a plasticizer but with a guaranteed reduction of at least 12% in the mixing water requirement for a given slump.

The current generation of superplasticizers is based on polycarboxylates (PCE); several types are available but a common characteristic is that the chemical composition is based on long polymeric organic chains (Plank et al., 2015). Their effectiveness mostly depends on balancing the reactivity of the interstitial aluminate phases of the cement with the sulfate availability (which enhances the adsorption to the early hydration agglomerates), as well as on the variation of the addition times (a delay favours the effect of the plasticizer), and on the selected usage rates (the relationship between dosage and setting time might not be linear) (Cheung et al., 2011).

The sulfates availability favours the early reaction of the aluminate faces, which in turn form the initial hydrates to which the superplasticizer adheres. If enough sulfates are unavailable, or if the addition of the admixture occurs at the wrong time, part of the superplasticizer will be consumed (absorbed instead of adsorbed) by the early chemical reactions, thus reducing the efficiency since a lesser amount will be available for the desired dispersion effect (Flatt & Houst, 2001).

Efficiency is important given the magnitude of the PCE-based superplasticizers consumption. It is estimated that their annual production is close to 15 million tons, with a carbon footprint that ranges between 2.40 – 2.98 kg of CO_2 per kg of produced PCE, which could potentially be reduced by almost 80% with the use of renewable energies (Schiefer & Plank, 2023). However, efficiency is not always a synonym of robustness. The latter can be defined as when the overall behaviour of a system will not be affected by a slight change in one of its components (Nkinamubanzi et al., 2016); therefore, compatibility between cement and admixture can severely impact the mix performance.

Parallel to the PCE-based superplasticizers, a new generation of admixtures is being developed, the so-called super absorbent polymers (SAP). They have the advantage of controlling the water content and its associated macro-porosity. As their name indicates, they can absorb and release water at different stages, which makes them suitable for the control of the fresh and hardened states. One of the potential advantages of these admixtures is the improvement in the curing process, and the associated shrinkage reduction (Liu et al., 2017, 2019; Mechtcherine et al., 2021).

2.2.3. Next generation binders

Different alternatives have been proposed to curb the emissions coming from the cement production to meet the carbon neutrality target by 2050. Development areas have been identified in the use of alternative fuels, improvements in the thermal efficiency of the cement production, reductions in the clinker-to-cement ratio, and the use of alternative

binders. In addition to these technological developments, other strategies that are being implemented to speed up the process come from new regulations, specifically via carbon taxes and emissions caps (Schneider, 2019).

The existing norms for hydraulic binders are conservative because the main goal is to protect the users of the final hardened products against errors coming from defective materials and/or from poor workmanship. Therefore, the development of new binders needs to focus on understanding how these new materials can be formulated to provide a microstructure similar to or better than PC, how they react until they reach a thermodynamic equilibrium, and how they can be modified to meet different requirements such as reaction rates for strength development and workability in terms of slump or flowability (Gartner & Hirao, 2015). The true potential of a new binder could be measured if it can effectively replace PC in a 1:1 ratio, such that it would be possible to gain insights into its performance and durability (Gartner & Macphee, 2011).

Additionally, these new generation binders will need to be economically viable to be able to compete with PC in the medium-term, and to replace it in the long-term. To achieve this goal, they must be attractive in pricing, which means the formulation and production costs must be low given the amount of concrete that is being used worldwide. They also need to have lower emissions in the manufacturing process when compared to PC, and be safe, which requires testing and updated regulations (Imbabi et al., 2012).

Most of the improvements and changes that PC has experienced during the last decades have been through the implementation of SCMs and admixtures, but there are still knowledge gaps in their structure, composition, and reaction mechanisms (Biernacki et al., 2017; Liew et al., 2017). Therefore, the development of new binders will be based on a deeper understanding of the cement hydration, especially the study of three physical effects, namely cement dilution, particle size distribution (PSD), and nucleation; and how

they relate in terms of chemical affinity, fineness, and the nucleation degree (homogeneous or heterogeneous) when they react (Lawrence et al., 2003).

Clinker replacement is based on increasing the amount of SCMs in the cement composition. This option is well-suited for the short-term because it allows a reduction in the emissions coming from PC, the raw materials are available, and is compatible with the current industrial processes (Miller et al., 2018). These new binders are often labeled as ternary blends, they favour the inclusion of adequate fillers (like limestone), and available results show increased resistance to crack propagation without compromising the mechanical properties and durability of concrete (Das et al., 2015). Nevertheless, the availability and extended use of SCMs could outweigh the environmental benefit because of the involved emissions in the manufacture and transportation processes, thus making efficiency a key factor and a challenge (Miller, 2018).

Another alternative that has gained support in the last couple of years to reduce the clinker content is the use of calcined clay limestone cements, or LC^3. Acknowledging the limited supply of SCMs in many parts of the world, this approach utilizes one of the most widely available materials on Earth's surface: kaolinitic clays. These materials can be calcined at much lower temperatures than regular PC, around 700 – 850 degrees Celsius. The effectiveness of these cements relies on the reactivity of the clay, which with at least 40% of kaolinitic content can lead to similar performances compared to PC. One example is the LC^3-50 cement, whose composition includes 50% clinker, 30% calcined clay, 15% limestone and 5% gypsum. These cements are still being studied to understand the effects of the clays on the hydration processes, but they have shown good potential, which can be further increased with the development of the next-generation SAP admixtures (Avet & Scrivener, 2018; Popa et al., 2025; Scrivener et al., 2018).

When referring to alternative binders, two options are promising for the short-term: cements coming from reactive belite-rich Portland cement (RBPC), and cements based on

calcium sulfoaluminates (CSAs). RBPC shares the same raw materials used for PC production, but the final chemical composition is different. They tend to harden more slowly but require less temperature for their production, which could generate an emissions reduction close to 10% (Gartner & Sui, 2018). On the other hand, cements coming from CSAs were originally developed in China during the 1970s and have the advantage that they are not based on carbonate sources like limestone, but on alumina-rich stones. The emissions reduction potential when compared to the current Chinese PC and PC-blends would be close to 36%, and 52% when used with RBPC. However, the main drawback comes from costs of the raw materials, since alumina sources are also sought for aluminum production (Nie et al., 2022).

In the case of alternative binders that can provide solutions in the medium- and long-term, four groups are identified: alkali-activated materials (AAM), belite-ye'elimite-ferrite clinkers (BYF), carbonatable calcium silicate clinkers (CCSC), and magnesium oxides derived from magnesium silicates (MOMS).

AAM, or geopolymers, are a combination of SCMs and an activator, with the latter accounting for 5 – 10% of the mass composition. Their costs are mainly driven by the SCMs availability and the chosen activator, which is the most expensive component. When compared to PC, emissions are lower and the overall mix design is similar, but it requires an optimization depending on the selected SCM-activator combination, and a good curing method selection (sealed curing is recommended). It has been reported that the activator might leach and stall the strength development process when immersed in water, while dry curing has led to surface cracking (Provis, 2018).

Another aspect that needs attention is the compatibility between AAM and modern admixtures, which were originally developed for PC. The use of SCMs like slag presents a challenge given that they have different surface chemistry, zeta potential, and dissolution mechanisms when compared to PC. The use of short-chain PCE-based admixtures has

proven effective to control the rheological properties of these mixes, although the overall optimization with different binders and activators has yet to be systematically understood and tested (Shi et al., 2019).

One of the main issues that affect the performance of AAM is their dependence on the activator's nature. In the case of slag-AAM, when the activator is sodium hydroxide ($NaOH$), the initial strength is acceptable but its development stalls in the medium-term; whilst the use of sodium metasilicates (also known as water glass, WS) activators slows the initial reaction but delivers a better strength development over time (Winnefeld et al., 2015). This strength development behaviour can also be observed when applying different mixing protocols, as longer mixing times affect the rheology of $NaOH$-activated slag-AAM, whilst they improve the rheology and mechanical properties of the WS-activated ones.

The difference in the strength development could be associated to the size of the microstructure, especially because coarser particles increase the porosity levels (Puertas et al., 2018). Furthermore, the activator can also give slag-AAM green-blue tones, different from the traditional grey of PC-based concrete, whose duration might be influenced by the curing methods and exposure conditions (Chaouche et al., 2017).

The second group are the BYF clinkers, they were originally created in China and their development is closely tied to the technology used in the manufacture of CSAs cements, with the potential to have 20 – 30% less emissions that those of PC (Gartner & Sui, 2018). As their name indicates, this clinker targets a high belite content (45 – 75%), which favours strength development over time, but also has the advantage of requiring less alumina content (20 – 45%), which is the most expensive component. Nevertheless, a complete understanding of the clinkering process, hydration, and binder formulation is still pending before upscaling the production process; therefore, commercialization and standardization are also non-existent or at early stages (Shi et al., 2019).

The third group are the CCSC, which are distinct from the previous two groups because the curing process is based on carbonation, which absorbs CO_2 and makes it very efficient in terms of emissions (30 – 40% less than normal PC production, or even 70% if the supply of the CO_2 for the curing process comes from other industries), which would fulfill the principles of a circular economy (Gartner & Sui, 2018). However, their implementation has two major limitations: its curing process requires high CO_2 atmospheres (thus mainly suited to precast facilities) and carbonation lowers the pH of the concrete, which would become an issue for RC because of the loss of the protective passive layer (Shi et al., 2019).

Finally, the fourth group are composed by the MOMS, magnesium oxide (MgO)-based binders that have good performance compared to PC but whose raw materials are scarce, and their manufacturing process is very energy demanding. MOMS would improve these issues with the addition of magnesium silicate, which have no chemically-bound CO_2 in their composition, and the possibility of using carbonate curing. However, the development is still at very early stages to assess their potential for PC replacement (Gartner & Sui, 2018).

2.3. Recycled concrete aggregates

2.3.1. Conception and definition

Recycled concrete aggregates (RCA) are a byproduct of the concrete industry that can be used as coarse or fine aggregate replacement in new concrete mixes. In terms of physical appearance, uncontaminated RCA (free from impurities such as asphalt or bricks) present a pale-grey or white colouration. When compared to natural aggregates, the colour is noticeably lighter, and it is due to the presence of a layer of residual mortar (RM) that is attached to the original aggregate. Since they are crushed following similar processes to those used in the natural aggregates production in quarries, shapes tend to be angular but with a rougher surface and a RM that will vary depending on the size, with the smaller ones presenting the highest RM contents (Mehta & Monteiro, 2014; Silva et al., 2014).

The use of RCA is not a new topic; it first came to life after World War II in countries like Germany and the UK, where great amounts of rubble were left in several cities due to the extensive bombing suffered during the war effort. Their use in Germany was expedited because of the lack of raw materials and the weak post-war economy; the rubble was screened, crushed, and then graded for aggregate use. Meanwhile, in the UK the use of RCA was more controlled due to fears of suffering sulfate attacks, thus making the source origin more selective. Moreover, a wider use became difficult because of the high costs of its processing, especially when separating it from the reinforcement; therefore, much of it ended up being waste (Nixon, 1976).

Nevertheless, the continuous development of society in the 1970s – 1980s vastly increased the number of new buildings and waste coming from demolitions. When adding the concerns regarding the potential scarcity of new aggregates near urban areas, RCA attracted renewed interest, which manifested in several studies regarding their properties and performance. Testing results of that time are not different from what can be found in recent literature; issues with higher absorption, poor workability, lower density, and lower compressive strength were reported for uncontaminated sources. Furthermore, it was deemed that more efforts were needed to study the RCA durability and large-scale implementation, especially with the development of effective recycling processes that could favour the use of RCA coming from construction waste (Hansen, 1986; Nixon, 1978).

The source from which the RCA is obtained has traditionally been labeled as construction and demolition waste (CDW), encompassing all residues from previous structures that have been demolished, decommissioned, or reached the end of their lifespan. CDW includes materials such as concrete, asphalt, bricks, glass, among others; based on the predominant material of the waste that is being recycled, the batch will be labeled accordingly. In the case of RCA, to be considered as such, the consensus has been that it must be comprised of at least 90% (by mass) by derivates coming from concrete aggregates and PC products, although efforts have been made to reduce this threshold to

increase the usage spectrum along with the establishment of RCA quality categories (Oikonomou, 2005; Silva et al., 2014; Wang et al., 2021).

Nowadays, CDW poses a major challenge since it constitutes a major portion of all generated solid waste, and the traditional disposal of these large amounts of residues in landfills is no longer an acceptable option in countries like Japan. The main reasons are attributed to the scarcity of landfill space and the associated pollution (Meyer, 2009). The major producers of CDW are China (2360 million tonnes), the United States (600 million tonnes), India (530 million tonnes), and the European Union (500 million tonnes) (Wang et al., 2021). Given that these numbers are likely to increase over the coming years, it is expected that more pressure will be applied to recycle CDW.

An RCA-subcategory that has gained attention as a potential high-quality source is the so-called returned unused concrete (RUC) or hardened concrete. This group includes all concrete wastes that are returned or generated in ready-mix plants, and subsequently dumped and left to harden, giving place to RCA stockpiles. The production of RUC is tightly related to the efficiency of the plant and the construction industry; it is estimated that its production is close to 125 million tonnes per year, which by mass is between 1 – 9% of all generated concrete, with the US and Brazil having the largest numbers (Hansen, 1986; Xuan et al., 2018). Even if these figures are a fraction of the total generated waste, they are significant for the concrete producers, since they suffer the same spacing issues as the landfills. When adding the advantage that the composition of RUC can be traced and is more uniform, and that it has not been exposed to the environment for a long period of time like CDW, there is an incentive for potential acceptance and use.

2.3.2. Properties

Traditional implementation of RCA in research and in real-life structures has been made through the so-called Direct Replacement Method (DRM). This means that, once the RCA source is characterized, a parent concrete mix (upon which the RCA mix will be compared

to) is designed using conventional volumetric proportioning methods, such as ACI 211.1, of which a portion of the coarse and/or fine aggregate is then replaced with RCA (either by volume or mass). Since coarse and fine aggregates have different purposes in a concrete mix, researchers tend to study the RCA effects in new concrete mixes by replacing only one of them at a time.

The use of RCA for fine aggregate replacement has been characterized by the high amount of RM and impurities that have been found across several sources. When implemented in new concrete mixes, the common denominator has been the loss of workability, which translates in lower slumps and compaction issues. The high RM contents have been signaled as the main contributor to the observed absorption levels, mostly due to the RM's porosity. Properties such as compressive strength, modulus of elasticity, and tensile strength have shown a decrease with higher replacement ratios, while creep and shrinkage increased with the fine RCA replacement. The use of fine RCA has been more limited than coarse RCA due to their negative effects, but recent studies are focusing on the use of fine RCA as fillers, and in the potential reactivation of their mortar content (Evangelista & De Brito, 2014; Verian et al., 2018).

In the case of coarse RCA replacement, results are similar to those of fine RCA. The impact is typically studied for various replacement levels between 0% and 100% to determine if a certain optimum can be achieved (Verian et al., 2018; Wang et al., 2021; Xiao et al., 2005). Higher absorption levels have led to new concrete mixes that present lower workability and compaction issues. Absorption has been found to be around 4.7%, while the oven-dry density on average is 2327 kg/m^3, and the surface-saturated-dry (SSD) density is around 2442 kg/m^3 (Silva et al., 2014)

Besides the flowability or slump value, other properties that have observed reductions in their values include fresh density (5% on average for 100% replacement), compressive strength (14% on average for 100% replacement), elastic modulus (23% on average for

100% replacement), tensile strength (16% on average for 100% replacement) (Wang et al., 2021). These values are averages of several studies available in the literature; therefore, it is important to bear in mind that the drop might not be proportional to the replacement ratio, and that their dispersion might lead to even more negative results, with reductions of up to 40%, which can be a consequence of the different RCA sources, as well as different design parameters such as the W/C ratio.

On the other hand, properties like shrinkage, carbonation, creep, and permeability have shown increases with the coarse RCA replacement (McGinnis et al., 2017; Silva et al., 2015a, 2015d). Most interesting, it has been observed that a higher RCA replacement has been detrimental since the negative effects magnify, although there is consensus that a replacement up to 30% does not significantly affect performance when compared to conventional concrete (Colangelo et al., 2020; Damdelen, 2018; Hansen, 1986; Lotfy & Al-Fayez, 2015; McGinnis et al., 2017; Silva et al., 2014, 2015b, 2015c; Tam et al., 2005; Topçu & Şengel, 2004; Verian et al., 2018; Wang et al., 2021).

As observed, the RCA nature plays a role in the reported results as each particle is a composite of original aggregate and old mortar; the latter increases the RCA porosity, which explains the higher absorption levels and decreased density and flowability, independently of the RCA source in use (Omary et al., 2016). Further observations included the presence of microcracks, especially in the old mortar matrix of the RCA (Leite & Monteiro, 2016), which indicates the influence of the Interfacial Transition Zone (ITZ) in the overall behaviour.

For normal strength concrete, the failure will not take place in the aggregates but in the cement paste matrix, which is the weakest component and explains the brittleness of concrete when exposed to tensile loads. The reason behind this behaviour is the presence of the ITZ, which lies between the aggregate and the hydrated cement paste. The ITZ is complex in form and highly variable, with large volumes of capillary pores and microcracks, whose quantity and extension will depend on factors such as W/C ratio, aggregate grading,

and compaction techniques, among others (Mehta & Monteiro, 2014). The thickness of the ITZ is variable, reaching up to 50 μm and represents 20 – 40% of the cement matrix (Neville, 2011; Tam et al., 2005).

Porosity can be as high as 25% when close to the aggregate, which is inversely proportional to the ITZ thickness mainly due to the cement particles being unable to become closely packed against the aggregate, a phenomenon known as “wall-effect” (Neville, 2011). The size difference between the aggregate and the cement grains can be up to a few orders of magnitude, meaning the latter will have difficulties to create a seamless bonding with the aggregate surface, which in turn generates the presence of voids due to a lack of effective hydration (Wang et al., 2021). When RCA is included as an aggregate replacement, the new mix will have two ITZs, one given by the RCA nature, and a second one between the RCA and the new cement paste. Therefore, questions have been raised regarding how to improve these zones to avoid lower performance (Li et al., 2012).

On average, RCA are composed by 65 – 70% of original aggregates and 30 – 35% of RM, with the latter presenting carbonation development due to the first endured hydration process. It has been determined that the ITZ quality is strongly related to the quality of the parent concrete, meaning that RCA coming from high-performance concrete will in general tend to have better performance due to the quality of the original aggregate, and because of a more homogeneous and less porous ITZ; thus facilitating the formation of new hydration products that can yield better performance when using RCA (de Brito et al., 2016; Poon et al., 2004; Verian et al., 2018).

Likewise, another strategy devised for a better-quality RCA, besides the source origin, comes from treatments that can modify their surface and pore structure (Poon et al., 2004; Shi et al., 2016). One way is by improving the recycling process, which means that more crushing and filtering stages can be implemented to improve the grading and quality of the RCA, targeting a reduction in the attached RM (Lotfi et al., 2017; Paranhos et al., 2016; Silva

et al., 2017). Another alternative comes from heat and acid treatments, which induce mechanical and chemical stresses that target RM as a way to improve the RCA surface and reduce their water absorption (Al-Bayati et al., 2016). Alternatively, in the case of RUC, the implementation of washing systems to reclaim the aggregates while the concrete is still fresh can lead to RCA that are almost identical to fresh new aggregates in terms of quality, since most of the paste can be removed (Xuan et al., 2018).

A different approach to improve the RCA performance focuses on the mix design, especially targeting the fresh state. The "two-stage-mixing-approach" (TSMA) is one of the proposed alternatives that splits the mixing process in two halves with different timing to enhance hydration; the first stage will create a slurry that can fill the voids and cracks in the RCA area, to then improve the ITZ quality with the hydration products of the second stage (Tam et al., 2005). The TSMA was later modified to allow the inclusion of SCMs, which also reported improvements in the fresh state, and consequently in the hardened state (Tam & Tam, 2008). The only drawback of this alternative method is the extended mixing time when compared to standard procedures (Verian et al., 2018).

To improve the fresh state of RCA concrete mixes, it is required to address the flowability and compaction issues, and the elevated water absorption levels of RCA play an important role. One common solution is the addition of extra water in the mixing process to account for the absorption levels. Nevertheless, the time required to reach the absorption equilibrium is greater than the mixing time, which favours the formation of air bubbles that will not help the mix performance (Leite & Monteiro, 2016).

Hence, another mitigation strategy is the use of presoaking techniques (i.e., partially saturated or fully saturated aggregates) which aim to fill the capillary pores of the RCA prior to their mix incorporation, thus allowing the mixing water to effectively react with the cement and not be lost in absorption (Brand et al., 2015; Lotfy & Al-Fayez, 2015; Verian et al., 2018). However, a potential drawback would be the permeability of the RCA, which

favours water bleeding, which in high W/C ratio mixes could lead to segregation, water loss, and higher shrinkage levels. On the other hand, in low W/C ratio mixes or in dry environments, the water release could help during the curing process (Souche et al., 2017).

Finally, as with regular concrete, the use of admixtures has also been studied, especially to improve the fresh state properties. Superplasticizers have emerged as the natural candidate given their track record for normal aggregate concrete. Different scenarios have been tested, including different RCA replacement ratios, lower W/C ratios, use in combination with saturated aggregates, among others. Results have shown that their use is an effective way to offset many of the fresh state issues and provide stability and slump retention for longer periods of time, although their performance tends to decrease with higher RCA contents or drier aggregates, which lead to superplasticizer absorption in the high porosity areas (Kannan et al., 2021; Lotfy & Al-Fayez, 2015; Silva et al., 2015b).

A further concern comes from the RCA source when CDW is being used. Impurities such as clays are known for affecting the performance of PCE-based superplasticizers, which emphasizes the importance source quality, and how it might affect the compatibility with modern admixtures (Bravo et al., 2018).

2.3.3. Implementations and future potential

Ever since RCA were first considered an aggregate source, two main factors have been a common denominator in reported studies. The first one is the high variability in the source origin, which presents challenges for their classification, production, and quality control. The second factor is the performance drop in almost every category in both fresh and hardened states. Therefore, there is consensus that clients, contractors, and regulators lack confidence in their implementation, which has limited their use to roads, concrete pavements, and backfills amid the lack of knowledge regarding their structural performance (Abbas et al., 2008; Butler et al., 2013; Colangelo et al., 2020; Fathifazl et al., 2009a; Hansen, 1986; Kisku et al., 2017; Rao et al., 2007; Silva et al., 2014, 2017; Tam et al., 2005).

The lack of confidence in RCA concrete extends beyond civil engineering and affects the performance of the concrete industry from an economic perspective. As in any business, growth and development will be closely connected to investment and confidence. As long as the latter is not present, neither consumers, businesses nor governments will make the necessary investments to allow the industry to change and take the next step (Seiler & Duer, 2019). Moreover, to create confidence, RCA do not only need to perform well, but they also must create social benefits and be easy to use and/or adopt, otherwise there will be no incentives for their implementation (Silva et al., 2021).

The lack of incentives is primarily driven by the low cost of natural aggregates production. As of today, it is still less competitive to process and recycle CDW given the elevated transportation and manufacturing costs, especially when considering that they might come form multiple sources, which could lead to a lack of consistent good quality RCA supply (Meyer, 2009; Silva et al., 2014, 2017). In view of that, measures that have been considered are green taxes for natural aggregates and cement production, as well as policies that mandate and expand RCA implementation (Garbarino & Blengini, 2013).

Policies that mandate a wider use of RCA will have an impact on their production, especially when assuring their quality. It has been devised that recycling processes will need optimization, as well as an integration to the natural aggregate supply chain and concrete production line (Garbarino & Blengini, 2013; Lockrey et al., 2018; Silva et al., 2017; Wijayasundara et al., 2016). A way to improve the recycling process and reduce its environmental impact is by prioritizing selective demolition, which emphasizes reclamation of raw materials with less impurities, thus adding value (Hansen, 1986; Nixon, 1978; Silva et al., 2014; Xuan et al., 2018).

Another alternative is to develop consistent RCA classifications so that their integration in production lines would be more streamlined (Lockrey et al., 2018; Silva et al., 2014). In Canada, for example, guidelines for RCA selection and use have been proposed; they set

four performance classes that are driven by the RCA properties, their comparison to natural aggregates, and the intended application (Butler et al., 2013). Likewise, quality requirements and technical specifications have been enacted in Europe to ensure RCA performance and durability, which are of upmost importance given the efforts to achieve a minimum CDW replacement target (Garbarino & Blengini, 2013).

When it comes to regulation, there are different realities. In the case of the United States, the guide *ACI PRC-555-01: Removal and Reuse of Hardened Concrete* (ACI, 2001) provides information and recommendations for the use of RCA, but is has not been updated in more than 20 years. Moreover, aggregates for concrete applications need to comply with the requirements of *ASTM C33/C33M - Standard Specification for Concrete Aggregates* (ASTM, 2024a). In this standard, the concept of RCA is present, although there are no special categories; therefore, it is implied that if used, they must comply with the requirements for natural aggregates (Butler et al., 2013).

In the case of Japan, the push for recycling RCA started in the 1980s – 1990s with the first studies mandated by the Japanese Government. The use of RCA is regulated by the Japanese Industrial Standards (JIS) A 5021 – A 5023 (JSA Group, 2024a, 2024b, 2024c), which classify RCA based on properties and potential use. In most cases, a 100% coarse RCA replacement is allowed, and they can be used in ready-mix concretes with compressive strengths up to 45 MPa. Nevertheless, the production of high-quality RCA still remains costly, which has led RCA to be used in pavements and backfills applications (Eguchi et al., 2007; Gartner & Hirao, 2015; Koga et al., 2022).

The case of China is different: even though the concept of CDW was introduced by the Chinese Government in 2003, the country is estimated to recycle only 10% of their generated CDW. Financial and political incentives, in addition to the lack of technical data and social acceptance have been signaled as the main causes (Wang et al., 2021).

In Europe, Switzerland has been indicated as one of the pioneers in the use of RCA for structural applications. The first pilot studies include the construction of a school with up to 80% RCA, and the e-science lab of the ETH Zurich in the Hönggerberg Campus (Wang et al., 2021). RCA use is currently regulated by the Swiss Standards SIA 2030, which was based on OT 70,085 and SIA 162/4 standards (SIA Group, 1994, 2021). The first one established two categories, namely classified and unclassified concrete. The difference between them is that the first one complies with the requisites of SIA 162/4 for aggregate use in concrete applications, which can lead to RCA replacements of up to 100%, while the latter is destined for plain concrete applications (Tam et al., 2018).

The case of Germany is a bit different: even though CDW recycling rates are very high (almost 85%), the use of RCA for either roads or concrete applications is around 21% (Wang et al., 2021). The approach for the RCA quality is like the Swiss one, with different categories differentiated by properties and source origin. The DAfStb (German for Guideline of the German Committee for Reinforced Concrete) through the DIN EN 206:2021-06 (concrete specification), DIN 1045-2:2023-08 (RC requirements), and DIN 4226-101:2017-08 (RCA requirements) standards set the regulatory framework. However, the maximum RCA replacement rates are set to 35% for concretes up to 35 MPa, and 25% for concretes up to 25 MPa (DIN, 2017, 2021, 2023; Koga et al., 2022; Tam et al., 2018).

In Canada, the latest 2024 update of the CSA A23.1/CSA A23.2 Canadian Standards introduced key modifications to allow the use of RCA in replacement ratios up to 30% (CSA Group, 2024a). Likewise, RCA will be labeled as Reclaimed Concrete Material (RCM) or Returned Hardened Concrete (RHC), and they are defined by CSA A23.1 as follows:

RCM are concrete material made from end-of-life concrete with minimal tolerable contamination from non-concrete materials obtained from the demolition of built concrete elements. Examples of RCM are sidewalks, concrete pavements, concrete infrastructure, and

concrete from buildings not contaminated by foreign materials. RCM is subcategorized into two types:

- *Type 1 — where a single source of concrete (such as a section of concrete pavement) is utilized in the production of RCM and for which there is an expectation of greater consistency; and*
- *Type 2 — where multiple sources of concrete are processed together at a single production site to produce RCM. Note: RCM does not include construction and demolition waste containing foreign materials.*

RHC are concrete material made from unused plastic concrete from known sources that has been returned directly to the concrete plant or obtained from in-plant concrete waste streams, which is allowed to harden and then processed by crushing. RHC is subcategorized into two types:

- *Type 1 — where the RHC is from a single source and known to have been produced from non-reactive aggregates; and*
- *Type 2 — where the RHC is from multiple sources or is known to have been produced with reactive aggregate utilizing mitigation measures.*

Given the development rates that modern society are experiencing, there is little doubt that RCA will be implemented in structural applications in the near future (Neville, 2011). In an industry that is known for its slow changes, the potential that newer technologies, computing power and materials bring, will help innovation and to fill the current knowledge gaps (Biernacki et al., 2017). The industry will need to be resilient and adapt to the new challenges created by the latest population, climate, and geopolitical trends. The implementation of the mentioned policies can be the incentives the industry needs to expand and improve the RCA use in the upcoming decades (Seiler & Duer, 2019).

2.4. Equivalent Mortar Volume method

2.4.1. Fundamentals

As mentioned in the previous sections, most of the research involving the use of coarse RCA has been carried using conventional methods and DRM mixes for the RCA replacement. Nevertheless, these methods do not differentiate the original virgin aggregate fraction from the RM in the RCA composition. This was the motivation for the development of the Equivalent Mortar Volume (EMV) Method, which states that RCA cannot be considered just as coarse aggregate because doing so means the total mortar content in the new concrete mix will be increased by the RM presence. This effect creates an imbalance in the proportions of the ingredients and could contribute to the performance drop observed in the fresh and hardened states (Fathifazl et al., 2009a).

As with DRM mixes, the EMV Method does not create a mix from scratch, but it is based on a parent mix designed under conventional volumetric methods. Once the initial proportions are determined, the target is to keep the same total mortar and coarse aggregate volumes while incorporating RCA into the mix. To accomplish this objective, the RCA material characterization needs to include an extra parameter, the RM content, or RMC for further simplification. This way, it would be possible to determine the amount of original virgin aggregates (OVA) and attached mortar that an RCA source would provide.

The replacement ratio is based on the amount of fresh new aggregates in an RCA mix (V_{NA}^{RCA-C}) when compared to the amount used in the parent conventional concrete (V_{NA}^{NAC}), as shown in Eq. 2.4 – 1:

$$R = \frac{V_{NA}^{RCA-C}}{V_{NA}^{NAC}} \qquad (2.4-1)$$

$R = 0$ means that the new mix will be comprised only by RCA, while $R = 1$ means that no RCA will be used. The idea is that in the new mix, the total mortar content (V_{TM}^{RCA-C}) will

be the sum of the RM (V_{RM}^{RCA-C}) and the fresh new mortar (V_{NM}^{RCA-C}), matching the mortar content of the parent conventional mix (V_{M}^{NAC}), as shown in Eq. 2.4 – 2. In the same way, the total coarse aggregate content (V_{TNA}^{RCA-C}) will be the sum between the OVA (V_{OVA}^{RCA-C}) and the fresh aggregates (V_{NA}^{RCA-C}) to be added to the mix, and it must be equivalent to the natural aggregate content of the parent mix (V_{NA}^{NAC}), as highlighted in Eq. 2.4 – 3.

$$V_{M}^{NAC} = V_{TM}^{RCA-C} = V_{RM}^{RCA-C} + V_{NM}^{RCA-C} \qquad (2.4-2)$$

$$V_{NA}^{NAC} = V_{TNA}^{RCA-C} = V_{OVA}^{RCA-C} + V_{NA}^{RCA-C} \qquad (2.4-3)$$

The EMV also places an upper limit on the RCA replacement level depending on the RMC. The dry-rodded density is used to compute the amount of natural aggregates that can fill a determined unit volume of concrete. Hence, for a determined RCA, it might not be possible to compensate the RMC with the addition of fresh new aggregates, which would exceed the capacity of said volume. Therefore, for a given natural aggregate and RCA source, the maximum RMC that the new RCA mix can incorporate (which is not necessarily the true RMC of the source) to achieve a complete replacement must not exceed:

$$RMC_{max}\ (\%) = \left(1 - V_{DR-NA}^{NAC} * \frac{SG_b^{NA}}{SG_b^{RCA}}\right) * 100 \qquad (2.4-4)$$

Where V_{DR-NA}^{NAC} represents the dry-rodded density of the natural aggregates, while SG_b^{NA} and SG_b^{RCA} are the specific gravity values of the natural aggregate and RCA, respectively. If the RMC of a determined RCA source exceeds this maximum, it will not be possible to use a 100% coarse-RCA replacement and fresh new aggregates will be necessary. On the other hand, if the RMC is below the limit, the selected source could be used for 100% replacement. For the first scenario, the minimum fresh aggregate content to be added to the mix can be computed as:

$$R_{min} = 1 - \left(\frac{1 - RMC}{V_{DR-NA}^{NAC}}\right) * \frac{SG_b^{RCA}}{SG_b^{OVA}} \qquad (2.4-5)$$

In the case of the second scenario, R_{min} would be zero since the RCA source can be used in its entirety and without any fresh new aggregate addition. Once these boundaries are known, the RMC of the source can be used to compute the optimum replacement level, which is the replacement in the new mix of the RM of the RCA with fresh aggregates. Therefore, the ideal replacement ratio can be defined as:

$$R = \frac{V_{RM}^{RCA-C}}{V_{RCA}^{RCA-C}} = \left[1 - (1 - RMC) * \frac{SG_b^{RCA}}{SG_b^{OVA}}\right] \qquad (2.4-6)$$

Where V_{RM}^{RCA-C} and V_{RCA}^{RCA-C} are the volumes of RM and RCA in the new RCA mix, respectively; and SG_b^{OVA} is the specific gravity of the OVA. With the final R and RMC values, the new proportions can be computed. The presence of the RM will therefore result in a reduction of the cement, mixing water, and fine aggregate content added to the fresh mix. These reductions will limit the amount of fresh paste in the new mix, which might impact its workability. However, the use of admixtures can help provide the necessary slump and compaction characteristics to keep identical performance to that of the parent mix (Fathifazl et al., 2009a).

2.4.2. Residual mortar characterization

The advantage of the EMV Method lies in its ability to use the RMC as the key parameter to rearrange the proportions of the conventional concrete mix to allow the use of RCA. Thereby, it is critical to have a methodology that can yield consistent results among the many sources from which RCA can come from, which inevitably will bring variability and create challenges when determining the RMC content without damaging the aggregates.

Parallel to the EMV Method development, a procedure to determine the RMC of different RCA sources was also proposed (Abbas et al., 2008). For simplicity, it will be

referred as the *"Sodium Sulphate RMC Method"*. The *"Sodium Sulphate RMC Method"* is based on a combination of mechanical and chemical stresses that help disintegrate the RM from the surface of the RCA without damaging the original aggregate. The influences come from the soundness tests that are normally applied to natural coarse aggregates used for concrete applications. These tests combine freeze-and-thaw cycles with immersions in chemical solutions, like sodium chloride, to simulate the field effects.

The main references used for the *"Sodium Sulfate RMC Method"* were the *MTO LS-614 Method of Test for Freezing and Thawing of Coarse Aggregate* (MTO, 2024) and the *Standard Test Method for Soundness of Aggregates by Use of Sodium Sulfate or Magnesium Sulfate* (ASTM, 2024b). The first one is a Provincial Standard mandated by the Ministry of Transportation of Ontario, while the second one is the American Standard for coarse aggregates soundness testing. A similar method in the Canadian Standards can be found in CSA A23.2-24A - *Test Method for the resistance of unconfined coarse aggregate to freezing and thawing* (CSA Group, 2024a).

It was observed that a combination of freeze-and-thaw cycles while keeping the saline solution immersion was an effective way to degrade the RM from the RCA surface. LS-614 uses a sodium chloride solution with a 3% concentration, while ASTM C88 opts for sodium sulphate solutions (with a 26% by mass concentration), magnesium sulphate solutions (with a 26% by mass concentration), and barium chloride solutions (with a 5% by mass concentration). Out of these options, it was determined that the sodium sulphate solution was the most effective at removing the RM without damaging the OVA (Abbas et al., 2008). The procedure can then be described as it follows:

1) *Representative RCA samples are obtained through mechanical sieving; proposed quantities of materials are 1000 g of the 4.75 mm retained fraction, 1250 g of the 9.5 mm retained fraction, 1500 g of the 12.7 mm retained fraction, and 2000 g of*

the 19 mm or larger retained size fractions. At least 3 repetitions per size are recommended.

2) *After 24 h at 105°C, the oven-dried samples' mass is measured (W_{RCA}), and then they are immersed for 24 hours in a 26 % by weight sodium sulphate solution.*
3) *RCA samples, while still immersed in the sodium sulphate solution, are subjected to a minimum of three and a maximum of five daily freeze-and-thaw cycles, i.e., overnight for 16 hours at −17°C and 8 hours in an oven at 80°C.*
4) *After the last freeze-and-thaw cycle, the solution is drained from the sample, and the aggregates are washed with tap water over a No. 4 – 4.75 mm sieve.*
5) *The aggregates are then placed in an oven for 24 hours at 105°C, they are visually inspected for impurities, and then their oven-dried mass is measured (W_{OVA}).*
6) *The Residual Mortar Content RMC is then obtained by weight difference using Eq. 2.4 – 7:*

$$RMC = \left(\frac{W_{RCA} - W_{OVA}}{W_{RCA}}\right) \qquad (2.4-7)$$

The *"Sodium Sulphate RMC Method"* was verified using image analysis to separately quantify the RMC. The results showed good correlation, although it was indicated that more studies were necessary to determine if different RCA sources might experience different behaviours, especially due to their chemical composition and possible impurities (Abbas et al., 2008; Hayles et al., 2018).

Another alternative for the determination of the RMC is the "*Quantification by Hydrochloric Acid Solution"* (Akbarnezhad et al., 2013; Yang & Lim, 2018). This technique has the advantage of requiring less time, because the RCA samples are soaked for only for 24 hours in a hydrochloric acid solution and then dried to get the RMC content by weight difference using the same equation of the *"Sodium Sulphate RMC Method"*. Aside from its shorter testing time, another benefit is that it does not require human intervention to

remove the remaining RMC particles in the visual inspection phase; but as with the previous case, it still needs to be studied with different RCA sources to test its effectiveness.

2.4.3. Mechanical properties

To better understand the application of the EMV Method, a few mix examples will be analyzed. The first family is comprised of the mixes used for the validation of the EMV Method (Fathifazl et al., 2009a), and is presented in Table 2-1. Mixes 7 and 14 were the control ones designed by conventional volumetric methods and with fresh new aggregates. The design also considered a W/C ratio of 0.45 and a target compressive strength of 35 MPa at 28 days. Mixes 1 – 3 and 8 – 10 used 100% RCA replacement under the DRM mixing method, as well as the incorporation of SCMs in the total cementitious materials content. The first group used an RCA source with an RMC of 41% (RCA-M), while the second group used an RCA source with an RMC of 23% (RCA-V).

Table 2-1: EMV mixes for the method validation (Fathifazl et al., 2009a).

#	Mix ID	Water [kg/m^3]	Cement [kg/m^3]	Fly Ash [kg/m^3]	GGBFS [kg/m^3]	Sand [kg/m^3]	RCA [kg/m^3]	NA [kg/m^3]
1	CM-C	156	349	0	0	888	792	0
2	CM-F	157	262	87	0	888	792	0
3	CM-B	155	227	0	122	888	792	0
4	EM-C	151	335	0	0	630	720	414
5	EM-F	151	251	84	0	630	720	414
6	EM-B	149	218	0	117	630	720	414
7	CL-C	193	430	0	0	808	0	833
8	CV-C	156	349	0	0	857	867	0
9	CV-F	157	262	87	0	857	867	0
10	CV-B	155	227	0	122	857	867	0
11	EV-C	161	358	0	0	645	813	281
12	EV-F	161	269	90	0	645	813	281
13	EV-B	160	233	0	125	645	813	281
14	CG-C	191	424	0	0	765	0	898

*Nomenclature: [Mixing Method]: Conventional (C) or EMV Method (E) / [Aggregate Type]: Natural limestone (L), Natural gravel (G), RCA-M (M) or RCA-V (V) / [Cementitious Materials]: Portland Cement (C), PC and Fly Ash (F) or PC and Ground-granulated-blast-furnace-slag (B).

The EMV mixes were 4 – 6 and 11 – 13; the first group used the RCA with the RMC of 41% (RCA-M), and the latter the RCA source with the RMC of 23% (RCA-V). When analyzing the designs, one way to measure the RCA replacement is by computing the ratio between the RCA weight and the total aggregate weight. By doing this, the replacement ratio in mixes 4 – 6 is 63.5%, and 74.3% for mixes 11 – 13. These values exemplify the concept of the ideal RCA replacement, which is the volumetric equivalent of the RMC, and where RCA with lower RMC will be able to replace a larger amount of natural aggregates.

Furthermore, another advantage comes from the cement reduction given the lower amount of fresh new mortar. For mixes 4 – 6, the cement reduction is 22%, and 15% for mixes 11 – 13. As expected, an RCA source with a lower RMC will require more fresh new mortar; likewise, RCA sources with higher RMC can increase the cement reduction, but with the trade-off that they will necessarily need to incorporate fresh new aggregates.

Table 2-2: Admixtures content and mechanical properties for EMV Method validation (Fathifazl et al., 2009a).

#	Mix ID	WRA [ml/m^3]	AE [ml/m^3]	Air Content [%]	Slump [mm]	Fresh Density [kg/m^3]	f'_c [MPa]	E_c [GPa]
1	CM-C	1396	35	6.9	70	2265	42	27
2	CM-F	-	209	7.4	130	2220	34	28
3	CM-B	523	35	6.0	55	2270	42	-
4	EM-C	1005	33	6.0	105	2295	39	30
5	EM-F	606	201	5.7	120	2295	34	31
6	EM-B	1339	33	5.7	80	2320	42	32
7	CL-C	-	86	6.3	175	2300	37	31
8	CV-C	1047	35	7,4	70	2285	40	28
9	CV-F	-	209	6.0	85	2280	35	31
10	CV-B	1047	35	7.1	110	2290	39	33
11	EV-C	1075	36	6.0	140	2320	40	33
12	EV-F	-	215	5.5	140	2305	35	34
13	EV-B	1792	36	6.8	150	2325	40	33
14	CG-C	-	85	6.3	210	2325	36	31

It is important to mention that water-reducer (WRA) and air-entrainer (AE) admixtures were used to improve the fresh state properties given the reduction in the RM of the RCA mixes. The results of the fresh state properties, as well as the compressive strength and elastic modulus averages at 28 days are available in Table 2-2.

When analyzing the fresh state properties, the slump averages for the first family of mixes that only used PC as cementitious material and the RCA-M were approximately 175 mm, 105 mm, and 70 mm for the conventional, EMV and DRM mixes, respectively. For the same mixes but with RCA-V the averages were 210 mm, 140 mm, and 70 mm, respectively. As appreciated, the conventional mixes still have the highest slump values, which was expected given the difference in the amount of fresh mortar and absorption when compared to the RCA mixes. Nevertheless, the improvement in the slump value between the DRM and EMV mixes is significant, with a 50% increase.

In the case of the fresh density, results confirmed the principles behind the EMV Method, which are to keep the same volumetric ingredients proportions between the parent and RCA mixes. For the mixes that used PC and RCA-M, the values were 2300 kg/m^3 for the conventional mix, 2295 kg/m^3 for the EMV mix, and 2265 kg/m^3 for the DRM mix. For the same combinations but with RCA-V, the values were 2325 kg/m^3, 2320 kg/m^3, and 2285 kg/m^3 for the conventional, EMV, and DRM mixes, respectively. As observed, conventional and EMV mixes show similar results, while DRM mixes present lower densities due to the 100% RCA replacement, which does not consider the amount of RM that is being incorporated into the mix.

The results of the compressive strength were slightly different. For the PC and RCA-M mixes, the averages at 28 days for the conventional, EMV, and DRM mixes were 37 MPa, 39 MPa, and 42 MPa, respectively. Meanwhile, the PC and RCA-V mixes had averages of 36 MPa, 40 MPa, and 39 MPa for the conventional, EMV, and DRM mixes, respectively. These

values are mainly a consequence of the admixture's addition, which improved the consistency of the RCA mixes' fresh state.

However, the biggest difference comes from the elastic modulus results. The PC and RCA-M mixes reported 31 GPa for the conventional mix, 30 GPa for the EMV mix, and 27 GPa for the DRM mix. Likewise, the PC and RCA-V mixes reported 31 GPa, 33 GPa, and 28 GPa for the conventional, EMV, and DRM mixes, respectively. These results further validated the theory behind the EMV Method, since the stiffness values between the conventional and EMV mixes are similar, which is a direct result of mixes having the same ingredients proportions, which was not the case when using the DRM technique for the RCA replacement, as reflected in the fresh density values.

Additionally, creep and drying shrinkage were tested for mixes 1, 4, 7, 8, 11, and 14. In contrast to the previous results reported for these two tests, the EMV Method showed comparable and even lower creep and shrinkage levels when compared to the conventional natural aggregate mixes. The aggregate effect was not a major contributor to the results since the EMV Method matched the volumetric proportions, thus linking the performance drop of the DRM mixes to the presence of the extra RMC (Fathifazl et al., 2011a).

The second family of mixes comes from a subsequent project that used the EMV Method to minimize the amount of required cement for eco-efficient concretes (Hayles et al., 2018), and is available in Table 2-3. Mixes 1 and 7 were used as the control ones and were designed under conventional methods for a target compressive strength of 25 MPa (W/C of 0.61) and 35 MPa (W/C of 0.47), respectively. The RCA replacement targets were different from the previous case, since the goal was to maximize the cement reduction instead of replacing the RMC of the RCA source with fresh new aggregates; therefore, 50% and 100% replacements were targeted to study the effects of lower cement contents.

Table 2-3: EMV mixes for eco-efficient concrete (Hayles et al., 2018).

#	Mix ID	Water [kg/m^3]	Cement [kg/m^3]	Sand [kg/m^3]	RCA [kg/m^3]	NA [kg/m^3]
1	0-NA-25	192	314	790	0	1029
2	50-RU-25	135	220	555	887	515
3	50-RT-25	162	264	665	697	509
4	81-RU-25A	99	162	405	1440	193
5	81-RU-25B	134	219	405	1440	193
6	100-RT-25	132	215	542	1380	0
7	0-NA-35	174	370	790	0	1029
8	50-RU-35	122	260	555	867	515
9	50-RT-35	147	312	666	690	515
10	81-RU-35A	90	191	408	1440	193
11	81-RU-35B	118	250	408	1440	193
12	100-RT-35	119	254	542	1380	0

*Nomenclature: [RCA Replacement Ratio]: Based on the coarse NA requirement for conventional mix / [Aggregate Type]: Natural (NA), RCA-U (RU) or RCA-T (RT) / [Target strength]: 25 MPa or 35 MPa / [Batch Letter]: A or B.

The RMC of the two RCA sources was 41% for the RU source, and 25% for the RT source. Nevertheless, given the designs of the control mixes, the maximum RMC allowed for the RU-RCA source was 27.4%, which required a minimum of 18.8% fresh new aggregates; hence, the maximum RCA replacement came down from 100% to 81.2%. On the other hand, the RMC of the RT-RCA source was below the 28.2% limit, thus allowing a 100% RCA replacement according to the EMV Method.

When analyzing the EMV designs, the replacement levels using the approach of the previous case (RCA weight to total aggregate weight) show values of 63%, 58%, and 88% for mixes 2 – 4; while mixes 8 – 10 have almost identical results, namely 63%, 57%, and 88%, respectively. On the other hand, the cement reduction for mixes 2 – 4 are 30%, 16%, and 48%, respectively. Likewise, mixes 8 – 10 follow the same trend and the reductions are the same, 30%, 16%, and 48%, respectively.

In contrast to the first family, the second family of mixes did not incorporate any admixtures given the main goal of studying eco-efficient mixes by testing the limits of the EMV Method. As a result, the mixes with the highest replacement ratios suffered from lower workability, hence the presence of mixes 5 and 11, which increased the amount of fresh mortar to account for this issue. The results of the fresh state properties, as well as the compressive strength and elastic modulus at 28 days are presented in Table 2-4.

Table 2-4: Mechanical properties for eco-efficient mixes (Hayles et al., 2018).

#	Mix ID	Slump [mm]	Air Content [%]	Fresh Density [kg/m^3]	f'_c [MPa]	E_c [GPa]
1	0-NA-25A	190	2.1	2471	27	32
2	0-NA-25B	195	1.4	2489	29	30
3	50-RU-25A	135	1.8	2406	17	28
4	50-RU-25B	110	2.1	2417	18	23
5	50-RT-25A	20	2.9	2371	19	26
6	50-RT-25B	15	5.5	2314	23	25
7	81-RU-25A	45	2.0	2406	16	23
8	81-RU-25B	30	3.0	2374	12	15
9	100-RT-25A	0	12.5	2084	22	23
10	100-RT-25B	0	3.7	2374	21	26
11	0-NA-35A	90	1.6	2483	36	37
12	0-NA-35B	85	1.0	2483	39	36
13	50-RU-35A	25	6.0	2483	30	33
14	50-RU-35B	20	2.4	2431	30	34
15	50-RT-35A	10	-	2360	37	29
16	50-RT-35A	0	5.1	2414	33	38
17	81-RU-35A	0	4.9	2266	14	22
18	81-RU-35B	0	-	2331	20	25
19	100-RT-35A	0	6.1	2243	31	32
20	100-RT-35B	10	7.2	2277	30	29

The fresh state properties showed drops in both slump and fresh density values, which progressively increased with the RCA replacement. These values are a consequence of having less fresh new mortar in the EMV mixes, and they are further worsened by the lack of admixtures that can help with the dispersion and paste flowability. As expected, the

mechanical properties such as compressive strength and elastic modulus followed the same trend and suffered form a performance drop, which is a direct result of the low quality of the fresh paste and corroborated by the measured entrapped air content.

These workability issues led to the proposal of an optimized EMV Method to improve its efficiency in low-cement RCA mixes. The M-EMV Method changes the mortar proportions to improve the performance of the concrete in the fresh state by calculating the required weights of fine aggregate and cement as a function of the desired ratio of the specific volumes of cement and sand, which is given by the designer (Hayles et al., 2018). Similarly, a modified EMV Method was also developed on the assumption that a certain volume fraction of RM may be mathematically treated as OVA, and the other as effective RM (Yang & Lee, 2017a; Yang & Lim, 2018).

Another alternative has been the development of the Equivalent Volume (EV) Method, which assumes the RCA mix is based on a conventional control mix having the same volumetric proportions of cement paste and aggregates as opposed to having the same amount of coarse aggregates and mortar, which is the assumption of the EMV Method. Therefore, the EV Method treats the RM in the RCA as a combination of residual paste and residual fine aggregates; hence, the total cement paste of a given RCA mixture is then considered as the sum of its residual paste and fresh paste volumes (Ahimoghadam et al., 2020; De Souza et al., 2022).

The EMV Method is a simple and effective way to implement RCA in new concrete mixes, and even though it might lead to workability issues due to the lack of fresh new mortar, the use of admixtures and presoaking techniques could potentially help solve them without requiring further modifications or the use of alternative methods.

2.4.4. EMV flexural behaviour

The performance study of RCA reinforced concrete mixes has primarily been through DRM-made specimens, and consequently, they cover most of the available information. In the case of the flexural behaviour, most studies focus on the performance of concrete beams, which are traditionally tested under a four-point bending configuration. This test methodology has the advantage of producing a pure bending stress state over a significant area of the specimen at a constant monotonic load, which will lead to failure or a pre-defined deformation. At the same time, this test provides an indirect way to estimate the tensile stresses the beams are experiencing (Silva et al., 2021).

The design of the beams varies upon the intended application, which will determine the amount and type of reinforcement, plus the required compressive strength. Therefore, different cross section geometries and reinforcement placements can be expected, but they will be under-reinforced to allow the flexural failure development. Among several studies, direct coarse RCA replacements of 50% and 100% are common, although intermediate fractions like 30% are also considered to better refine the results spectrum.

Upon testing, one immediate difference between beams made with conventional concrete and RCA concrete is the cracking pattern of the latter. Even though the failure mechanisms are the same, cracks in RCA beams were wider and more closely spaced than in beams made with conventional concrete; likewise, the number of cracks and microcracks also increased. This led to lower cracking moments for RCA beams, while the yielding moments did not suffer noticeable changes due to the presence of the reinforcement. Nevertheless, the ultimate capacity of the beams showed a decrease, which was greater with a higher RCA replacement ratio. The reported results also indicated a higher stiffness degradation and deflections in short- and long-term, which had an impact on the shrinkage and creep levels (Arezoumandi et al., 2015b; Deng et al., 2018; Peng et al., 2021; Silva et al., 2021; Sryh & Forth, 2022; Yang et al., 2020; Zhu et al., 2020).

It has been estimated that the use of coarse RCA in structural members is usually linked to a decrease in compressive strength, splitting tensile strength, flexural capacity, and elastic modulus by 20%, 15%, 15%, and 45%, respectively. Moreover, there are also increases in the water absorption (50%), drying shrinkage (50%), and creep (50%) when compared to members made with conventional concrete (Sryh & Forth, 2022).

However, the RCA mixes that used the EMV Method for the mix proportioning showed a different behaviour. Beams whose minimum and maximum reinforcement ratios were computed according to the requirements of CSA A23.3 were tested under the same four-point bending configuration. The results showed that the RCA beams had lower cracking moments than those of conventional concrete beams, but the yielding and ultimate capacity moments were on par if not superior.

The cracking pattern showed lower crack spacing, which led to slightly greater mid-span deflections, possibly due to shrinkage, although they were within the serviceability limits given by ACI 318. The results validated the effectiveness of the EMV Method to control the stiffness degradation when using RCA, and that the structural provisions for conventional concrete could potentially be applied for RCA (Fathifazl et al., 2009b).

Similar tests were also applied to test the Modified EMV Method, where the ultimate beam capacities showed slightly superior results for the RCA beams when compared to the conventional ones. It was also observed that the elastic modulus of the RCA concrete was on par with the conventional one, thus highlighting the dependence of the latter on the volumetric fractions of the concrete ingredients. Another observation was the decrease in the drying shrinkage levels, which were related to the lower fresh mortar content of the RCA mixes (Yang & Lee, 2017b).

2.4.5. EMV shear behaviour

The study of the shear capacity of reinforced concrete members is traditionally divided between members with and without shear reinforcement. In the case of the latter, the consensus is that four parameters affect the concrete contribution to shear strength (Reineck et al., 2003):

- Depth of member or size effect (d).
- Shear span-to-depth ratio (a/d).
- Compressive strength of concrete (f_c').
- Longitudinal reinforcement ratio (ρ).

As with the flexural behaviour, the shear behaviour of structural elements involving the use of RCA has been tested using DRM mixing techniques and four-point-loading test setups, with 50% and 100% being the most recurrent replacement ratios, although intermediate fractions such as 20%, 30% and 75% have also been tested for more refined results. The same failure mechanism (crack morphology and progression) has been reported in both RCA and natural aggregate beams, only with minor differences in the crack inclination, although the RCA beams tended to have more closely spaced cracks.

In the case of beams without reinforcement, the performance tends to be similar with up to 20% – 30% RCA replacement, and then it drops as the replacement level increases. Meanwhile, for beams with shear reinforcement (stirrups), the performance is similar among the RCA and natural aggregate beams, which is mainly due to the contribution of the steel reinforcement, thus making the replacement ratio less influential (Adams et al., 2016; Arezoumandi et al., 2014, 2015a; Ignjatović et al., 2017; Ju et al., 2021; Kachouh et al., 2021; Katkhuda & Shatarat, 2016; Rahal & Alrefaei, 2017, 2018; Tošić et al., 2016).

The performance drop in non-shear-reinforced beams is attributed to the RCA nature. For this type of beam configuration, two factors contribute to the shear capacity: dowel

effect and aggregate interlock. The dowel effect is given by the longitudinal reinforcement, which by being placed across the cracks, helps to transmit the shear stresses. Aggregate interlock, on the other hand, refers to the load transfer capacity of the aggregates and their resistance to sliding.

For beams without stirrups, this latter effect is the major contributor to the overall shear capacity. When considering the RCA nature, the ITZ between the RM and the original aggregate will be a failure area, which will be added to the new ITZ between the RCA and the new mortar. Therefore, if the quality of the RCA's ITZ is low, cracks will go through them and around the aggregates, thus impacting the shear capacity. This effect is less pronounced in RCA with lower RM contents, which can be associated with better ITZ quality and better interface behaviour with the new mortar (Adams et al., 2016; Ceia et al., 2016; Katkhuda & Shatarat, 2016; Rahal & Alrefaei, 2018).

When it comes to the performance of the EMV Method, structural beams with and without shear reinforcement were tested under the same four-point loading configuration. Regardless of the depth or shear-to-span ratio, the failure modes and cracking patterns were identical to those of natural aggregate mixes. The major differences when comparing the EMV Method with the traditional DRM technique come from the unreinforced beams, where the performance of the former is superior and on par with the conventional mixes (Fathifazl et al., 2011b).

Beams with shorter span-to-depth ratios developed better shear strengths and ductility mainly due to the arch mechanism, while beams with higher ratios suffered failures closely after the formation of the principal shear crack. The same tendency was observed for the beam depth, where shallower beams had better performance due to the effectiveness of the aggregate interlock, which is influenced by the size effect (probability of having defects increases with the size of the elements), and because crack spacing and width increase with the depth. However, all these results had been reported for conventional concrete, and

when comparing the performance between the two mixes, the EMV Method had comparable if not superior performance, while also fulfilling the code requirements for maximum crack width (Fathifazl et al., 2009c).

In the case of EMV beams with shear reinforcement, the results had the same tendency as those of DRM-made RCA beams, meaning that there were not major differences in the performance when compared to the conventional mixes, mainly due to the contribution of the reinforcement to the overall resistance. Nevertheless, the EMV-made beams did not show performance drops but had higher ultimate shear stresses when compared to natural aggregate mixes. As was the case without shear reinforcement, the aggregate type did not make a major difference since the RM of the two RCA sources was considered in the volumetric proportions (Fathifazl et al., 2010).

In both cases, when applying the equations from ACI 318 and CSA A23.3 for shear resistance, the results of those equations were conservative when compared to those observed in the testing phase. Therefore, and given the good results of the EMV-made beams when compared to the ones made with natural aggregates, it was concluded that those provisions could potentially be applied without major modifications when using the EMV Method for RCA mixes (Fathifazl et al., 2011b).

2.5. Bond behaviour

2.5.1. Definition

Reinforced concrete will work as a composite if the concrete is able to take the compressive stresses and the reinforcing steel the respective tensile stresses. This occurs when there is a transfer mechanism between the two materials; otherwise, the rebar will pullout and the drop in the tensile capacity will lead to failure. This transfer mechanism is known as bond (Wight, 2021).

Bond allows the transfer of the longitudinal forces taken by the reinforcing steel to the surrounding concrete. This transfer force changes along the bar length, as well as in the concrete embedment; therefore, if the steel strains differ from the concrete ones, a relative displacement known as slip will occur (Tepfers et al., 2000). ACI 408R-03 attributes the force transfer to three factors (ACI, 2003), which can be visualized in Figure 2-3:

- Chemical adhesion between the bar and the concrete.
- Frictional forces arising from the roughness of the interface, forces transverse to the bar surface, and relative slip between the bar and the surrounding concrete.
- Mechanical anchorage of the bearing of the ribs against the concrete surface.

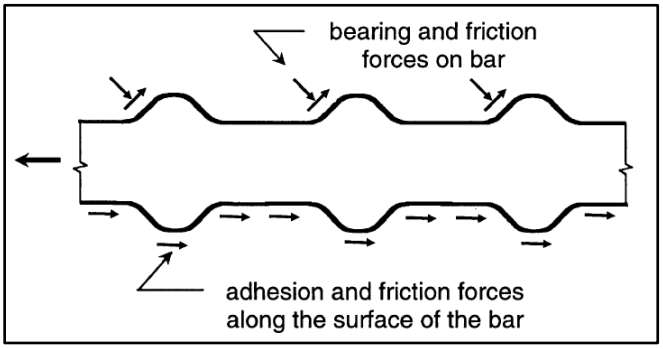

Figure 2-3: Bond force transfer mechanisms (ACI, 2003).

The local bond behaviour of the reinforcement is well described by the fib-CEB *"Bond of reinforcement in concrete"* report (Tepfers et al., 2000). Until the concrete cracks, bond is mainly given by chemical adhesion, but once the first cracks take place, adhesion is lost due to slippage. If the reinforcement is plain (with no deformations or ribs), the next phase will rely on the frictional forces between the bar and the concrete, ultimately ending up in an anchorage failure. This is the reason why reinforcing steel includes the bar deformations, since they enable mechanical bearing, and subsequently, bond development.

If deformed rebars are being used, once the first cracks take place, the lugs will start inducing bearing stresses to the concrete, thus generating microcracks at their tips that

allow bar slippage, but since the wedging action of the lugs is still limited, no splitting failure will occur. As the bond stresses increase, the concrete in front of the lugs will start crushing, thus enhancing the wedging action and the development of the splitting crack. If the concrete member has transverse reinforcement, this will provide confinement and delay the expansion of the splitting crack. On the other hand, if the member is not transversely reinforced, the splitting crack will keep developing until it reaches the outer surface of the member. This latter phenomenon is known as splitting failure.

If the member has light or moderate transverse reinforcement, the splitting failure will occur because of the longitudinal cracks developing between the bar and the outer concrete cover. As the transverse reinforcement increases, the nature of the failure will be less abrupt, the member will bear the bond stresses after the peak, and the slippage capacity will also increase. If the member is well reinforced, the splitting cracks will be contained, and the high slippage ratios will cause a general crushing of the concrete keys between the rebar lugs, which will reduce the bearing capacity.

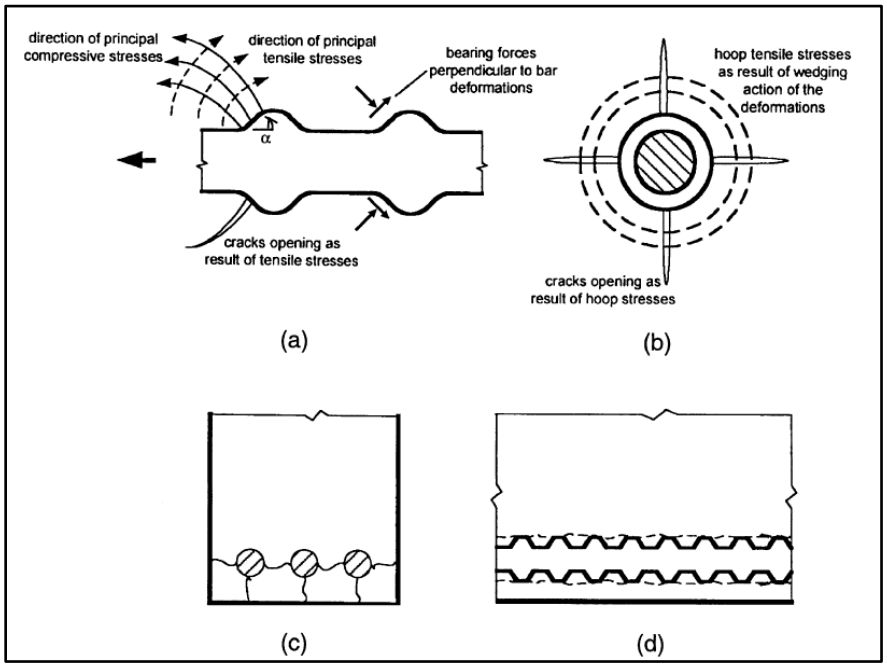

Figure 2-4: Cracking and damage mechanisms in bond (ACI, 2003).

This crushing of the concrete keys will lead to the development of frictional forces that will smoothen the surface between the concrete and the rebar, ultimately leading to a shearing of the interface, a phenomenon known as pullout failure. For members with high anchorage ratios ($l_d/\phi_b > 10$), a combination of these failure modes will likely take place. For members with no confinement or very thin concrete covers, splitting failures will dominate. In case the member has light or medium confinement, splitting-induced pullout failures with visible cracking will dominate. Finally, for well-confined members, the splitting-induced pullout failure will develop without visible cracking.

Figure 2-4 shows the cracking and damage mechanisms in more detail. (a) refers to the side view of a deformed rebar, where the deformation face angle shows the formation and development of the Goto cracks. (b) refers to the end view of the rebar, which shows the formation of the splitting cracks parallel to it. (c) refers to the end view of a member, where the splitting cracks develop between the rebars and through the concrete cover. Finally, (d) refers to the side view of a member where shear cracks and/or local concrete crushing are taking place due to the bar pullout (ACI, 2003).

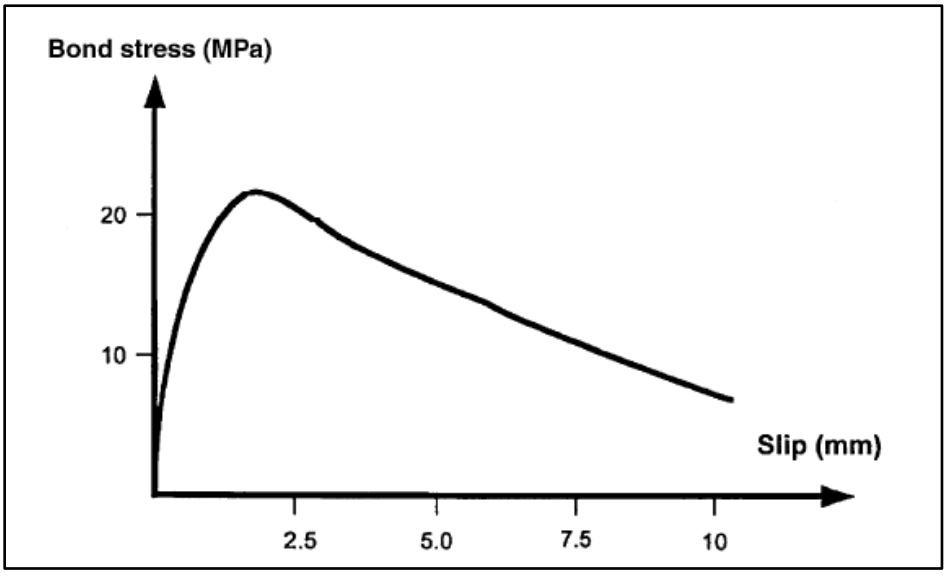

Figure 2-5: Example of bond stress slip curve (ACI, 2003).

The local bond behaviour applies to an ideal segment of the rebar, while the global bond behaviour in a reinforced concrete member applies to the entire embedment length of the rebar. If the embedment or anchorage of the rebar is enough, the bar might be able to yield and enter the strain hardening region, otherwise it will suffer the anchorage failure. Bond is usually studied through bond-stress or bond-force slip curves, which basically describe the bond behaviour against the slippage of the free- or loaded-end of the bar, which account for the elongation suffered by the rebar during the loading process (ACI, 2003).

Figure 2-5 shows a typical bond-stress slip diagram for a rebar with adequate embedment confinement that failed by pullout in a monotonic loading test. The very steep first section is dominated by the chemical adhesion, which gives place to the mechanical bearing once the concrete starts cracking. This bond transfer mechanism will reach a peak, after which the concrete surrounding the lugs will start crushing and allowing more relative slippage, which will result in a bond loss. The less effective mechanical bearing will combine with the frictional forces until the entire section shears to failure, also known as pullout (ACI, 2003; Tepfers et al., 2000; Wight, 2021).

Bond is a property, and as such, it depends on several factors that can improve or affect its performance. ACI 408R-03 classifies them in three big families. The first one is formed by the structural properties, including:

- *Concrete volume around the bars: It is related to the concrete cover and bar spacing parameters. Higher bond will be in concordance with larger cover and bar spacings, which limit the expansion of the splitting cracks.*
- *Development and splice length: Higher values lead to higher bond capacities, although they are not linear with the strength increase, since bond failures are incremental.*
- *Transverse reinforcement: It provides confinement to the developed bars, which helps delay and control the splitting crack propagation. Higher transverse*

reinforcement helps increase the bond capacity and can make pullout the final bond failure.

- *Bar casting position: Top-cast reinforcement tends to need more development length due to the settlement effect in concrete, where the heavier fractions tend to go to the bottom of the member, thus leaving the top sections with less quality material. Generally, bond strength decreases with the depth of the member, although the top cover effects are more detrimental.*
- *Non-contact lap splices: They provide reinforcement continuity without direct contact by overlapping the ends of the rebars; however, the maximum transverse spacing should be controlled to avoid creating an unreinforced zone that can lead to a zig-zag cracking pattern. This is due to the bond transfer, which goes from the loaded end of the rebar to the concrete, and from the concrete to the next rebar.*

The second family of bond affecting factors groups the bar properties, including:

- *Bar size: Larger bars require higher development lengths to allow yielding, and they also reach higher bond strengths for the same degree of confinement when compared to smaller bars. This is why the use of several smaller bars is preferred over single larger bars.*
- *Bar geometry: Related to the design and pattern of the deformations, which are based on the relative rib area, also known as the bearing area divided by the shearing area, as shown in Figure 2-6. These designs are standardized per country, and include deformation height, spacing, width, and face angle. Generally, in non-confined sections the rib area does not influence the bond behaviour; however, a higher rib area increases the bond capacity in well-confined sections (Darwin et al., 1996).*

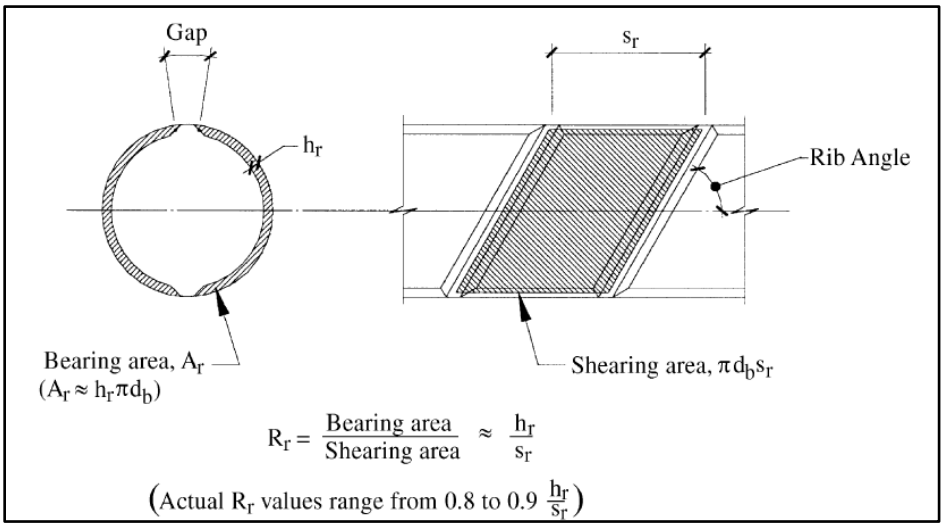

Figure 2-6: Relative rib area concept (ACI, 2003).

- *Steel stress and yield strength: High strength rebars develop higher steel stresses that might not reach yielding before the bond failure, although the bond stresses are comparable to normal strength rebars that yield before the bond failure.*
- *Bar surface condition: It affects the friction between the rebar and the concrete, plus the ability of the ribs to transfer the stresses between the two materials. Lack of bar cleanliness, epoxy coatings, and corrosion reduce the bond capacity.*

The third family is related to the concrete properties, namely:

- *Compressive strength: Traditionally, the effect of the compressive strength is seen by normalizing the bond behaviour by $\sqrt{f_c'}$, which works well for normal strength concrete (up to 55 MPa), but yields unconservative bond capacity for high strength concrete. This is attributed to the lesser crushing near the rib areas for these types of concrete, where the cement paste has much better quality and resistance.*
- *Aggregate type and quantity: If the aggregate has higher strength, so will the fracture energy, thus increasing the resistance to crack propagation. On the*

other hand, a higher aggregate quantity tends to improve the contribution of the transverse reinforcement to the bond capacity.

- *Tensile strength and fracture energy: For unconfined rebars, the peak load is governed by the tensile response of the concrete, which depends on both tensile capacity and energy dissipation capacity, normally described as fracture energy. Higher compressive strengths tend to moderately increase the bond capacity, but the failure mode becomes more brittle.*
- *Lightweight concrete: Bond capacity decreases due to the presence of lighter aggregates, which reduces the tensile strength, fracture energy and bearing capacity.*
- *Concrete slump and workability admixtures: If the concrete consistency is not controlled in the fresh state, settlement and bleeding will affect the bond between with the rebar. The use of admixtures that delay the setting times can also affect the bond characteristics, which are worse in top cast bars.*
- *Use of SCMs: SCMs can improve the compressive strength over time, which can lead to unconservative bond capacity estimations when normalizing them with* $\sqrt{f_c'}$*, which overestimates the effect of* f_c' *although better correlation is obtained using* $\sqrt[4]{f_c'}$*.*
- *Fibre reinforcement: The use of fibres can improve the tensile strength capacity, although the ratio will be much less than when compared to compressive strength. The greater effects of their use come in the improvement of the post-cracking resistance.*
- *Consolidation: The use of high-frequency vibration helps the local uniformity of concrete by removing the air voids and by avoiding settlement and bleeding; therefore, the quality of the concrete improves around the reinforcement areas.*

2.5.2. Analytical models and design equations

Two of the most accepted analytical bond-slip stress curves are the ones proposed by the ACI and the fib Model Code 2010 (FIB, 2010; Pochanart & Harmon, 1989). The former is based on a series of studies in the 1980s that evaluated the mentioned factors that affect the bond behaviour, and that were key in the standardization of the rebar deformations design. The model is shown in Figure 2-7:

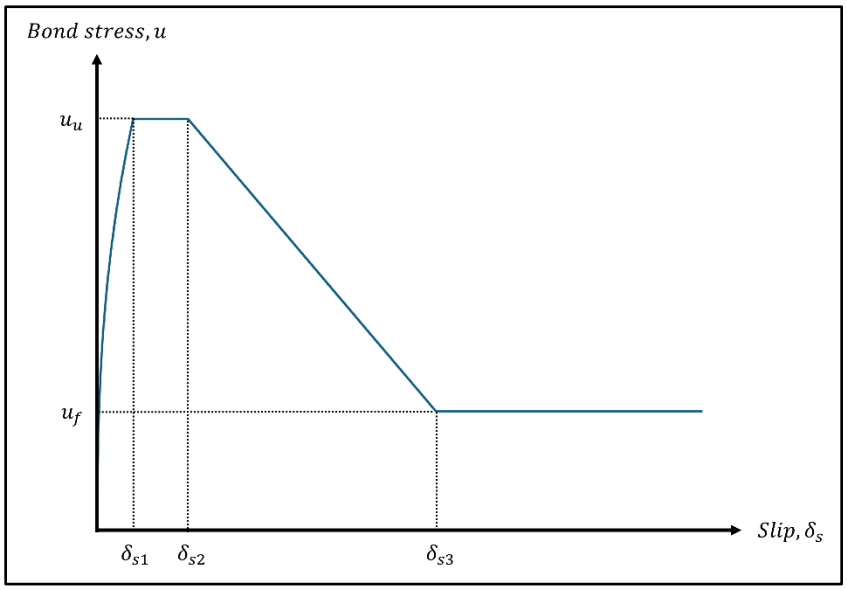

Figure 2-7: Bond stress-slip relationship adopted by ACI (Pochanart & Harmon, 1989).

The equations that describe the bond development in the ascending branch, ultimate plateau, and final plateau are the following:

$$u = u_u \left(\frac{\delta_s}{\delta_{s1}}\right)^{\alpha} \quad \forall \quad 0 < \delta_s \leq \delta_{s1} \qquad (2.5-1)$$

$$u_u = \left(20 - \frac{d_b}{4}\right)\sqrt{\frac{f_c'}{30}} \quad \forall \quad \delta_{s1} < \delta_s \leq \delta_{s2} \qquad (2.5-2)$$

$$u_f = \left(5.5 - 0.07\frac{s_L}{h_L}\right)\sqrt{\frac{f_c'}{27.6}} \quad \forall \quad \delta_{s2} < \delta_s \leq \delta_{s3} \qquad (2.5-3)$$

Where $\alpha = 0.4$ for the ultimate bond condition, and the descending branch can be computed using linear interpolation. Meanwhile, the equations that describe the slips are:

$$\delta_{s1} = \sqrt{\frac{30}{f_c'}} \qquad (2.5-4)$$

$$\delta_{s2} = 3.0\ mm \qquad (2.5-5)$$

$$\delta_{s3} = s_L \qquad (2.5-6)$$

As seen in Eq 2.5 – 3 and Eq. 2.5 – 6, s_L and h_L refer to the rebars' lug spacing and height, respectively. This showcases the importance of the deformations and how the models are calibrated around their design.

On the other hand, the analytical bond slip-stress model proposed by the fib Model Code 2010 is seen in Figure 2-8. The equations that govern the ascending branch, ultimate plateau, descending branch, and final plateau are:

$$\tau_o = \tau_{max}\left(\frac{s_s}{s_1}\right)^a \quad \forall \quad 0 < s_s \leq s_1 \qquad (2.5-7)$$

$$\tau_o = \tau_{max} = 2.5\sqrt{f_c'} \quad \forall \quad s_1 < s_s \leq s_2 \qquad (2.5-8)$$

$$\tau_o = \tau_{max} - \left(\tau_{max} - \tau_f\right)\frac{(s_s - s_2)}{(s_3 - s_2)} \quad \forall \quad s_2 < s_s \leq s_3 \qquad (2.5-9)$$

$$\tau_o = \tau_f = 0.4\,\tau_{max} \quad \forall \quad s_3 < s_s \qquad (2.5-10)$$

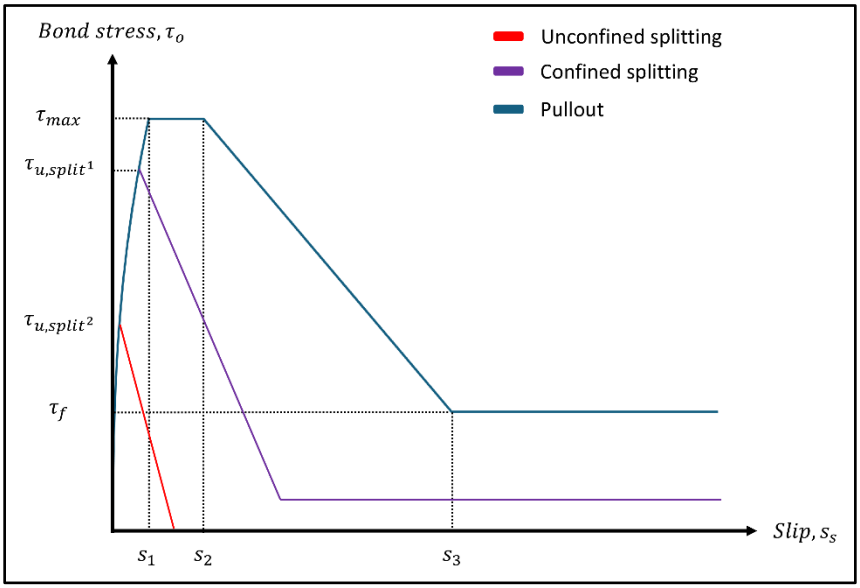

Figure 2-8: Analytical bond stress-slip relationship for monotonic loading (FIB, 2010).

As with the previous model, the coefficient α is taken as 0.4 for the ultimate condition and basically represents how steep the initial ascending branch will be. The slip values can be taken from a pullout with good bond conditions:

$$s_1 = 1.0\,mm \qquad (2.5-11)$$

$$s_2 = 2.0\,mm \qquad (2.5-12)$$

$$s_3 = s_L \qquad (2.5-13)$$

Alternatively, if the bond condition is not adequate, or if the splitting failure with or without confinement needs to be analyzed, the Model Code provides extra boundary conditions that will change the ultimate bond stress and the slip parameters, as seen with the red and purple curves in Figure 2-8.

When it comes to bond equations, they have been empirically developed over the years as a result of a better understanding of the force transfer mechanism. In 1963, ACI 318 developed the first bond equation for design purposes, which set a limit for the bond development:

$$u = 20\frac{\sqrt{f_c'}}{d_b} \leq 5.52\ MPa \qquad (2.5-14)$$

Where:

- $u =$ Bond stress (MPa)
- $f_c' =$ Compressive strength of concrete (MPa)
- $d_b =$ Bar diameter (mm)

Since the actual bond stress varies along the length of a bar anchored in tension zone, CSA A23.3 and ACI 318 use the concept of *development length (l_d)* rather than bond stress. The development length refers to the shortest rebar length in which the steel stresses can increase from zero up to yielding (Wight, 2021). From 1971 until 1995, ACI 318 used the following equation to compute it:

$$l_d = 0.019\ A_b\frac{f_y}{\sqrt{f_c'}} \qquad (2.5-15)$$

Where:

- $l_d =$ Bar development length (mm)
- $A_b =$ Area of the developed bar (mm^2)
- $f_y =$ Yielding stress of the rebar (MPa)

Nevertheless, advancements in research led to more detailed descriptive equations that better matched the results of several tests (Darwin et al., 1996). For instance, ACI 408 developed two sets of descriptive equations that considered the effects of normalizing the bond by the fourth root rather than the traditional square root (better representation of the concrete strength across the development length), and the contribution of the transverse reinforcement, as seen in Eq. 2.5 – 16 and Eq. 2.5 – 17.

$$\frac{T_c}{\sqrt[4]{f_c'}} = \frac{A_b f_s}{\sqrt[4]{f_c'}} = [1.43 l_d (c_{min} + 0.5 d_b) + 57.4 A_b] \left(0.1 \frac{c_{\max}}{c_{min}} + 0.9\right) \qquad (2.5 - 16)$$

$$\frac{T_b}{\sqrt[4]{f_c'}} = \frac{T_c + T_s}{\sqrt[4]{f_c'}} = \frac{A_b f_s}{\sqrt[4]{f_c'}} = [1.43 l_d (c_{min} + 0.5 d_b) + 57.4 A_b] \left(0.1 \frac{c_{\max}}{c_{min}} + 0.9\right) + \left(8.9 t_r t_d \frac{N A_{tr}}{n} + 558\right) \sqrt{f_c'} \qquad (2.5 - 17)$$

Where:

- T_b = Total bond force of a developed or spliced bar (kN)
- T_c = Concrete contribution to total bond force (kN)
- T_s = Steel contribution to total bond force (kN)
- f_s = Stress in the rebar (MPa)
- c_{min} = Minimum combination between cover and bar spacing (mm)
- c_{max} = Maximum combination between cover and bar spacing (mm)
- t_r = Term representing the effect of relative rib area on T_s
- t_d = Term representing the effect of bar size on T_s
- A_{tr} = Area of each stirrup or tie crossing the potential splitting plane (mm^2)
- N = Number of transverse stirrups, or ties, within the development or splice length
- n = Number of bars being developed or spliced

However, even if the descriptive equations are effective to predict the bond behaviour, the design provisions should be understandable, simple, and provide conservative approaches that can prevent failures (ACI, 2003). In 1995, ACI 318 introduced a simplified version of the descriptive equations, and further revisions considered safety factors to account for the effect of certain agents in the bond properties (Idun & Darwin, 1999). ACI 318-19 (ACI, 2019) uses the following general equation for development length in tension:

$$l_d = \left(\frac{f_y}{1.1\lambda\sqrt{f_c'}} \frac{\Psi_t \Psi_e \Psi_s \Psi_g}{\left(\frac{c_b + K_{tr}}{d_b}\right)} \right) d_b \qquad (2.5-18)$$

$$K_{tr} = \frac{40 A_{tr}}{sn} \qquad (2.5-19)$$

Where:

- $\Psi_t =$ Bar casting position factor
- $\Psi_e =$ Epoxy coating factor
- $\Psi_s =$ Bar size factor
- $\Psi_g =$ Reinforcement grade factor
- $\lambda =$ Lightweight aggregate concrete factor
- $c_b =$ Bottom cover of the rebar (mm)
- $K_{tr} =$ Transverse confinement index
- $s =$ Spacing of transverse reinforcement (mm)

In the case of CSA A23.3, the general equation for the development of a rebar has a similar expression:

$$l_d = 0.9 \frac{k_l k_c k_d k_s k_g}{\left(\frac{d_{cs} + K_{tr}}{d_b}\right)} \frac{f_{yg}}{\sqrt{f_c'}}\, d_b \qquad (2.5-20)$$

$$K_{tr} = \frac{A_{tr} f_{yt}}{10.5sn} \qquad (2.5-21)$$

Where:

- k_l = Bar location factor
- k_c = Bar coating factor
- k_d = Concrete density factor
- k_s = Bar size factor
- k_g = Reinforcement grade factor
- d_{cs} = Smaller between minimum concrete cover to the bar centre, and two-thirds of the centre-to-centre spacing of the bars being developed
- f_{yg} = Minimum yield strength as defined in the applicable material standard for the specified grade of reinforcing steel

Both CSA A23.3 and ACI 318 provide simplified equations depending on combinations between spacing, cover, and bar size conditions. Likewise, both codes also provide general equations for the calculation of the development length in compression. In the case of ACI 318, the value is the maximum between:

$$l_{dc} = \max\left(\left(\frac{0.24 f_y \Psi_r}{\lambda\sqrt{f_c'}}\right) d_b \; ; 0.043 f_y \Psi_r d_b \; ; 200\ mm\right) \qquad (2.5-22)$$

Where:

- l_{dc} = Development length of bar in compression (mm)

In the case of CSA A23.3, the equation is:

$$l_{dc} = \left(\frac{k_c k_d f_{yg}}{1.3\left(1 + \frac{0.1K_{tr}}{d_b}\right)\sqrt{f_c'}} - 21 \right) d_b \geq 300\ mm \qquad (2.5-23)$$

For both cases, the development length in compression is less than in tension given that the bond transfer is facilitated by the higher resistance of concrete in compression.

2.5.3. Testing methods

The study of the bond behaviour can be divided into small-scale and large-scale tests, in which the nature of the specimen will determine the characteristics of the bond response. Figure 2-9 shows the most common tests, namely: pullout test (a), beam-end test (b), beam-anchorage test (c), and splice test (d).

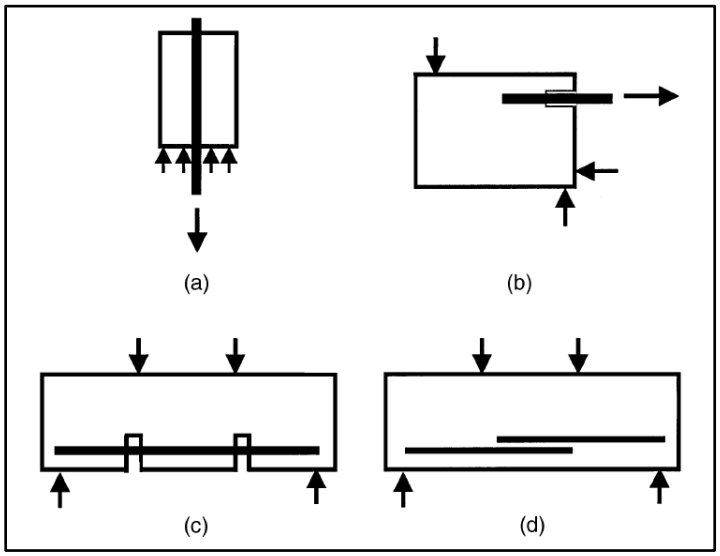

Figure 2-9: Bond testing specimens (ACI, 2003).

Pullout tests are one of the most common for the study of the bond properties given their simplicity in terms of specimen design and test setup, and they were also normalized by RILEM (Vieito et al., 2018). In this test, small rectangular blocks or cylinders are cast with the embedded rebar in the middle, then tension loads are applied to test the bond. However, since the concrete surrounding the rebar is subjected to compression, and only

the rebar is in tension, the results will only be comparable to other pullout tests and will not represent the real-life behaviour (ACI, 2003; Tepfers et al., 2000).

The second small-scale test, known as beam-end, presents the advantage of developing a stress-state that replicates the real-life behaviour. To accomplish this, the rebar is cast in one end of the tall beam, away from where the compression loads are going to generate; therefore, both the rebar and the concrete surrounding it will be in tension, which is the desired configuration that closely matches the results of large-scale tests. Beam-end specimens also are reinforced with stirrups placed on the longitudinal plane instead of the conventional transverse one to allow the development of the splitting crack along the rebar. Another advantage is that the specimen design is standardized in ASTM A944, which provides a solid base to compare different bar/embedment configurations (ACI, 2003; ASTM, 2022b; Darwin & Graham, 1993).

Finally, when it comes to large scale tests, both beam-anchorage and splice tests are designed to directly study the bond behaviour in full size members. The former considers a member tested in flexure with a known crack and embedment length, and where the reactions are laterally displaced from the centreline to avoid a bond enhancement. This test was also normalized by RILEM (Vieito et al., 2018). On the other hand, splices are much easier to fabricate since they are placed in constant moment regions and given that the stress-states are realistic and comparable to the anchorage test, they are the preferred choice when it comes to full-scale bond testing. In fact, the bulk of the data for the development of the ACI 318 embedment length equations comes from this particular test setup (ACI, 2003).

2.5.4. EMV bond behaviour

The study of the bond behaviour for RCA concrete has traditionally been made using different direct replacement ratios, as with the properties reviewed in previous sections. Pullout tests and beam anchorage have been the preferred test specimens, although the

former concentrates most of the available data. One of the main reasons is the ease of fabrication and testing that pullout specimens present, which saves time when compared to the beam anchorage test. Therefore, different sets of databases are available since the results of both tests are not directly comparable due to the stress-state difference in the concrete region surrounding the rebar (Zhou et al., 2023).

Replacement ratios of 20%, 30%, 50%, and 100% are used to study the RCA effect. Likewise, different combinations of bar size, embedment lengths, splice lengths, W/C ratios, and concrete covers have been used to test the variations in the bond properties. There is consensus that failure modes between normal and RCA concrete are similar, although higher replacement ratios tend to have more detrimental effects on the overall capacity, and an increase in the cover helps the bond capacity. The effect of the RCA is more notorious in shorter embedment lengths since concrete is exposed to more localized stresses and has less slippage capacity, but also in the bond capacity since the splitting failure will depend on the tensile capacity and fracture energy release of the concrete. In the case of longer embedment lengths and bigger bar sizes, bond capacity tends to be reduced (Gaurav & Singh, 2021; Guerra et al., 2014; Kim et al., 2015; Moallemi Pour & Alam, 2016; Prince et al., 2018).

Bond studies with traditional replacement methods have also covered the effects of freeze-and-thaw cycles, fire resistance, transverse reinforcement, and the use of high-strength concrete. The results confirm that confinement helps reduce the drop in the bond capacity, which is directly related to the concrete quality, where the loss of stiffness due to the higher mortar contents favors the development of the splitting cracks. In the case of high-strength concrete, the quality of the paste has a direct effect on the bond behaviour, which tends to benefit from the increased tensile capacity of the cement paste (Li et al., 2012; Lv et al., 2018; Sierens et al., 2021; Yang et al., 2016; Zhang et al., 2022).

The use of beam-end tests to study the bond behaviour has also provided interesting information. One of these studies covered the effect of the concrete cover and the embedment length in mixes that were made with both coarse and fine RCA coming from a recycling plant, where they were cleaned and crushed. The concrete mixes were set at a W/C ratio of 0.39, and with a combination of RCA replacements of 25%, 50%, 75%, and 100%, and a Canadian 15M rebar (d_b = 16 mm). For the same embedment length, it was found that bond increased by 5 – 10% when the cover went from 25 mm to 40 mm, although the bond peaks were 15% to 28% lower than those of the companion natural aggregate concrete (Rockson et al., 2020).

For the same mix designs and a set cover of 25 mm, two different embedment lengths were tested, 200 mm and 300 mm, respectively. As with the cover case, the average bond performance between the RCA mixes and the companion natural mixes suffered drops of 15% to 28% for the 200 mm embedded lengths, and 9% to 13% for the 300 mm ones. However, the bond force increased between the RCA mixes when going from 200 mm to 300 mm, specifically by 21% to 30%. In contrast, companion mixes showed an increase of 16%. Even if the bond results for the RCA mixes were lower than those with natural aggregate concrete, which were attributed to the RM of the RCA, they were still above the values recommended by the descriptive and code equations for development length (Rockson et al., 2021).

The study of the previous parameters highlights the relevance of the RCA quality in the bond results. Research has also been conducted in this area, and one of these studies considered three RCA sources coming from decommissioned sidewalks, crushed concrete from the Pearson International Airport in Toronto, Canada, and crushed returned concrete from a ready-mix plant. The RM contents for these sources were 46%, 50%, and 56%, respectively. The mix design considered compressive strength values of 30 MPa, 40 MPa, 50 MPa, and 60 MPa; with W/C ratios going from 0.70 to 0.30. The RCA was used with a 100% coarse aggregate replacement using the DRM technique; and presoaking was applied

for both natural coarse aggregate and RCA to limit their effect on the workability and fresh state properties. Therefore, the use of water-reducing admixtures was only necessary for the lowest W/C ratio (Butler et al., 2011, 2015a).

For the beam-ends, the selected rebar was a Canadian 25M (d_b = 25.2 mm), and the embedment lengths were set at 125 mm, 375 mm, and 450 mm. One interesting detail was that the test setup considered a vertical test instead of the traditional horizontal one. This configuration has also been proposed in recent years given that most laboratories are equipped with rigid frames designed to apply vertical loads only. Moreover, this configuration also allows an easier instrumentation installation (Trujillo Pasquale et al., 2018). However, one important consideration is that the vertical test must not alter the stress-state condition of the rebar-concrete interface.

The tests results reported lower bond capacities for the RCA mixes, even when the compressive strengths were on par with those of the natural aggregate mixes. For the 30 MPa and 50 MPa mixes with 125 mm and 375 mm of embedment, the differences were 10% to 21% in favour of the companion mixes. Meanwhile, for 40 MPa and 60 MPa mixes with 125 mm and 450 mm of embedment, the drop was reduced to a range between 3% and 13%. It was also determined that the aggregate crushing value had a good correlation with the splitting tensile strength. Therefore, the quality of the RCA has an important role in the bond capacity, where aggregates with lower crushing values had a better strength, and by consequence, a better performance (Butler et al., 2011, 2015a).

When it comes to the EMV Method, the bond behaviour has also been studied using beam-end specimens (Fathifazl et al., 2012). As with the previous studies to validate the EMV Method, the same RCA sources with RM contents of 20% and 40% were used. The design of the beam-end considered two testing bars, both Canadian 15M (d_b = 16 mm) and 30M (d_b = 29.9 mm), with covers of 60 mm and 70 mm, respectively. Different combinations of embedment lengths were also used, ranging from 250 mm to 320 mm, and

the traditional horizontal tests were force-controlled, with 20 kN/min for the 30M bar, and 10 kN/min for the 15M bar.

The test results had two failure modes, the traditional bond splitting failures for the 30M bar, and bar failure/rupture for the 15M. Given this difference, it was deemed by the researchers that the 15M bars were able to fully develop with the provided embedment lengths, with no signs of visible cracking, which is in line with the bar size effect, where larger bars require longer embedment to develop the yielding stresses.

When it comes to the effect of the EMV Method on the RCA mixes, the bar size and aggregate type had no influence on the performance; even more, the EMV bond capacity was comparable and even higher than that of natural aggregate mixes. These results can be attributed to the tensile capacity and stiffness of the EMV mixes, which are close to those of companion mixes by matching the volumetric proportions of mortar and aggregate. Finally, it was also considered that the Canadian CSA A23.3 provisions for development length could be used since they provided conservative results (Fathifazl et al., 2012).

2.6. Seismic applications

2.6.1. Fundamentals

Reinforced concrete is a composite material that can perform well in seismic applications as part of a proper lateral-force-resisting system, which provides the necessary stiffness, strength, and ductility (or deformation capacity) to keep the structural integrity under an acceptable performance when subjected to earthquake loads (Moehle, 2015).

Earthquakes are a consequence of the movement of tectonic plates; they are ground motions with vertical and horizontal accelerations that will go through the base of the structures. The effects will largely depend on the range of frequencies and maximum values of the base acceleration of the earthquake, as well as on the period of the buildings, which are designed to accommodate large deformations without strength loss. Earthquakes will

vary depending on the magnitude (related to the amount of released energy) and location (hypocenter or depth where it originated), they are highly complex and the procedures for the analysis and design of structures to resist their effects are in a continuous state of development (Wight, 2021).

When it comes to design, modern computing techniques based on the principles of mechanics are useful tools, but they can be inaccurate at times. Therefore, large-scale testing representing field conditions are still needed to understand the behaviour of reinforced concrete structures, especially in the inelastic regions. However, much of these tests lack consistency in terms of loading histories, data collection, and results presentation. Three categories can be used to describe the experimental tests used for earthquake engineering (ACI, 2013):

- Tests under slowly applied and incrementally increasing or decreasing loads (quasi-static loads).
- Pseudo-dynamic tests.
- Dynamic tests.

Tests under slowly applied loads can be grouped into tests under cyclic or reversed cyclic loading; and tests under monotonically increasing load/deflection increments. ACI 374.2R developed a test protocol aimed for the first category, with the objective of providing consistency and maximize the usefulness of the generated data. The idea behind the use of slowly applied loads is to limit the effects of the dynamic inertia and strain rate on the materials. To accomplish this objective, the test can be load- or deformation-controlled with a predetermined slow loading regime.

ACI 374.2R recommends the use of deformation-controlled tests given the difficulty of controlling loads in the inelastic range of deformations due to strength decay and significant deformations with little load variation. Load-controlled tests can be applied for the elastic

range when the deformations are still small. Another aspect to be considered is the $P-\delta$ effect, or secondary moments due to off-axis displacements, when gravity loads are applied. These moments can reduce the moment capacity and induce faster stiffness and force degradation rates. Hence, to limit such effects, it is important to ensure that the line of action passes through the centroid of the critical section in vertically loaded specimens.

The testing protocol also acknowledges the development of the new instrumentation and data collection devices, such as fibre optic sensors and image processing. These new technologies can help sharpen the data analysis, especially in high strain ranges, where traditional strain gauges used to measured localized effects can detach. However, independently of the selected instruments, the data collection should allow a continuous measurement throughout the tests.

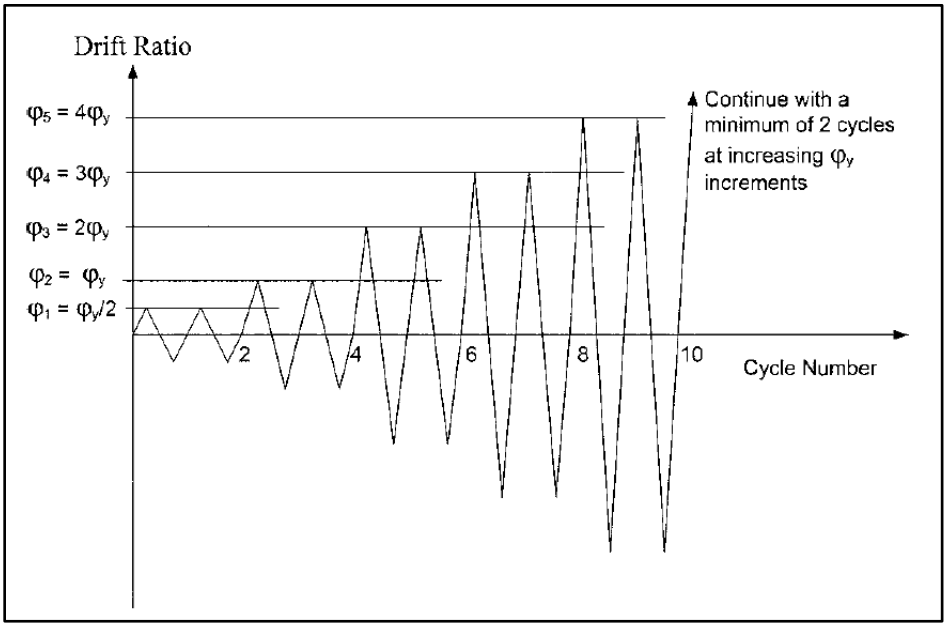

Figure 2-10: Deformation history for tests under unidirectional load reversals (ACI, 2013).

In the case of the loading protocols, ACI 374.2R recommends the use of increasing loads or increasing deformations for monotonic tests, which should continue until a severe strength degradation is observed. Monotonic tests are usually used to construct the

backbone curves used for the calibration of dynamic models. On the other hand, for unidirectional load reversals, the loading protocol will depend on two factors: the increment of the deformation control parameter that defines each deformation level or step; and the number of cycles at each step.

Figure 2-10 shows the recommended loading protocol for reversed loading. The deformation control parameter is usually related to pre-defined values (i.e. based on the results of the monotonic curve) or performance levels (i.e. when using performance-based design). For the number of cycles, a minimum of two per each deformation step is required to guarantee sufficient damage, although the use of three cycles per deformation step has been the more traditional approach. The final decision should be made upon the degradation characteristics of the test configuration and the deformation range selected for the study. Two cycles are better suited for systems in which high degradation is expected; whilst three cycles are better tailored for systems with more gradual degradation.

2.6.2. Influence of the loading protocol

The implementation of quasi-static tests has been widely adopted in earthquake engineering research. They are a tool that can provide benchmarks for different structural configurations. Moreover, they are relatively easy to implement and do not require much specialized equipment when compared to other dynamic setups like shaking tables. However, the main criticism comes from the selection of the loading protocol, which not necessarily recreates the effects of a real-life earthquakes, thus leading to lower ductility capacities or unrealistic damage (Carrillo & Alcocer, 2013; Maison & Chao, 2024; Marder et al., 2018; Park et al., 2024; Rodríguez et al., 2024).

The conservative nature comes from the symmetric fully reversed cycles, which have the same loading rates and displacement amplitudes, thus creating greater demands on the structure. When compared to earthquake time-histories, the latter are characterized by having a one-direction bias with relatively few large drift excursions. Studies have shown

that when using loading protocols that recreate the earthquake demands, the median spectral capacity can increase between 25% and 50%, while the drift capacities gains are 1.6 to 2.9 times higher when compared to the traditional fully reversed symmetrical protocol (Maison & Chao, 2024).

To address this topic, research has been focused on the development of testing protocols that can better simulate the effects of the earthquake. One clear alternative is the use of time-histories from real-life earthquakes, and the second one is through simulations of possible events (Carrillo & Alcocer, 2013). There are different aspects to consider in the simulation, on one side is the earthquake's nature (i.e. crustal, subcrustal, subduction); and on the other the ductility capacity, which depends on the structural configuration and the established performance levels. Once these two aspects are defined, the protocol will need to consider two extra parameters: the number of inelastic cycles and the total cumulative damage (Krawinkler, 1996; Rodríguez et al., 2024).

Another alternative that has been explored is a mixed protocol, which includes a combination of dynamic and quasi-static tests, where the former is applied first using a time-history that replicates a seismic event, to then be followed by the traditional reversed loading protocol. The advantage lies in the consideration of the dynamic effects on the assessment of the residual capacity and damage after the earthquake, thus favouring the analysis of the behaviour of the low and moderate displacements. This extra step can provide useful information before taking the structure to its ultimate capacity with the use of traditional quasi-static loading protocols (Marder et al., 2018).

The dynamic effects are closely related to the loading rate, with higher strains that are typical in earthquakes influencing properties such as stiffness and strength degradation (Bischoff & Perry, 1991; Li & Li, 2012). They also have effects on the strength mechanisms (failure mode), low-cycle fatigue (number of cycles), drift ratio, and energy dissipation (Carrillo & Alcocer, 2013). These effects are purposely avoided in the ACI 374.2R protocol,

thus highlighting the lack of consensus among researchers when it comes to the definition of a standard protocol, or whose effects should be considered to allow a better understanding of the behaviour and design while still providing a conservative approach.

The loading rates between quasi-static and dynamic tests (simulating earthquakes) have differences of a few orders of magnitude. The former are around 10^{-5} sec^{-1}, while the latter oscillate in the range of $10^{-3} - 10^{-2}$ sec^{-1}. The main impacts are reflected on the enhancement of the material properties since the material under high strain rates does not have time to relax. However, dynamic effects are more difficult to understand given their complexity, and the testing equipment can also lead to erroneous readings or misinterpretations (Bischoff & Perry, 1991). Therefore, loading protocols for quasi-static tests consider very low rates, usually in the range of 1 to 10 mm/min, while dynamic tests can go up to 600 – 2400 mm/min (Deng et al., 2019; Lemcherreq et al., 2023; Wang et al., 2013; Xiao et al., 2018, 2020).

Dynamic tests do not create essential changes in the failure mechanisms but tend to generate more brittle failures with less cracks (which are more uniformly distributed) than in quasi-static protocols. Moreover, these higher strains have little influence on the stiffness, but they increase the yielding and ultimate capacities of the structural member, with the yielding having the most notorious changes. Another effect relates to the energy dissipation capacity, where the post-peak slopes are steeper than in lower rates; and the ductility factor can be reduced due to the larger increment in the yielding deformation with respect to the ultimate deformation. This is why Dynamic Increasing Factors (DIF) have been developed and proposed for design considerations (Bischoff & Perry, 1991; Fan et al., 2014; Li & Li, 2012; Marder et al., 2018; Wang et al., 2013; Xiao et al., 2018, 2020).

The effect of higher loading rates has also been studied for structural RCA concrete. Scaled 4.5-metre high structural frames simulating a six-storey building with two spans and two bays have been tested using a direct 100% coarse RCA replacement in China (with a

30% RM content), where the shaking table results showed there was no variation in the desired "strongest joints, stronger columns, and weaker beams" behaviour, and that the energy dissipation capacity worked well under the dynamic loads (Xiao et al., 2012).

These findings prompted the question of whether the RCA concrete properties could be more susceptible to the high-rate effects given the reported performance drop when compared to conventional concrete. For the same structural frame, a dynamic constitutive model was calibrated and tested with combinations of RCA replacement ratios of 30%, 70%, and 100%; and strain rates of 10^{-1}, 10^{-2}, 10^{-3}, and 10^{-5} sec^{-1}.

Table 2-5: Effects of strain rate and RCA replacement ratio increments on the performance of RCA concrete (Wang et al., 2022).

Parameter	Strain rate (↑ $\dot{\varepsilon}$)	RCA replacement ratio (↑ R)
Cracking load (P_c)	↑ 22.7%	↑ 15.4%
Cracking deformation (Δ_c)	↑ 59.6%	↑ 53.1%
Yielding load (P_y)	↑ 32.1%	↓ 10.1%
Yielding deformation (Δ_y)	↑ 37.7%	↑ 16.2%
Peak load (P_m)	↑ 29.9%	↓ 10.3%
Peak deformation (Δ_m)	↓ 16.3%	↑ 10.3%
Ultimate load (P_u)	↑ 17.3%	↓ 7.0%
Ultimate deformation (Δ_u)	↓ 19.0%	↓ 8.2%
Structural ductility (μ)	↓ 27.0%	↓ 9.8%

Table 2-5 shows the effects of these two parameters at different stages of the modelled tests, where it can be appreciated that the rate sensitivity has a more significant influence than the RCA ratio, and that the yielding displacement and load have the most notorious increments as found in previous cases. Furthermore, another key finding is the decrease in the ultimate load and deformation capacity, as well as in the structural ductility when a higher RCA replacement is used. These results follow the same tendencies showed in the study of the mechanical properties, and can be associated to the stiffness of the RCA members (Wang et al., 2022; Wang & Xiao, 2018).

2.6.3. Cyclic bond

The study of the bond behaviour is relevant for seismic applications, as all the ductility requirements rely on the rebars developing their yielding stresses. As reviewed in previous sections, the interaction between the reinforcement and concrete is traditionally considered in the development length equations of the structural codes. These equations were developed for conventional concrete and are different for compression and tension loads, with the latter having the most conservative requirements. These lengths must be considered in the design of the structures, and sometimes they create major restrictions depending on the structural application of a determined member (i.e. column length).

Cyclic tests whose loading protocols are based on the symmetrical reversed approach led to more severe damage when the displacement amplitudes increase, and the slope of the bond stress curves can also reflect the influence of the loading rates. Once the splitting cracks develop, they accelerate the bond degradation until failure. Another relevant aspect is the contribution of the steel reinforcement to the degradation rate, which directly impacts the number of cycles the structures can sustain before developing the bond failures, which are higher than those of unconfined concrete (Alavi-Fard & Marzouk, 2002; Hu et al., 2019; Lu et al., 2019).

Under monotonic tests, the use of beam-end specimens has provided a good understanding of the bond behaviour; they do not overestimate the bond stresses as when using the pullout tests, and they also allow the study of the splitting failures due to the smaller concrete covers. However, the design is purposely made to allow the development of the longitudinal splitting cracks, which might prevent the testing of fully reversed loads due to the lack of proper transverse confinement. Modified beam-ends have been proposed considering different shear reinforcement spacings, as well as in the location of the testing bar (on a different plane) with respect to the support longitudinal ones (Asghari Ghajari & Yousefpour, 2023; Baktheer et al., 2021; Camps et al., 2018).

Another aspect comes from the testing position, beam-ends are traditionally tested in a horizontal position, but as mentioned before, vertically applied loads are easier to implement in many research facilities. One of the first challenges is to create a setup that can allow the measurement of the bar free-end slip (Shao et al., 2022). Another challenge comes from the possible effects of the support reactions on the embedded section, which might provide extra unintended confinement. Hence, one of the proposed alternatives is to move this section to the middle of the beam-end to allow a better bond study (Asghari Ghajari & Yousefpour, 2023; Butler et al., 2015b; Martí-Vargas & García-Taengua, 2015).

One final aspect that can impact the study of the cyclic bond behaviour is the selected instrumentation. Traditional strain gauges are effective at measuring localized strains, but they require the grinding of the rebar to provide plain surfaces to glue them. The wiring can also create a predetermined cracking point; and if the gauges are closely spaced, these factors will influence the bond readings. An alternative is to install the gauges inside the rebar, but the process is time and labour intensive, and the wiring places a physical limitation. Nevertheless, the development of newer techniques such as the use of distributed fibre optical sensing (DFOS) can improve the resolution of the measurements without further surface intervention (Lemcherreq et al., 2023).

Examples of the advantages of a higher resolution can be appreciated in the study of the bond behaviour under repeated loadings using pullout tests. Results have shown the repeated fatigue loads do not have a major influence on the ultimate bond capacity if they do not initiate the bond failures. Furthermore, residual bond stresses have been measured after partial and complete unloading (Lemcherreq et al., 2023; Oh & Kim, 2007; Rehm & Eligehausen, 1979). Moreover, the use of DFOS allow a better understanding of the bond stress distribution and confirm its non-uniformity, showing that on the loaded side, the values are smaller, and the peak value tends to shift towards the unloaded end of the specimen followed by a decrease in the bond stress. However, DFOS costs and required

equipment are still too high for most applications when compared to traditional gauges, and they also involve a higher complexity analysis (Lemcherreq et al., 2023).

2.7. Summary and research gaps

Based on the different topics reviewed in this Chapter, the most important outcomes for the upcoming experimental phase are listed below:

1) The use of alternative binders that can replace the traditional clinker is still at early stages. Most of the research is focused on the hydration phases, mechanical properties, and compatibility with modern admixtures. However, there is a lack of information regarding the structural performance of concrete made with those materials.
2) There is a lack of incentives to implement RCA in new concrete mixes for structural applications. On one side, the recycling processes are more costly than the production of fresh new aggregates. On the other hand, designers and regulators are still not convinced given the high scatter in the properties of RCA coming from different sources, and in the reported lower performance when compared to conventional concrete.
3) Traditional RCA implementation in new concrete mixes has been made via DRM techniques, which leads to mixes that will have less workability and hardened densities due to the attached residual mortar. Nevertheless, the EMV Method provides an effective solution by balancing the volumetric proportions of the concrete ingredients. This method computes the RMC of the RCA, and it can be applied to multiple sources.
4) One of the main drawbacks of the EMV Method is the workability loss due to the diminished fresh cement paste. Techniques like aggregate presoaking and a more tailored use of admixtures, such as PCE-based superplasticizers, could help improve its performance without the need of major modifications.

5) Structural tests that involve the use of EMV Method have been developed for the study of the flexural, shear, and monotonic bond performances, with results that are comparable to those of conventional concrete. However, there is a research gap in the cyclic performance of the bond behaviour.
6) The descriptive and design bond equations were calibrated for conventional concrete. Hence, their applicability for RCA concrete made with the EMV Method is another research gap.
7) Beam-ends are the best suited small-scale testing specimens for the bond behaviour study. Their design provides more realistic results since both concrete and steel are in tension. Moreover, they allow the development of the splitting failures and different combinations of concrete covers and embedment lengths. However, their design does not consider transverse reinforcement, which might impact the implementation of fully reversed loads.
8) Beam-ends are tested horizontally, but most research facilities have the equipment to apply vertical loads. Therefore, if vertical tests are considered, it is important to verify the support reactions will not alter the bond section.
9) Quasi-static tests are one of the most accepted ways to study the cyclic performance of a structure, guidelines are available, and loading protocols include slowly applied loads in fully reversed cycles. However, they do not consider the dynamic effects of the earthquake loads, and the induced stiffness degradation at high amplitudes can lead to conservative results.

3. Concrete mix design

This chapter focuses on the design of four concrete mixes developed for the subsequent structural tests. The first section will go over the chosen raw materials, the second section will be dedicated to the trial batches that led to the final mix designs, and the final section will consist of a discussion of the key findings and their implications.

3.1. RCA characterization

Two RCA sources were selected for the project, and both were returned hardened concrete (RHC). The decision of selecting RHC as the primary RCA source was partially made upon availability, and because its uniformity and quality present advantages when studying the bond behaviour since less variability is incorporated. Thus, the sources were:

1) RCA-1: RHC from a ready-mix plant based in Montreal, QC.
2) RCA-2: RHC from a ready-mix plant based in Ottawa, ON.

Figure 3-1: RCA-1 from Montreal, QC.

Figure 3-2: RCA-2 from Ottawa, ON.

RCA-1 was delivered already crushed to the University of Ottawa's structural facilities. The shipment consisted of three containers, accounting for approximately 4 tonnes of material (Figure 3-1). On the other hand, RCA-2 was sampled directly on-site at the supplier's facility (Figure 3-2). Sampling in different locations was executed according to CSA Standard Practice A23.2-1A (CSA Group, 2024a). No additional information regarding the composition or reactivity of both sources was available; therefore, it was not possible to classify them as Type 1 or Type 2 RHC.

3.1.1. RCA particle size distribution

The first step of the aggregate characterization was the determination of their respective particle size distribution (PSD) curves. The PSD was made according to the requirements of Table 11 of CSA A23.1 for Group I – Coarse Aggregates (destined for combined grading and normal concrete applications), and the 19 mm nominal maximum aggregate size that was obtained for both sources. Table 3-1 presents a summary of the requirements, while Figure 3-3 showcases the sieving process with the help of an aggregate screen shaker machine.

Table 3-1: Grading requirements for Group I – Coarse Aggregates (CSA Group, 2024a).

Sieve [mm]	Min Passing [%]	Min Retained [%]	Max Passing [%]	Max Retained [%]
25.00	100%	0%	100%	0%
19.00	85%	15%	100%	0%
12.70	50%	50%	90%	10%
9.50	25%	75%	60%	40%
4.75	0%	100%	10%	90%
2.36	0%	100%	5%	95%

Figure 3-3: RCA sieving process and storage.

Table 3-2: RCA-1 sample grading.

Sieve [mm]	Passing [kg]	Retained [kg]	Passing [%]	Retained [%]	Accumulated [%]
25.00	60.00	0.00	100%	0%	0%
19.00	60.00	0.82	99%	1%	1%
12.70	59.19	31.19	47%	52%	53%
9.50	27.99	14.52	22%	24%	78%
4.75	13.47	5.46	13%	9%	87%
Bottom tray	8.01	8.01	0%	13%	100%
Total		**60.00**		**100%**	

The representative samples of both sources consisted of approximately 60 kg for RCA-1, and 80 kg for RCA-2. The grading results are presented in Table 3-2 and Table 3-3, while the PSD curves are available in Figure 3-4.

Table 3-3: RCA-2 sample grading.

Sieve [mm]	Passing [kg]	Retained [kg]	Passing [%]	Retained [%]	Accumulated [%]
25.00	79.77	3.48	96%	4%	4%
19.00	76.29	11.13	82%	14%	18%
12.70	65.16	23.11	53%	29%	47%
9.50	42.05	10.32	40%	13%	60%
4.75	31.73	15.33	21%	19%	79%
Bottom tray	16.40	16.40	0%	21%	100%
Total		**79.77**		**100%**	

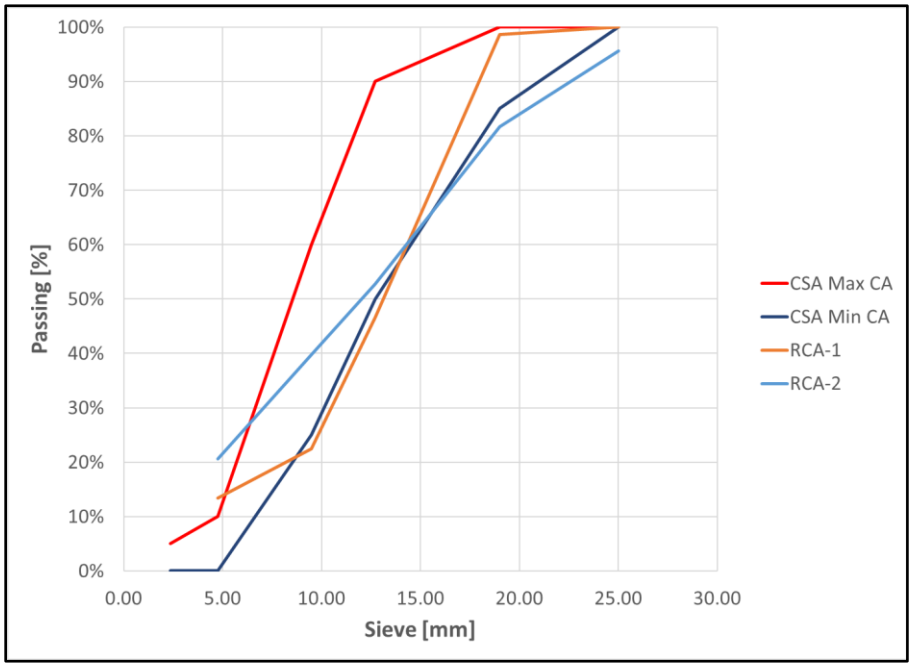

Figure 3-4: RCA particle size distribution.

As observed in Figure 3-4, both sources fall slightly outside the standard curves, especially at the 4.75 mm sieve, which is a common for RCA. The maximum allowance for this size is 10%, and the results were 13% for RCA-1 and 21% for RCA-2. When comparing

both sources, RCA-1 presents a curve that closely follows the required minimums for the 9.5 mm and 12.7 mm fractions. However, the retained 19 mm portion was 1%, which is close to the maximums. In contrast, RCA-2 shows a more balanced distribution for all fractions but also below the minimums at the 19 mm fraction. Therefore, to comply with the CSA requirements, both PSD curves needed adjustments for the mix design.

3.1.2. RCA residual mortar content

The residual mortar content of the RCA sources was obtained following the "*Sodium Sulphate RMC Method*", which was introduced and described in the previous chapter. The recommended sample quantities per sieve size are shown in Table 3-4.

Table 3-4: *"Sodium Sulphate RMC Method"* sample weights per sieve size.

Sieve [mm]	Weight [g]
19.00	2000
12.70	1500
9.50	1250
4.75	1000

The required equipment for the test includes a freezer capable of maintaining a temperature of -17^{o}C, and an oven that could keep temperatures between 80^{o}C and 110^{o}C. Due to their size and availability, especially the oven, it was decided that for each RCA source the RMC tests would be executed with three samples per sieve size (12 samples in total), and three freeze-and-thaw cycles (the minimum required by the method).

Once the RCA samples were weighed and oven-dried, they were immersed in a solution with a 26% sodium sulphate concentration. After 24 hours, they were subjected to three freeze-and-thaw cycles while still immersed. Once the last thawing cycle was completed, the samples were washed, oven-dried and visually inspected. Finally, the RMC was determined according to Eq. 2.4 – 7. The RCA immersion in the 26% sodium sulphate solution and the placement inside the freezer are shown in Figure 3-5. Meanwhile, the

drying in the oven and the final visual inspection, which shows the differences between the original RCA and the retrieved OVA, are presented in Figure 3-6.

Figure 3-5: *"Sodium Sulfate RMC Method"*, Part 1.

Figure 3-6: *"Sodium Sulfate RMC Method"*, Part 2.

The RMC results, including the average, standard deviation, and coefficient of variation per each sieve size, are presented in Table 3-5 for RCA-1, and Table 3-6 for RCA-2. For both cases, the initial and final weights are in oven-dry condition.

Table 3-5: RMC per size of RCA-1.

	Initial Weight [g]				**Final Weight [g]**				**RMC [%]**			
	RCA-1 size [mm]				RCA-1 size [mm]				RCA-1 size [mm]			
Sample	**4.75**	**9.5**	**12.7**	**19**	**4.75**	**9.5**	**12.7**	**19**	**4.75**	**9.5**	**12.7**	**19**
S1	955	1206	1449	1929	654	863	1040	1410	32%	28%	28%	27%
S2	956	1205	1506	1937	647	859	1060	1449	32%	29%	30%	25%
S3	943	1207	1482	2017	637	866	1040	1511	32%	28%	30%	25%
								Avg	**32%**	**28%**	**29%**	**26%**
								STD	**0.00**	**0.00**	**0.01**	**0.01**
								CoV	**0.01**	**0.01**	**0.03**	**0.04**

Table 3-6: RMC per size of RCA-2.

	Initial Weight [g]				**Final Weight [g]**				**RMC [%]**			
	RCA-2 size [mm]				RCA-2 size [mm]				RCA-2 size [mm]			
Sample	**4.75**	**9.5**	**12.7**	**19**	**4.75**	**9.5**	**12.7**	**19**	**4.75**	**9.5**	**12.7**	**19**
S1	979	1227	1472	1970	718	838	970	1270	27%	32%	34%	36%
S2	978	1223	1466	1968	719	835	1002	1106	27%	32%	32%	44%
S3	971	1224	1472	1950	632	850	1077	1185	35%	31%	27%	39%
								Avg	**29%**	**31%**	**31%**	**40%**
								STD	**0.05**	**0.01**	**0.04**	**0.04**
								CoV	**0.16**	**0.02**	**0.12**	**0.11**

The RMC of RCA-1 is evenly distributed among the sieve sizes, although the concentration is superior in the 4.75 mm fraction, and inferior in the 19 mm fraction. In the case of RCA-2, the tendency is reversed, the 4.75 mm fraction has the lowest concentration, and the 19 mm fraction the highest. Another detail worth considering is the impact of performing three and not five freeze-and-thaw cycles. The execution of three cycles was effective at removing most of the RMC; however, it required an extended visual inspection and quality control to remove the remaining RM that was still attached to the aggregates.

3.1.3. RCA general properties

Absorption and relative density (or specific gravity) were calculated based on the CSA Test Method A23.2.12A (CSA Group, 2024a), with the latter being divided into bulk oven-dry (OD) relative density, bulk surface-saturated-dry (SSD) relative density, and apparent relative density. Meanwhile, the bulk density (also known as unit weight), which includes loose and rod-compacted bulk densities, was computed according to the CSA Test Method A23.2-10A (CSA Group, 2024a).

Additionally, the voids and moisture contents were also calculated, with the former determined according to the specifications of ASTM C29 (ASTM, 2023). Since the PSD curves of both RCA sources required adjustments, it was decided to determine the properties per sieve size, with 3 repetitions each, and using weighted averages for the reported results. The reasoning behind this decision was the need for a reconstructed grading curve using different size fractions. The results are presented in Table 3-7.

Table 3-7: Summary of RCA properties.

Property	RCA-1	RCA-2
Bulk Relative Density (OD)	2.40	2.38
Bulk Relative Density (SSD)	2.50	2.49
Apparent Relative Density (OD)	2.67	2.66
Absorption	4.30%	4.39%
Moisture	1.76%	1.57%
Loose Bulk Density UW (OD)	1.26	1.25
Bulk Density UW (OD)	1.42	1.40
Bulk Density UW (SSD)	1.48	1.46
Voids Content	40.78%	41.04%
Residual Mortar Content (RMC)	29.24%	32.18%

A visual comparison between both sources is presented in Figure 3-7, where there are minor differences in terms of size, but not in terms of shape (both are crushed aggregates). Likewise, the properties presented in Table 3-7 are nearly identical in every category. Consequently, it was decided to only use one RCA source for the remainder of the project;

RCA-1 was selected for use in the subsequent tests since enough material was already in stock at the University of Ottawa's facilities.

Figure 3-7: Visual comparison between RCA-1 and RCA-2.

3.2. Natural aggregates characterization

For the natural fine aggregates, also referred to as "sand", the relative densities and absorption values were determined according to CSA A23.2-6A (CSA Group, 2024a). Additionally, the moisture and fineness modulus were also computed. The acquired sand was certified for concrete use under the FA1 category of Table 10 of CSA A23.1 (which is adapted and presented in Table 3-8).

Meanwhile, in the coarse aggregates case, the characterization followed the same methods described in the previous section, but unlike RCA, the properties were determined based on a bulk sample of 3 kg. This decision was made because the natural coarse aggregate, which was crushed aggregate coming from a local quarry in the Ottawa region, would be used in the delivered condition since it was already certified for concrete use. The results for both natural aggregate types are presented in Table 3-9.

Table 3-8: Grading requirements for FA1 – Fine Aggregates (CSA Group, 2024a).

Sieve [mm – μm]	Min Passing [%]	Min Retained [%]	Max Passing [%]	Max Retained [%]
10 mm	100%	0%	100%	0%
5 mm	95%	5%	100%	0%
2.5 mm	80%	20%	100%	0%
1.25 mm	50%	50%	90%	10%
630 μm	25%	75%	65%	35%
315 μm	10%	90%	35%	55%
160 μm	2%	98%	10%	90%
80 μm	0%	100%	3%	97%

Table 3-9: Summary of natural coarse and fine aggregates properties.

Property	Old-NA	New-NA-1	New-NA-2	Sand
Bulk Relative Density (OD)	2.72	2.53	2.70	2.60
Bulk Relative Density (SSD)	2.76	2.62	2.73	2.62
Apparent Relative Density (OD)	2.82	2.78	2.78	-
Fineness Modulus	-	-	-	2.79
Absorption	1.24%	3.55%	1.12%	0.82%
Moisture	0.11%	1.10%	0.11%	1.00%
Loose Unit Weight (OD)	1.25	1.49	1.49	-
Compacted Unit Weight (OD)	1.39	1.73	1.73	-
Compacted Unit Weight (SSD)	1.41	1.79	1.75	-
Voids Content	48.76%	31.47%	35.70%	-

In Table 3-9, three types of coarse aggregates are characterized, namely “Old-NA”, “New-NA-1”, and “New-NA-2”. The first source, “Old-NA”, was used in the first trial batch. However, some inconsistencies were detected in the voids content and bulk density. The measured compacted value was 1392 kg/m^3, and the range for regular coarse aggregates is between 1450 – 1750 kg/m^3. Therefore, and because there was not enough stock for further batches, it was decided to get a fresh delivery from a local supplier.

This new material was labeled as “New-NA”, and 4 tonnes were shipped to the university’s facilities. The first characterization round is presented under the “New-NA-1” label and was used for the subsequent trial batches and final mixes. The specific gravity in

oven-dry condition, 2.53, was on the lower end of the range for natural coarse aggregates, which is typically between 2.5 – 3.0. Moreover, the absorption value at 3.55% was also higher than usual, but since absorption values have been reported in the range of 0.2 – 4% depending on the source origin of the aggregate (i.e. limestone, basalt, etc.), the results were deemed to be within the range.

However, when revisiting the results after the completion of the structural tests, it was decided to verify the "New-NA" absorption content, whose updated value came down from 3.55% to 1.12%. Since the relative density values depend on this parameter, they were also verified and are presented under the "New-NA-2" label in Table 3-9. The updated results are like those of the "Old-NA" source, but with a compacted bulk density (1732 kg/m^3) now within the expected range. The error most likely came from the original SSD weight, which probably had an over-saturated aggregate, and its implications will be further addressed in the discussion section.

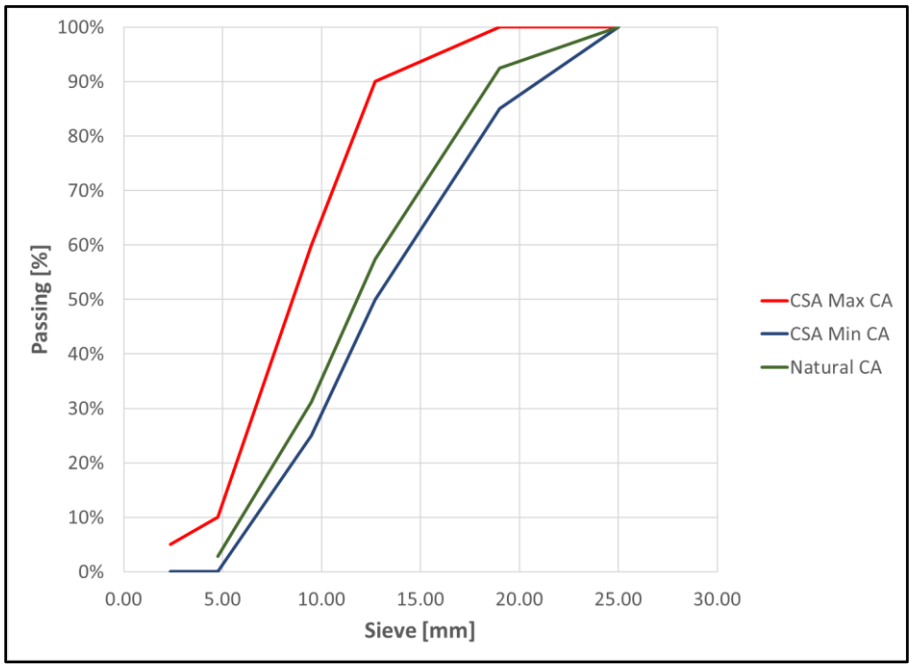

Figure 3-8: Natural coarse aggregate particle size distribution.

The PSD curve of the “New-NA” source is presented in Figure 3-8, and it effectively shows the aggregate is within the limits given by CSA A23.1, being closer to the minimum band. Finally, Figure 3-9 shows a visual comparison between the “New-NA” and the RCA-1 aggregates. It can be observed the colouration is different, with the RCA having a whiter tone (light blue oval) due to the presence of the RMC; while the natural coarse aggregate has a darker colour (red circle) like the one of the OVA in Figure 3-6.

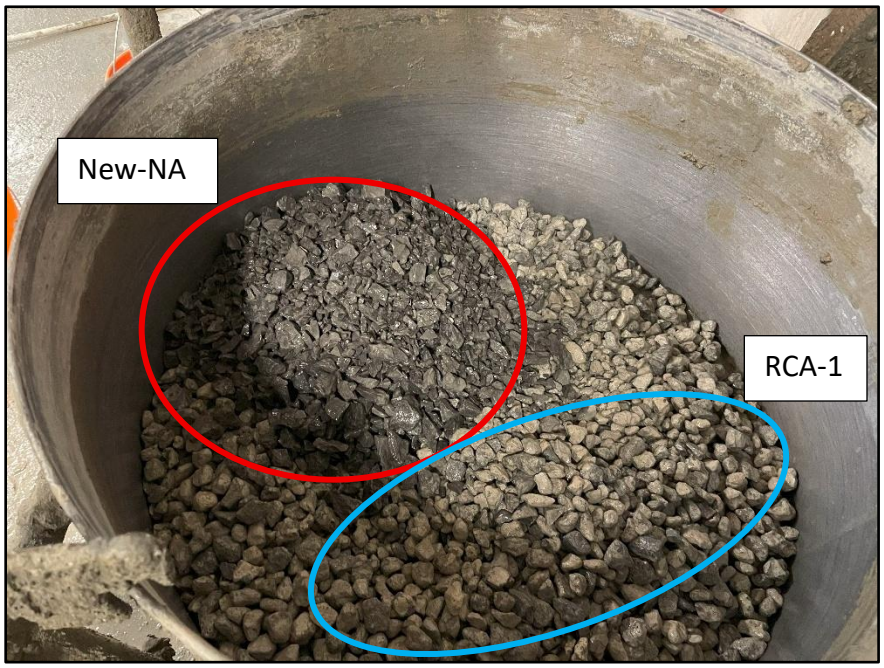

Figure 3-9: Visual comparison between natural coarse aggregate and RCA.

3.3. Binders

Two hydraulic cements were selected for this research. The first one was the regular Portland-limestone cement (PLC), or General Use Portland-limestone cement (GUL) according to the CSA A3000 nomenclature. This binder has a limestone filler content of 15% and is the most commonly used binder for ready-mix concrete destined for regular structural applications.

The second binder is a proprietary material developed by C-Crete Technologies, a new-generation low-carbon hydraulic cement. This binder, hereinafter referred to as “C-Crete

Binder", can be considered as an activated slag with calcium compounds, calcium silicate compounds, and other calcium compounds containing iron and aluminum making up most of the product (C-Crete Technologies, 2023). Its composition is summarized as it follows:

- Ground Granulated Blast Furnace Slag: 90% – 100%
- Alkali Materials: 0% – 10%
- Admixtures: 0% – 1%

The use of SCMs was not considered for this project since they would have added another variable to the testing matrix. The effects that SCMs could bring to the EMV mixes will be addressed in the discussion section.

3.4. Admixtures

Two admixture types were used throughout the research: an air-entrainer (AE), and a high-range-water-reducer (HRWR) or superplasticizer. For the first trial batch, the products were the following:

- AE-1: Eucon *"AIR MAC 12"*, with a recommended dosage of 6 – 260 mL per 100 kg of cementitious materials.
- HRWR-1: Eucon *"PLASTOL 341"* (PCE-based), with a recommended dosage of 130 – 650 mL per 100 kg of cementitious materials.

From the second round of trial batches onwards, it was decided to obtain both admixture types from the same GUL cement supplier to ensure their chemical compatibility. The details are the following:

- AE-2: Master Builders *"MasterAIR AE 200"*, with a recommended dosage of 8 – 98 mL per 100 kg of cementitious materials.

- HWRW-2: Master Builders *"Master Glenium 1466"* (PCE-based), with a recommended dosage of 130 – 650 mL per 100 kg of cementitious materials.

3.5. Mix design requirements

The class of exposure for the concrete was based on the Canadian climate characteristics, which include long winters and an elevated use of de-icing salts. Therefore, according to the definitions established in Table 1 of CSA A23.1, the selected class of exposure was Class C-1: *"Concrete exposed to chlorides with or without freezing and thawing conditions where the reinforcing steel must be protected from corrosion"* (CSA Group, 2024a). Class C-1 concretes must comply with the following requirements available in Table 2 of CSA A23.1:

- Maximum water-to-cementitious materials (W/C) ratio of 0.40.
- Minimum specified compressive strength (f_c') of 35 MPa at 56 days.
- If exposed to freeze-and-thaw cycles, and for the given 19 mm nominal maximum aggregate size, the air content should be in the range of 5 – 8%.
- Curing of 7 days at temperatures equal or greater than 10°C and for the time necessary to attain 70% of the specified strength.

Based on the available raw materials and on the research objectives of the project, it was decided to design four concrete mixes, namely:

1) ACI: Natural aggregate mix designed according to the requirements of a C-1 class concrete and proportioned using conventional methods (ACI Method).
2) DRM: RCA mix based on the original ACI design, but with a full volumetric RCA coarse aggregate replacement proportioned by the Direct Replacement Method.
3) EMV: RCA mix based on the original ACI design, but with an RCA coarse aggregate replacement proportioned by the Equivalent Mortar Volume Method.

4) EMVc: RCA mix with the exact same proportions of the EMV Method, but with the "C-Crete Binder" replacing the traditional GUL cement in a 1:1 mass ratio.

The conventional mix proportioning method, or ACI Method, has a series of clauses and adjustments that are fully explained in the ACI 211.1 Guide (ACI, 2022). A summarized version that highlights the main considerations is presented below:

- Once the material properties and exposure conditions are determined, the target slump is chosen based on the construction type. For instance, beams, reinforced walls, and building columns are suggested to have a minimum slump of 25 mm, and a maximum of 100 mm.
- The nominal maximum size of the coarse aggregate is set according to the application and workability requirements, which are available in Clause 4.3.2.2 of CSA A23.1 (CSA Group, 2024a). For this project, the restriction comes from the concrete cover, set at 40 mm. Since the maximum nominal size of the coarse aggregate is 19 mm, the requirement is satisfied.
- ACI 211 provides two sets of tables to determine the mixing water and air content, and the difference between them is set by the air-entrainment consideration. Once this parameter is clear, the mixing water and air content are determined based on the slump and nominal size of the aggregate. Air-entrained concrete will have more air content and less mixing water than non-air-entrained concrete.
- The cementitious materials are computed based on the W/C ratio and the water content. The total amount must be greater than the minimum required for the nominal maximum size of the aggregate, which is 320 kg/m^3 for the 19 mm coarse aggregate.
- For the estimation of the coarse aggregate content, ACI 211 provides relationships based on the fineness modulus of the sand and the nominal maximum size of the aggregate. With these values, the bulk fraction of the

coarse aggregate (or dry-rodded density) can be determined, and when multiplied by the bulk density or unit weight, the final weight can be obtained.

- The last component, the fine aggregate, is computed considering a volumetric unit, usually 1 m^3. Once the water, cementitious materials, coarse aggregate, and air contents are known, their respective volumetric fractions are computed and added. This value is subtracted from the volumetric unit, and the difference will be the required fine aggregate content.

Finally, the decision to include an RCA mix proportioned by the Direct Replacement Method was made to be consistent with previous studies and to highlight the benefits of the EMV Method in the implementation of RCA in new concrete mixes. Therefore, its inclusion is relevant for the creation of a benchmark that can help assess the bond behaviour of EMV-proportioned RCA mixes under cyclic loading.

3.6. Trial Batch 1

For the first trial batch, the evaluated parameters were the cement content, RCA replacement, slump, and use of admixtures. Three mixes were developed and tested, each with a batch volume of 10 litres and with the use of “Old-NA” as the primary natural coarse aggregate source. The concrete was made on a 60-litre pan mixer (Figure 3-10) and following the requirements of the CSA Standard Practice A23.2-2C (CSA Group, 2024a) for the mixing protocol, slump test, and elaboration of the standard 100x200 mm cylinders used for the compressive strength tests. The mix details are described below, their proportions are available in Table 3-11, and the admixtures content in Table 3-12.

The first mix, ACI-TB1-1, was proportioned by the ACI Method with a W/C ratio of 0.40. This mix was not air-entrained and considered a target design slump of 50 mm. This mix was developed to have a reference for the workability without the use of admixtures. The main restriction comes from the W/C ratio, which for non-air-entrained concrete requires

the design of a mix for a compressive strength of 42.5 MPa resulting in a high amount of cementitious materials.

Figure 3-10: 60L pan mixer and accessories.

Table 3-10: Adjusted RCA-1 grading.

Sieve [mm]	Adj. Passing [%]	Adj. Retained [%]
25.00	100%	0%
19.00	100%	0%
12.70	60%	40%
9.50	30%	70%
4.75	0%	100%
2.36	0%	100%

The second mix, ACI-TB1-2, was also proportioned by the ACI Method with a W/C ratio of 0.40, but was air-entrained and targeted a design slump of 50 mm. This mix also considered the use of a superplasticizer to improve the slump and workability. By using air-entrainment, it was possible to design a mix for 35 MPa with the same W/C ratio, and more importantly, it allowed a reduction in the mixing water and cementitious materials.

The third mix, DRM-TB1-1, was based on ACI-TB1-2 with 100% coarse aggregate replacement with RCA-1 by mass. The main objective of this mix was to compare its workability with the control mixtures. This mix was also used to test the adjusted RCA-1 grading curve which was modified to fit within the CSA limits (Table 3-10 and Figure 3-11).

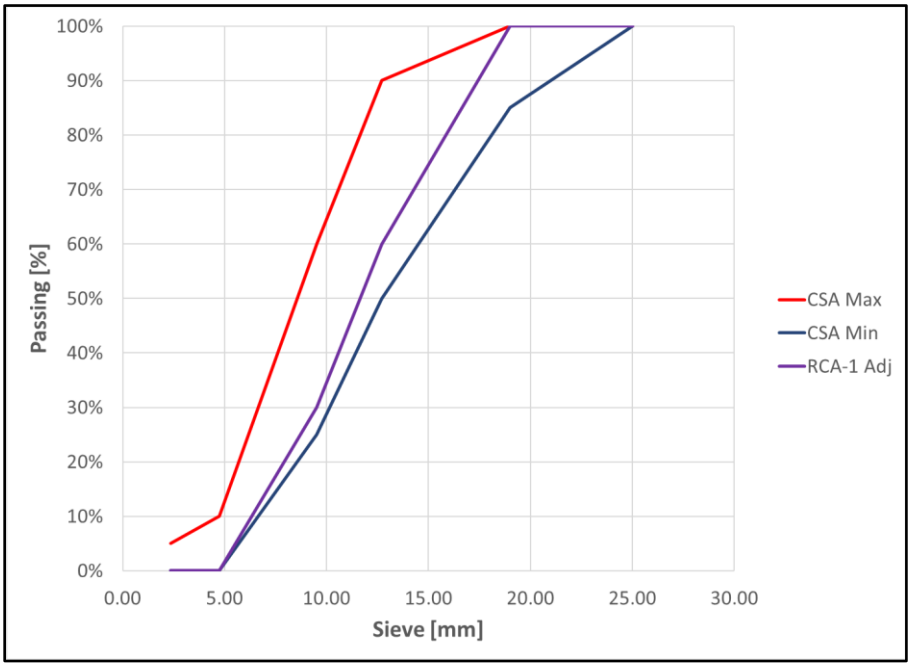

Figure 3-11: Adjusted RCA-1 PSD curve.

Table 3-11: Trial Batch 1 Mixes.

		ACI-TB1-1		ACI-TB1-2		DRM-TB1-1	
Component	**SG**	**[kg/m³]**	**[m3/m³]**	**[kg/m³]**	**[m³/m³]**	**[kg/m³]**	**[m³/m³]**
Cement	3.15	462.50	0.147	412.50	0.131	412.50	0.131
Water	1.00	185.00	0.185	165.00	0.165	165.00	0.165
Coarse Aggregate	2.72	862.89	0.317	862.89	0.317	0.00	0.000
RCA	2.40	0.00	0.000	0.00	0.000	862.89	0.360
Fine Aggregate	2.60	860.90	0.331	824.17	0.317	712.36	0.274
Air	0.00	0.00	0.020	0.00	0.070	0.00	0.070
Total		**2371.29**	**1.000**	**2264.56**	**1.000**	**2152.75**	**1.000**

As observed in Table 3-11, the cement reduction between ACI-TB1-1 and ACI-TB1-2 is approximately 11%. On the other hand, the direct replacement by mass creates an

imbalance in the volumetric coarse aggregate proportion that is compensated with a reduction of 13.5% in the fine aggregate content. However, as noticed in the design density, there is a 5% decrease, which is attributed to the RCA nature and reflected in the specific gravity value. For the fresh state properties, only the slump value was measured since workability was extremely low for all mixes (Table 3-13).

Table 3-12: Trial Batch 1 Admixtures.

		ACI-TB1-1		ACI-TB1-2		DRM-TB1-1	
Admixture	**SG**	**[mL/100kgCM]**	**[mL]**	**[mL/100kgCM]**	**[mL]**	**[mL/100kgCM]**	**[mL]**
AE-1	1.01	0	0	25	103	25	103
HRWR-1	1.05	0	0	85	351	121	499

Table 3-13: Trial Batch 1 fresh properties.

Property	**ACI-TB1-1**	**ACI-TB1-2**	**DRM-TB1-1**
Slump [mm]	0	10	20

Table 3-14: Trial Batch 1 Compressive Strength at 28 days.

	ACI-TB1-2		DRM-TB1-1	
Cylinder	**Age [d]**	**f'_c [MPa]**	**Age [d]**	**f'_c [MPa]**
1	28	25.44	28	25.68
2	28	33.17	28	23.88
3	28	31.99	28	36.63
4	28	36.86	28	21.08
5	28	26.09	-	-
	Avg	**30.71**	**Avg**	**26.82**
	Std	**4.35**	**Std**	**5.90**
	CoV	**0.14**	**CoV**	**0.22**

Cylinders were cast only for the ACI-TB1-2 and DRM-TB1-1 mixes to test the compressive strength at 28 days. Five cylinders were obtained from ACI-TB1-2 and four from DRM-TB1-1. The results are presented in Table 3-14, and a visual comparison between them is available in Figure 3-12.

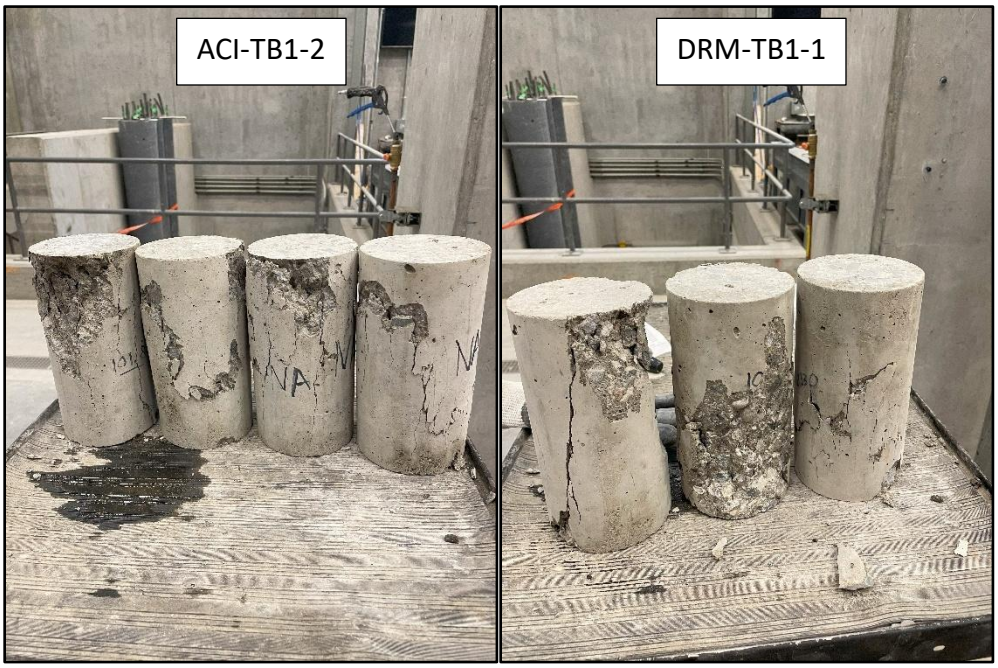

Figure 3-12: Trial Batch 1 tested cylinders.

The results of the compressive strength tests were clearly superior for the ACI-TB1-2 mix, which had both a higher mean and less scatter when compared to the DRM-TB1-1 mix. However, these results were expected since the RCA replacement was made by mass and not by volume, and because the DRM mix had a higher mortar content due to the RCA nature. Besides that, the low workability could have also played a role in their performance, which can affect mechanical properties if the cylinders are not well compacted.

3.7. Trial Batch 2

Based on the results of the first trial batch, a few general modifications were considered:

- Batch size was increased from 10 to 25 litres for all mixes, both to cast more cylinders and to have more fresh cement paste to evaluate workability. It was empirically determined that the pan mixer filled with 25 litres was able to produce consistent mixes whose fresh and hardened state properties were representative of much larger volumes.

- The natural coarse aggregate source was replaced with the “New-NA” source. This material was subsequently used in all remaining trial batches and final mixes, and the considered properties were those under the “New-NA-1” label.
- All coarse aggregates, including natural and RCA, were incorporated to the mix in a presoaked SSD condition in a bid to avoid the loss of water due to the high absorption levels. In the previous trial batch, moisture adjustments were considered in the mixing water content, but they had little effects.
- Fresh density and air-content tests were added to the slump measurement to further complement the fresh state properties.
- To record the evolution of the compressive strength, standard 100x200 mm cylinders were cast for tests at 3, 7, and 28 days.
- Both admixtures, air-entrainer and superplasticizer, were different than in the previous batch. The new pair, AE-2 and HRWR-2, was obtained from the same GUL cement supplier to guarantee their compatibility with the cement.

For this new batch, three mixes were considered. The first mix, ACI-TB2-1, was designed according to the ACI Method with same W/C ratio of 0.40, but with a slightly different design slump, which came down from 50 to 35 mm. This decision had two impacts, the first one was to reduce cement content, but also to set the benchmark for the superplasticizer effect, which had to be incorporated to increase the slump from 35 to 150 mm. In other words, without the use of the superplasticizer, the required mixing water to achieve 150 mm of slump with the same W/C ratio would have been approximately 193 kg. Therefore, the superplasticizer targeted a 17% reduction in the mixing water.

The second mix, DRM-TB2-1, was based on ACI-TB2-1 but with 100% volumetric RCA-1 coarse aggregate replacement using the DRM. A volumetric replacement is a better way to assess the RCA impact since it does not alter the remaining fractions. For the RCA-1 source, the grading adjustment used in the first trial batch (Table 3-10) was checked against the grading of the “New-NA” source (Figure 3-13). The PSD curves are similar in the

intermediate fractions, and no extra adjustments were needed given that not enough RCA-1 19 mm material was available to match the coarser section.

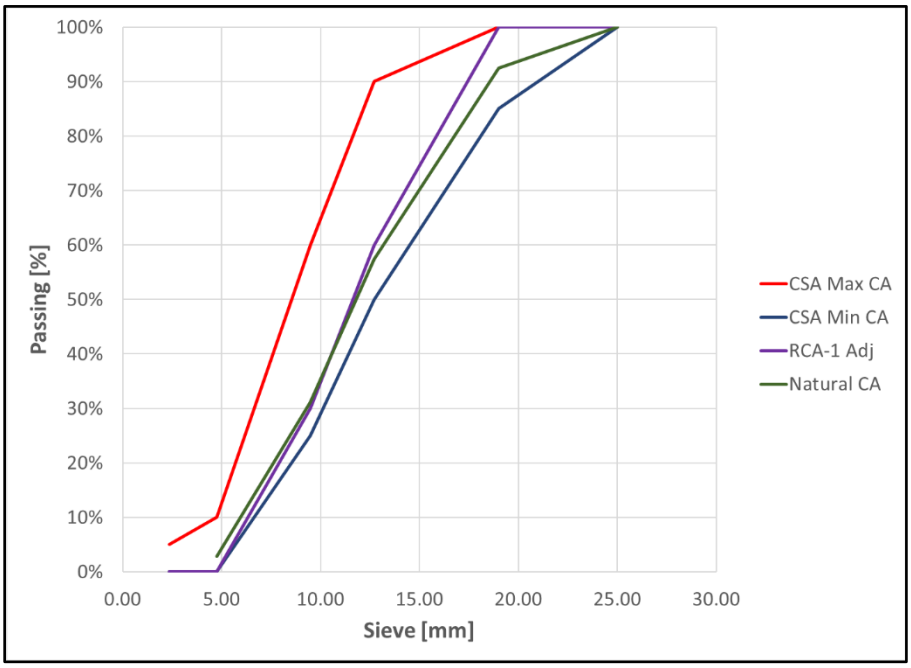

Figure 3-13: "New-NA" and RCA-1 PSD curves.

Table 3-15: EMV-TB2-1 parameters.

Parameter	Equation	Value
RMC	-	29.24%
RMC_{max}	3.7 – 1	34.49%
R_{min}	3.7 – 2	0.000
R	3.7 – 3	0.330
V_{NA}^{NAC}	-	0.424
V_{M}^{NAC}	3.7 – 4	0.506
V_{RCA}^{RCA-C}	3.7 – 5	0.424
V_{NA}^{RCA-C}	3.7 – 6	0.140
V_{NM}^{RCA-C}	3.7 – 7	0.366

The third mix, EMV-TB2-1, was also based on ACI-TB2-1 but used the EMV Method to incorporate the RCA into the mix. As explained in the literature review section, the EMV Method uses the RMC of the RCA to determine the necessary adjustments in the volumetric proportions of the ingredients to match those of the parent conventional concrete. Table

3-15 presents a summary of the parameters and a more detailed description of the calculation process for better understanding is provided below.

The first step is the verification of the allowed RCA replacement ratios, using Eq. 3.7 – 1 and Eq. 3.7 – 2 it is possible to determine the maximum RMC content (RMC_{max}) and minimum coarse aggregate replacement ratio (R_{min}).

$$RMC_{max}\ (\%) = \left(1 - V_{DR-NA}^{NAC} * \frac{SG_b^{NAC}}{SG_b^{RCA}}\right) * 100 \qquad (3.7-1)$$

$$R_{min} = 1 - \left(\frac{1 - RMC}{V_{DR-NA}^{NAC}}\right) * \frac{SG_b^{RCA}}{SG_b^{OVA}} \qquad (3.7-2)$$

Since the RMC_{max} is greater than the actual RMC of the RCA-1 source, it is possible to have a full coarse RCA replacement ($R_{min} = 0$). However, the target replacement ratio (R) aims to compensate the RMC of the RCA with the addition of enough fresh natural coarse aggregates to match the volumetric proportions of the parent mix (Eq. 3.7 – 3).

$$R = \frac{V_{RM}^{RCA-C}}{V_{RCA}^{RCA-C}} = \left[1 - (1 - RMC) * \frac{SG_b^{RCA}}{SG_b^{OVA}}\right] \qquad (3.7-3)$$

With the original volumetric proportions of the parent mix and the replacement ratio already known, it is possible to calculate the volumes of the RCA (Eq. 3.7 – 5) and natural coarse aggregate (Eq. 3.7 – 6) required for the new EMV mix.

$$V_M^{NAC} = 1 - V_{NA}^{NAC} \qquad (3.7-4)$$

$$V_{RCA}^{RCA-C} = V_{NA}^{NAC} \qquad (3.7-5)$$

$$V_{NA}^{RCA-C} = R * V_{NA}^{NAC} \qquad (3.7-6)$$

Finally, the volume of the new mortar in the EMV mix is the difference between the original mortar of the parent mix and the RM embedded in the RCA (Eq. 3.7 – 7).

$$V_{NM}^{RCA-C} = V_{M}^{NAC} - V_{RM}^{RCA-C} = V_{M}^{NAC} - R * V_{RCA}^{RCA-C} \qquad (3.7-7)$$

One way to verify the equivalence of the mix proportions between the parent and the new EMV mixes is by adding and comparing their overall volumetric fractions in Table 3-15 ($V_{NA}^{NAC} + V_{M}^{NAC} = V_{RCA}^{RCA-C} + V_{NA}^{RCA-C} + V_{NM}^{RCA-C}$), where both additions will have the same result: 0.930. The final mix designs of the second trial batch are available in Table 3-16, while the admixtures content is presented in Table 3-17.

Table 3-16: Trial Batch 2 mixes.

		ACI-TB2-1		DRM-TB2-1		EMV-TB2-1	
Component	**SG**	**[kg/m³]**	**[m³/m³]**	**[kg/m³]**	**[m³/m³]**	**[kg/m³]**	**[m³/m³]**
Cement	3.15	400.00	0.127	400.00	0.127	289.25	0.092
Water	1.00	160.00	0.160	160.00	0.160	115.70	0.116
Coarse Aggregate	2.53	1073.74	0.424	0.00	0.000	354.74	0.140
RCA	2.40	0.00	0.000	1016.17	0.424	1016.17	0.424
Fine Aggregate	2.60	569.39	0.219	569.39	0.219	411.75	0.158
Air	0.00	0.00	0.070	0.00	0.070	0.00	0.070
Total		**2203.13**	**1.000**	**2145.55**	**1.000**	**2187.61**	**1.000**

Table 3-17: Trial Batch 2 admixtures.

		ACI-TB2-1		DRM-TB2-1		EMV-TB2-1	
Admixture	**SG**	**[mL/100kgCM]**	**[mL]**	**[mL/100kgCM]**	**[mL]**	**[mL/100kgCM]**	**[mL]**
AE-2	1.01	48	192	40	160	97	281
HRWR-2	1.11	250	1000	250	1000	692	2002

As previously noted, the DRM mix keeps the same coarse aggregate fraction, but the mass is different due to the lower specific gravity of the RCA-1, which is also reflected in the design density being 2.6% lower than the control mix. In the case of the EMV mix, the RCA fraction remains the same, but more coarse aggregate and less fresh mortar are required to keep the same proportions. There is a reduction in the fresh cement, mixing water, and

fine aggregate content of around 28% each, while the natural coarse aggregate content decreases by almost 67%. Therefore, the RCA replacement can be evaluated as the effective fresh natural coarse aggregate replacement, 67%, or as the ratio to the total coarse aggregate content, which is approximately 74%.

Table 3-18: Trial Batch 2 fresh properties.

Property	ACI-TB2-1	DRM-TB2-1	EMV-TB2-1
Slump [mm]	225	125	55
Fresh Density [kg/m^3]	2424.70	2244.74	2285.42
Relative Yield	1.10	1.05	1.04
Air Content [%]	5.00%	3.30%	4.10%

Figure 3-14: ACI-TB2-1 fresh state.

In the admixtures case, they were added to the mix separately, each with half of the mixing water. The air content for the ACI and DRM mixes was in the middle of the recommended range (8 – 98 mL/100kgCM), and closer to the upper limit in the case of the EMV mix. Likewise, the superplasticizer dosages followed the same pattern considering that

the recommended range is between 130 – 630 mL/100kgCM. The results of the fresh properties are presented in Table 3-18, and Figure 3-14 to Figure 3-16, respectively.

Figure 3-15: DRM-TB2-1 fresh state.

Figure 3-16: EMV-TB2-1 fresh state.

For the ACI-TB2-1 mix, the amount of incorporated admixtures led to a mix with an excessive flowability, resulting in a slump of 225 mm. The air content and relative yield were within the design tolerances; therefore, it was determined that the admixtures content required an adjustment in future batches, especially a reduction in the superplasticizer.

In the case of the DRM-TB2-1 mix, it was determined that the admixtures content was almost ideal, with a slump value close to the targeted 150 mm, and with air content and yield values within the tolerances. The consistency of the mix was satisfactory with no signs of segregation or bleeding and was easy to work with.

Finally, the EMV-TB2-1 development was more complex. The superplasticizer was added in increments to test the initial workability in a conservative way. Initially, 30 mL were added with little effect; then an additional 5 mL were incorporated but the workability was similar with a high viscosity. Finally, a last addition of 15 mL improved the mix's plasticity with good air content and yield values, but with a slump that was still far from the targeted 150 mm. It was determined that a final batch was necessary to fine tune the admixtures content, especially the superplasticizer.

Besides the fresh state properties, 100x200 mm cylinders were cast to test the compressive strength at 3, 14, and 28 days of age (Figure 3-17 to Figure 3-19). The results for each testing day are available in Table 3-19, Table 3-20, and Table 3-21, respectively.

Table 3-19: Trial Batch 2 compressive strength at 3 days.

	ACI-TB2-1		**DRM-TB2-1**		**EMV-TB2-1**	
Cylinder	**Age [d]**	**f'_c [MPa]**	**Age [d]**	**f'_c [MPa]**	**Age [d]**	**f'_c [MPa]**
1	3	21.45	3	16.81	3	13.64
2	3	14.82	3	17.35	3	12.87
	Avg	**18.13**	**Avg**	**17.08**	**Avg**	**13.26**
	Std	**3.32**	**Std**	**0.27**	**Std**	**0.39**
	CoV	**0.18**	**CoV**	**0.02**	**CoV**	**0.03**

Table 3-20: Trial Batch 2 compressive strength at 7 days.

	ACI-TB2-1		DRM-TB2-1		EMV-TB2-1	
Cylinder	**Age [d]**	**f'_c [MPa]**	**Age [d]**	**f'_c [MPa]**	**Age [d]**	**f'_c [MPa]**
1	7	19.07	7	19.70	7	19.72
2	7	17.32	7	24.33	7	14.40
	Avg	**18.20**	**Avg**	**22.02**	**Avg**	**17.06**
	Std	**0.88**	**Std**	**2.31**	**Std**	**2.66**
	CoV	**0.05**	**CoV**	**0.11**	**CoV**	**0.16**

Table 3-21: Trial Batch 2 compressive strength at 28 days.

	ACI-TB2-1		DRM-TB2-1		EMV-TB2-1	
Cylinder	**Age [d]**	**f'_c [MPa]**	**Age [d]**	**f'_c [MPa]**	**Age [d]**	**f'_c [MPa]**
1	28	38.49	28	35.72	28	25.05
2	28	32.01	28	40.41	28	26.13
3	28	37.44	28	36.02	28	27.77
4	28	35.36	28	32.30	28	19.04
5	28	27.50	28	39.80	28	28.88
6	-	-	28	35.42	28	30.19
	Avg	**34.16**	**Avg**	**36.61**	**Avg**	**26.17**
	Std	**4.00**	**Std**	**2.76**	**Std**	**3.61**
	CoV	**0.12**	**CoV**	**0.08**	**CoV**	**0.14**

Only two cylinders per mix were tested at 3 and 7 days since the objective was to determine the compressive strength at 28 days with precision. The mix that had the best performance across the 3 ages was DRM-TB2-1. This was not a surprise since the fresh state properties showed this mix had the best consistency overall, thus improving the batch quality. In the case of the ACI-TB2-1 mix, the results were close to those of the DRM mix, but with a higher scatter. These results are attributed to the excessive slump of the fresh state, which impacted the batch quality and may have caused segregation in the cylinders.

In the case of the EMV-TB2-1 mix, the results at all testing days were inferior to those of the ACI and DRM mixes. The cause is attributed to the low slump of the mix and poor compaction which resulted in voids in the cylinders as seen in Figure 3-19. Therefore, an open question was left whether the mix could have performed better with proper

compaction. The compaction differences are clear when doing a visual comparison between the cylinders of all mixes (Figure 3-17 to Figure 3-19).

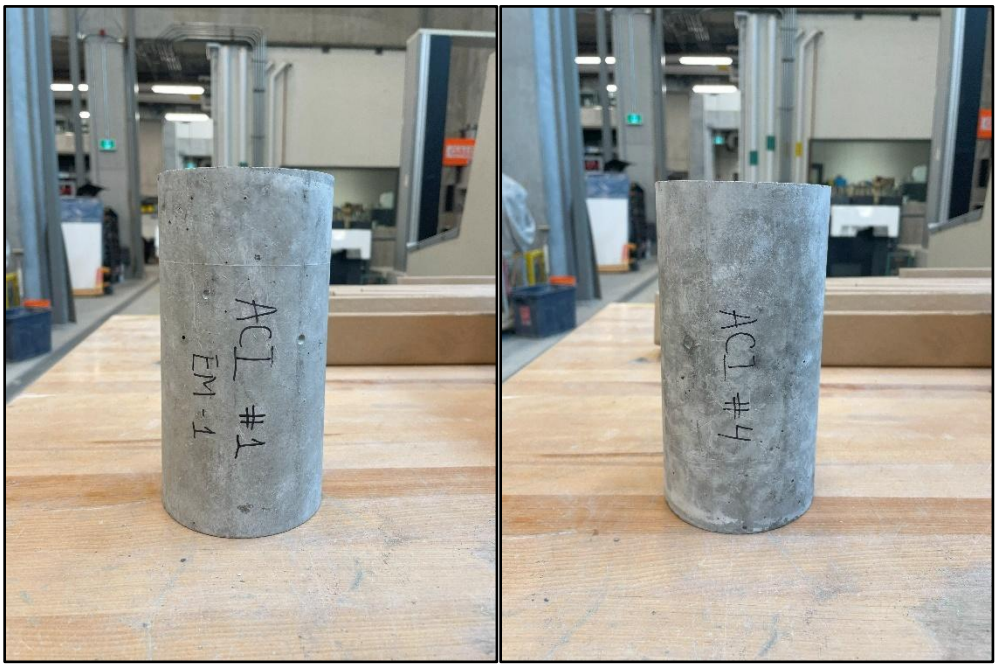

Figure 3-17: ACI-TB2-1 cylinders.

Figure 3-18: DRM-TB2-1 cylinders.

Figure 3-19: EMV-TB2-1 cylinders.

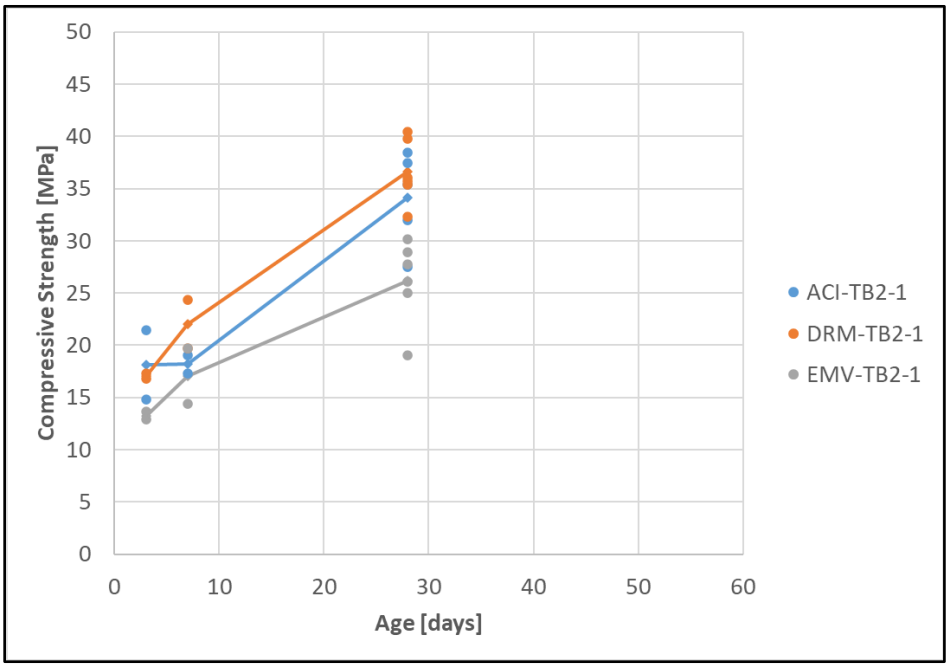

Figure 3-20: Trial Batch 2 – Compressive Strength Curves.

Figure 3-20 shows the data points of all tested cylinders at 3, 7, and 28 days of age, with solid lines representing the average for each respective mix. As stated before, the DRM mix

had a better trend than the other two mixes, although the ACI mix was not far behind, especially at 28 days. However, the biggest discrepancies were observed with the EMV mix, where the results and projections showed that, unlike the other two mixes, it was not likely to reach the minimum of 35 MPa at 56 days with the current design and admixtures content. Therefore, a new trial batch was deemed necessary to fix those issues.

Even though the EMV-TB2-1 mix performance was below the expectations, the second trial batch was considered an overall success. When compared to the first trial batch, all mixes had better workability and consistency, and it is believed that the use of the coarse aggregates in an SSD condition played a major role. Moreover, the fact that DRM-TB2-1 had the best strength performance gave confidence that the design of the other two mixes was on the right path, at least on the volumetric fractions. DRM mixes are expected to have the lesser performance among the three mixes because of having more RM and less density. In consequence, it was determined that tweaks to the admixtures content and cylinders' workmanship would unlock the expected performance for the ACI and EMV mixes.

3.8. Trial Batch 3

Based on the results of the second trial batch, it was decided to keep the batch size of 25 litres and the test of the fresh density, air content, and slump cone for the fresh state. The modifications that were considered are listed below:

- Only ACI and EMV mixes were tested in the new batching round; their volumetric fractions would be the same as in the previous batch, but with adjustments in the admixtures content.
- For all mixes, the mixing water was divided in two halves: the first one had the superplasticizer agent, while the second contained the air-entrainer. The first half would be added with the coarse aggregate, while the second half would be added after the cement and fine aggregates.

- To cast the cylinders, besides the rod compaction, it was decided to incorporate the use of a vibrating table (as seen in Figure 3-10) to improve their quality and avoid the presence of unwanted voids.
- Cylinders were tested for compressive strength at 7 and 28 days.

The volumetric fractions and admixtures are detailed in Table 3-22 and Table 3-23, respectively. For the ACI mix, the first new admixture combination proved successful; therefore, no other combinations were deemed necessary.

Table 3-22: Trial Batch 3 ACI mix.

		ACI-TB3-1	
Component	**SG**	**[kg/m^3]**	**[m^3/m^3]**
Cement	3.15	400.00	0.127
Water	1.00	160.00	0.160
Coarse Aggregate	2.53	1073.74	0.424
RCA	2.40	0.00	0.000
Fine Aggregate	2.60	569.39	0.219
Air	0.00	0.00	0.070
Total		**2203.13**	**1.000**

Table 3-23: Trial Batch 3 ACI mix admixtures.

		ACI-TB3-1	
Admixture	**SG**	**[mL/100kgCM]**	**[mL]**
AE-2	1.01	50	200
HRWR-2	1.11	100	400

When compared to the previous batch, the superplasticizer dosage decreased by 60%. On the other hand, for the EMV mixes, three different admixture combinations were tested for the same volumetric fractions, as seen in Table 3-24 and Table 3-25, respectively.

In this case, the first EMV mix had a superplasticizer content (6.9%) below the manufacturer's limit of 650 mL/100kgCM. Meanwhile, the second and third EMV mixes went beyond this mark with increases of 30.8% and 58.5%, respectively. In the case of the

air content, the dosage was close to the maximum recommended by the manufacturer, 98 mL/100kgCM. It is important to note that these calculations are based on the amount of fresh cement added to the mix, and do not consider the RMC of the RCA.

Table 3-24: Trial Batch 3 EMV mixes.

		EMV-TB3-1		EMV-TB3-2		EMV-TB3-3	
Component	**SG**	**[kg/m^3]**	**[m^3/m^3]**	**[kg/m^3]**	**[m^3/m^3]**	**[kg/m^3]**	**[m^3/m^3]**
Cement	3.15	289.25	0.092	289.25	0.092	289.25	0.092
Water	1.00	115.70	0.116	115.70	0.116	115.70	0.116
Coarse Aggregate	2.53	354.74	0.140	354.74	0.140	354.74	0.140
RCA	2.40	1016.17	0.424	1016.17	0.424	1016.17	0.424
Fine Aggregate	2.60	411.75	0.158	411.75	0.158	411.75	0.158
Air	0.00	0.00	0.070	0.00	0.070	0.00	0.070
Total		**2187.61**	**1.000**	**2187.61**	**1.000**	**2187.61**	**1.000**

Table 3-25: Trial Batch 3 EMV mix admixtures.

		EMV-TB3-1		EMV-TB3-2		EMV-TB3-3	
Admixture	**SG**	**[mL/100kgCM]**	**[mL]**	**[mL/100kgCM]**	**[mL]**	**[mL/100kgCM]**	**[mL]**
AE-2	1.01	100	289	100	289	100	289
HRWR-2	1.11	605	1750	850	2459	1030	2979

The results of the fresh state properties are presented in Table 3-26, while Figure 3-21, Figure 3-22, Figure 3-23, and Figure 3-24 show the mix consistency in the pan mixer and during the slump test.

Table 3-26: Trial Batch 3 fresh state properties.

Property	**ACI-TB3-1**	**EMV-TB3-1**	**EMV-TB3-2**	**EMV-TB3-3**
Slump [mm]	170	10	130	234
Fresh Density [kg/m^3]	2355.35	2200.81	2342.92	2108.99
Relative Yield	1.07	1.01	1.07	0.96
Air Content [%]	3.10%	4.20%	2.85%	1.40%

For the ACI mix, the results were better than in the previous batch, with a slump decrease of 24.4% but closer to the targeted 150 mm. Fresh density was also satisfactory,

although the air content came down from 5.00% to 3.10%. As observed in Figure 3-21, the paste consistency was much improved with a good slump retention and no signs of bleeding or visible voids, as suffered in the previous batch.

Figure 3-21: ACI-TB3-1 fresh state.

In the case of the first EMV mix, EMV-TB3-1, the slump was almost non-existent with a very viscous concrete. Meanwhile, the fresh density and yield were close to the design values, while the air content was higher than in the ACI mix at 4.20%. As observed in Figure 3-22, the paste consistency was still showing signs of a lack of fresh paste, as reflected in the voids appreciated in the slump test.

The second mix, EMV-TB3-2, had a better performance, with its fresh state properties matching those of the ACI mix. During the air content test, a malfunction was detected in the air metre apparatus, with one of the pipes clogged with hardened concrete. Efforts were made to clean it but there is a high chance the air content readings were affected because, even after the cleaning, the water pumping and air release were not smooth.

Figure 3-22: EMV-TB3-1 fresh state.

Figure 3-23: EMV-TB3-2 fresh state.

Besides this issue, another detail came from the superplasticizer effect, which took several minutes to manifest. At the beginning, the consistency was almost identical to the

one experienced with the EMV-TB3-1 mix. However, once the superplasticizer came into effect, the concrete's viscosity decreased and showed a more traditional behaviour and slump retention, as observed in Figure 3-23. The 130 mm of slump gave enough confidence the EMV mix would have had enough workability for the structural phase of the project.

Figure 3-24: EMV-TB3-3 fresh state.

In contrast, the third mix, EMV-TB3-3, suffered from an excessive dispersion effect due to the superplasticizer content. Clear signs of bleeding and segregation were observed (Figure 3-24), and they did not change for several minutes. The fresh state properties confirmed the observations with a slump of 234 mm and a relative yield below 1. Nevertheless, the air content value was not trusted due to the mentioned clogging issue.

Given the results of the fresh state, it was decided to cast standard 100x200 mm cylinders for all mixes except EMV-TB3-3. The results of the compressive strength tests at 7 and 28 days of age are presented in Table 3-27 and Table 3-28, respectively.

Table 3-27: Trial Batch 3 compressive strength at 7 days.

	ACI-TB3-1		EMV-TB3-1		EMV-TB3-2	
Cylinder	**Age [d]**	**f'_c [MPa]**	**Age [d]**	**f'_c [MPa]**	**Age [d]**	**f'_c [MPa]**
1	7	18.24	7	14.34	7	20.25
2	7	23.84	7	16.22	7	19.95
3	7	27.01	7	21.37	7	26.15
4	7	26.01	7	10.35	7	32.87
	Avg	**23.78**	**Avg**	**15.57**	**Avg**	**22.58**
	Std	**3.40**	**Std**	**3.96**	**Std**	**2.56**
	CoV	**0.14**	**CoV**	**0.25**	**CoV**	**0.11**

Table 3-28: Trial Batch 3 compressive strength at 28 days.

	ACI-TB3-1		EMV-TB3-1		EMV-TB3-2	
Cylinder	**Age [d]**	**f'_c [MPa]**	**Age [d]**	**f'_c [MPa]**	**Age [d]**	**f'_c [MPa]**
1	28	30.42	28	21.86	28	34.06
2	28	29.84	28	27.36	28	31.60
3	28	34.53	28	23.96	28	30.31
	Avg	**31.59**	**Avg**	**24.39**	**Avg**	**31.99**
	Std	**2.09**	**Std**	**2.27**	**Std**	**1.56**
	CoV	**0.07**	**CoV**	**0.09**	**CoV**	**0.05**

When comparing the results, there is a clear sign the behaviour between the ACI-TB3-1 and EMV-TB3-2 mixes is similar, with their respective compressive strength values almost identical at both 7 and 28 days, respectively. Considering that in the previous batch the DRM mix had averages of 22.02 MPa and 36.61 MPa for the same ages, the performance of the new mixes is better at 7 days, but approximately 14% inferior at 28 days. On the other hand, the performance of the EMV-TB3-1 mix is clearly inferior, which is attributed to the low workability and voids encountered during the mixing process.

Another interesting aspect is the quality of the produced cylinders, which is vastly different from the previous batch. The incorporation of the vibrating table considerably helped to improve the quality control and manufacturing process. As observed in Figure 3-25, Figure 3-26, and Figure 3-27, there are practically no visual differences, especially considering the decreased amount of fresh paste in the EMV mixes.

Figure 3-25: ACI-TB3-1 cylinders.

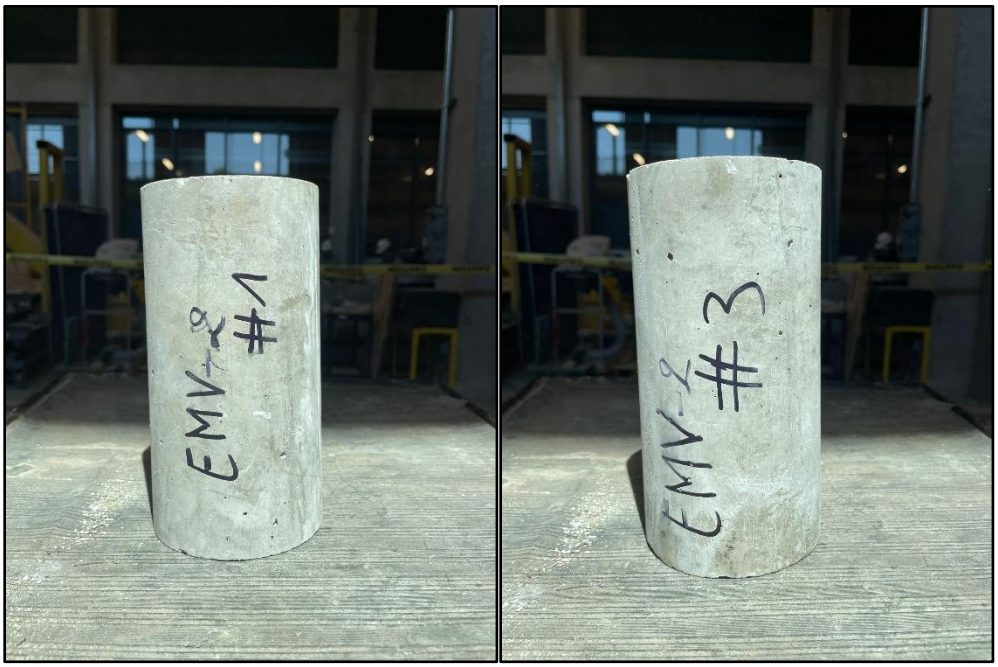

Figure 3-26: EMV-TB1-1 cylinders.

Nevertheless, a good-looking cylinder does not always correlate with a better performance, since an over-vibration could alter its quality by creating a differentiated

settlement. This effect could have altered the performance of the cylinders tested at 28 days and was noted as part of the quality control improvement for the next batches.

Figure 3-27: EMV-TB3-2 cylinders.

As with the previous trial batch, the compressive strength performance of the tested cylinders was plotted at 7 and 28 days of age, with solid lines connecting the average values for each mix. As observed in Figure 3-28, the data points and trends for the ACI-TB3-1 and EMV-TB3-2 mixes were projected to satisfactorily fulfill the requirement of 35 MPa at 56 days, while it is not clear whether the EMV-TB3-1 mix would have reached the target.

Even though the strength results were slightly inferior when compared to the DRM mix of the previous batch, they were still acceptable and within the natural concrete variability. Moreover, the biggest difference would be in the potential improvement of the elastic modulus of the EMV mixes when compared to the DRM ones due to the improved RCA incorporation. When accounting for the learning curve of the manufacturing process, it was expected that future batches would improve the results' consistency and scatter.

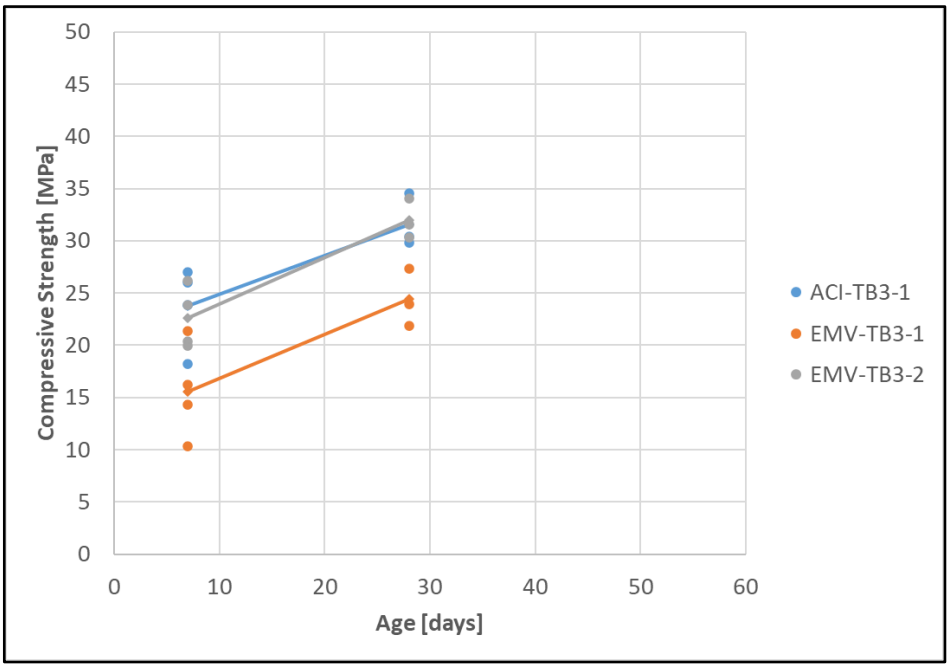

Figure 3-28: Trial Batch 3 – Compressive Strength Curves.

3.9. Trial Batch 4

The last trial batch was focused on testing the EMV mix with the new "C-Crete Binder", hence the EMVc mix label. Since not much information regarding the composition and behaviour of the binder was available at the time, it was determined to benchmark it against the EMV mix to see if there could be any improvements in the fresh and hardened states.

Given the timeframe, it was decided to shorten the testing stage of the cylinders to just 7 days of age; the rest of the fresh state properties remained unaltered. Further modifications came from the batch size, which was reduced from 25 to 12 litres, and the implementation of two curing methods: moist curing, and water-submerged curing.

The mix design and admixtures content are presented in Table 3-29 and Table 3-30, respectively. They are based on the formulation of the EMV-TB3-2 mix, and the only change was the replacement of the GUL cement with the "C-Crete Binder" in a 1:1 mass ratio; the rest, including the admixtures content, remained the same. Meanwhile, Figure 3-29

contains pictures taken during the mixing process, and Table 3-31 shows the results of the fresh state properties.

Table 3-29: Trial Batch 4 EMVc mix.

		EMVc-TB4-1	
Component	**SG**	**[kg/m³]**	**[m³/m³]**
Cement	3.15	289.25	0.092
Water	1.00	115.70	0.116
Coarse Aggregate	2.53	354.74	0.140
RCA	2.40	1016.17	0.423
Fine Aggregate	2.60	411.75	0.158
Air	0.00	0.00	0.070
Total		**2187.61**	**1.000**

Table 3-30: Trial Batch 4 EMVc admixtures.

		EMVc-TB4-1	
Admixture	**SG**	**[mL/100kgCM]**	**[mL]**
AE-2	1.01	100	289
HRWR-2	1.11	850	2459

Table 3-31: Trial Batch 4 fresh state properties.

Property	**EMVc-TB4-1**
Slump [mm]	10
Fresh Density [kg/m³]	2283.45
Relative Yield	1.04
Air Content [%]	3.40%

As appreciated in Table 3-31, the fresh state properties are like those obtained for the EMV-TB3-1 mix. An interesting detail noted while mixing the concrete was the reduced workability even with the admixtures content matching the dosages of the EMV-TB3-2 mix. The first factor that could have influenced the results is the nature of the “C-Crete Binder”, which might be finer than the GUL cement. The second factor could be a potential unknown compatibility with the used admixtures. Finally, a third factor could be related to the batch size reduction, which severely impacted the fresh paste availability.

Figure 3-29: EMVc-TB4-1 fresh state.

Figure 3-30: EMVc-TB4-1 demoulded cylinder.

Two other important observations were made during the batching process. The first one was the detection of a peculiar odor emanating from the fresh concrete, which was like a

rotten egg. The second detail came from the colouration change after the concrete was mixed. The “C-Crete Binder” has a light brown tone, and that directly influenced the colour of the fresh mix, which was paler than when using GUL cement. After the cylinders were demoulded, rich green tones were observed in the parts that were not completely dry.

The results obtained for the compressive strength test of the moist- (M) and submerged-cured (S) cylinders are presented in Table 3-32, while Figure 3-31 shows a visual comparison between them.

Table 3-32: Trial Batch 4 compressive strength at 7 days.

	EMVc-TB4-1 (M)		**EMVc-TB4-1 (S)**	
Cylinder	**Age [d]**	**f'_c [MPa]**	**Age [d]**	**f'_c [MPa]**
1	7	20.67	7	23.39
2	7	22.19	7	23.91
3	7	21.07	7	22.99
	Avg	**21.31**	**Avg**	**23.43**
	Std	**0.64**	**Std**	**0.38**
	CoV	**0.03**	**CoV**	**0.02**

Figure 3-31: EMVc-TB4-1 moist- and submerged-cured cylinders.

The results for the fully submerged cylinders were approximately 9.5% higher than those of the moist-cured cylinders. However, when compared to the results of the EMV-TB3-2 mix at the same age (average of 22.58 MPa), the performance was similar. Furthermore, the standard deviation was low for both curing types, highlighting the consistency of the batch. Therefore, it was decided that moist curing, which was being applied to the mixes evaluated in the previous batches, could be applied without major considerations for mixes made with this alternative binder.

Finally, the colouration changes were also appreciated at the age of 7 days. When taken out of the curing pails, the cylinders were visibly green but once exposed to the air they started gaining the pale brown tones back. The results gave enough confidence to try the EMVc mix in the final batching stage without further modifications. It was deemed that a batch size increase would help offset the experienced workability loss, while keeping the admixtures ratios unchanged.

3.10. Mixes for structural specimens

After the trial batches, the final mix designs with their respective admixtures content were ready for the casting of the structural specimens, which will be discussed in detail in the next chapter. The major considerations that applied to this section were:

- Given the size of each specimen and the required volume to cast the necessary cylinders, it was decided to increase the batch size from 25 to 100 litres. To accommodate this new volume, a 200-litre pan mixer was selected (Figure 3-32).
- In total, 18 batches were made in 5 days of casting. The batch distribution was: 6 for the ACI Mix, 2 for the DRM Mix, 6 for the EMV Mix, and 4 for the EMVc mix.
- All coarse aggregates, including the RCA, were added in an SSD condition following a presoaking process of at least 24 hours. Moreover, the RCA-1 grading was the same used in all trial batches (Figure 3-13).

Figure 3-32: 200-litre pan mixer.

Figure 3-33: Vibration of structural specimens.

- The mixing process followed the guidelines of the CSA Standard Practice A23.2-2C (CSA Group, 2024a), which was also applied in the trial batches stage. Based

on the characteristics of the pan mixer, the mixing protocol can be summarized in the following steps:

  - Add the coarse aggregates and some of the mixing water (in this case, half of the mixing water with the superplasticizer) into the mixer.
  - Let the mixer spin for a few seconds, then stop it and add the fine aggregates, cementitious materials, and the rest of the mixing water (in this case, half of the mixing water with the air-entrainer).
  - With all the ingredients already incorporated, mix for 3 minutes, then pause and let it rest for 3 minutes, to then finally mix again for 2 minutes.
  - Precautions were taken to avoid a mortar retention on the side walls of the pan mixer. Once the mixing process was finished, the concrete was dumped into a wheelbarrow and remixed with a shovel until it appeared uniform and had no segregation signs.

- For the fresh state, the values of the slump, fresh density, relative yield, and air content were measured following the guidelines of the CSA A23.2-4C, A23.2-5C, and A23.3-6C (CSA Group, 2024a). On the other hand, the testing of the hardened state was expanded with the addition of the elastic modulus and tensile splitting tests. The former was performed following the guidelines of the ASTM C469/C469M Standard (ASTM, 2022a), while the latter was performed according to the requirements of the CSA A23.2-13C. For these new tests, standard 150x300 mm cylinders were cast.
- For the compression strength development, it was chosen to test standard 100x200 mm cylinders at 7, 14, 28, and 56 days of age following the guidelines of CSA A23.2-9C (CSA Group, 2024a).
- For the structural specimens' fabrication, internal and external vibration was applied with a standard 1500W concrete vibrator (Figure 3-33). On the other hand, the compaction of the cylinders was made with the help of the steel rod and the vibrating table used in the third and fourth trial batches.
- Moist curing was applied to the structural specimens and all cylinder types.

The mix designs are presented in Table 3-33 and Table 3-34 for the ACI and DRM mixes, while the EMV and EMVc mixes are available in Table 3-35 and Table 3-36, respectively.

Table 3-33: ACI-FM-1 and DRM-FM-1 mix designs.

		ACI-FM-1		DRM-FM-1	
Component	**SG**	**[kg/m³]**	**[m³/m³]**	**[kg/m³]**	**[m³/m³]**
Cement	3.15	400.00	0.127	400.00	0.127
Water	1.00	160.00	0.160	160.00	0.160
Coarse Aggregate	2.53	1073.74	0.424	0.00	0.000
RCA	2.40	0.00	0.000	1016.17	0.424
Fine Aggregate	2.60	569.39	0.219	569.39	0.219
Air	0.00	0.00	0.070	0.00	0.070
Total		**2203.13**	**1.000**	**2145.55**	**1.000**

Table 3-34: ACI-FM-1 and DRM-FM-1 admixtures content.

		ACI-FM-1		DRM-FM-1	
Admixture	**SG**	**[mL/100kgCM]**	**[mL]**	**[mL/100kgCM]**	**[mL]**
AE-2	1.01	50	200	40	160
HRWR-2	1.11	100	400	250	1000

Table 3-35: EMV-FM-1 and EMVc-FM-1 mix designs.

		EMV-FM-1		EMVc-FM-1	
Component	**SG**	**[kg/m³]**	**[m³/m³]**	**[kg/m³]**	**[m³/m³]**
Cement	3.15	289.25	0.092	289.25	0.092
Water	1.00	115.70	0.116	115.70	0.116
Coarse Aggregate	2.53	354.74	0.140	354.74	0.140
RCA	2.40	1016.17	0.424	1016.17	0.424
Fine Aggregate	2.60	411.75	0.158	411.75	0.158
Air	0.00	0.00	0.070	0.00	0.070
Total		**2187.61**	**1.000**	**2187.61**	**1.000**

Table 3-36: EMV-FM-1 and EMVc-FM-1 admixtures content.

		EMV-FM-1		EMVc-FM-1	
Admixture	**SG**	**[mL/100kgCM]**	**[mL]**	**[mL/100kgCM]**	**[mL]**
AE-2	1.01	100	289	100	289
HRWR-2	1.11	850	2459	850	2459

As seen throughout the trial batches phase, the ACI mix with a W/C ratio of 0.40 represents the benchmark upon which all other mixes will be compared to. The DRM mix has the same volumetric proportions, but a full 100% coarse RCA-1 replacement and a design density reduced by 2.6%. Meanwhile, the EMV and EMVc mixes allow a reduction in the fresh new mortar content by accounting for the RMC of the RCA-1 source. The cement reduction for these mixes is approximately 27.7%, the RCA-to-total coarse aggregate ratio is 74.26%, and the design density only reduces by 0.7%. Finally, the binder type is the main difference between the EMV and EMVc mixes, with the latter using the "C-Crete Binder" instead of the regular GUL cement in a 1:1 ratio.

When analyzing the admixtures content, the air-entrainer doubles for the EMV and EMVc mixes when compared to the ACI and DRM mixes. However, the superplasticizer is the agent with the biggest changes, with the DRM, EMV, and EMVc mixes having increases of 250%, 850%, and 850% per unit of cement, respectively. The DRM increase is directly related to the RCA incorporation, which is a more porous material than the natural coarse aggregate. Meanwhile, the EMV and EMVc increases are exacerbated by the reduced amount of fresh cement, which is 27.7% less than the ACI and DRM mixes, and does not account for the cement embedded in the residual mortar of the RCA.

Table 3-37: Batch distribution of the final mixes.

Day	ACI-FM-1	DRM-FM-1	EMV-FM-1	EMVc-FM-1
D1	4	-	-	-
D2	2	2	-	-
D3	-	-	4	-
D4	-	-	2	-
D5	-	-	-	4

The batch distribution per casting day is presented in Table 3-37. When further referring to a specific mixing day, the suffix -DX (where X is the corresponding day) will be added to the end of the label. For instance, ACI-FM-1-D1 groups all the ACI-FM-1-D1 batches that were made on the first casting day.

The results of the fresh properties for each of the performed batches are presented in Table 3-38 and Figure 3-34 for the ACI mix, Table 3-39 and Figure 3-35 for the DRM mix, Table 3-40 and Figure 3-36 for the EMV mix, and Table 3-41 and Figure 3-37 for the EMVc mix. All figures show the fresh mixes inside the 200-litre pan mixer and the representative samples taken for the slump test. Finally, Table 3-42 presents the averages of each mix for the evaluated categories.

Table 3-38: ACI-FM-1 fresh properties.

Batch	Slump [mm]	Fresh Density [kg/m^3]	Relative Yield	Air Content [%]
D1-1	130.00	2213.24	1.00	3.00%
D1-2	120.00	2379.22	1.08	2.60%
D1-3	195.00	2355.77	1.07	2.90%
D1-4	175.00	2341.93	1.06	2.20%
D2-1	166.00	2382.61	1.08	2.10%
D2-2	190.00	2352.38	1.07	2.30%
Avg	**162.67**	**2337.52**	**1.06**	**2.52%**
Std	**28.41**	**57.43**	**0.03**	**0.34%**
CoV	**0.17**	**0.02**	**0.02**	**0.14**

Figure 3-34: ACI-FM-1 fresh state.

Table 3-39: DRM-FM-1 fresh properties.

Batch	Slump [mm]	Fresh Density [kg/m^3]	Relative Yield	Air Content [%]
D2-1	180.00	2308.03	1.08	2.80%
D2-2	170.00	2282.46	1.06	2.40%
Avg	**175.00**	**2295.24**	**1.07**	**2.60%**
Std	**5.00**	**12.78**	**0.01**	**0.20%**
CoV	**0.03**	**0.01**	**0.01**	**0.08**

Figure 3-35: DRM-FM-1 fresh state.

Table 3-40: EMV-FM-1 fresh properties.

Batch	Slump [mm]	Fresh Density [kg/m^3]	Relative Yield	Air Content [%]
D3-1	178.00	2387.84	1.09	2.80%
D3-2	205.00	2351.53	1.07	2.25%
D3-3	195.00	2376.68	1.09	2.25%
D3-4	220.00	2360.86	1.08	1.80%
D4-1	202.00	2424.99	1.11	1.00%
D4-2	195.00	2358.45	1.08	1.60%
Avg	**199.17**	**2376.72**	**1.09**	**1.95%**
Std	**12.64**	**24.74**	**0.01**	**0.57%**
CoV	**0.06**	**0.01**	**0.01**	**0.29**

Figure 3-36: EMV-FM-1 fresh state.

Table 3-41: EMVc-FM-1 fresh properties.

Batch	Slump [mm]	Fresh Density [kg/m^3]	Relative Yield	Air Content [%]
D5-1	160.00	2411.57	1.10	0.60%
D5-2	200.00	2404.93	1.10	1.50%
D5-3	155.00	2329.92	1.07	2.40%
D5-4	90.00	2407.90	1.10	1.80%
Avg	**151.25**	**2388.58**	**1.09**	**1.58%**
Std	**39.43**	**33.95**	**0.02**	**0.65%**
CoV	**0.26**	**0.01**	**0.01**	**0.41**

Table 3-42: Fresh properties summary for the final mixes.

Property	ACI-FM-1	DRM-FM-1	EMV-FM-1	EMVc-FM-1
Slump [mm]	163	175	199	151
Fresh Density [kg/m^3]	2377.52	2295.24	2376.72	2388.58
Relative Yield	1.06	1.07	1.09	1.09
Air Content [%]	2.52%	2.60%	1.95%	1.58%

For the ACI mix, the first two batches presented lower slump values, 30% on average than the other four. However, only the first batch had consistent differences in all

categories, the fresh density was below 2300 kg/m^3 and the relative yield was exactly one. The remaining five batches had similar values for the same categories, with fresh density and relative yield values that on average were 2362 kg/m^3 and 1.07, respectively.

Figure 3-37: EMVc-FM-1 fresh state.

The slump values of the DRM mix were consistent with the findings of the second trial batch, where good workability was achieved for the tested admixtures combination. When compared to the ACI mixes, the average values were close but higher than in the previous trial batches, which can be attributed to the batch size effect where more fresh cement paste is available. Furthermore, another good indicator came from the fresh density values, which were lower than those of the ACI mixes because of the higher RCA content.

Contrary to the ACI and DRM mixes, the EMV batches required more handling care and understanding, especially at the beginning. During the mixing of the first batch, two aspects that heavily influenced the results were noted. The first one was the slow torque of the pan mixer, which was preventing the full homogenization of the concrete, and was further exacerbated by an excess of fines sticking to the walls of the mixer. This issue was solved by

shoveling the walls during the 3-minute pause in between mixing cycles, and after dumping the concrete on the wheelbarrow.

The second aspect came from the superplasticizer effect. Once all ingredients were getting mixed in a more consistent way, an increased fresh paste fluidity was observed. It is highly probable that the SSD condition in which the coarse aggregates were incorporated favoured the dispersion action of the superplasticizer by avoiding its absorption. However, this increased paste fluidity put the concrete on the verge of segregation, which was evident when some bleeding appeared during the slump test.

At the beginning it was thought the admixtures content was incorrect, but after dumping and remixing the concrete on the wheelbarrow, the latter started to gain consistency, which got even better after it was vibrated following its pour into the structural specimens' moulds; hence, the mix was qualitatively found to be quite workable.

Nevertheless, the compaction effects achieved with the use of the vibrator were difficult to replicate when performing the slump tests. Among the obtained results, the first one is the most representative one since an extra 2-minute mixing round plus shoveling was applied to improve concrete's uniformity. However, this extra step was not applied for the rest of the batches given the similarities in the fresh density contents, which was a good consistency indicator, and the required physical effort.

The EMVc mixes also resulted in interesting observations. Like the fourth trial batch, the concrete was observed to have a rotten egg smell and light-brown colour during mixing. The second observation came from the reduced workability when compared to the EMV mixes. Since the only difference between both mix designs was the binder type, it is clear the "C-Crete Binder" played a role. Possible causes can be attributed to its fineness and admixtures' compatibility.

Finally, the air content category requires special consideration, since it is the only one where the results lack confidence. The relative yield showed that an excess of concrete was produced in almost all cases, which can be attributed to a lower than anticipated air content, but other factors such as fluctuations in the specific gravity and weights of the ingredients could have played a role (ACI, 2022).

Moreover, persistent issues were experienced with the air-metre even after recalibration; examples include the looseness of the clamps (preventing a good seal) and the clogging of the release valve. Nevertheless, it is also possible that over-vibration led to the reduced air content readings, especially considering the air-entrainer dosage for the EMV mixes was near the maximum recommended by the manufacturer.

As with the previous trial batches, standard 100x200 mm cylinders were tested for compressive strength at different ages, in this case 7, 14, 28, and 56 days. Starting with the 7-day test, the results are presented in Table 3-43.

Table 3-43: Compressive strength of Final Mixes at 7 days.

	ACI-FM-1		**EMV-FM-1**		**EMVc-FM-1**	
Cylinder	**Age [d]**	**f'_c [MPa]**	**Age [d]**	**f'_c [MPa]**	**Age [d]**	**f'_c [MPa]**
1	7	17.70	7	24.95	7	23.45
2	7	27.55	7	15.86	7	24.88
3	7	19.74	7	25.17	7	23.72
4	7	30.26	-	-	7	21.96
5	7	24.20	-	-	7	26.14
	Avg	**23.89**	**Avg**	**22.00**	**Avg**	**24.03**
	Std	**4.68**	**Std**	**4.34**	**Std**	**1.40**
	CoV	**0.20**	**CoV**	**0.20**	**CoV**	**0.06**

Only three mixes were tested at this age since the only two DRM batches did not produce enough cylinders to cover the remainder of the tests. Besides the generated cylinder stock, there was also information from the previous trial batches at the same age; therefore, it was decided to skip this age to prioritize the tests at 14, 28, and 56 days. On

the other hand, the average strength for the tested mixes is similar, with the EMVc mix having the best results in terms of performance and batch uniformity.

The compressive strength results at 14 days are presented in Table 3-44 for the ACI and DRM mixes, and Table 3-45 for the EMV and EMVc mixes.

Table 3-44: Compressive strength of Final Mixes at 14 days, Part 1.

	ACI-FM-1		DRM-FM-1	
Cylinder	**Age [d]**	**f'_c [MPa]**	**Age [d]**	**f'_c [MPa]**
1	14	19.20	14	21.16
2	14	18.49	14	20.38
3	14	24.22	14	20.39
4	14	29.23	-	-
5	14	18.68	-	-
6	14	33.50	-	-
7	14	25.69	-	-
	Avg	**24.14**	**Avg**	**20.64**
	Std	**5.37**	**Std**	**0.37**
	CoV	**0.22**	**CoV**	**0.02**

Table 3-45: Compressive strength of Final Mixes at 14 days, Part 2.

	EMV-FM-1		EMVc-FM-1	
Cylinder	**Age [d]**	**f'_c [MPa]**	**Age [d]**	**f'_c [MPa]**
1	14	38.60	14	24.71
2	14	25.09	14	31.00
3	14	35.77	14	30.41
4	14	31.91	14	30.32
5	14	31.99	14	29.43
6	14	28.51	-	-
7	14	23.57	-	-
	Avg	**30.78**	**Avg**	**29.17**
	Std	**5.05**	**Std**	**2.29**
	CoV	**0.16**	**CoV**	**0.08**

At 14 days of age, the results presented some discrepancies. The ACI mix had a lower average value than the EMV and EMVc mixes, which can partly be attributed to the quality

of the tested cylinders, where 3 had results below 20 MPa. When these low values are excluded, the average rises to 28.16 MPa and sits closer to that of the EMV mixes. The DRM values were also low but showed better consistency. However, after they were tested an issue with the lubrication of the upper plate of the compression machine was detected (black plate highlighted in red in Figure 3-38) that affected the coupling angle of the top face of the cylinders. Therefore, it is highly probable this issue was detrimental to the cylinders' performance, as seen in the diagonal failure modes of Figure 3-39, where it can be observed that the cracks started at a localized point and caused splitting failures.

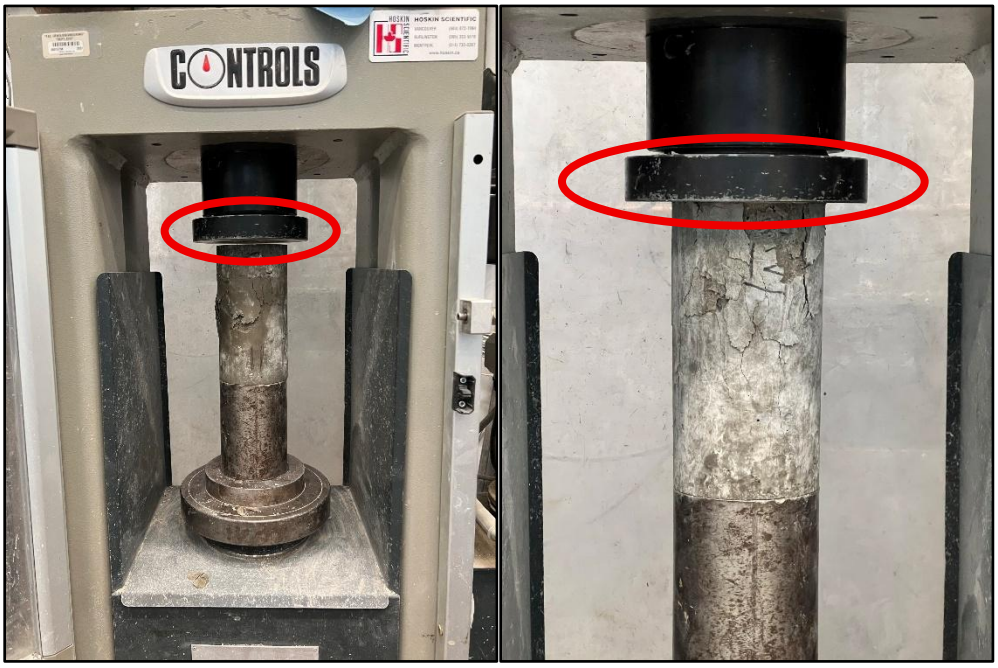

Figure 3-38: Automatic concrete compression machine.

The results of the EMV and EMVc mixes were taken after the compression machine was lubricated, and they clearly show a performance improvement with no cylinders failing before 20 MPa. When comparing both mixes, the EMVc showed better consistency, which was expected given that its fresh state was easier to handle as mentioned before. Nevertheless, the EMV mixes had a slightly higher mean strength, which confirmed the observations made during the mixing stage, where the concrete achieved a good compaction given the effect of the superplasticizer.

Figure 3-39: Failure mode prior to compression machine lubrication.

The next compressive strength tests were at 28 days of age. The results are available in Table 3-46 for the ACI and DRM mixes, and in Table 3-47 for the EMV and EMVc mixes, respectively.

Table 3-46: Compressive strength of Final Mixes at 28 days, Part 1.

	ACI-FM-1		DRM-FM-1	
Cylinder	**Age [d]**	**f'_c [MPa]**	**Age [d]**	**f'_c [MPa]**
1	28	34.25	28	30.71
2	28	38.31	28	38.86
3	28	27.13	28	35.76
4	28	38.50	-	-
5	28	35.21	-	-
6	28	33.80	-	-
7	28	31.78	-	-
8	28	32.81		
	Avg	**33.98**	**Avg**	**35.11**
	Std	**3.43**	**Std**	**3.36**
	CoV	**0.10**	**CoV**	**0.10**

Table 3-47: Compressive strength of Final Mixes at 28 days, Part 2.

	EMV-FM-1		EMVc-FM-1	
Cylinder	**Age [d]**	**f'_c [MPa]**	**Age [d]**	**f'_c [MPa]**
1	28	37.87	28	30.74
2	28	37.80	28	31.13
3	28	29.87	28	31.33
4	28	41.33	28	31.89
5	28	40.02	28	29.13
6	28	38.39	28	30.78
7	28	29.65	28	31.53
8	28	34.70	28	26.44
9	-	-	28	34.34
10	-	-	28	31.32
	Avg	**36.20**	**Avg**	**30.86**
	Std	**4.13**	**Std**	**1.92**
	CoV	**0.11**	**CoV**	**0.06**

An improvement in the consistency of the tests is evident, with less variability across all mix designs. In terms of performance, the ACI, DRM, and EMV mixes had the best results, with averages that indicated the target of 35 MPa at 56 days would be met. On the other hand, less confidence applied to EMVc mixes, where the average strength was almost 15% lower when compared to the EMV mix, which indicated the "C-Crete Binder" might have experienced a lower rate of strength gain after 14 days given its 90% slag composition. However, another possibility was that the mix was indeed suffering from a worse performance, which could only be verified with the results of the 56-day test.

The results at 28 days of age provided a good benchmark. When compared to the previous batches, the DRM mix performed closely to the results gathered in the second trial batch; while the ACI and EMV mixes showed improvements of 7.6% and 13.2% when compared to the performance observed in the third trial batch.

The final cylinder tests were conducted at 56 days. The results are available in Table 3-48 for the ACI and DRM mixes, and in Table 3-49 for the EMV and EMVc mixes.

Table 3-48: Compressive strength of Final Mixes at 56 days, Part 1.

	ACI-FM-1		DRM-FM-1	
Cylinder	**Age [d]**	**f'_c [MPa]**	**Age [d]**	**f'_c [MPa]**
1	56	39.14	56	32.06
2	56	39.03	56	40.49
3	56	45.80	56	39.83
4	56	39.91	-	-
5	56	40.68	-	-
6	56	39.37	-	-
7	56	38.55	-	-
8	56	37.14		
	Avg	**39.95**	**Avg**	**37.46**
	Std	**2.41**	**Std**	**3.83**
	CoV	**0.06**	**CoV**	**0.10**

Table 3-49: Compressive strength of Final Mixes at 56 days, Part 2.

	EMV-FM-1		EMVc-FM-1	
Cylinder	**Age [d]**	**f'_c [MPa]**	**Age [d]**	**f'_c [MPa]**
1	56	39.72	56	35.70
2	56	46.42	56	37.82
3	56	38.04	56	35.28
4	56	35.13	-	-
5	56	39.36	-	-
6	56	36.85	-	-
7	56	30.81	-	-
8	56	45.83		
	Avg	**39.02**	**Avg**	**36.27**
	Std	**4.87**	**Std**	**1.11**
	CoV	**0.12**	**CoV**	**0.03**

When analyzing the results, all mixes accomplished the minimum target of 35 MPa, although with some differences. In the case of the ACI mix, results showed that the average strength was 14% higher than the target, and this time the scatter was reduced. For the DRM mix, the results followed the same trend of the 28-day test, but with two cylinders being nearly identical; therefore, despite the low amount of tested cylinders, the results were deemed trustworthy.

Furthermore, the EMV mix showed a similar performance to the ACI mix, with an average strength within 2.4% of the conventional concrete, which confirms the EMV Method is an effective tool to incorporate RCA into new concrete mixes without losing performance. Since eight cylinders were tested, the confidence level was acceptable despite the greater scatter.

In the case of the EMVc mixes, the average strength was 20% higher than at 28 days, but still 7% lower than that of the EMV mix, following the trend observed at 28 days, where its strength gain was slower or simply not on the same level as the other mixes. Therefore, despite not having a complete knowledge about the "C-Crete Binder" formulation, it was determined that its nature was causing the difference since it was the only modification when compared to the EMV mix design.

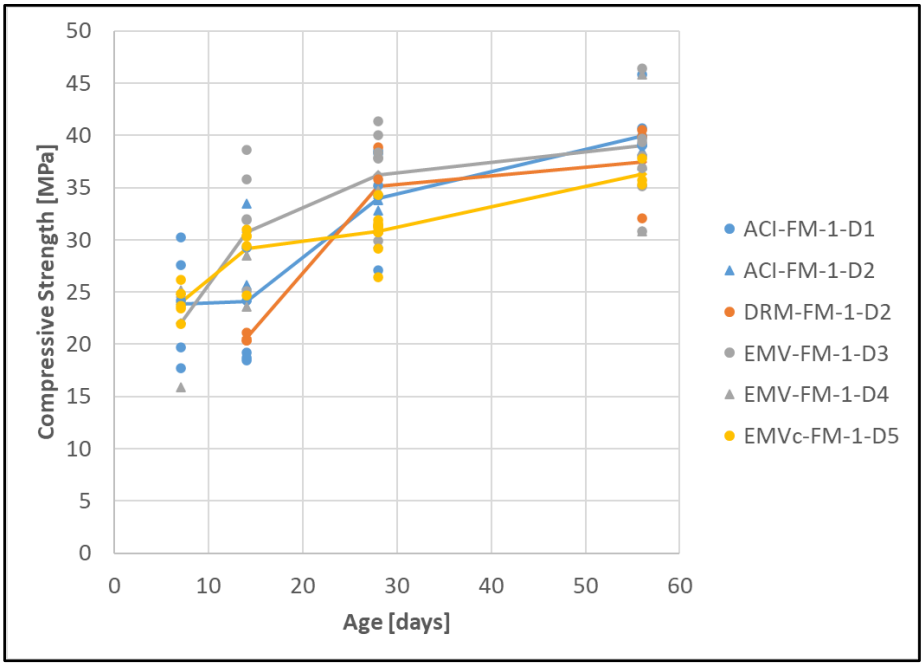

Figure 3-40: Compressive strength development of Final Mixes at 56 days.

The mentioned trendlines are better appreciated in Figure 3-40, where the data points are plotted with solid lines connecting the averages of the tested ages. Meanwhile, a visual comparison between the different mixes' cylinders can be obtained by taking a look at

Figure 3-41, Figure 3-42, Figure 3-43, and Figure 3-44 for the ACI, DRM, EMV, and EMVc mixes, respectively.

Figure 3-41: ACI-FM-1 cylinders.

Figure 3-42: DRM-FM-1 cylinders.

Figure 3-43: EMV-FM-1 cylinders.

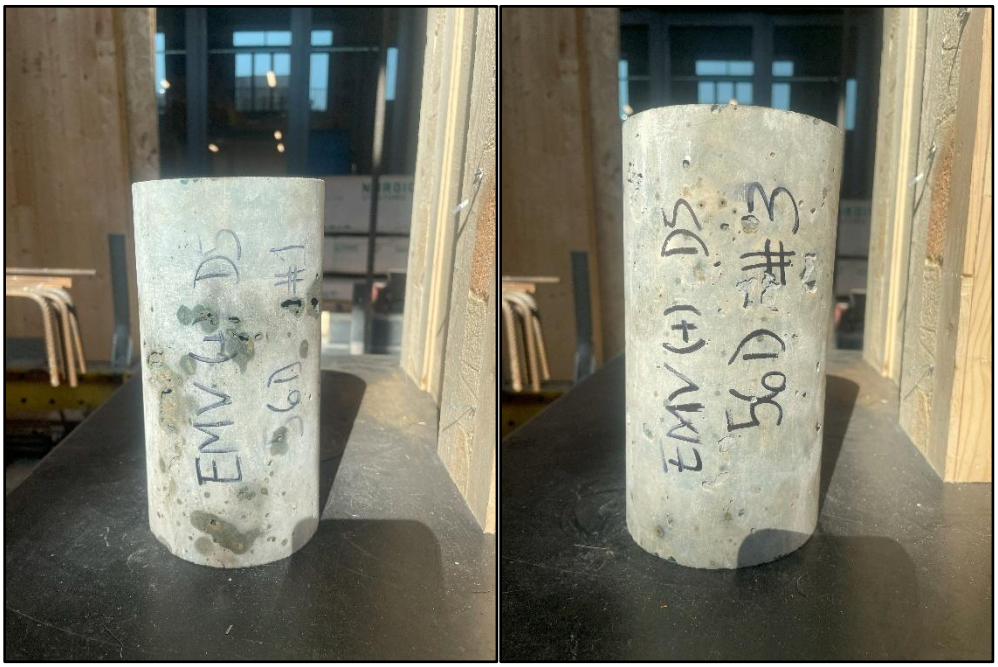

Figure 3-44: EMVc-FM-1 cylinders.

The mixes that used GUL cement as the hydraulic binder presented the same colouration and there were practically no visual differences. In contrast, the EMVc cylinders

subtly presented the greener tones observed during the fourth trial batch. Their characteristics remained unchained, the sections that were moist kept the green tones, and those exposed to the air changed their colouration to pale brown tones.

Two additional tests were conducted for a better understanding of the hardened state properties, namely elastic modulus and splitting tensile strength. For the former, standard 100x200 mm and 150x300 mm cylinders were tested, while the latter only considered 150x300 mm cylinders. These two tests were performed in the concrete laboratory of the National Research Council Canada. The elastic modulus results are divided per cylinder type and presented through Table 3-50 to Table 3-55 according to their respective batching days.

Table 3-50: ACI-FM-1-D1 Elastic modulus results.

	100x200 mm Cylinders			**150x300 mm Cylinders**		
Cylinder	**Age [d]**	**f'_c [MPa]**	**E_c [GPa]**	**Age [d]**	**f'_c [MPa]**	**E_c [GPa]**
1	51	40.13	27.45	72	44.43	30.52
2	51	37.78	30.27	72	45.05	29.22
3	51	47.35	30.07	72	44.19	28.65
4	-	-	-	72	39.92	30.08
	Avg	**41.76**	**29.26**	**Avg**	**43.40**	**29.62**
	Std	**4.07**	**1.29**	**Std**	**2.03**	**0.73**
	CoV	**0.10**	**0.04**	**CoV**	**0.05**	**0.02**

Table 3-51: ACI-FM-1-D2 Elastic modulus results.

	100x200 mm Cylinders			**150x300 mm Cylinders**		
Cylinder	**Age [d]**	**f'_c [MPa]**	**E_c [GPa]**	**Age [d]**	**f'_c [MPa]**	**E_c [GPa]**
1	121	56.22	40.16	203	46.60	30.70
2	121	47.70	30.53	203	50.19	32.44
3	121	57.47	33.81	-	-	-
	Avg	**53.80**	**34.83**	**Avg**	**48.39**	**31.57**
	Std	**4.34**	**4.00**	**Std**	**1.79**	**0.87**
	CoV	**0.08**	**0.11**	**CoV**	**0.04**	**0.03**

For the ACI mix, the results for the first batching day averaged approximately 29 GPa. Meanwhile, the results of the second batching day showed increases for both cylinder sizes,

though these were also tested at later ages. Another detail comes from the continuous compressive strength gain after the last testing age at 56 days, which shows the constant evolution over time. According to the requirements of CSA A23.3, concrete's elastic modulus can be computed according to Eq. 3.10 – 1 (CSA Group, 2024b).

$$E_c = 4500\sqrt{f_c'} \qquad (3.10-1)$$

For the nominal 35 MPa compressive strength required at 56 days, the calculated value for the elastic modulus is 26.62 GPa. However, when using the measured compressive strength results, the expected values are almost identical to the reported readings. Furthermore, the increments for ACI-FM-1-D2 might be related to the age at which the tests were performed, with 70 and 131 days of difference for each cylinder type, respectively.

Table 3-52: DRM-FM-1-D2 Elastic modulus results.

	100x200 mm Cylinders			**150x300 mm Cylinders**		
Cylinder	**Age [d]**	**f_c' [MPa]**	**E_c [GPa]**	**Age [d]**	**f_c' [MPa]**	**E_c [GPa]**
1	121	41.05	22.43	203	48.12	24.03
2	121	40.12	24.16	-	-	-
3	121	41.42	22.48	-	-	-
4	121	40.57	20.62	-	-	-
	Avg	**40.79**	**22.42**	**Avg**	**48.12**	**24.03**
	Std	**0.49**	**1.25**	**Std**	**N/A**	**N/A**
	CoV	**0.01**	**0.06**	**CoV**	**N/A**	**N/A**

In the case of the DRM mix, the elastic modulus results of the 100x200 mm cylinders at 121 days of age are on average 35.6% lower than those of the ACI mix, while the single 150x300 mm cylinder tested at 203 days of age is 23.9% lower than its conventional counterpart. These results were expected given the nature of the RCA replacement, which did not account for the RMC; therefore, even if the compressive strength results can be comparable, the modulus of elasticity establishes a clear difference between them.

Table 3-53: EMV-FM-1-D3 Elastic modulus results.

	100x200 mm Cylinders			150x300 mm Cylinders		
Cylinder	**Age [d]**	**f'_c [MPa]**	**E_c [GPa]**	**Age [d]**	**f'_c [MPa]**	**E_c [GPa]**
1	109	29.22	33.49	191	41.22	26.46
2	109	49.57	28.77	191	45.71	27.29
3	109	53.49	26.88	191	43.84	26.57
4	109	54.05	29.49	-	-	-
5	109	44.41	-	-	-	-
	Avg	**46.15**	**29.66**	**Avg**	**43.59**	**26.77**
	Std	**9.14**	**2.41**	**Std**	**1.84**	**0.37**
	CoV	**0.20**	**0.08**	**CoV**	**0.04**	**0.01**

Table 3-54: EMV-FM-1-D4 Elastic modulus results.

	100x200 mm Cylinders			150x300 mm Cylinders		
Cylinder	**Age [d]**	**f'_c [MPa]**	**E_c [GPa]**	**Age [d]**	**f'_c [MPa]**	**E_c [GPa]**
1	98	44.43	-	180	36.99	23.72
2	98	40.75	30.49	-	-	-
3	98	51.76	28.15	-	-	-
4	98	48.98	31.50	-	-	-
	Avg	**46.48**	**30.05**	**Avg**	**36.99**	**23.72**
	Std	**4.22**	**1.40**	**Std**	**N/A**	**N/A**
	CoV	**0.09**	**0.05**	**CoV**	**N/A**	**N/A**

For the EMV mix, the results were expected to be higher than the DRM ones and closer to those of the conventional ACI mix. For the 100x200 mm cylinders, the testing ages were younger than the ACI-FM-1-D2 cylinders tested at 121 days. The EMV-FM-1-D3 and EMV-FM-1-D4 cylinders were 12 and 23 days younger, respectively. The average between them is 29.86 GPa, which is slightly superior to the ACI-FM-1-D1 results, and 14.3% lower than those of the ACI-FM-1-D2 batch, which were tested at a later age. Nevertheless, when considering the gap between the testing ages, the EMV results seem to be reasonable.

In contrast, a bigger gap was encountered for the 150x300 mm cylinders, where the results were marginally better than the DRM ones, and subsequently much lower when compared to the ACI mix. In the case of the sole EMV-FM-1-D4 cylinder, it is likely that its quality was substandard due to its poor performance. Meanwhile, the EMV-FM-1-D3

cylinders showed good uniformity in their results, but they were still 15.2% lower on average than their ACI counterparts. Possible effects that might have contributed to the decreased performance are associated with the manufacturing process, specifically the consolidation when using the vibrating table given the size and weight of the cylinder, but also in the mix design. This topic will be further assessed in the discussion section.

Table 3-55: EMVc-FM-1-D5 Elastic modulus results.

	100x200 mm Cylinders			150x300 mm Cylinders		
Cylinder	**Age [d]**	**f'_c [MPa]**	**E_c [GPa]**	**Age [d]**	**f'_c [MPa]**	**E_c [GPa]**
1	91	20.98	29.46	173	24.79	17.52
2	91	38.05	26.54	173	27.55	19.60
3	91	30.09	21.56	173	25.21	18.88
4	91	37.78	27.49	-	-	-
5	91	34.05	24.02	-	-	-
6	91	30.44	23.75	-	-	-
	Avg	**31.90**	**25.47**	**Avg**	**25.85**	**18.67**
	Std	**5.80**	**2.63**	**Std**	**1.21**	**0.86**
	CoV	**0.18**	**0.10**	**CoV**	**0.05**	**0.05**

Finally, the results of all EMVc cylinders confirmed the observations taken during the testing of the compressive strength at 28 and 56 days of age. The average of the 100x200 mm cylinders is 13.6% higher than the DRM mix, but 14.9% lower than the EMV mix, with only the binder being the main difference with the latter. The case of the 150x300 mm cylinders is even more interesting, since the results are uniform but noticeably lower than all the other mixes by a large margin.

The same hypothesis presented for the EMV mix can be applied to this situation, where the results of the 150x300 mm cylinders might have been influenced by the consolidation in the manufacturing process, as their compressive strength is also lower than the 100x200 mm cylinders at 91 days. However, the difference against the EMV mix hints at possible cement paste qualities, which could only be confirmed with the tensile splitting test.

The results of the compressive strength and elastic modulus tests allowed a better understanding of all mixes. The use of a novel binder instead of Portland cement in the EMVc mixes meant that no previous studies were available as benchmarks. For the designs using the GUL cement, the results were generally as expected given the volumetric compositions, with only the 150x300 mm cylinders having a noticeable performance drop in the elastic modulus.

Figure 3-45: EMVc structural sample failure close-up.

Nevertheless, during the structural tests—discussed in more detail later—the EMVc samples exhibited brittle behaviour, as appreciated in Figure 3-45, where it is also seen that the green tones remained in the core of the sample, while the light brown ones were concentrated on the sections that were exposed to the environment. Upon closer inspection of the failed section, the ITZ of the cement paste was deemed to be the weak link as the cracks were clearly surrounding the aggregates. For normal strength concrete this is the expected behaviour but, when compared to conventional cement paste, the EMVc paste disintegrated easily between one's fingers, as when manipulating chalk.

Therefore, it was decided to test the splitting tensile strength and compare it with the performance of the other mixes. These tests were conducted using some of the 150x300 mm cylinders originally destined for the elastic modulus tests. Unfortunately, there were no ACI-FM-1 cylinders available at this stage because they had already been tested. Table 3-56 presents the results of the remaining mixes, where one 150x300 mm cylinder per batching day was tested.

Table 3-56: Splitting tensile strength results.

Property	DRM-FM-1-D2	EMV-FM-1-D3	EMV-FM-1-D4	EMVc-FM-1-D5
d [mm]	151	151	151	151
L [mm]	301	298	304	302
F [kN]	223.19	261.92	249.69	189.94
f_{spt} [MPa]	3.14	3.72	3.47	2.66

In Table 3-56, d is the cylinder diameter, L the cylinder length, F the applied force, and f_{spt} the calculated splitting tensile strength based on Eq. 3.10 – 2.

$$f_{spt} = \frac{2F}{\pi dL} \qquad (3.10 - 2)$$

As observed, the results confirmed the lower splitting tensile capacity of the EMVc mix, with a performance drop of 26% compared to the average of the EMV cylinders. Furthermore, it was the only mix design with a f_{spt} below 3 MPa, and 15.3% inferior compared to the DRM capacity. Moreover, the EMV mix performed as expected with the highest splitting tensile capacity, which can be attributed to its balanced volumetric proportions. Naturally, given that only one cylinder per batching day was tested, the results can present more variability, although they were deemed representative.

Finally, when adding the data points of all cylinders tested for compressive strength, including the ones reserved for the structural testing days and the ones previously tested for the elastic modulus, the complete history evolution can be generated for each mix. The

results are presented separately in Figure 3-46, Figure 3-47, Figure 3-48, and Figure 3-49 for the ACI, DRM, EMV, and EMVc mixes, respectively.

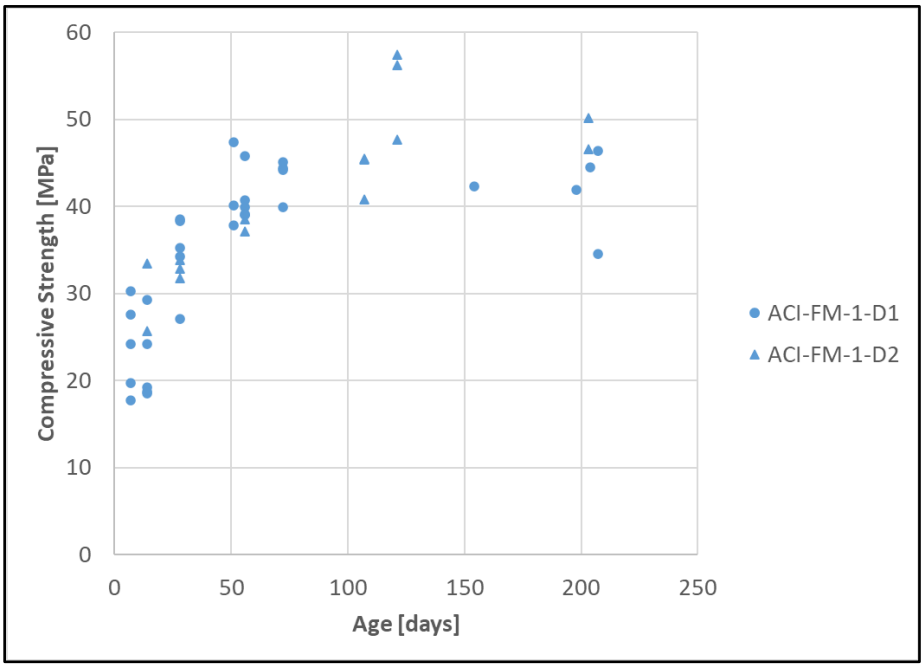

Figure 3-46: ACI-FM-1 compressive strength history.

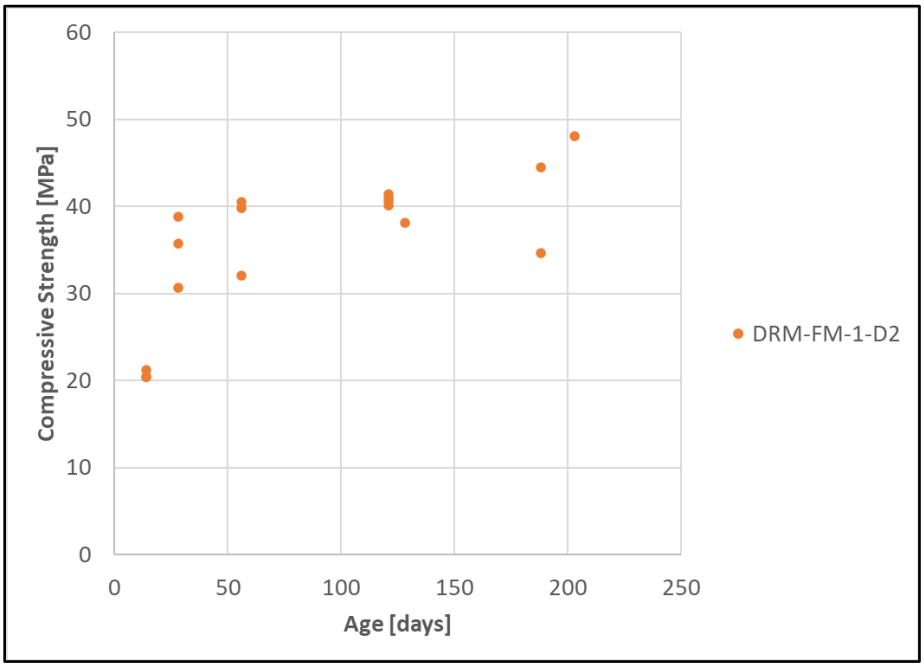

Figure 3-47: DRM-FM-1 compressive strength history.

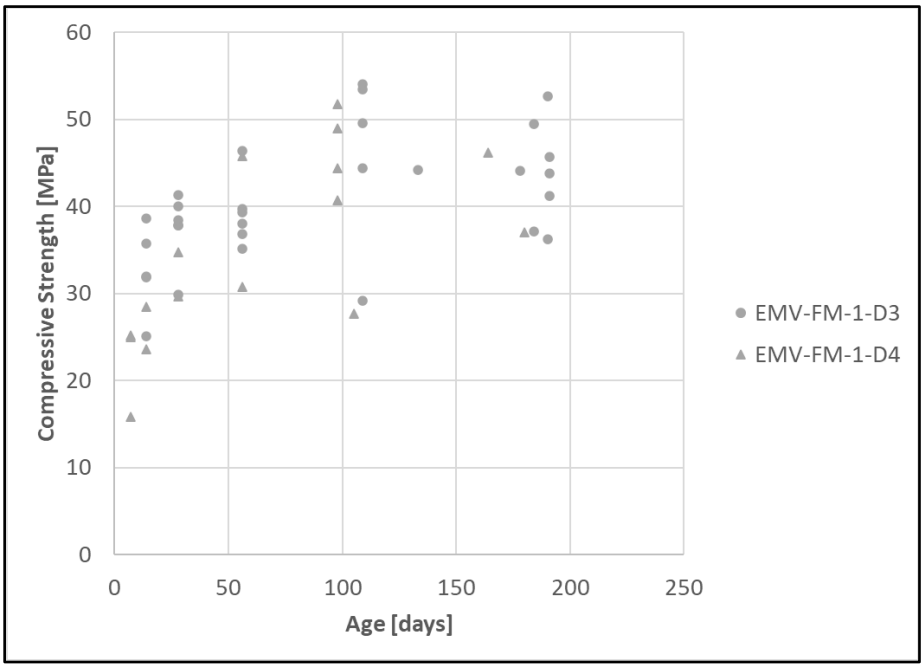

Figure 3-48: EMV-FM-1 compressive strength history.

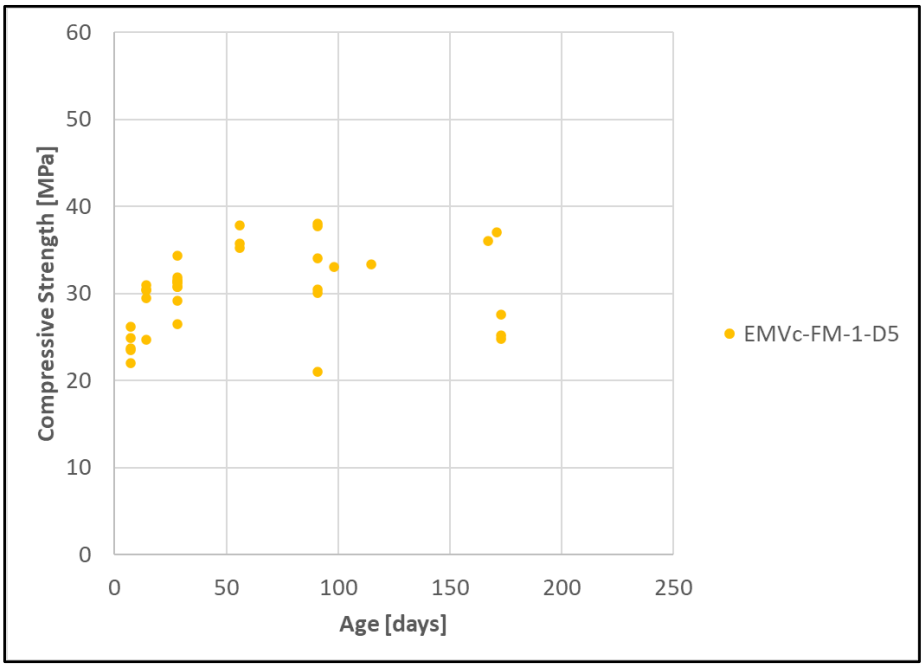

Figure 3-49: EMVc compressive strength history.

In the case of the ACI mix, it is observed that after 200 days the strength stabilization around 46 MPa becomes clearer, although the scatter shows some results greater than 50

MPa, and lower than 40 MPa. These discrepancies can be attributed to the quality of the manufactured cylinders, like the one observed after 200 days, and because the results include the compressive strength of the cylinders that were previously tested for the elastic modulus, which could have potentially reduced their capacity.

A similar trend can be appreciated for the DRM mix results, where the stabilization seems to be around 42 MPa after 200 days, 8.7% below the conventional ACI mix. Even though the number of tested cylinders was reduced due to only having 2 batches, the results are consistent and uniform, as it was observed during the second trial batch.

The results of the EMV mix, on the other hand, present the highest scatter across all mixes. As mentioned before, it is highly probable the workmanship in the cylinders' elaboration might have played a role in the performance, especially when it comes to the applied vibration. However, despite the scatter, a trend with an average value between 45 – 46 MPa after 200 days is observed, which is close to the results of the ACI mix, and 8.3% higher than the average of the DRM mix.

Finally, the EMVc mix presents a contrasting case, with an average that after 200 days sits in the 36 MPa region, which is 21.7% lower than the averages of the ACI and EMV mixes. Another interesting observation is that the strength development started to lose momentum after 14 days, and it became almost stagnant after 56 days. Considering that the "C-Crete Binder" is an activated slag, this behaviour was not expected. Slags are known for having a slower initial reaction than PC, but they tend to develop their strength over time. When adding the results of the elastic modulus and splitting tensile tests, it is evident that the binder's composition or its reaction with the used admixtures played a major role. This topic will be discussed in the upcoming section.

3.11. Discussion

3.11.1. Effect of freeze-and-thaw cycles in the RMC characterization.

Upon the results presented in the previous sections, some aspects require discussion. The first one relates to the effect of the freeze-and-thaw cycles in the *"Sodium Sulphate RMC Method"*; according to the developers of the method, a minimum of three and a maximum of five cycles are recommended (Abbas et al., 2008). The reasoning behind this range is to be able to disintegrate the RMC of the RCA without damaging the OVA.

The characterized RCA sources for the verification of the EMV Method used five cycles to determine their respective RMC, and no issues were reported (Fathifazl et al., 2009a). For this project, it was decided to use the minimum value of three cycles given the constraints in the equipment availability, and they were enough to degrade most of the RMC. However, the samples needed an extended inspection to manually remove the remaining patches, thus taking more time than anticipated to complete the entire process with an acceptable degree of precision.

Therefore, when answering the question of which number is the optimum to improve the efficiency of the method, five would probably be the best option. If the equipment is available, five cycles should degrade the RMC to the minimum, thus expediting the inspection process. Despite this, the effectiveness also relies on the type of salt: the sodium sulphate proved effective for the RHC, but it needs more testing to check its performance against RCA coming from CDW, where more impurities will be present and they might get affected by the salt action, thus altering the final RMC value (Hayles et al., 2018).

3.11.2. Residual mortar content and aggregates comparison

In terms of the RMC, the values vary depending on the source; a few examples are listed in Table 3-57. For the first reference, RCA-1B was obtained from crushed sidewalks, curbs and gutters from Waterloo, ON. RCA-2B was sourced from crushed runway, apron, and

terminal structures from the Pearson International Airport of Toronto, ON. Lastly, RCA-3B comes from RHC that was stockpiled and crushed in a ready-mix plant (Butler et al., 2012). An important detail is that the characterization process followed a thermal expansion procedure, different from the "*Sodium Sulphate RMC Method*".

Table 3-57: RMC references from previous studies.

Reference	RCA-1X	RCA-2X	RCA-3X
(Butler et al., 2012) (B)	46%	56%	50%
(Fathifazl et al., 2009a) (F)	41%	23%	-
(Hayles et al., 2018) (H)	28%	27%	-
Current Project	29%	32%	-

For the second reference, both RCA sources were used in the EMV Method validation and came from recycled demolition concrete processing plants, the first one (RCA-1F) located in Montreal, QC, where crushed limestone was the primary OVA; and the second one (RCA-2F) located in Vancouver, BC, where river-bed gravel was the main OVA (Fathifazl et al., 2009a). In the case of the third reference, RCA-1H was reclaimed concrete material (RCM) produced from waste coming from multiple demolition sites. Meanwhile, RCA-2H was returned hardened concrete or RHC. (Hayles et al., 2018)

When comparing the RMC of the RCA sources used for this project with the mentioned references, they sit in between RCA-1F and RCA-2F, with an average of 30%, and below the RMC of the only RHC source, RCA-3X, whose value is 50%. These differences show the natural variability of the RCA, where the RMC will depend on the parent source and on the production/recycling processes. Consequently, it is of upmost importance to test the RMC before incorporating RCA into new concrete mixes, especially if multiple sources are going to be blended, since they will impact the EMV designs.

The quality of the RCA depends on several factors, including the parent concrete strength and ITZ, the OVA quality and reactivity, age, exposure conditions, among others. In general, a higher quality RCA tends to be directly related to a better-quality RMC, which

is a result of the parent concrete strength and a less porous ITZ. Likewise, the RMC presence is also influenced by the OVA's angularity and surface roughness, where an increase in the latter propitiates a higher RMC adherence (Ahimoghadam et al., 2020).

Table 3-58: Aggregate properties comparison.

			Relative Density		
Reference	**Aggregate**	**Absorption [%]**	**Bulk**	**SSD**	**Apparent**
(Fathifazl et al., 2009a)	RCA-1F	5.40%	2.31	2.42	2.64
	RCA-2F	3.30%	2.42	2.50	2.64
	CA-1F	0.34%	2.70	2.71	2.73
	CA-2F	0.89%	2.72	2.74	2.79
	FA-1F	0.54%	2.70	2.72	2.76
(Butler et al., 2012)	RCA-1B	4.66%	2.36	2.48	-
	RCA-2B	6.15%	2.28	2.43	-
	RCA-3B	7.81%	2.22	2.41	-
	NA-1B	1.52%	2.67	2.71	-
(Lotfy & Al-Fayez, 2015)	RCA-1L	11.57%	2.05	2.28	2.68
	RCA-2L	5.40%	2.36	2.50	2.71
	Blend-1L	1.20%	2.69	2.72	2.78
	Blend-2L	1.54%	2.66	2.72	2.78
	Blend-3L	1.90%	2.62	2.67	2.76
	CA-1L	0.89%	2.73	2.75	2.79
	FA-1L	0.60%	2.67	2.68	2.71
(Hayles et al., 2018)	RT-1H	3.13%	2.39	-	-
	RU-1H	3.43%	2.36	-	-
	NA-1H	0.58%	2.68	-	-
	FA-1H	0.50%	2.60	-	-
Current Project	RCA-1	4.30%	2.40	2.50	2.67
	RCA-2	4.39%	2.38	2.49	2.66
	Old-NA	1.24%	2.72	2.76	2.82
	New-NA-1	3.55%	2.53	2.62	2.78
	New-NA-2	1.12%	2.70	2.73	2.78
	Sand	0.82%	2.60	2.62	-

When adding the absorption and relative density values, a more complete comparison can be made. A summary of these properties is presented in Table 3-58, where in addition

to the RCA sources, natural coarse and fine aggregates were added to expand the benchmark with the ones used for this project.

Complementing the previous three references, a fourth one is added under the (L) subcategory (Lotfy & Al-Fayez, 2015). For this case, the RMC of the two RCA sources was not reported, and the difference between them is that RCA-1L contained a higher granular material (20-0 mm) than RCA-2L (20-7 mm). Instead of using 100% RCA replacement, blends containing 10% (Blend-1L), 20% (Blend-2L), and 30% (Blend-3L) of coarse RCA were used.

When analyzing the absorption content, it is appreciated that RCA-1 is comparable to RCA-2F, RCA-1B and RCA-2L. Both bulk and SSD relative densities are similar, and the main difference lies in the absorption content, which is 30% higher than RCA-2F but 7.7% and 20.3% lower than the other two. If the RMC effects are added, then RCA-1 fits as an intermediate source for the first reference, which was used in the EMV Method validation. Nevertheless, it is difficult to assure that the sources are similar since no information regarding their previous mix design and chemical composition is available.

Table 3-58 also helps to compare the variation in the natural aggregates' properties. In previous sections, it was mentioned that a mistake was made in the SSD weight of the "New-NA" source, resulting in an absorption content higher than expected, 3.55%. After updating the properties with the corrected values (see "New-NA-2" label), the new absorption and relative densities are comparable to all mentioned references by staying between 0.80% – 1.20% for the former, and 2.67 – 2.73 for the oven-dry category of the latter.

3.11.3. Updated mix designs

Since the designed mixes considered the "New-NA-1" properties, an error was carried over the proportions of the RCA, natural coarse, and fine aggregates. The W/C ratio, original cement and mixing water contents remained unchanged since they do not depend on these

properties. The updated mix designs are presented in Table 3-59, while the admixtures content remained unchanged (refer to Table 3-34 and Table 3-36 for details).

Table 3-59: Revised ACI, DRM, and EMV mix designs.

		ACI-RM-1		DRM-RM-1		EMV-RM-1	
Component	**SG**	**[kg/m³]**	**[m³/m³]**	**[kg/m³]**	**[m³/m³]**	**[kg/m³]**	**[m³/m³]**
Cement	3.15	400.00	0.127	400.00	0.127	288.84	0.092
Water	1.00	160.00	0.160	160.00	0.160	115.54	0.116
Coarse Aggregate	2.70	1073.74	0.398	0.00	0.000	399.13	0.148
RCA	2.40	0.00	0.000	953.43	0.398	953.43	0.398
Fine Aggregate	2.60	637.45	0.245	637.45	0.245	460.31	0.177
Air	0.00	0.00	0.070	0.00	0.070	0.00	0.070
Total		**2271.20**	**1.000**	**2150.88**	**1.000**	**2217.24**	**1.000**

When comparing the new mixes to those presented in Table 3-33 and Table 3-35, the changes in the volumetric proportions of the aggregates are visible. For the ACI mix, the natural coarse aggregate kept the same weight since the bulk density had no variations, but its new volumetric fraction altered the fine aggregate's one, causing a 11.95% weight increase. In the case of the DRM mix, the RCA weight reduces by 6.72% and the fine aggregate increases by 11.95%. Finally, for the EMV mix, natural coarse aggregate increases by 12.51%, RCA decrease by 6.17%, and fine aggregate increases by 11.79%.

The ramifications of this mistake were not severe since they did not affect the W/C ratio and the water and cement weights, and consequently the admixtures content remained unmodified. For the ACI mix, the mix had fewer fine aggregates, which could have affected the fresh state since less fresh mortar was available. On the other hand, the DRM mix incorporated more RCA and less fines, thus affecting the fresh state with a decreased workability, although the overall mortar content did not suffer a greater imbalance because the lack of fines was partially compensated with the excess of RCA.

Moreover, the same explanation applies to the EMV mix, where the overall mortar content was not as affected as the fresh state, where the extra fine aggregates would have

improved the mix behaviour with an increased fresh paste content, thus enhancing the compaction and slump retention. Additionally, the modified EMV design parameters before and after the updates in the "New-NA" properties are presented in Table 3-60.

Table 3-60: Updated EMV design parameters.

Parameter	Equation	Old	New
RMC	-	29.24%	29.24%
RMC_{max}	3.7 – 1	34.49%	30.18%
R_{min}	3.7 – 2	0.000	0.000
R	3.7 – 3	0.330	0.387
V_{NA}^{NAC}	-	0.424	0.398
V_{M}^{NAC}	3.7 – 4	0.506	0.532
V_{RCA}^{RCA-C}	3.7 – 5	0.424	0.398
V_{NA}^{RCA-C}	3.7 – 6	0.140	0.148
V_{NM}^{RCA-C}	3.7 – 7	0.366	0.384

As observed, the design parameters suffered minor changes since the updated natural aggregate's relative density was not high enough to alter the RMC_{max}, which was still above the RMC of RCA-1. With this parameter almost unchanged, the rest only suffered minor adjustments to fit the volumetric fraction upon the design volumetric unit.

Even though the mistake was unfortunate and carried over to the mix designs, it produced conservative results. With the proposed readjustments based on the updated "New-NA-2" properties, all mixes should get a performance boost in the fresh and hardened states. It is difficult to quantify the effects given concrete's variability, but some of them can be qualitatively assessed. For example, the superplasticizer effect would be reduced for the same dosages since the addition of more fines would increase the cement paste content, thus improving the mix consistency and lowering the slump readings, which should get closer to the 150 mm. These effects would have a greater impact on the EMV mixes given their reduced fresh mortar content.

In the case of the compressive strength, no meaningful differences would be expected with new updates, perhaps an increase in the averages or less scatter, but the trends between the three mixes should remain unaltered. However, the category with the biggest changes will most likely be the elastic modulus, where the updated proportions could lead to more closer results between the ACI and EMV mixes.

3.11.4. Mix design and performance comparison

Regarding the comparison between the mix designs in this study and those available in the literature, there are no mixes that can be directly compared in a 1:1 basis. There are differences in the W/C ratio, cementitious materials, admixtures content, and aggregate properties. For the EMV mixes, the best benchmarks are the ones presented in Table 2-1 to Table 2-4, where the design W/C ratios varied between 0.45 and 0.61. Table 3-61 presents a summary with the most relevant designs that aimed for designs strengths of 35 – 40 MPa and the use of RCA.

The mix designs of the RCA blends (Lotfy & Al-Fayez, 2015) were not included; although they were based on the requirements established for a C-1 class concrete, 35% of the cementitious materials were replaced with slag. For the mixes listed in Table 3-61, the cement content used for the EMV mixes of this project was 13.8% and 19.3% lower than the EM-C and EV-C mixes, 6.6% higher than all RCA mixes in the second reference, and 15.5% and 13.7% higher than 81-RU-35B and 100-RT-35.

When using the EMV Method, the RCA content is a function of the maximum RMC that can be fitted into the mix, although the actual replacement might be lower if the intention is to replicate the volumetric fractions of the original mix. This was the case for the EM-C and EV-G mixes, where the ratio between RCA and total coarse aggregate content was 36.5% and 74.3%, respectively. For the second reference, all mixes considered a 100% volumetric RCA direct replacement, while the mixes of the third reference used the EMV Method for the highest possible replacement, with values of 81% and 100%. For this project,

the effective replacement was 70.5%, which is closer to the EV-G mix but with a higher RMC (30% v 23%) and lower W/C (0.40 v 0.45) ratio in the mix design.

Table 3-61: RCA concrete mix designs from references.

		Weights [kg/m^3]				
Reference	**Mix**	**Cement**	**Water**	**Coarse Aggregate**	**RCA**	**Fine Aggregate**
(Fathifazl et al., 2009a)	CL-C	430	193	833	0	808
	EM-C	335	151	720	414	630
	CG-C	424	191	898	0	765
	EV-C	358	161	281	813	645
(Butler et al., 2012)	NAC-40C	271	160	1099	0	861
	RCA1-40D	271	160	0	974	860
	RCA2-40D	271	160	0	940	860
	RCA3-40D	271	160	0	912	860
(Hayles et al., 2018)	0-NA-35	370	174	1029	0	790
	81-RU-35A	191	90	193	1440	408
	81-RU-35B	250	118	193	1440	408
	100-RT-35	254	119	0	1380	542
Current Project	ACI-RM-1	400	160	1074	0	637
	DRM-RM-1	400	160	0	953	637
	EMV-RM-1	289	116	399	953	460
	EMVc-RM-1	289	116	399	953	442

In terms of performance, a summary with a comparison between the obtained results and the mentioned references is presented in Table 3-62. For the air content category, the first and third references are within the tolerances for the C-1 concrete class, 5 – 8%. As mentioned in the results section, issues with the air metre and workmanship prevented more accurate readings. Moreover, the mistake in the properties of the “New-NA” source might have contributed as well given that the volumetric proportions were not balanced, but it is difficult to quantify the effect.

No major differences are found in the fresh density category, with all mixes in the range of 2260 – 2490 kg/m^3. Notwithstanding, the fresh density of the EMV mixes in the first reference matches those of the companion conventional concrete mixes, as it was the case

with the mixes designed in this project. For the slump, all mixes but those of the second and fourth references used admixtures, as reflected in their results. The slump differences are attributed to the chosen dosages and the admixture type. The mixes of the third reference used a mid-range-water-reducer, while the mixes from the first reference and those used in this project chose a high-range-water-reducer.

Table 3-62: RCA concrete mix performance from references.

Reference	Mix	Air Content [%]	Slump [mm]	Fresh Density [kg/m3]	f'_c [MPa]	E_c [GPa]
(Fathifazl et al., 2009a)[a]	CL-C	6.30	175	2300	37	31
	EM-C	6.00	105	2295	39	30
	CG-C	6.30	210	2325	36	31
	EV-C	6.00	140	2320	40	33
(Butler et al., 2012)[a]	NAC-40C	-	115	-	38	-
	RCA1-40D	-	30	-	43	-
	RCA2-40D	-	45	-	38	-
	RCA3-40D	-	85	-	32	-
(Lotfy & Al-Fayez, 2015)[b]	GUL	7.80	104	-	36	-
	C10	8.10	110	-	37	-
	C20	8.30	112	-	35	-
	C30	8.10	110	-	36	-
(Hayles et al., 2018)[a]	0-NA-35	1.60	90	2483	36	37
	81-RU-35A	4.90	0	2266	14	22
	81-RU-35B	-	0	2331	20	25
	100-RT-35	7.20	10	2277	30	29
Current Project[b]	ACI-FM-1	2.52	163	2338	34	31
	DRM-FM-1	2.60	175	2295	35	23
	EMV-FM-1	1.95	199	2377	36	28
	EMVc-FM-1	1.58	151	2389	31	22

*Nomenclature: [Cementitious Materials]: GU Cement (a), GUL Cement (b).

Given the RCA characteristics, where higher absorption and the RMC play an important role in the new mix performance, the EMV Method provides a useful tool that helps to integrate RCA without modifying the volumetric proportions of the companion conventional mix. However, the reduced fresh mortar content is an aspect to consider,

especially when the RCA replacement ratios are high. The idea behind producing eco-efficient mixes is to minimize the cement content and the use of chemical admixtures, which is difficult to achieve for all EMV mixes.

One way to reduce the carbon footprint of the mixes would be to add SCMs such as fly ash, silica fume, or slag to reduce the fresh cement content. The concept of fresh new mortar in the EMV mixes is the minimum paste required to coat the aggregates and match the original volumetric fraction; therefore, that minimum paste must be able to glue all the new aggregates, including the RCA. In consequence, the use of admixtures such as HRWR is a helpful tool.

For the EMV mixes of this project, the cement reduction is close to 27.8% when compared to the reference mix, which can be viewed as a justification for the use of admixtures. Since the constituent materials of an EMV mix are the same as those in conventional mixtures, no compatibility issues arise from the use of chemical admixtures. However, as observed during the mix design phases, the dosages are considerably higher than for regular mixes. The dosages are typically computed based on the amount of cementitious materials added to the mix, hence the higher values since the fresh cement content is much lower.

Since EMV-proportioned RCA concrete is different from conventional concrete, the fine tuning of the admixtures content will most likely exceed the normal ranges that were developed for conventional concrete. As a result, a possible solution would be to closely work with the admixtures supplier to develop a formulation that can better optimize the dosages without risking suffering effects such as low slump retention or accelerated setting, which can be a consequence of using a higher concentration of the available PCE-based products. A second solution to reduce the amount of superplasticizer is by delaying its incorporation to the mix, as it allows the early hydration reactions (the aluminum products),

and whose products enhance the dispersion effect (Cheung et al., 2011; Flatt & Houst, 2001; Nkinamubanzi et al., 2016).

In terms of compressive strength, the average results of this project are close to the first and third references, which were used for the EMV Method validation, and the testing of Class C-1 concrete using RCA, respectively. Despite the different used cementitious materials (GU v GUL cement), there are no major impacts in terms of performance, which is line with the requirements established for GUL cement. Moreover, in the case of the EMV mixes, the limestone filler might have helped in terms of nucleation and dispersion in the hydration stages of the fresh GUL cement.

Finaly, the fresh density results of the EMV mixes are close to their conventional references. Nevertheless, differences are found in the elastic modulus where, opposite to the trend observed for the first reference, the performance of the ACI and EMV mixes had differences of approximately 10.7% on average. It is probable the results would have been much closer if the corrected mixes were used instead, since the disparities can be a consequence of the altered volumetric fractions.

3.11.5. Batching considerations

Another topic that requires attention is the learning curve of making concrete in a laboratory. In contrast to concrete made in ready-mix plants, the equipment size and power are reduced, and a good understanding of them is essential to produce good concrete in a consistent manner. For instance, the size of the 60-litre pan mixer, and its torque capacity generated inconsistent results when the batch size was lower than 25 litres. On the other hand, the 200-litre mixer produced consistent 100-litre batches, although it required an elevated amount of physical effort to recover the paste that was sticking to the walls.

In the industry, the equipment is automated and bigger in size, and the torque capacity is also higher. In consequence, it is of vital importance to know how the lab equipment

works and the volumes at which the concrete is representative to replicate the industry conditions on a smaller scale. Otherwise, there is a chance the results might be affected by factors other than those exclusively related to the mix design. The same reasoning applies to the compaction and concrete vibration. The use of the vibrating table helped reduce the scatter compared to batches where only the rod was used for the cylinders' compaction. Many times, the concrete seemed initially difficult to work with but was easily vibrated within the forms, though the cylinders' quality was not improved since the vibrator's power could not be applied to them.

Another aspect that significantly improved the performance of all mixes, especially the RCA ones, was the decision to add all coarse aggregates in an SSD condition. This technique was positively applied in other research studies, and the reasoning was the aggregates needed time to reach the absorption equilibrium, and this time was higher than the concrete mixing time (Butler et al., 2012; Lotfy & Al-Fayez, 2015). Therefore, even if the mixing water was adjusted to account for the absorption of the aggregates, the shorter mixing time would have not prevented the loss of water.

Nonetheless, the main drawback would be the water migration once the concrete sets, which could lead to higher shrinkage and creep values (Brand et al., 2015; Souche et al., 2017). These tests were not used for this project, but it would be interesting to see if they have a negative effect over the EMV mixes, since this water migration could help the internal curing considering the lower fresh paste content.

Finally, the workmanship is as relevant as the previous aspects. Much of the variability and scatter can be minimized with a good workmanship and should not be underestimated.

3.11.6. "C-Crete Binder" performance

The motivation behind the "C-Crete Binder" use was to test a next-generation binder to see how its integration with the EMV Method would be, since it would add another benefit

if the carbon footprint coming from the GUL cement could be further reduced. However, its performance was lower than the EMV mixes made with GUL cement. Besides the updated aggregate properties, additional tests were implemented to determine its specific gravity, which was effectively lower at a value of 2.92. The updated mix designs and admixtures content are presented separately in Table 3-63 and Table 3-64.

When compared to the EMV mixes, the increased water absorption and workability loss in the fresh state could be linked to the lower specific gravity and finer nature of this new binder. Traditionally, finer elements favour absorption due to their increased specific surface. Another possibility would be the compatibility with the chemical admixtures, especially the superplasticizer, since the rest of the ingredients remained the same.

Table 3-63: Revised EMVc mix design.

		EMVc-RM-1	
Component	**SG**	**[kg/m^3]**	**[m^3/m^3]**
Cement	2.92	288.84	0.099
Water	1.00	115.54	0.116
Coarse Aggregate	2.70	399.13	0.148
RCA	2.40	953.43	0.398
Fine Aggregate	2.60	441.53	0.170
Air	0.00	0.00	0.070
Total		**2198.47**	**1.000**

Table 3-64: Revised EMVc admixtures content.

		EMVc-RM-1	
Admixture	**SG**	**[mL/100kgCM]**	**[mL]**
AE-2	1.01	100	289
HRWR-2	1.11	850	2455

PCE-based admixtures require an adequate sulphate content in the cement to generate the early aluminum hydration products that will favour the dispersion effects and a delay in the nucleation. Besides that, a delay in the incorporation could also help increase its effectiveness given that early additions risk a superplasticizer absorption in long polymeric

reactions since they interfere in the hydration of the aluminum products (Cheung et al., 2011; Flatt & Houst, 2001; Shi et al., 2019).

However, the main roots of the mentioned issues might be in the nature of the binder. For activated slags, the activator plays a role in the strength development characteristics. As observed throughout the batching process, the compressive strength stalled after 14 – 21 days and the brittleness of the failed section was noticeably higher than for specimens made with GUL cement. There are reports that indicate that when using NaOH (sodium hydroxide) as the activator, the strength development reduces even for higher hydration ratios (Winnefeld et al., 2015).

Moreover, the use of the same activator has also caused the development of cement pastes that are bigger in size and more porous (Puertas et al., 2018). Nevertheless, even though these characteristics are very close to what was experienced in the lab, the binder is proprietary, and its exact composition is not available. Therefore, there might be other factors influencing its behaviour and that are unknown to the authors.

Finally, the green colouration observed at all ages might be linked to the sulphate content of the activated slag. Previous studies have detected the same patterns and discovered that the presence of the tri-sulfur radical anion (S^{-3}) might be the root cause of the green and blue colourations (Chaouche et al., 2017). This anion is also present in elements such as lapis lazuli, and tests observed that once oxidized, the slag progressively turned to grey tones, which is the exact phenomena experienced once the EMVc cylinders were taken out of the curing pails for testing.

4. Bond behaviour of steel-reinforced RCA beam-ends

This chapter focuses on the structural component of the research project, which is the bond behaviour study of steel-reinforced EMV-proportioned RCA concrete specimens under monotonic and cyclic loading. The organization of this chapter will begin with all the details that led to the final sample design and testing structure; to then proceed to the results presentation, analysis, and discussion.

4.1. Specimen design

As described in the literature review, there are four main specimen designs used for bond studies. Pullouts and beam-ends are suited for small-scale testing, while beam-anchorage and splice tests are oriented for large-scale tests (Figure 2-9). Given the scope and timeframe of the project, it was decided to proceed with small-scale tests.

Between pullout and beam-end specimens, the main difference lies in the stress-state of the concrete surrounding the rebar. Pullout tests grab and pull the rebar, and the reaction is placed on the concrete by means of plates, thus inducing compression. This effect means the results are only comparable to other pullout tests, and they are not representative of the real-life stresses in flexural members, in which both the rebar and the surrounding concrete are in tension (ACI, 2003). Beam-ends, on the other hand, reproduce a more accurate stress-state by moving the compression area away from the rebar.

Beam-ends also have the advantage of being standardized in ASTM A944 (ASTM, 2022b), and have been used in several bond studies that led to the normalization of rebar deformations (Darwin et al., 1996; Darwin & Graham, 1993; Idun & Darwin, 1999). Hence, it was determined that beam-ends provided the best option for the creation of a database that can help future large-scale tests, since the stress-states will be more representative and aid the design phase.

The beam-end dimensions are established in ASTM A944 and presented in Figure 4-1. The length is up to the designer, while the width depends on the diameter of the reinforcing bar. Finally, the height is a function of the bar diameter, concrete cover, and the chosen embedment length. The design also considers a few tolerances for the mentioned dimensions, while the rebar sections that are not going to be embedded are protected by bond breakers, which can be steel conduits or PVC pipes.

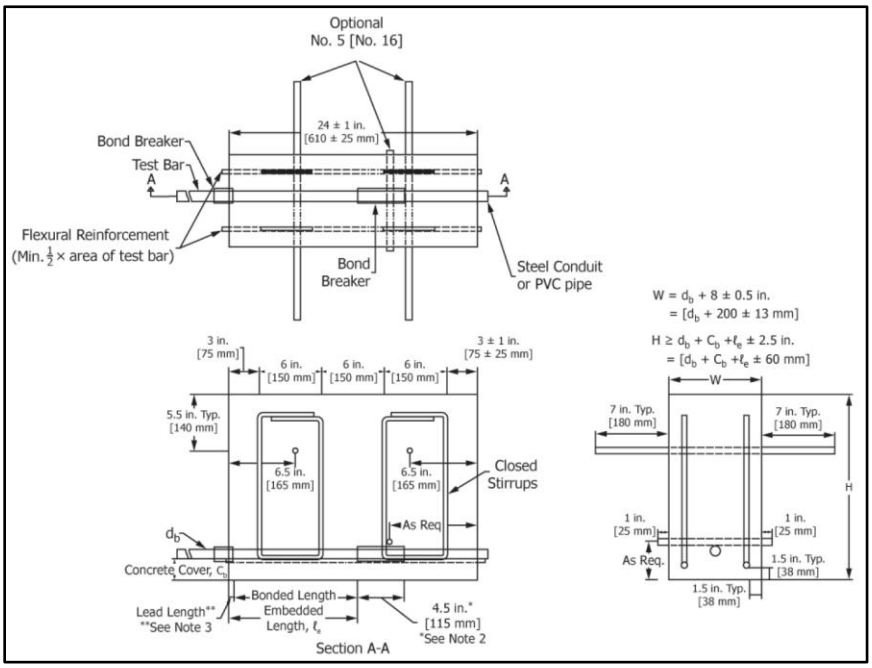

Figure 4-1: Beam-end standard dimensions (ASTM, 2022b).

Table 4-1: Canadian Grade 400W reinforcing bars details (CSA Group, 2021).

Bar Size	Area (A_b) [mm²]	Diameter (d_b) [mm]	Perimeter [mm]	Mass [kg/m]	Max. Spacing (s_L) [mm]	Min. Height (h_L) [mm]
15M	200	16.00	50.10	1.570	11.20	0.72
25M	500	25.20	79.20	3.925	17.60	1.26

For a Class C-1 concrete, Table 17 of CSA A23.1 (CSA Group, 2024a) mandates a minimum concrete cover of 60 mm for beams, girders, and columns, and 40 mm for the same members when only exposed to freeze-and-thaw cycles. Two Canadian Grade 400W

rebars were selected for the study, namely 15M and 25M, whose dimensions and deformation characteristics are presented in Table 4-1, and their nominal yielding and ultimate stresses are presented in Table 4-2. These rebars are commonly used for slab, beams, columns, and foundations in the Canadian practice.

Table 4-2: Canadian Grade 400W nominal properties (CSA Group, 2021).

Grade	$f_{y,min}$ [MPa]	$f_{y,max}$ [MPa]	$f_{u,min}$ [MPa]	$f_{u,max}$ [MPa]
400W	400	525	540	604

In an effort to keep the consistency of previous works, it was decided to use the same cross-section dimensions used in the original study on bond behaviour of EMV-proportioned RCA mixes (Fathifazl et al., 2009a). The dimensions for each specimen were 600 mm of length, 230 mm of width, and 500 mm of height. While the original study used 30M bars and a concrete cover of approximately 55 mm, the biggest bar size used in this study was 25M and the concrete cover was reduced to 40 mm, in accordance with the requirements for indoor applications (not exposed to freeze-and-thaw cycles or salts).

For the calculation of the embedment lengths, three equations were considered. The first one was the general design equation of CSA A23.3 (CSA Group, 2024b) for tension development length, whose general expression is given in Eq. 4.1 – 1:

$$l_d = 0.9 \frac{k_l k_c k_d k_s k_g}{\left(\frac{d_{cs} + K_{tr}}{d_b}\right)} \frac{f_{yg}}{\sqrt{f_c'}} \, d_b \geq 300 \, mm \qquad (4.1 - 1)$$

The code equation incorporates a series of factors that account for bar location, coating, concrete density, bar size, and reinforcement grade. Additionally, the expression in parentheses relates to the confinement provided by the concrete cover and the transverse steel (if present). For the beam-end configuration, the values for each coefficient are:

- $k_l = 1.0$, bar is located at the bottom of the beam-end.

- $k_c = 1.0$, uncoated reinforcement is being used.
- $k_d = 1.0$, normal-density concrete is being used.
- k_s accounts for the bar size effect, and its value is 0.8 and 1.0 for the 15M and 25M rebars, respectively.
- $k_g = 1.0$, yielding stress of the reinforcement is 400 MPa.
- d_{cs} is the distance between the surface to the centre of the rebar, meaning that when considering a concrete cover of 40 mm, its value is 48 mm for the 15M rebar, and 52.6 mm for the 25M one.
- $K_{tr} = 0$, no transverse reinforcement within the development length.

The second considered expression was the ACI 318 general design equation for development length in tension (ACI, 2019), whose expression is given in Eq. 4.1 – 2:

$$l_d = \left(\frac{f_y}{1.1\lambda\sqrt{f_c'}} \frac{\Psi_t \Psi_e \Psi_s \Psi_g}{\left(\frac{c_b + K_{tr}}{d_b}\right)} \right) d_b \qquad (4.1 - 2)$$

As with the CSA A23.3 expression, the ACI 318 equation also considers the same factors, but with a different notation and placement. For the beam-end configuration, the values for each coefficient are:

- $\Psi_t = 1.0$, bar is located at the bottom of the beam-end.
- $\Psi_e = 1.0$, uncoated reinforcement is being used.
- Ψ_s accounts for the bar size effect, and its value is 0.8 and 1.0 for the 15M and 25M rebars, respectively.
- $\Psi_g = 1.0$, yielding stress of the reinforcement is 400 MPa.
- $\lambda = 1.0$, normal-density concrete is being used.
- $K_{tr} = 0$, no transverse reinforcement within the development length.

- c_b is the distance between the surface to the centre of the rebar, meaning that for a concrete cover of 40 mm, its value is 48 mm and 52.6 mm for the 15M and 25M rebars, respectively.

Lastly, the third considered expression was the original ACI 318 equation for the development length in tension that was used before 1995 (ACI, 2003), which considered bond as a constant stress based on the bar area and yielding stress, and whose expression is given in Eq. 4.1 – 3:

$$l_d = 0.019\, A_b \frac{f_y}{\sqrt{f_c'}} \qquad (4.1-3)$$

This expression does not include the modern modification factors that tend to increase the level of conservatism; therefore, it is expected to give values closer to the actual development length of the bar. Table 4-3 presents the development lengths (l_d) of the 15M and 25M rebars for all three equations.

Table 4-3: Development lengths for the selected rebars.

	l_d [mm]		
Bar Size	**(Eq. 4.1-1)**	**(Eq. 4.1-2)**	**(Eq. 4.1-3)**
15M	315	315	260
25M	735	745	645

As expected, the CSA A23.3 and modern ACI 318 equations present almost identical results, while the original ACI 318 expression is less conservative. In consequence, the effective embedment lengths chosen for this project and their respective ratios to the CSA A23.3 expression (Eq. 4.1 – 1) are presented in Table 4-4.

The embedment lengths for the 15M rebar represent almost 55% and 100% of the code expression, while the value for the 25M rebar is approximately 45%. The first and third boundary conditions aim to study the cyclic bond in regions where the splitting or

anchorage failure governs, while the second aims to evaluate the performance close to the minimum threshold of 300 mm established by CSA A23.3 and ACI 318 for all scenarios.

Table 4-4: Effective embedment lengths for the selected rebars.

Bar Size	l_d [mm]	$l_d/l_{d,CSA}$	l_d/d_b	c/d_b
15M	170	0.54	10.63	1.57
15M	320	1.02	20.00	1.57
25M	320	0.44	12.60	2.50

In the original beam-end design, the embedded section of the tested bar is close to one of the ends, with a small bond breaker to prevent a pullout failure. However, to test the reversed cyclic bond behaviour, the available testing apparatus at the University of Ottawa required a vertical placement instead of the traditional horizontal one. This orientation change meant that extra verifications were needed to keep the load verticality and to provide enough clearance to measure the free-end slippage of the rebars.

To avoid stress concentrations near the supports and unintended confinement effects, it was decided to place the embedded section in the middle of the specimens (this aspect will be detailed in subsequent sections). The specimens' general dimensions are presented in Figure 4-2. Meanwhile, the reinforcement details for the 15M rebar with 170 mm and 320 mm of embedment are available in Figure 4-3, Figure 4-4, and Figure 4-5, respectively.

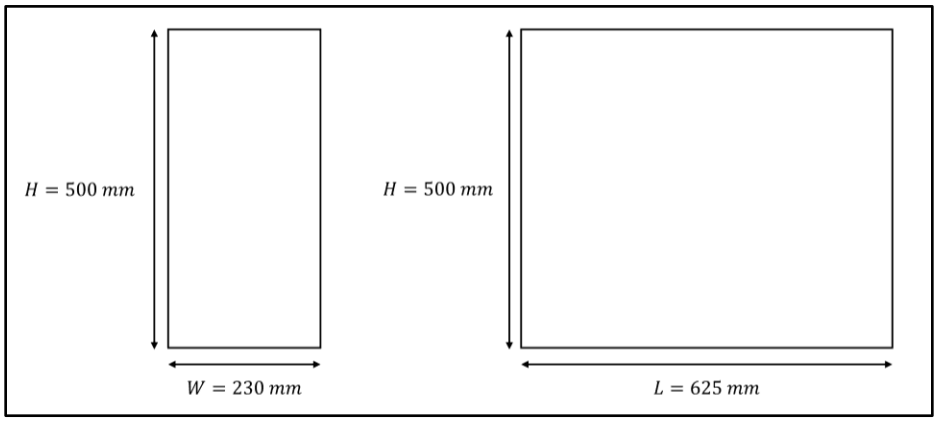

Figure 4-2: Bond RCA Beam-end general dimensions.

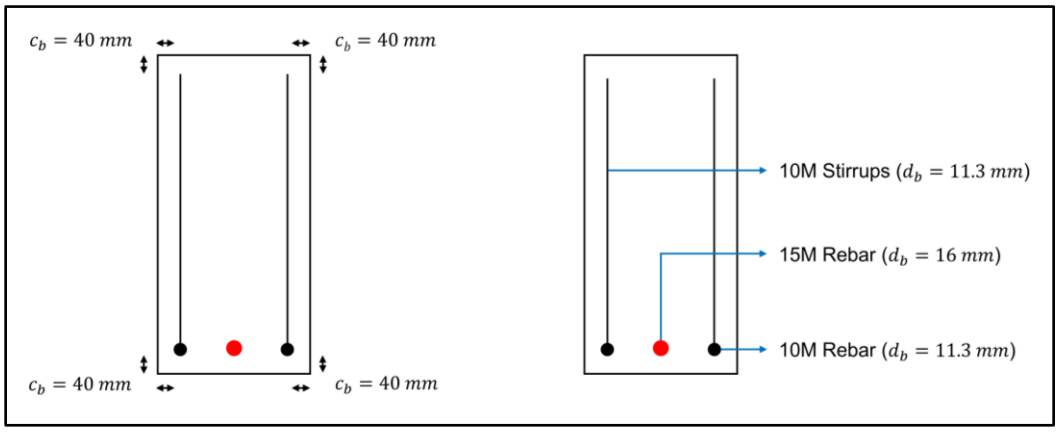

Figure 4-3: Bond RCA 15M Beam-end, section view.

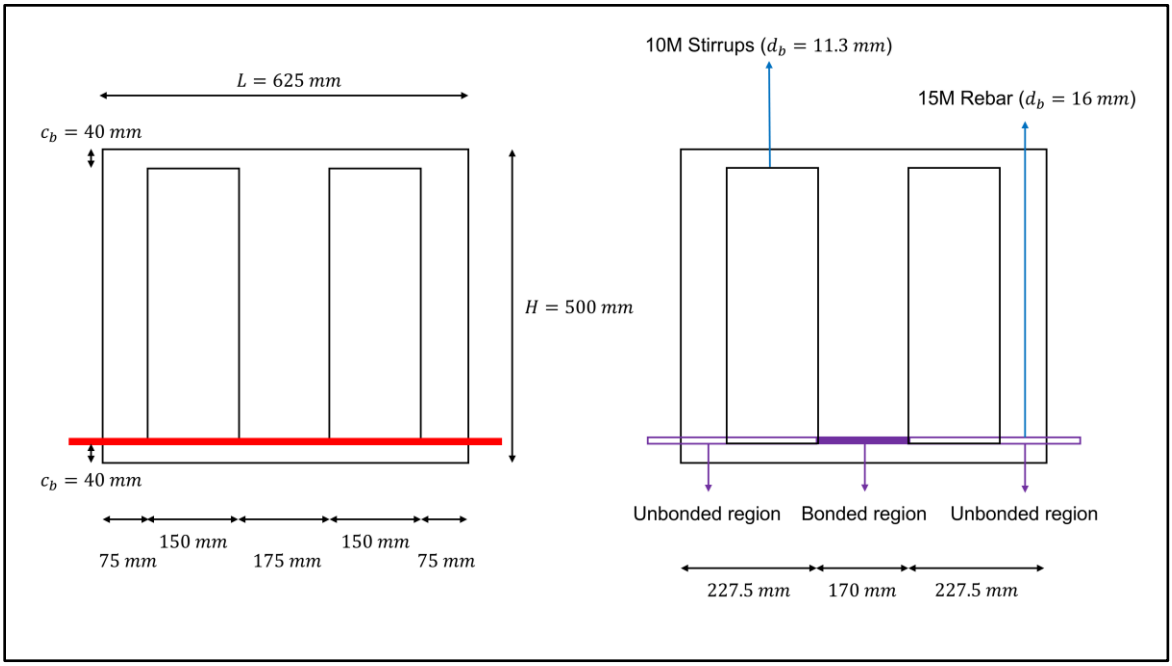

Figure 4-4: Bond RCA 15M Beam-end, 170 mm longitudinal view.

As observed, the beam-end has two sets of stirrups, which instead of being placed in the traditional transverse configuration, are placed on the longitudinal plane as per the requirements of ASTM A944. The reason behind this arrangement is to allow the development of the splitting longitudinal crack. Traditional shear reinforcement provides confinement that would restrain the crack development by stepping on its the path. Besides

that, this stirrup arrangement also helps in the fabrication and handling processes, which will be commented in subsequent sections.

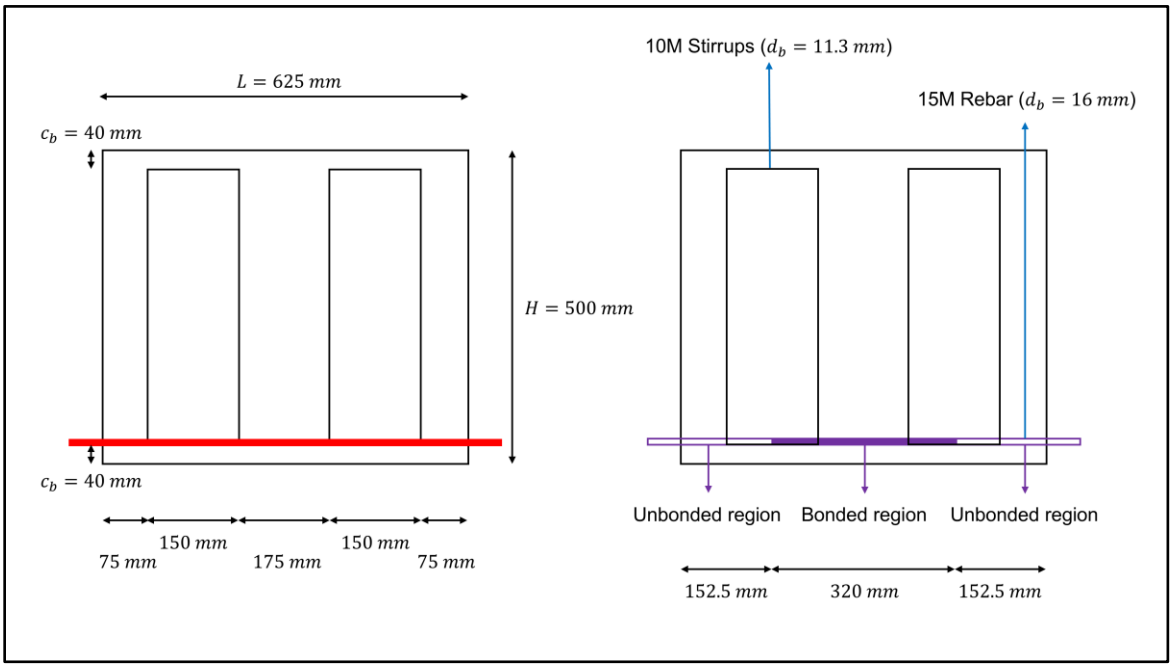

Figure 4-5: Bond RCA 15M Beam-end, 320 mm longitudinal view.

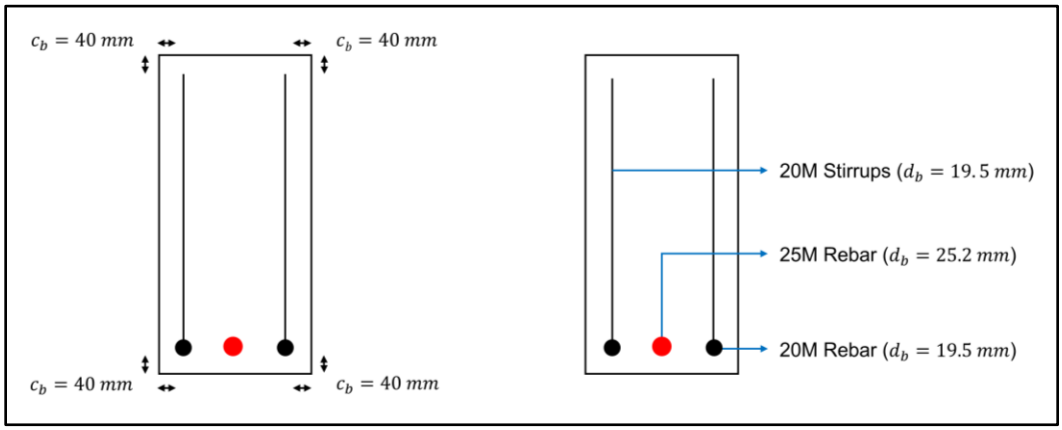

Figure 4-6: Bond RCA 25M Beam-end, section view.

Finally, the design of the beam-ends for the 25M rebar and 320 mm of embedment length is presented in Figure 4-6 and Figure 4-7. For this configuration, and according to the requirements of ASTM A944, the stirrups are made with 20M rebars. Morover, similar to

the 15M beam-end design, moving the embedded section to the middle of the beam-end allows a complete symmetry and reduces the complexities of the fabrication process.

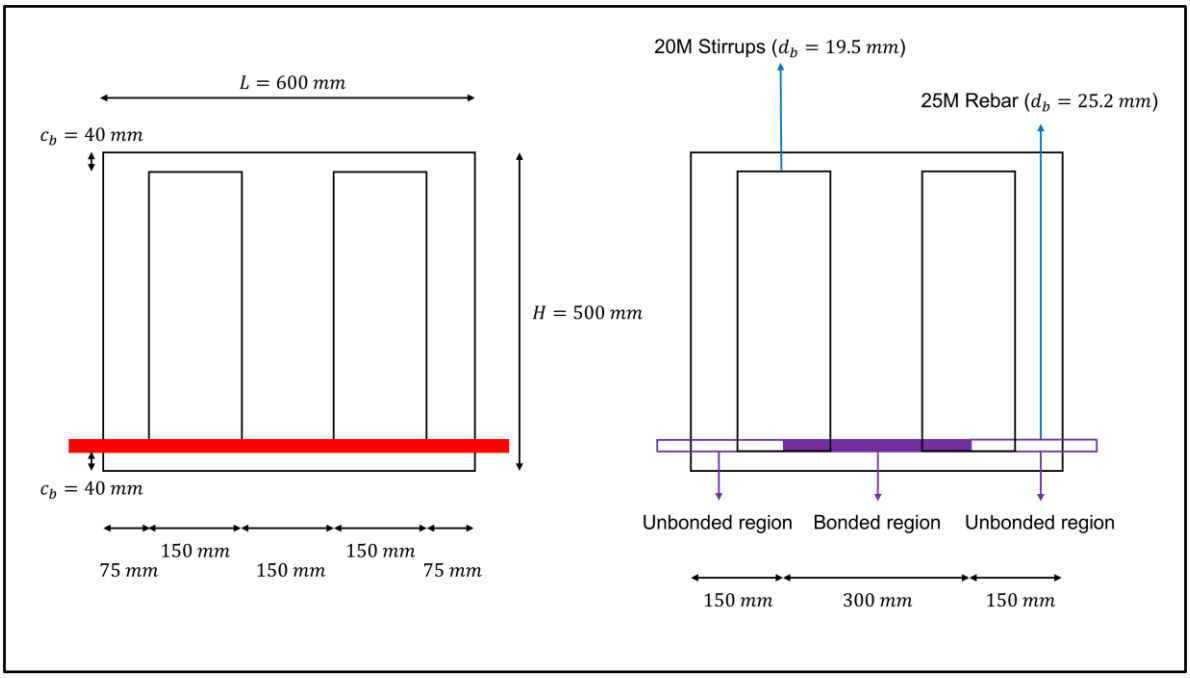

Figure 4-7: Bond RCA 25M Beam-end, 320 mm longitudinal view.

4.2. Testing matrix

As described in the literature review, bond characteristics are influenced by structural, reinforcement, and concrete properties. For the first group, the following were considered:

- Concrete cover to the outside of the rebar was set at 40 mm for all testing bars.
- Development and splice length: 170 mm and 320 mm.
- Transverse reinforcement: Not considered.
- Bar casting position: Only bottom-casting rebars were considered.

Meanwhile, for the second group (bar properties), the considerations were:

- Bar size: 15M and 25M.

- Bar geometry: All rebars are manufactured according to the requirements of CSA G30, where deformations are normalized (Table 4-1).
- Steel stress and yielding stress: Nominal properties were considered for the design, and tested properties were used for the final analysis (Table 4-2).
- Bar surface condition: No coatings or special surfaces were used.

Finally, the considerations for the third group (concrete properties) were:

- Compressive strength: A characteristic strength (f_c') of 35 MPa was chosen for the design, and tested strengths were used for the final analysis.
- Aggregate type and quantity: Fine aggregates remained unchanged. Coarse RCA and natural aggregates were selected and incorporated via four different mix designs, namely ACI, DRM, EMV, and EMVc. These are the mixes that were designed and tested in the previous chapter.
- Tensile strength and fracture energy: Nominal properties were considered for the design, and tested properties were used for the final analysis.
- Concrete slump and admixtures: Slump target was 150 mm, and all mixes considered the use of HRWR (superplasticizer) and air-entraining admixtures, as reviewed in detail in the previous chapter.
- Use of SCMs: No SCMs were used. However, a full GUL cement replacement with the “C-Crete Binder” was developed and tested for the EMVc mixes.
- Consolidation: Internal and external vibration was applied to all specimens with a standard 1500W concrete vibrator.

Therefore, four parameters can be considered as variables for the testing matrix: mix design, RCA type, bar size, and development length. Given the scope and timeframe of the project, it was decided to prioritize combinations over repetitions to develop a database that can orient future large-scale tests. Hence, nine twin pairs were made with only the loading protocol as their main difference, making a total of 18 samples. To compensate for

the lack of replicates, and to better understand the bond behaviour and its degradation, one twin was tested under monotonic loading (to obtain the backbone curve) and the other under cyclic loading. The final testing matrix is presented in Table 4-5.

Table 4-5: Beam-ends testing matrix.

Number	Label	Mix	RCA Type	Bar Size	l_d [mm]	Protocol
1	ACI-15M-170mm-M	ACI	-	15M	170	Monotonic
2	ACI-15M-170mm-C	ACI	-	15M	170	Cyclic
3	EMVc-15M-170mm-M	EMVc	RCA-1	15M	170	Monotonic
4	EMVc-15M-170mm-C	EMVc	RCA-1	15M	170	Cyclic
5	EMV-15M-170mm-M	EMV	RCA-1	15M	170	Monotonic
6	EMV-15M-170mm-C	EMV	RCA-1	15M	170	Cyclic
7	ACI-15M-320mm-M	ACI	-	15M	320	Monotonic
8	ACI-15M-320mm-C	ACI	-	15M	320	Cyclic
9	DRM-15M-320mm-M	DRM	RCA-1	15M	320	Monotonic
10	DRM-15M-320mm-C	DRM	RCA-1	15M	320	Cyclic
11	EMV-15M-320mm-M	EMV	RCA-1	15M	320	Monotonic
12	EMV-15M-320mm-C	EMV	RCA-1	15M	320	Cyclic
13	ACI-25M-320mm-M	ACI	-	25M	320	Monotonic
14	ACI-25M-320mm-C	ACI	-	25M	320	Cyclic
15	EMVc-25M-320mm-M	EMVc	RCA-1	25M	320	Monotonic
16	EMVc-25M-320mm-C	EMVc	RCA-1	25M	320	Cyclic
17	EMV-25M-320mm-M	EMV	RCA-1	25M	320	Monotonic
18	EMV-25M-320mm-C	EMV	RCA-1	25M	320	Cyclic

4.3. Testing apparatus and instrumentation

4.3.1. Testing apparatus

The available equipment for the testing of the beam-ends was a *Series 311.51 High-Force Test System* connected to a *FlexDAC-20* data acquisition system, both manufactured by MTS (Figure 4-8). This equipment is a servo-hydraulic machine which does not require anchorage to the strong floor, and whose load cell has a capacity of 5000 kN. It has four columns with a diameter of 20.32 cm each (8 in.), and a load frame with a height of 8.5 m (28 ft.) and 21.5 tonnes of weight.

Figure 4-8: MTS 311.51 High-Force Test System.

As appreciated in Figure 4-8, the machine had two Canadian W360x179 sections fixed to the base and the load frame. Therefore, to accommodate the beam-ends in a vertical position, a testing frame sitting between these two sections was required. The design was based on previous vertical beam-end configurations, where the rebar was placed in line with the actuator to avoid P-delta (or $P-\Delta$) effects, and with enough supports and restraints placed to take the reactions during the loading stages (Asghari Ghajari & Yousefpour, 2023; Butler et al., 2015a; Shao et al., 2022).

The testing frame was over-designed considering the worst-case scenario, which would have been the rupture of the 25M rebar at the maximum ultimate stress allowed by CSA G30 (Table 4-2). This stress is equivalent to 604 MPa for Grade 400W rebars, which translates to a force of 302 kN. The design conceptualization is presented in Figure 4-9.

As observed, on top of the bottom W360x179 girder, two W200x36 sections acting as columns were bolted, with two additional bolted FL130x15 flat bars connecting them. To effectively take the reactions, each column had two sets of welded rollers and shim plates,

while two additional sets were vertically placed on the opposite side of the rebar with four ¾ in. threaded rods clamping them to the bottom girder. These supports were aligned verifying the centreline of the roller was 40 mm away from the specimen's edge.

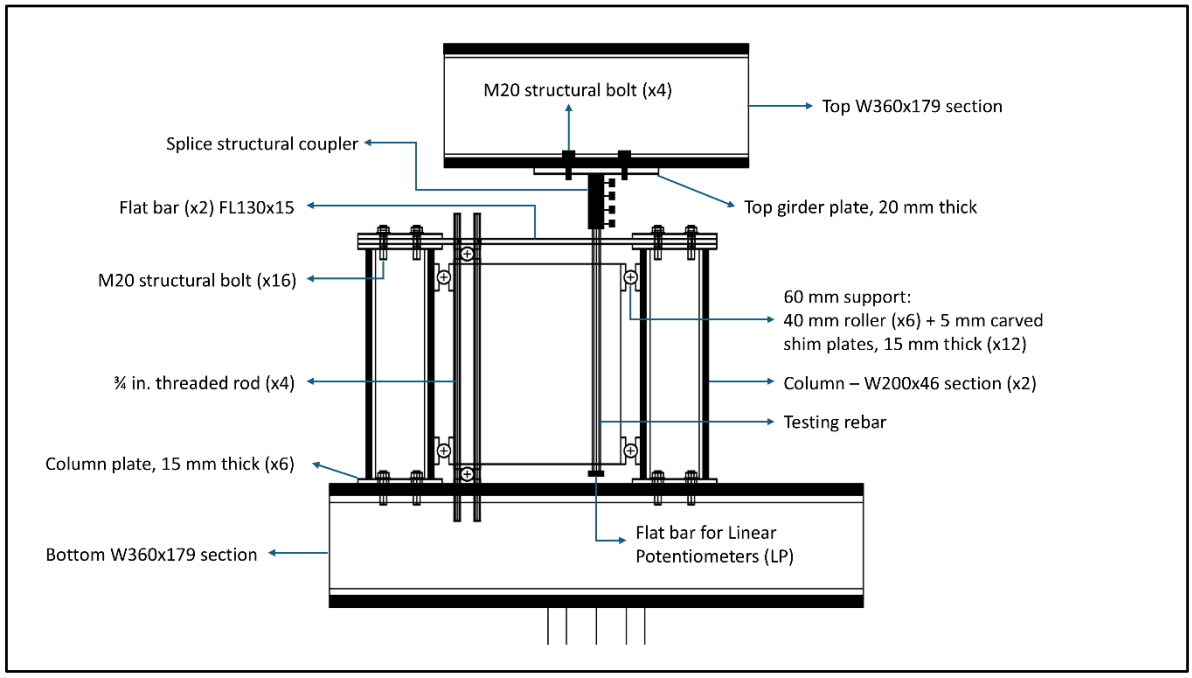

Figure 4-9: Beam-end testing frame conceptualization.

For the top section, structural *D250SCA Bar Lock Couplers* were welded to a 20 mm thick steel plate, which in turn was bolted to the top girder to provide the connection to the load cell. These couplers consist of a thick-walled tube with serrated grips, which help lock the rebar once the shear bolts are tightened. As appreciated in Figure 4-10, the original 15M coupler was shorter (11.43 cm or 4.5 in.) and had less bolts (only 4) than the 25M one, whose length was 25.91 cm (10.2 in.) and had 8 bolts. Therefore, an extension by welding an additional 8-bolt 15M coupler was made to provide enough redundancy and reduce the sliding risk. Meanwhile, the 25M coupler was used without additional modifications.

The original lock shear bolts were used interspersed with machined Class 12.9 bolts, with the 15M and 25M couplers requiring M12 and M16 bolts, respectively. Figure 4-11 presents a 3D visualization of the setup concept and the real-life implementation. For the

latter, extra shim plates were needed for the supports to make the final adjustments due to the variations in the beam-ends' dimensions.

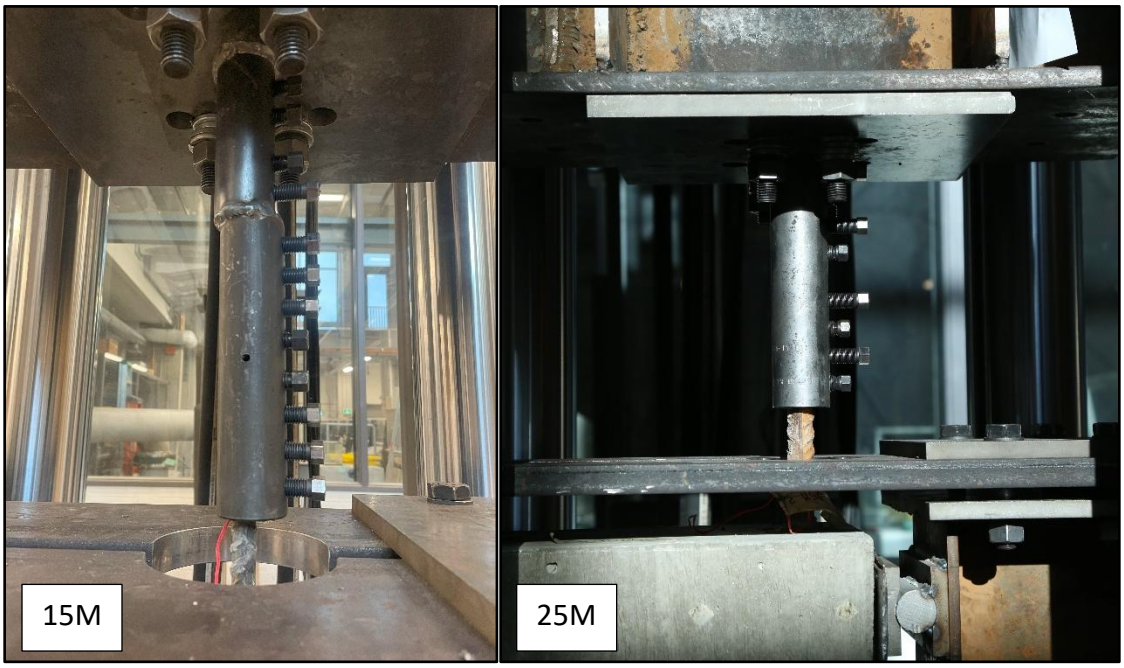

Figure 4-10: Structural splice couplers for beam-end tests (15M v 25M).

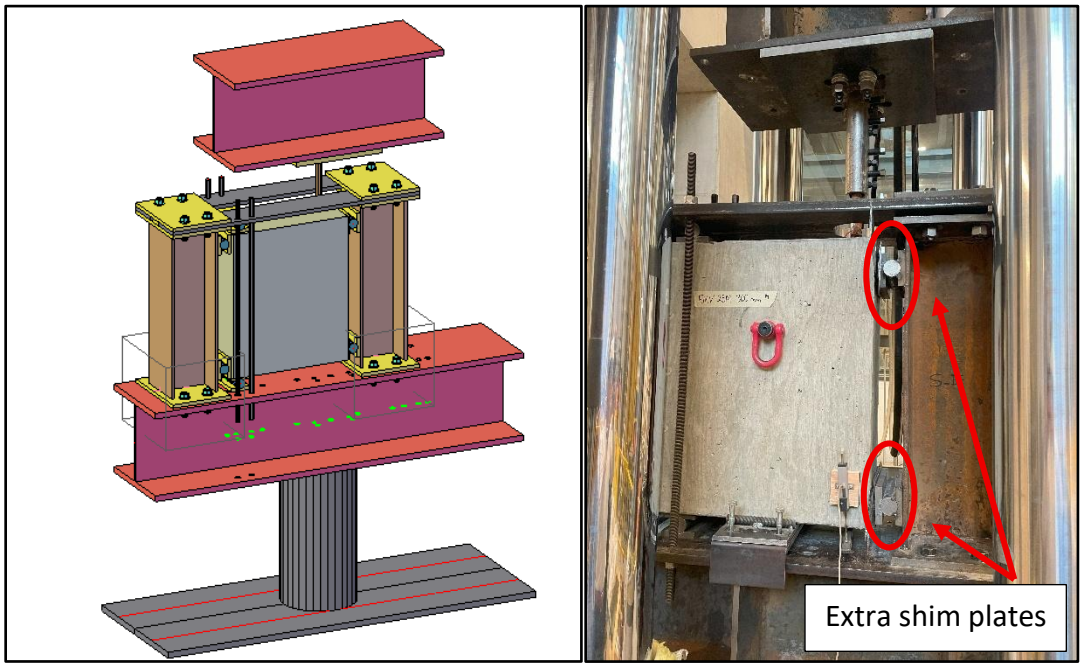

Figure 4-11: Beam-end 3D setup concept and real-life implementation.

4.3.2. Instrumentation

To measure the strain development in the embedded section and on the loaded end of the rebar, two sets of strain gauges were used (Figure 4-12). The first set was comprised of general use strain gauges, with three of them placed on the rebar surface in the embedded section, and one extra placed on the rebar but outside the concrete. The second set corresponded to a single mold strain gauge, which has the advantage of being directly placed into the concrete without needing to be glued to a surface. In consequence, this arrangement allowed the strain measurement on both materials.

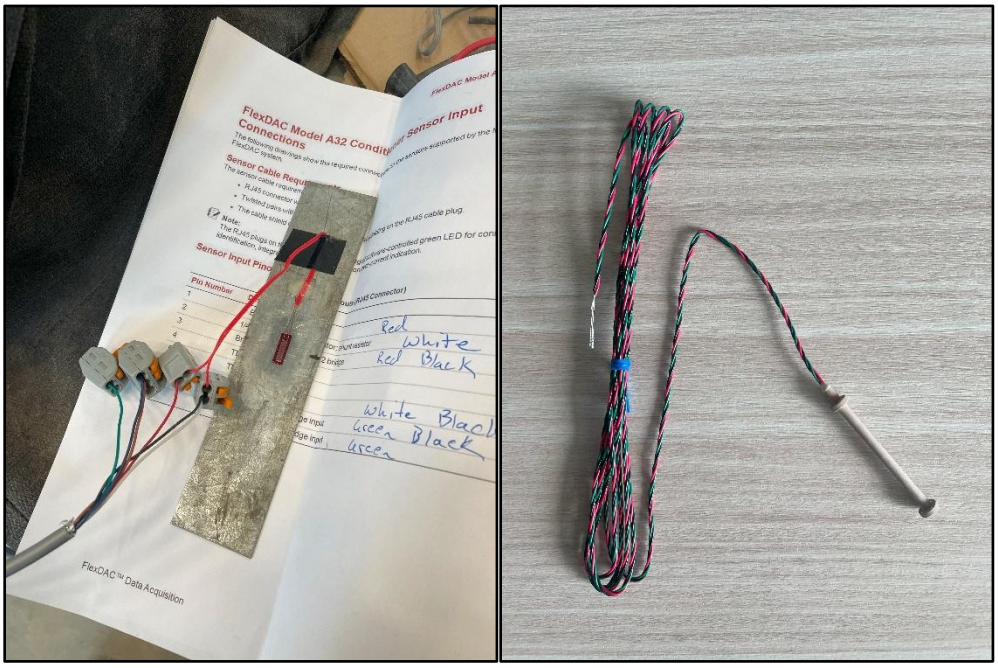

Figure 4-12: General use v mold strain gauges.

The positioning of each strain gauge is presented in Figure 4-13. As observed, the position does not depend on the bar size but on the embedded section. The installation of the general use strain gauges required the grinding of the rebars' surface (specifically between the ribs) for them to be glued, and a coating layer with a protective tape to isolate and waterproof them. This process was made with care to avoid a greater surface

intervention (Figure 4-14). Additionally, the mold strain gauge (or plastic strain gauge) was placed in the middle of the embedded section and was strapped to the rebar.

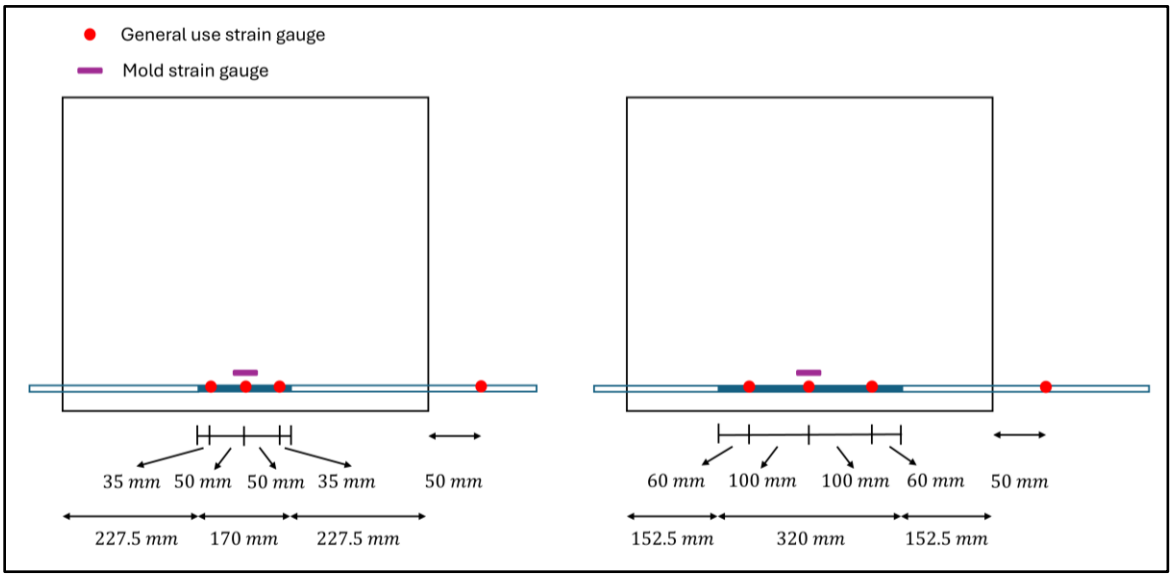

Figure 4-13: Strain gauge allocation for the testing rebars.

Figure 4-14: General use strain gauge installation (cables strapped for transportation).

The measurement of the free-end slip of the rebars was obtained by using two linear potentiometers (LPs) with a 50 mm range and an independent linearity of 0.15%, whose location in the testing frame is seen in Figure 4-9. The clearance between the bottom girder and the specimen was 60 mm; therefore, their installation required the glueing of two wood pieces on each side of the beam-end, to which the LPs were respectively screwed, as shown in Figure 4-15. The connection to the free end of the rebar was made through a small flat bar, which had a welded fitting ring that could be screwed to the rebar. Due to the differences in the bar size, two flat bar-and-ring combinations were used.

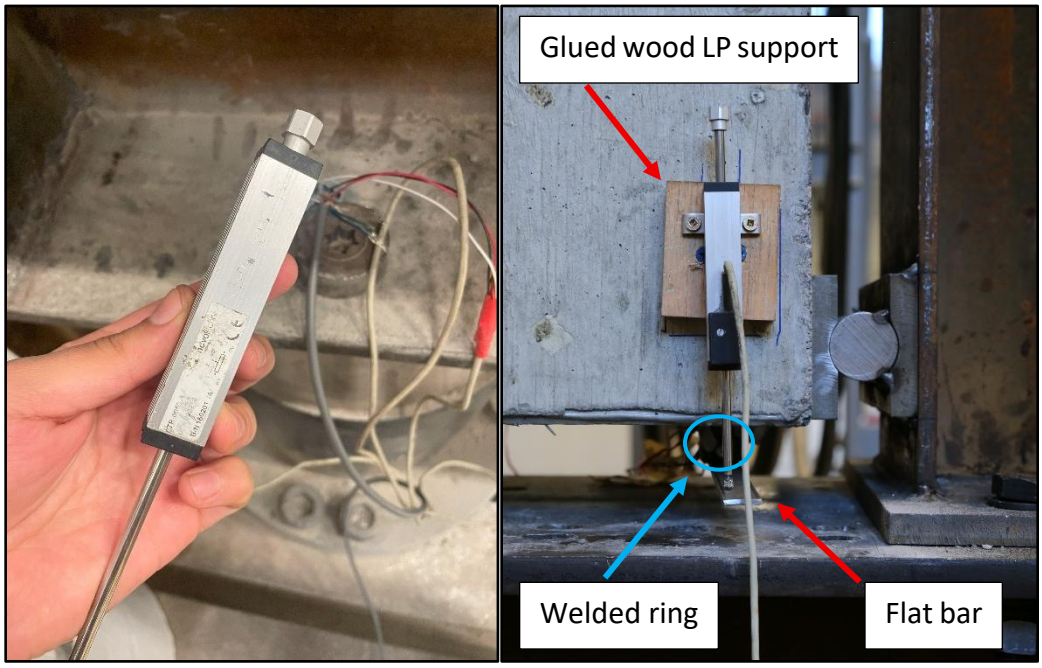

Figure 4-15: Linear potentiometer and placement on the beam-end.

4.4. Loading protocol

4.4.1. Steel rebar tests

Before defining the deformation steps of the loading protocol, both rebars were uniaxially tested in tension to determine their respective stress-strain curves, which were then compared to the nominal properties used in the design phase. These tests followed the requirements of CSA G30 (CSA Group, 2021) and Table 4-6 presents the respective

strains and stresses at four points: yielding plateau, strain hardening, ultimate, and maximum. On the other hand, Figure 4-16 presents the stress-strain curves of both rebars.

Table 4-6: Stress-strain of reinforcing bars at key sections.

	Strain (ε) [mm/mm]				Stress (σ) [MPa]			
Bar	ε_{yp}	ε_{sh}	ε_{u}	ε_{m}	σ_{yp}	σ_{sh}	σ_{u}	σ_{m}
15M	0.002	0.020	0.139	0.178	430.32	431.74	575.35	455.57
25M	0.003	0.016	0.116	0.179	457.07	455.01	611.57	573.05

Where the details of each region are:

- ε_{yp} / σ_{yp}: Strain/stress at the beginning of the yielding plateau
- ε_{sh} / σ_{sh}: Strain/stress at the beginning of the strain hardening region
- ε_{u} / σ_{u}: Strain/stress at the ultimate peak stress
- ε_{m} / σ_{m}: Strain/stress at the maximum elongation point before failure

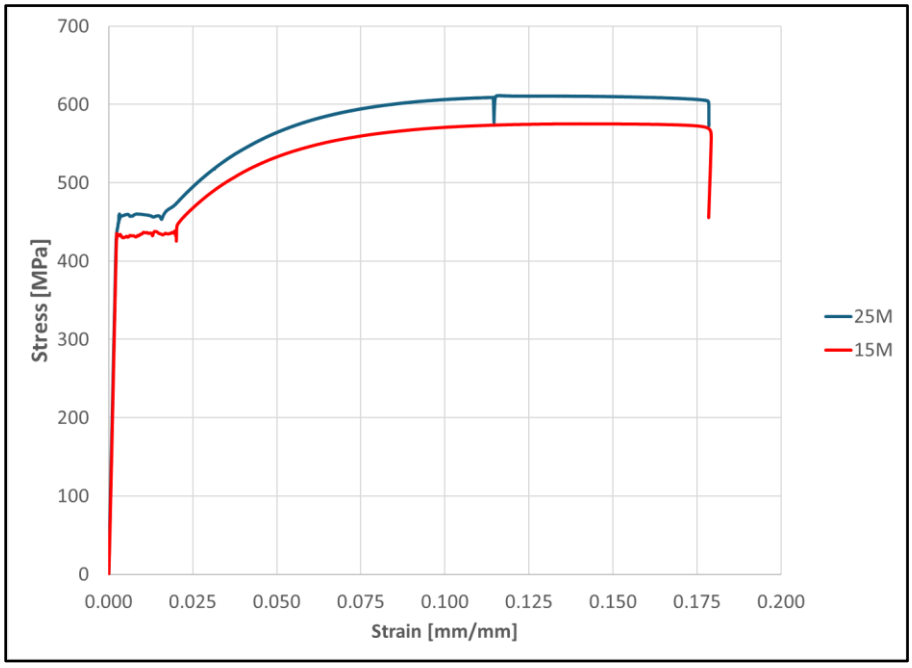

Figure 4-16: Stress-strain curves of reinforcing bars.

As observed, the shape and maximum elongation of both curves are similar, with the 25M rebar presenting higher stresses and a slightly shorter yielding plateau. To compute the yielding stress and the elastic modulus, the engineering 0.2% offset was applied, and the results are shown in Table 4-7.

Table 4-7: Rebar properties based on the 0.2% engineering offset.

Bar	ε_y [mm/mm]	σ_y [MPa]	E_c [GPa]	$\mu = \frac{\sigma_u}{\sigma_y}$	Elongation [%]
15M	0.00218	429.77	196.86	1.34	17.55%
25M	0.00234	459.52	192.40	1.33	17.55%

As appreciated, the yielding stress (σ_y), ductility ratio (μ), and elongation of both rebars are above the minimum of 400 MPa, 1.15 ratio, and 13% in within the tested region of 200 mm, respectively. In the case of the elastic modulus (E_c), both values are slightly inferior to the 200 GPa given by the nominal properties, but within the accepted tolerance.

4.4.2. Monotonic loading protocol

The ASTM A944 requirement for beam-ends tested under uniaxial tension is to load them at a rate that can lead to failure between 3 – 10 min after started the test. However, a more conservative approach based on previous research (Butler et al., 2011) was taken to capture the bond behaviour in more detail at all stages. It was decided to perform displacement-controlled tests at a fixed rate of 1 mm/min until experiencing either a splitting failure, a pullout failure, or a bar rupture.

4.4.3. Cyclic loading protocol

For the development of the cyclic testing protocol, the deformation history for tests under uniaxial loading reversals proposed by ACI 374.2R was considered (ACI, 2013). This loading protocol is deformation-controlled, and two or three cycles per deformation step are recommended to capture the degradation effects, with two cycles recommended for cases where high degradation is expected. The deformation steps are based on the yielding

of the specimen, where the elastic section is generally captured with a single step at half of the expected yielding point, whereas the inelastic region steps are yielding multiples.

Given the design of the beam-ends, where the embedded section of all three combinations should lead to either a partial or full bar development, it was decided to expand the deformation steps within the elastic region, and then progressively increase them after the yielding until reaching the ultimate bond or bar failure. The number of cycles per step was fixed at three, which is common for when gradual degradation is expected.

The effective deformation steps were computed based on the results of the monotonic tests, the failure mechanism, and the nominal properties of the rebars, meaning a yielding strain (ε_y) of 0.002 and a yielding stress (f_y) of 400 MPa. Since the tests were deformation-controlled, and the actuator readings were coming in a load v displacement format, the associated yielding loads of each rebar were necessary. Since the stroke displacement does not differentiate the slack or relative movement, the 15M and 25M beam-ends made with the ACI mix were used for calibration since the were made with conventional concrete and allowed the estimation of the required actuator displacement to reach the bar yielding.

In the case of the 15M, the monotonic test showed bar yielding due to the plateau formation; therefore, once the slack was removed, the load and associated displacement were divided into five deformation steps, which were multiples of the yielding stress, or yield factor (Φ) for the purposes of this loading protocol. On the other hand, the 25M beam-end failed before reaching the yielding plateau. For this case, to obtain the deformation steps, the peak load was compared to the expected nominal yielding load, and then an estimation was made to determine the actuator displacement at which the rebar would have yielded. Once this value was known, the load v displacement curve (with the slack removed) was divided by five to obtain the desired deformation steps.

Given the timeframe and personnel availability for the testing program, it was decided to keep the testing of each step to a fixed duration of twenty minutes. As a result, the loading rate was set to increase with each deformation step. Table 4-8 presents the deformation limits (Δ) and displacement rates ($\dot{\Delta}$) for the chosen reinforcement at each deformation step. An immediate difference can be appreciated when analyzing the displacement required for each rebar for the same yield factor, which is mainly attributed to the higher slack of the 25M rebar test.

Table 4-8: Unidirectional loading reversals parameters.

Step	Cycles	Yield Factor (Φ)	Δ_{15M} [mm]	$\dot{\Delta}_{15M}$ [mm/min]	Δ_{25M} [mm]	$\dot{\Delta}_{25M}$ [mm/min]
Φ_1	3	0.20	2.50	1.50	4.00	2.40
Φ_2	3	0.40	5.00	3.00	8.50	5.10
Φ_3	3	0.60	7.50	4.50	12.50	7.50
Φ_4	3	0.80	10.00	6.00	17.00	10.20
Φ_5	3	1.00	12.50	7.50	21.00	12.60
Φ_6	3	1.50	18.50	11.10	32.00	19.20
Φ_7	3	2.00	24.50	14.70	42.50	25.50
Φ_8	3	3.00	36.50	21.90	64.00	38.40
Φ_9	3	4.00	48.50	29.10	85.00	51.00
Φ_{10}	3	5.00	61.00	36.60	107.00	64.20

The reversed cyclic loading protocol is presented in Figure 4-17. As described, the first 15 cycles are within the elastic region, and after yielding the deformation steps increase by one unit. However, given the beam-end design did not include transverse reinforcement, and when considering the free length of the bar outside of the embedded region, it was anticipated that compressive loading might have led to premature failure.

Therefore, a second protocol was prepared with the same loading rates but for tension cycles only (Figure 4-18). To maintain the same loading rates, the total duration of each step was reduced from 20 to 10 minutes. For each beam-end combination, one cyclic specimen was selected and subjected to the reversed cyclic loading protocol. If, after one or two cycles within the elastic region, buckling or bar bending was observed, the test was

cancelled, and the tension cyclic loading protocol was applied instead. This aspect will be further commented on the results and discussion sections.

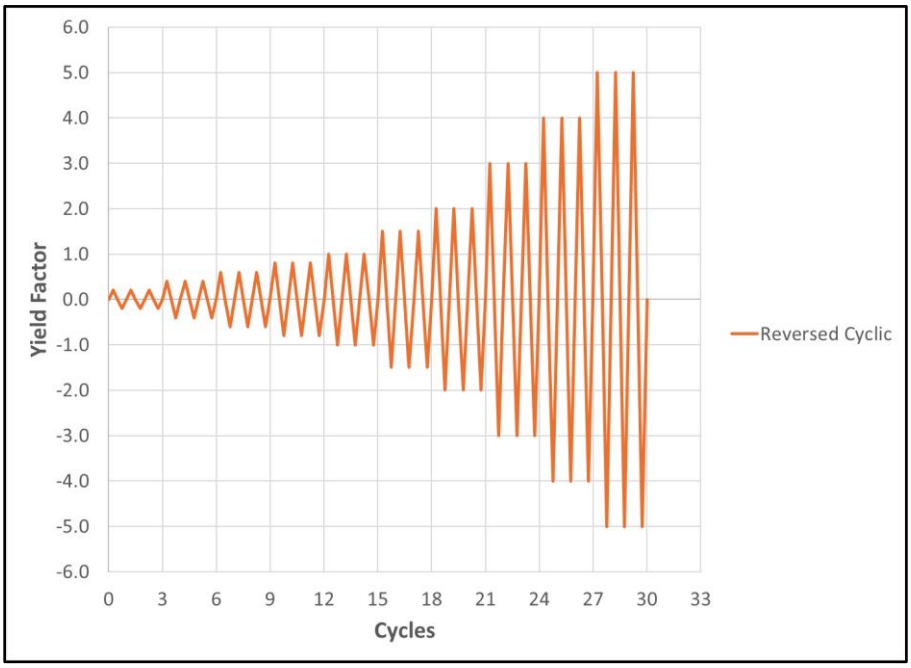

Figure 4-17: Reversed cyclic loading protocol for beam-ends.

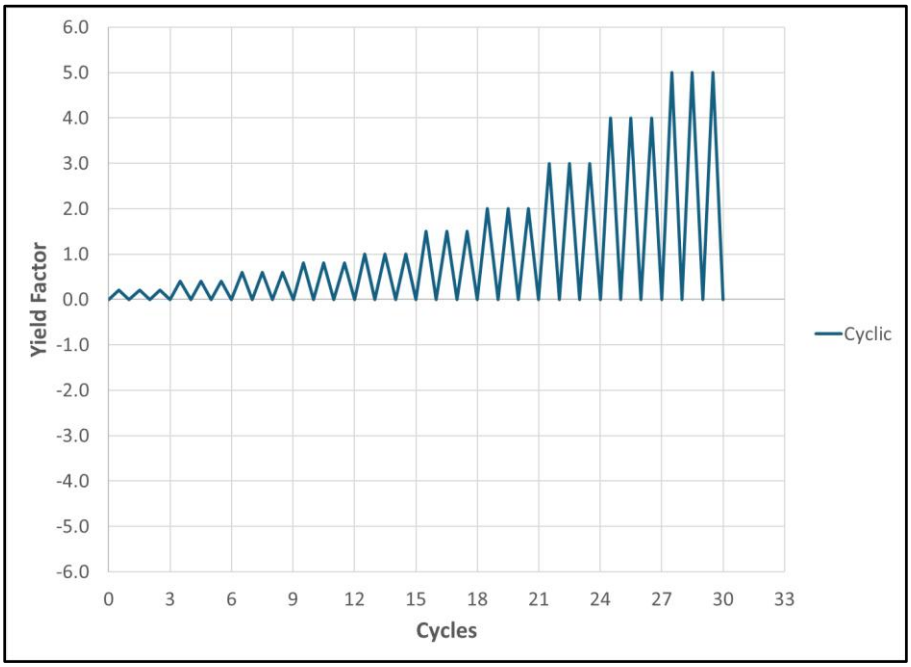

Figure 4-18: Tension cyclic loading protocol for beam-ends.

4.5. Casting

The testing setup of the beam-ends required a tight geometry control, especially for the surfaces that were going to be in contact with the supports. Therefore, custom panels were cut and screwed to a series of external horizontal and vertical stiffeners, as shown in Figure 4-19. This design allowed the modularization of the interior panels, which on the shorter side were milled to allow the passing of the 15M and 25M rebars in their respective PVC sleeves (or bond breakers). Therefore, the moulds were suitable for all combinations, were easy to assemble, and any damaged piece was easily replaced with a spare part.

The support reinforcement containing the longitudinal stirrups was manually tied with plastic straps and tie wire to restrain the movement, especially when placing it inside the moulds before casting and when vibrating the concrete. Two pieces of rebar were horizontally tied to keep the form and tension, and one of them contained the coupling nuts (red circles on the right side of Figure 4-19) that were later used to lift the samples with the bridge crane, since the weight of each specimen was approximately 180 kg.

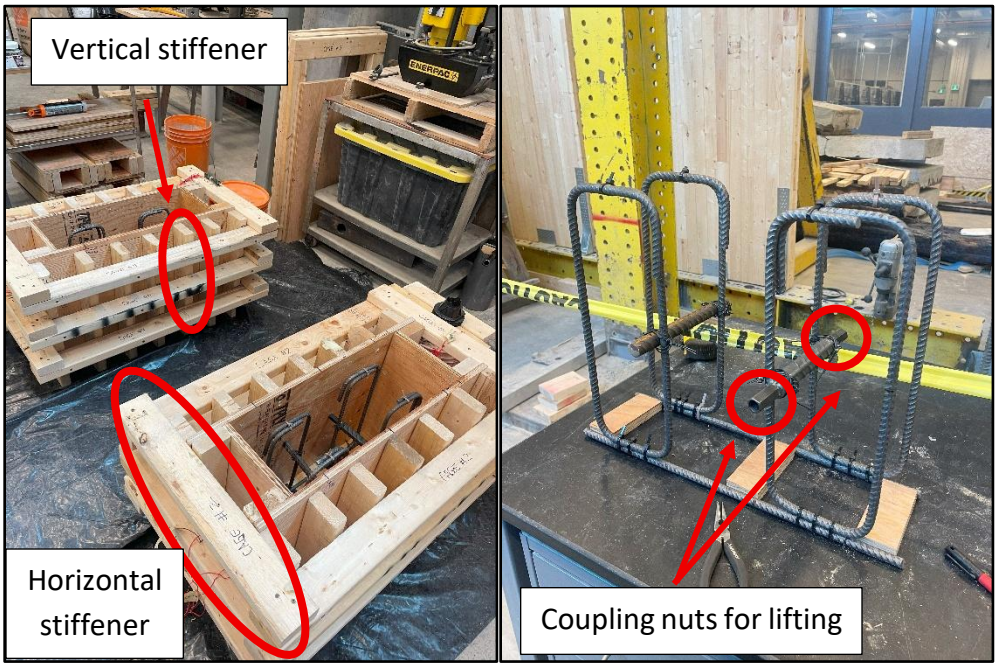

Figure 4-19: Beam-end moulds and support reinforcement.

Once the interior panels were cleaned, assembled and greased, the testing rebars (with the strain gauges already installed) and their respective PVC sleeves were placed first since they came in and out of the short panels. After the positioning of the testing rebar was fixed, the mold strain gauge was strapped on top of the middle reinforcing bar strain gauge. Finally, the support reinforcement was placed and fixed with rebar chairs before the final casting. Figure 4-20 shows the assembly of the 15M rebars with 170 mm and 320 mm of embedment, respectively.

Meanwhile, Figure 4-21 presents the assembly of the 25M rebars and how the transverse rebars of the support reinforcement prevented further movement during the casting due to their direct contact with the side panels. As mentioned in the previous chapter, the batching size for each specimen was 100 litres, and the moulds allowed the casting of a maximum of four specimens within a single day. Therefore, five batching days were required to complete the 18 beam-ends.

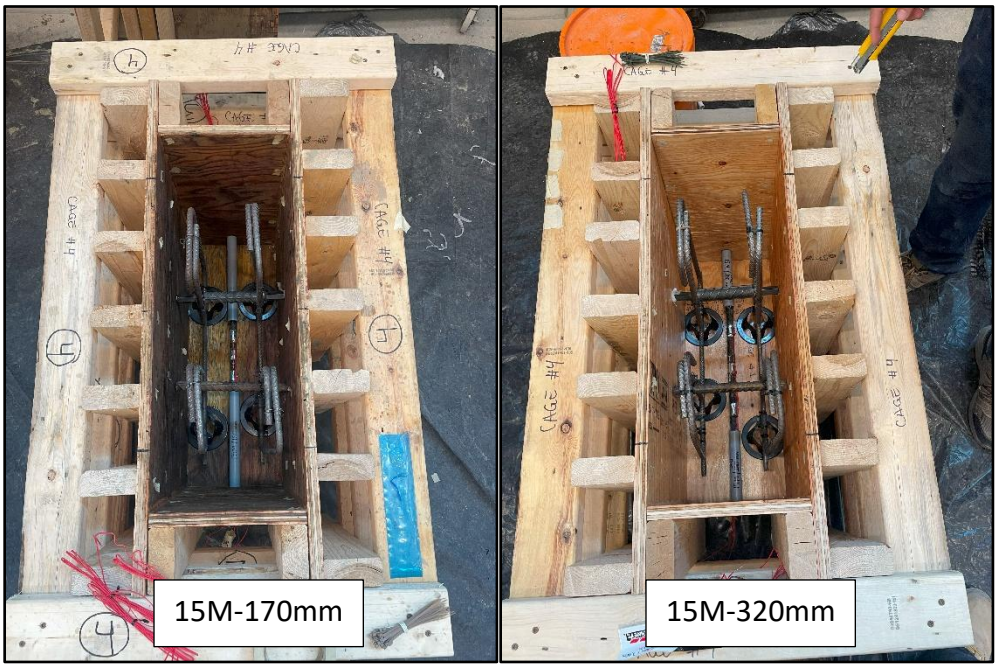

Figure 4-20: 15M reinforcing steel assembly of beam-end specimens.

Figure 4-21: 25M reinforcing steel assembly of beam-end specimens.

Figure 4-22: Concrete mixing of a 100-litre batch.

Figure 4-22 shows the process that immediately followed the mixing of the concrete. Once the last spinning cycle was completed, the concrete was dumped into a wheelbarrow,

the sides of the machine were scrapped to recover as much fresh paste as possible, and then the concrete was manually remixed with shovels before casting the specimens.

The casting of each specimen was made in two layers. The first layer reached almost 50% of the beam-end's height, followed by a first round of internal vibration. Then, the second layer was dumped until reaching the final height, and internal and external vibration were applied (Figure 4-23) to ensure a good concrete compaction and distribution across the entire volume. Finally, the top surface was finished by hand with the help of trowels, as observed in Figure 4-24.

After the casting completion, each beam-end was sealed and wrapped with polyethylene to keep its moisture until the disassembly (Figure 4-25). The moulds were removed after two days, and the samples were inspected before moving them to the testing area. Soon after, the casting area and the moulds were cleaned, and the same process was repeated throughout the five batching days until completing the last beam-end.

Figure 4-23: Beam-end internal and external vibration.

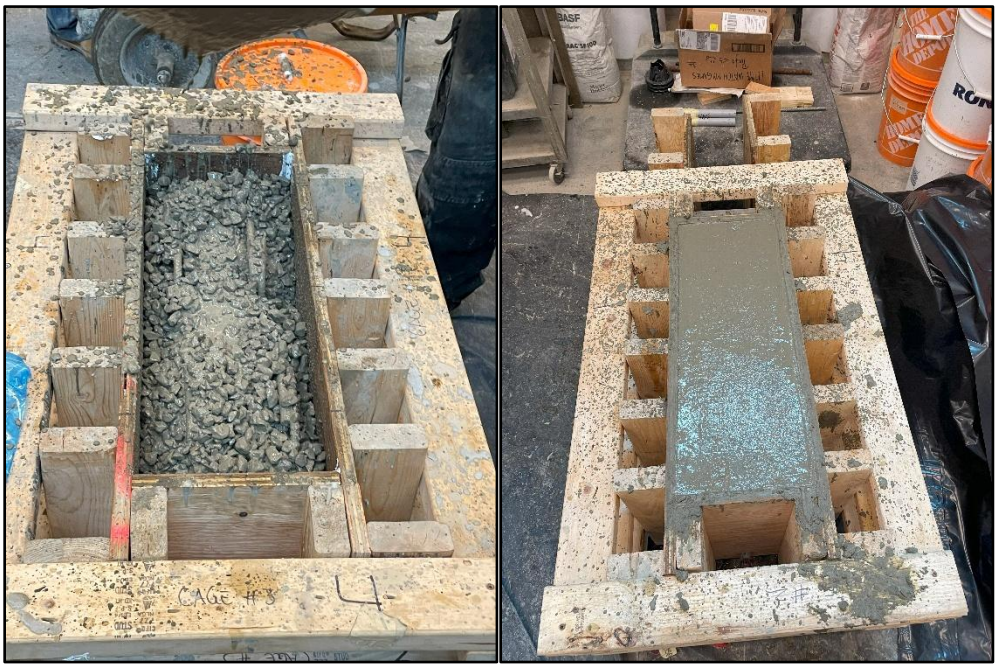

Figure 4-24: Beam-end casting and finishing.

Figure 4-25: Beam-end before and after mould disassembly.

All beam-ends were moist cured until reaching 28 days of age. Figure 4-26 shows their placement in the testing area, where all strain gauges were tested for voltage to check they

were not damaged in the process, as well as their cables. Once the testing apparatus was fitted to the MTS machine, each beam-end was placed with the help of the bridge crane and a custom-made dolly cart.

Figure 4-26: Beam-ends placing in the testing area.

4.6. Specimen testing

4.6.1. Assembly

For each speciment test, the assembly required the left column to be permanently bolted to the bottom girder. A custom-made dolly cart (showed in red in Figure 4-27) was used to slide the specimens into the test frame until they reached the left supports. Finally, the right column was put in its position and bolted to the bottom girder.

The next step consisted of bringing down the top girder which had the bar lock coupler. This stage required caution to ensure proper alignment. Once these adjusments were finalized, the coupler was brought to its final position where the bar was ready to be bolted.

With both columns in their final position and the bar alignment completed, the top left support, flat bars, top plates, and threaded rods were subsequently installed.

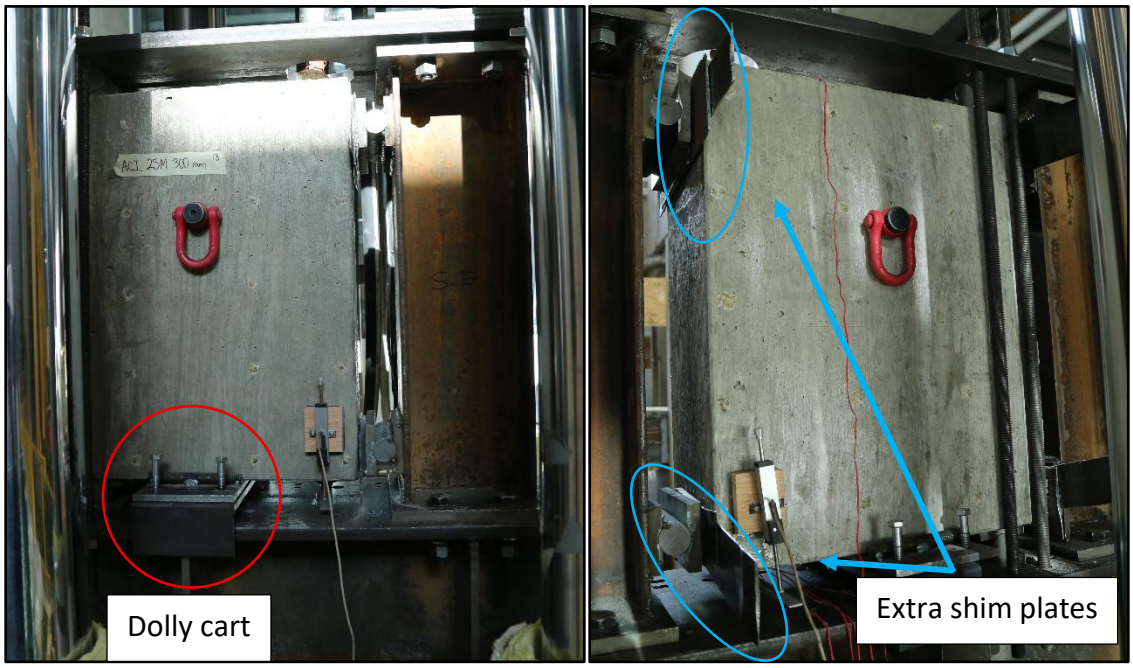

Figure 4-27: Specimen test assembly, Pt. I.

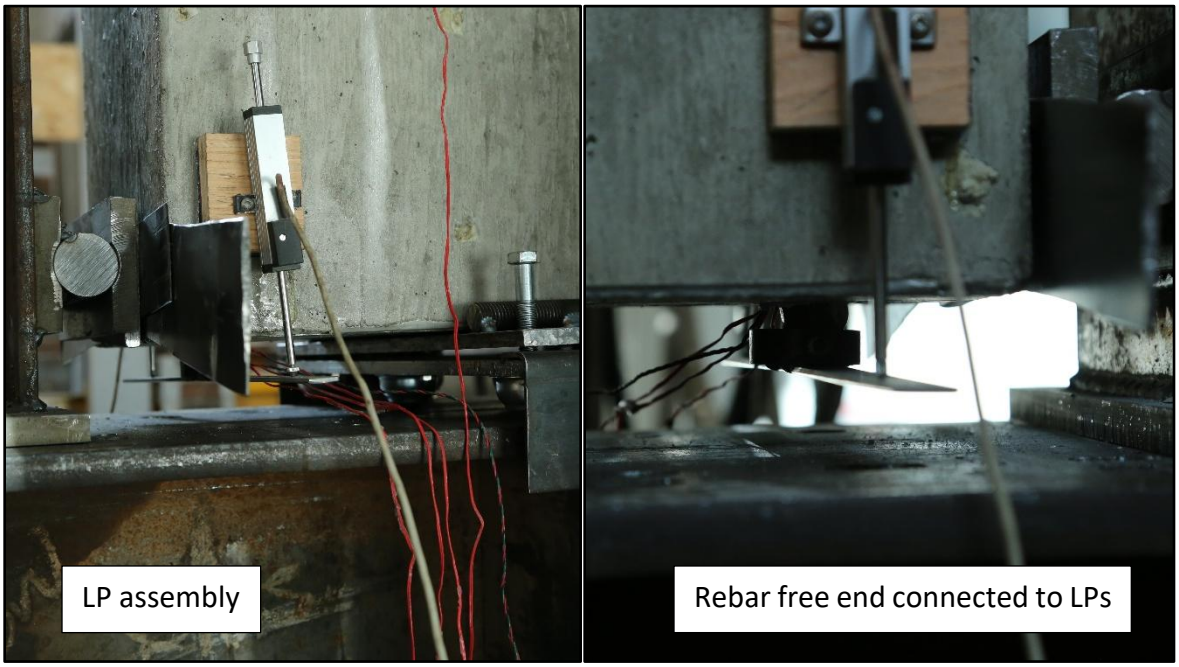

Figure 4-28: Specimen test assembly, Pt. II.

Each specimen had small variations in geometry; therefore, shim plates were used to make minor adjustments to ensure a tight fit, as shown in light blue in Figure 4-27. Once the specimen was finally locked, the bar was bolted to the coupler and the strain gauges were connected to the data acquisition system. The last step consisted of installing the linear potentiometers, or LPs. As observed in Figure 4-28, the connection was made through a small flat bar, which was screwed to the rebar using a welded custom ring (as previously detailed in Figure 4-15). Once the installation of the LPs was completed (including their vertical alignment), it was tested to ensure the flat bar would not fall. A general assembly view is presented in Figure 4-29.

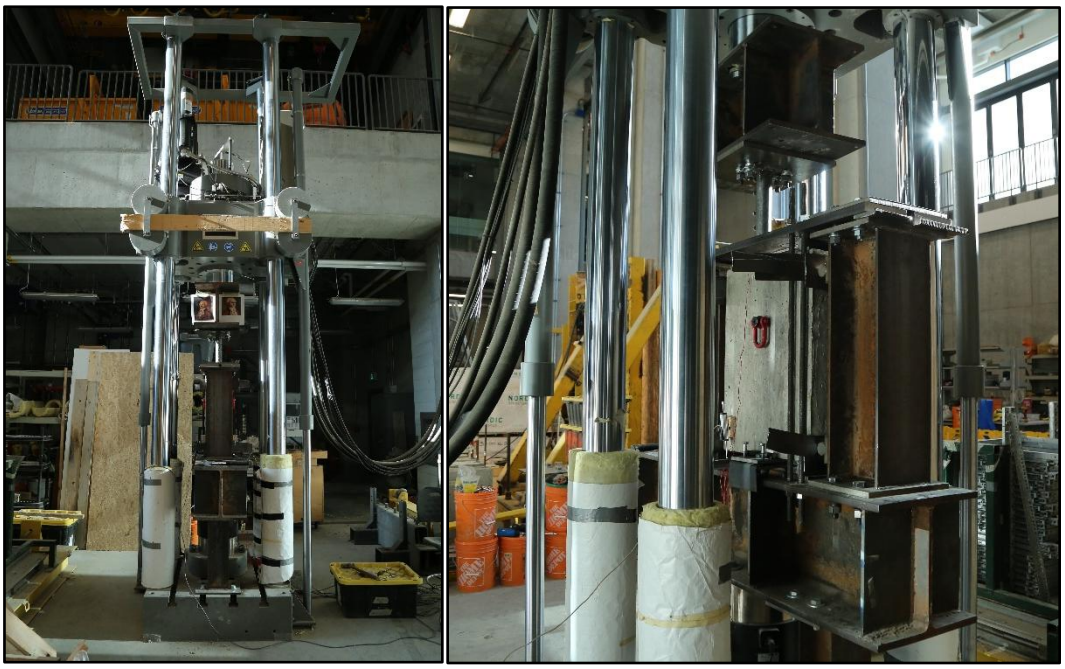

Figure 4-29: Specimen test assembly, Pt. III.

4.6.2. Test results – Load v Displacement

Throughout the testing stage, a few adjustments were made to correct issues that manifested once the test was running. As mentioned in the testing apparatus subsection, the initial 15M bar lock coupler only had space for 4 bolts, and the machined Class 12.9 bolts proved to be of inferior quality to the original shear bolts that came with the coupler.

The tips of the machined bolts were prone to deformations in the tightening process, even when controlling the tension with a torque ratchet.

Therefore, to avoid sliding issues, the 15M coupler was enlarged by welding another 8-bolt 15M coupler, and interspersed bolts (with the original bolts accounting for at least 50% of the total) were used. A ratchet was necessary to ensure a tight fit without shearing the original bolts. This new arrangement provided enough redundancy for the 15M specimens, but the 25M couplers also experienced sliding in the first two monotonic tests. Hence, the original bolts were used for all the remaining 25M specimens.

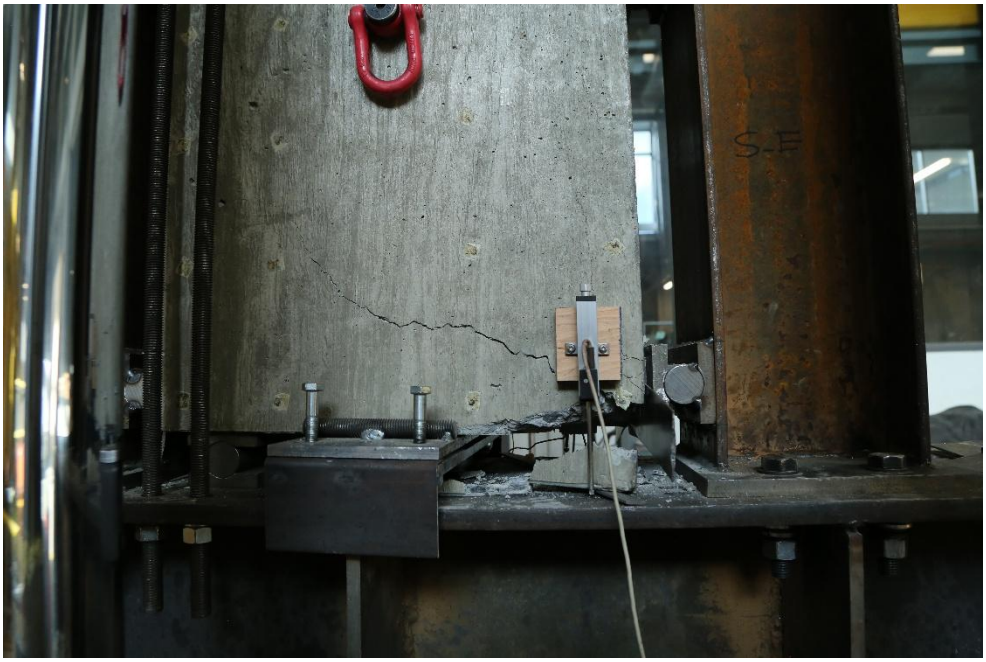

Figure 4-30: Crack induced by shim plates in the bottom right support.

The second issue came with the development of cracks near the bottom right support in some of the specimens, as appreciated in Figure 4-30. These cracks originated because of the shim plates installation to ensure a tight fit, which required hammering, and manifested only after initiated the tests. In many cases, shim plates of different thicknesses were needed to fill the gaps between the specimen and the support. Without a tight fit, the specimen tended to slide and rotate.

Nevertheless, this unintended effect impacted the readings of the LPs due to the cracking path. Likewise, the sliding and rotation tendencies were exacerbated with the expansion of these cracks. Therefore, to avoid these effects as much as possible, shim plates adjustments were made as the tests progressed to limit the movement of the specimen.

Finally, the third issue came with the fully reversed cyclic loading protocol. Even when the specimen's movement was well restricted, the loading levels were low, and the free section of the rebar in between the specimen's edge and the coupler was less than 100 mm, the rebars tended to bend/buckle, as shown in Figure 4-31.

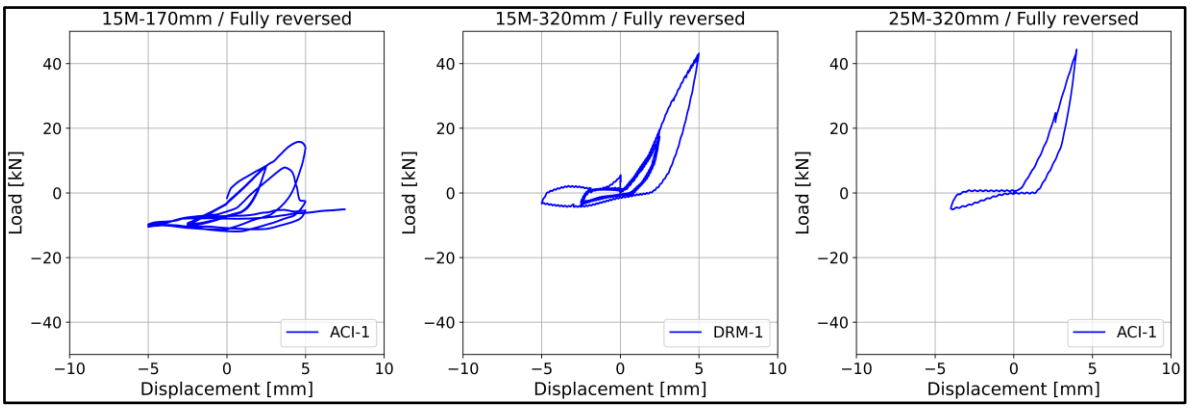

Figure 4-31: Fully reversed loading protocol results.

The tendency for all three specimen combinations was the same: the initial loading in tension showed no issues, whilst compression loading led to premature buckling/bending at lower load levels. Given the loading levels were still below the yielding of the rebars under normal conditions, and to guarantee reliable results in the inelastic region, it was decided to cancel the fully reversed loading protocol, and all specimens were tested according to the tension cyclic loading protocol instead.

The monotonic and cyclic loading versus the actuator displacement results (load cell readings) for each specimen combination, mix design, and test number are presented in Figure 4-32, Figure 4-33, and Figure 4-34, respectively.

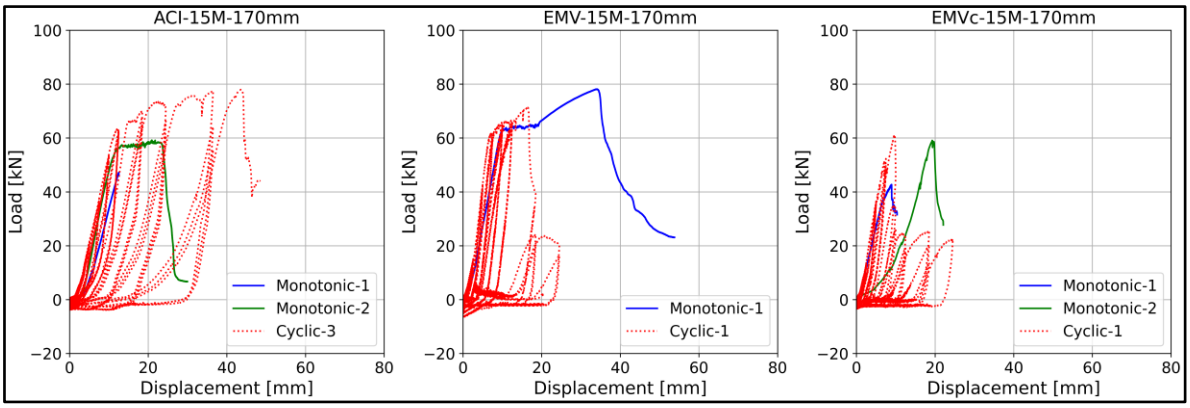

Figure 4-32: Load v Displacement, 15M – 170 mm per mix.

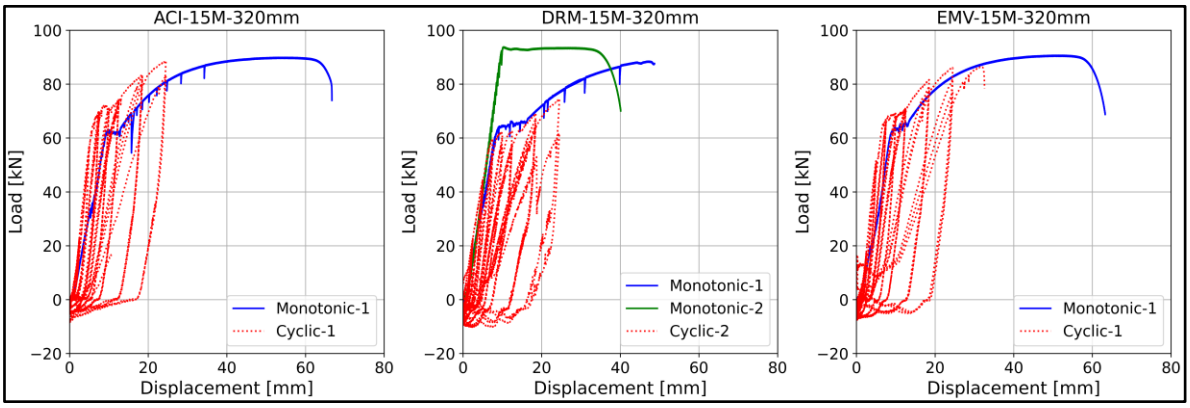

Figure 4-33: Load v Displacement, 15M – 320 mm per mix.

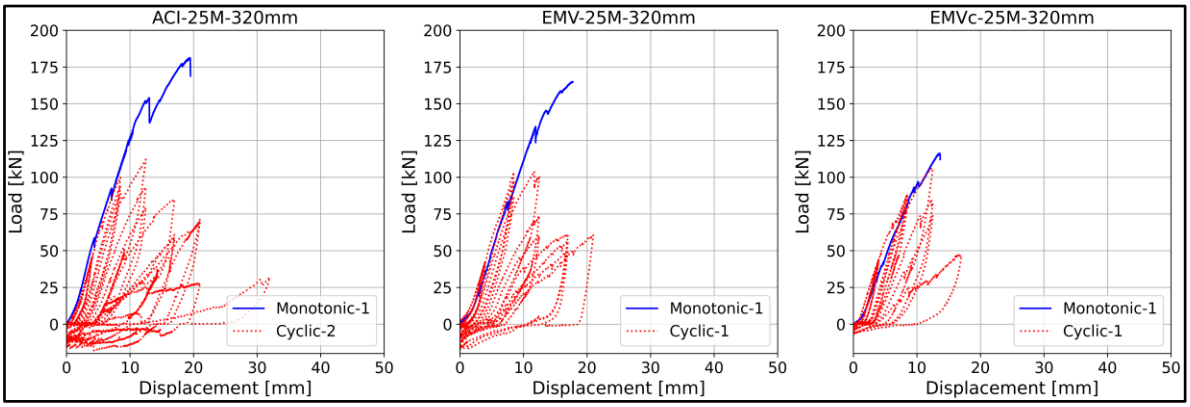

Figure 4-34: Load v Displacement, 25M – 320 mm per mix.

As appreciated in Figure 4-32, both ACI and EMV samples with 170 mm embedment suffered a bond failure in or after the yielding region. The ACI combination presents two

monotonic results because the test was stopped before reaching the yielding point on the first testing day, and the second one is the complete test that was restarted from zero the next day. In the case of the EMVc samples, the failure occurred before the yielding of the rebar and required two tests. The first run had to be stopped due to the quick expansion of the cracks formed at the bottom support. After a check-up and with the specimen fixed once again, a second test was performed until reaching the bond failure.

In the case of the 15M – 320 mm specimens, Figure 4-33 shows similar shapes for both monotonic and cyclic loading. All monotonic samples suffered a bar rupture (DRM test had to be restarted because the coupler slid, hence the two readings). The failure of the cyclic EMV specimen was due to a bar rupture, but at a lower displacement than the monotonic tests. The ACI beam-end was following the same pattern, but the welding on the top plate where the coupler was attached failed before reaching the bar failure. On the other hand, the cyclic DRM specimen suffered a bond failure in the strain hardening region. The details and nature of these failures will be discussed in the upcoming section.

Finally, the 25M – 320 mm specimens are presented in Figure 4-34. The failure mechanism in all cases was a splitting failure before reaching the yielding of the rebar. In the monotonic tests, the ACI and EMV mixes presented similar results, although the latter suffered a coupler sliding towards the end, hence the differences in the peak load. Meanwhile, the cyclic tests showed a similar peak load for all samples, but with a faster degradation in the EMVc specimen.

Another perspective can be drawn when comparing the three combinations based on the loading protocol. As observed in Figure 4-35, the 170 mm of embedment length were enough to allow a bar development in the ACI and EMV mixes. A splitting failure took place in between the yielding plateau and the strain hardening region. The performance between these two mixes was deemed to be similar given the peak loads. However, the concrete

quality of the EMVc samples influenced the brittle pre-yielding failure, which was evident due to the number of observed cracks, as it will be showed in the next section.

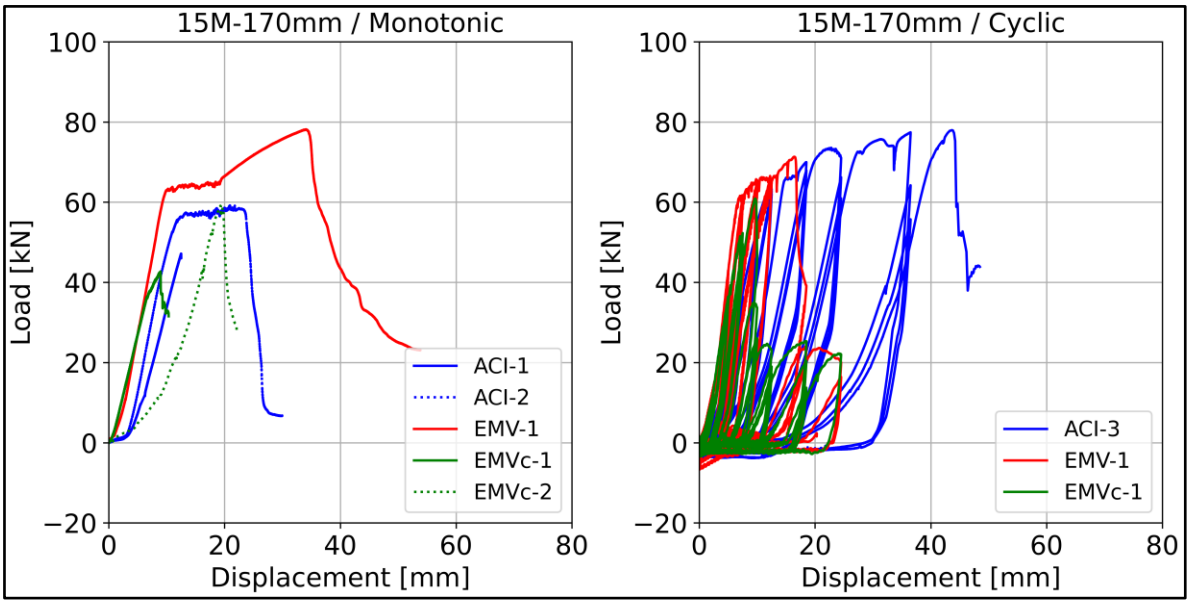

Figure 4-35: Load v Displacement, 15M – 170 mm per loading protocol.

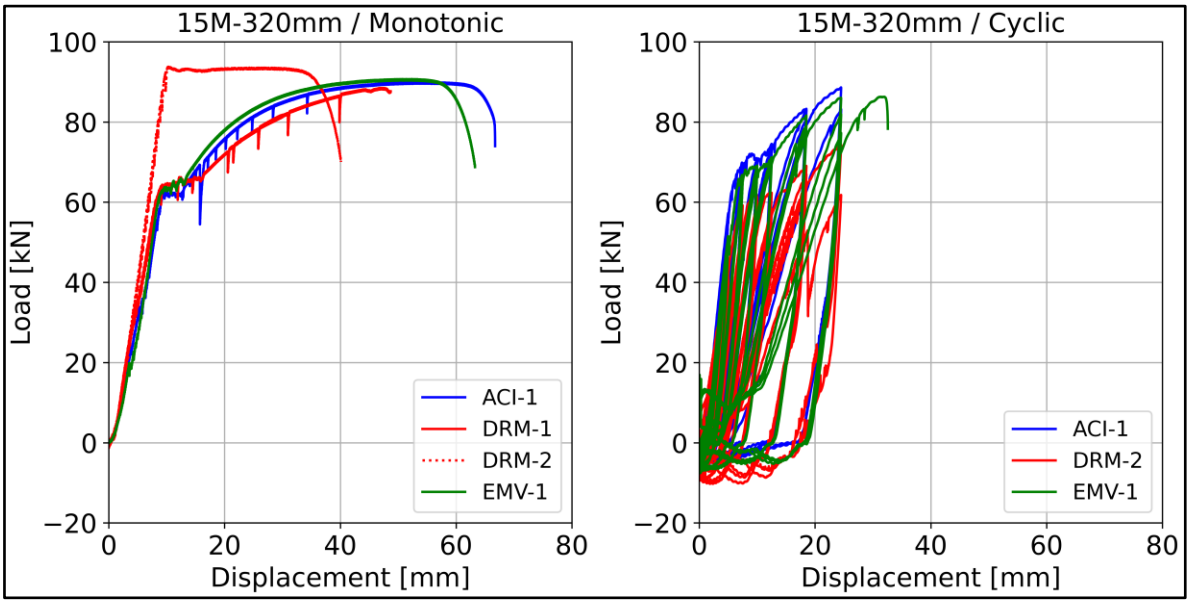

Figure 4-36: Load v Displacement, 15M – 320 mm per loading protocol.

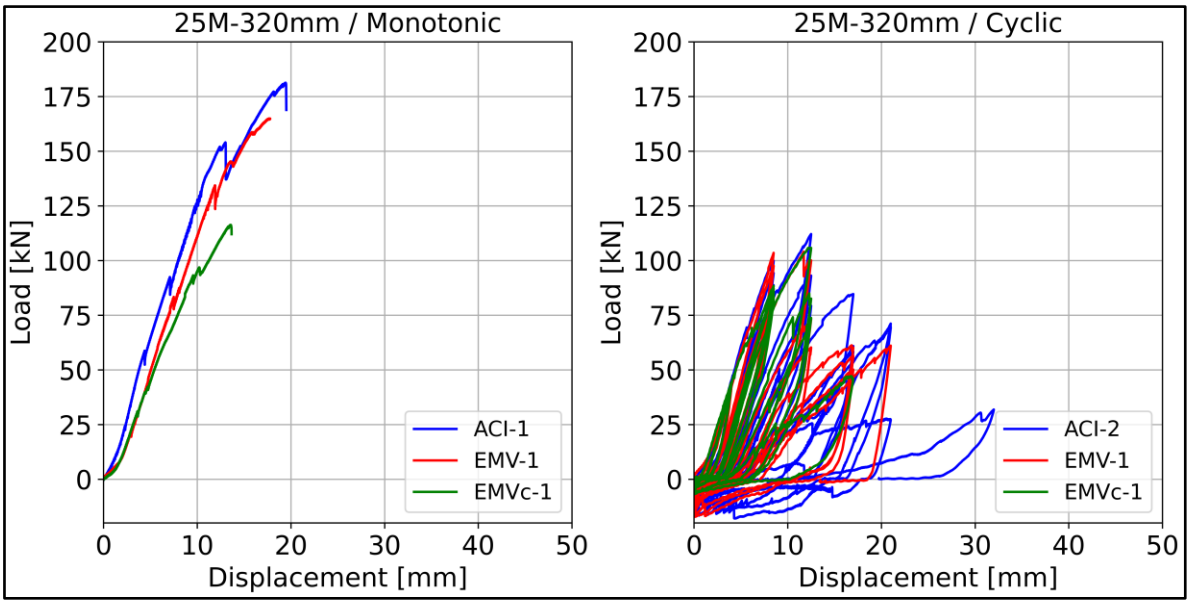

Figure 4-37: Load v Displacement, 25M – 320 mm per loading protocol.

An extra detail comes from the differences in the stroke displacement of the monotonic and cyclic tests, where the former presented longer readings. This effect is clear in Figure 4-36, which presents the 15M – 320 mm samples. The monotonic tests of all mixes ended up with a bar rupture. However, the same failure mechanism manifested in the cyclic test of the EMV sample, but with a lower overall stroke displacement. Possible causes that can explain are provided below:

- The accumulated damage in the cyclic tests, which was enhanced with three cycles per each deformation step.
- Deformation of the setup, which is associated to the slack and relative movement of the setup until the actuator started to effectively pull the rebar.
- Gripping issues, which are related to the bolts not being able to keep the rebar locked inside the coupler as the displacement kept increasing, thus inducing a coupler sliding.

These causes will be further commented in the discussion section. When comparing the overall performance between the 15M – 320 mm samples, the ACI and EMV mixes

performed similarly, with only minor differences in the loading peaks. In contrast, the DRM cyclic specimen showed a significant stiffness and capacity degradation, which is mainly due to the higher mortar content.

Figure 4-37 shows the same analysis but for the 25M – 320 mm specimens. In this case, there are no significant differences in the total displacement, which is attributed to the tests never leaving the elastic range. In terms of performance, the monotonic tests of the ACI and EMV samples were comparable, while the EMVc sample suffered from the same excessive cracking observed in the 15M – 170 mm specimen, which will be discussed later. In the case of the cyclic tests, the loading peaks across all three mix designs were similar, although the stiffness degradation rate when compared to the ACI mix was accelerated and noticeable for the EMVc and EMV specimens, respectively.

4.6.3. Test results – Scaling and strain profiles

Another detail observed in the load v displacement results is that, depending on the bar-embedment combination, the yielding plateaus and ultimate load peaks (in the cases where the rebar ruptured), for both monotonic and cyclic loading, were inferior to those obtained separately for the 15M and 25M rebar coupons, respectively. These differences can be better appreciated for each case in Table 4-9.

Given the failure mechanisms mentioned in the previous section, the load cell readings (located on the load frame of the machine) did not match the reference loads coming from the coupon tests at specific strain levels such as yielding. Even though the specimens were aligned to be on the centreline of the coupler, its welding to the top plate was not 100% vertical, thus creating a deviation angle. Once the tests started and the slack was removed, it was observed the bar was bending on the loaded end to align with the coupler inclination (Figure 4-38). It is believed that this effect could have influenced the readings by creating a uneven strain distribution. Therefore, it was decided to apply a scaling factor to correct them according to the coupon stress v strain references.

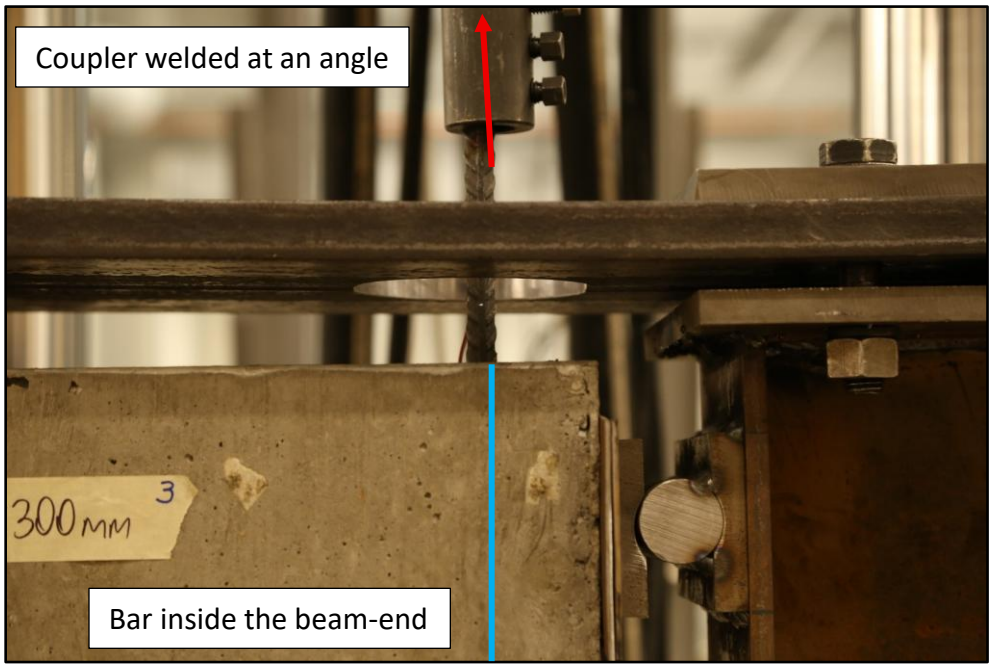

Figure 4-38: Bending in the loaded end of the rebar.

To compute the scaling factor for each case, the first stage consisted of locating the load peak and identifying the failure mechanism. Then, the next step was to focus on the yielding, strain hardening, and ultimate regions (if applicable) in the load v displacement results and extract their load readings. Once these values were obtained, they were compared against the references coming from the coupons and, based on the failure mechanism of each combination, it was determined whether the scaling factor had to be computed in relation to the yielding or ultimate load for better precision.

In the case of the cyclic tests, Dynamic Increasing Factors (DIF) were also considered. Since each deformation step had a fixed duration of 10 minutes, the respective loading rates ($\dot{\Delta}$) increased the further the test went, since higher displacements were achieved. This effect could have impacted the bar stresses by increasing them, especially for the 15M – 320 mm combination. The DIF can be computed for the yielding and/or ultimate load according to Eq. 4.6 – 1 and Eq. 4.6 – 2 (Malvar, 1998), respectively:

$$DIF - F_y = \left(\frac{\dot{\varepsilon}}{10^{-4}}\right)^{\alpha_{fy}} ; \alpha_{fy} = 0.074 - 0.040\left(\frac{f_y}{414}\right) \quad (4.6-1)$$

$$DIF - F_u = \left(\frac{\dot{\varepsilon}}{10^{-4}}\right)^{\alpha_{fu}} ; \alpha_{fu} = 0.019 - 0.009\left(\frac{f_y}{414}\right) \quad (4.6-2)$$

The α_{fy} and α_{fu} coefficients were empirically determined and are associated to the yielding and ultimate stresses, respectively. On the other hand, $\dot{\varepsilon}$ represents the strain rate of the cyclic protocol. To obtain this value for each deformation step, the associated loading rate, which is in mm/min and available in Table 4-8, was divided by the loaded section of the rebar (distance between the end of the embedment and the beginning of the coupler). Hence, it was possible to obtain the strain rate in sec^{-1} units and the associated DIF, which were applied to reduce the test load readings.

Table 4-9 presents a summary of the yielding (F_{yc}) and ultimate (F_{uc}) loads based on the results of the 15M and 25M coupon tests, and the associated DIF for the cyclic specimens. Besides these parameters, three experimental values (where applicable) were included, namely the yielding (F_y), ultimate (F_u), and test peak (F_p) loads. As appreciated, there is a noticeable difference between the experimental and the coupon values, with the 15M rebar bearing the greatest effects. When considering the 15M – 320 mm monotonic samples suffered a rebar fracture, the load should have reached at least 115 kN under normal conditions, but the tests showed readings around 90 kN. In consequence, it was decided to scale the load readings to reflect the known material properties.

For the 15M – 170 mm combination, the first ACI test run was stopped before reaching the yielding point. Therefore, the yielding values of the second run were used to calibrate the scaling factor. On the other hand, the EMVc specimens suffered bond failures before reaching the yielding plateau, as opposed to the ACI and EMV samples. Hence, the yielding values of the ACI sample were used as the main reference for the respective scaling factors.

In the case of the 15M – 320 mm combination, all monotonic samples reached the bar failure, although the DRM specimen needed two test runs. For this specific sample, the first run was stopped due to a coupler sliding (bolts failed to secure the lock) close to the ultimate loading region, meaning that when stopped, a residual deformation remained. In consequence, the rebar on the second run did not show a yielding plateau and went directly to the ultimate load, from which it kept elongating until its rupture.

Meanwhile, the 25M – 320 mm combination exclusively developed in the elastic region, and no plateaus were observed for any test regarding the protocol. Therefore, to compute the scaling factors, the readings were compared to the strain gauge readings and were estimated to be 10% lower than the reference yielding value.

Table 4-9: Differences between beam-end load readings and coupon tests.

Specimen	F_{yc} [kN]	F_y [kN]	DIF (F_y)	F_{uc} [kN]	F_u [kN]	DIF (F_u)	F_p [kN]
ACI-15M-170-M1	85.95	-	-	115.07	-	-	47.16
ACI-15M-170-M2	85.95	57.20	--	115.07	-	--	59.18
ACI-15M-170-C3	85.95	73.90	1.08	115.07	-	-	77.97
ACI-15M-320-M1	85.95	62.30	-	115.07	89.93	-	89.93
ACI-15M-320-C1	85.95	71.20	1.05	115.07	88.63	1.01	88.63
ACI-25M-320-M1	229.76	206.78	-	305.79	-	-	181.27
ACI-25M-320-C2	229.76	210.02	1.02	305.79	-	-	112.09
DRM-15M-320-M1	85.95	65.70	-	115.07	-	-	88.49
DRM-15M-320-M2	85.95	-	-	115.07	93.80	-	93.80
DRM-15M-320-C2	85.95	62.10	1.05	115.07	-	1.01	74.43
EMV-15M-170-M1	85.95	64.60	-	115.07	-	-	78.16
EMV-15M-170-C1	85.95	66.20	1.04	115.07	-	-	71.32
EMV-15M-320-M1	85.95	64.00	-	115.07	90.70	-	90.70
EMV-15M-320-C1	85.95	69.20	1.06	115.07	86.29	1.02	86.29
EMV-25M-320-M1	229.76	206.78	-	305.79	-	-	164.93
EMV-25M-320-C1	229.76	210.92	1.02	305.79	-	-	103.99
EMVc-15M-170-M1	85.95	-	-	115.07	-	-	42.71
EMVc-15M-170-M2	85.95	-	-	115.07	-	-	56.54
EMVc-15M-170-C1	85.95	-	1.02	115.07	-	-	60.90
EMVc-25M-320-M1	229.76	206.78	-	305.79	-	-	116.25
EMVc-25M-320-C1	229.76	210.92	1.02	305.79	-	-	105.77

Based on the comparisons between the readings and the reference values of Table 4-9, scaling factors for the yielding and ultimate loads were computed. In the case of the cyclic tests, the actuator readings were reduced using the associated DIF before dividing them by the reference value. Then, according to the failure mechanism of each sample, the respective scaling factor was chosen between the yielding and ultimate options. The scaling factors for each beam-end (in bold) and the scaled peak loads ($F_{p,s}$) are presented in Table 4-10. The 15M – 170 mm and 25M – 320 mm used the yielding scaling factor, whereas the the 15M – 320 mm combination was the only one where the ultimate scaling factor was considered given the bar rupture observed during the test runs.

Table 4-10: Beam-end scaling factors.

Specimen	F_p [kN]	Scale (F_y)	Scale (F_u)	$F_{p,s}$ [kN]
ACI-15M-170-M1	47.16	**0.67**	-	70.87
ACI-15M-170-M2	59.18	**0.67**	-	88.92
ACI-15M-170-C3	77.97	**0.80**	-	90.68
ACI-15M-320-M1	89.93	0.72	**0.78**	115.07
ACI-15M-320-C1	88.63	0.79	**0.76**	115.07
ACI-25M-320-M1	181.27	**0.90**	-	201.41
ACI-25M-320-C2	112.09	**0.89**	-	122.63
DRM-15M-320-M1	88.49	0.76	**0.82**	108.56
DRM-15M-320-M2	93.80	-	**0.82**	115.07
DRM-15M-320-C2	74.43	**0.69**	-	103.02
EMV-15M-170-M1	78.16	**0.75**	-	104.00
EMV-15M-170-C1	71.32	**0.74**	-	92.60
EMV-15M-320-M1	90.70	0.74	**0.79**	115.07
EMV-15M-320-C1	86.29	0.76	**0.74**	115.07
EMV-25M-320-M1	164.93	**0.90**	-	183.26
EMV-25M-320-C1	103.99	**0.90**	-	113.28
EMVc-15M-170-M1	42.71	**0.67**	-	64.18
EMVc-15M-170-M2	56.54	**0.67**	-	84.96
EMVc-15M-170-C1	60.90	**0.74**	-	80.62
EMVc-25M-320-M1	116.25	**0.90**	-	129.16
EMVc-25M-320-C1	105.77	**0.90**	-	115.22

One evident aspect in the factors of Table 4-10 is their non uniformity, they are the sum of three parameters:

- Bending effect
- Bar area reduction due to strain gauge installation
- DIF in the case of the cyclic tests

The effect of the DIF on the load readings was not major, as most cases required a 2% adjustment and only the ACI-15M-170mm specimen required an 8%. On the other hand, the strain gauge installation on the loaded-end of the rebar effectively reduced the cross section, 15% on average for the 15M rebar, and 10% for the 25M. Therefore, the rest of the scaling factor is accounted by bending effects, whose distribution presented the greatest variations throughout the tests.

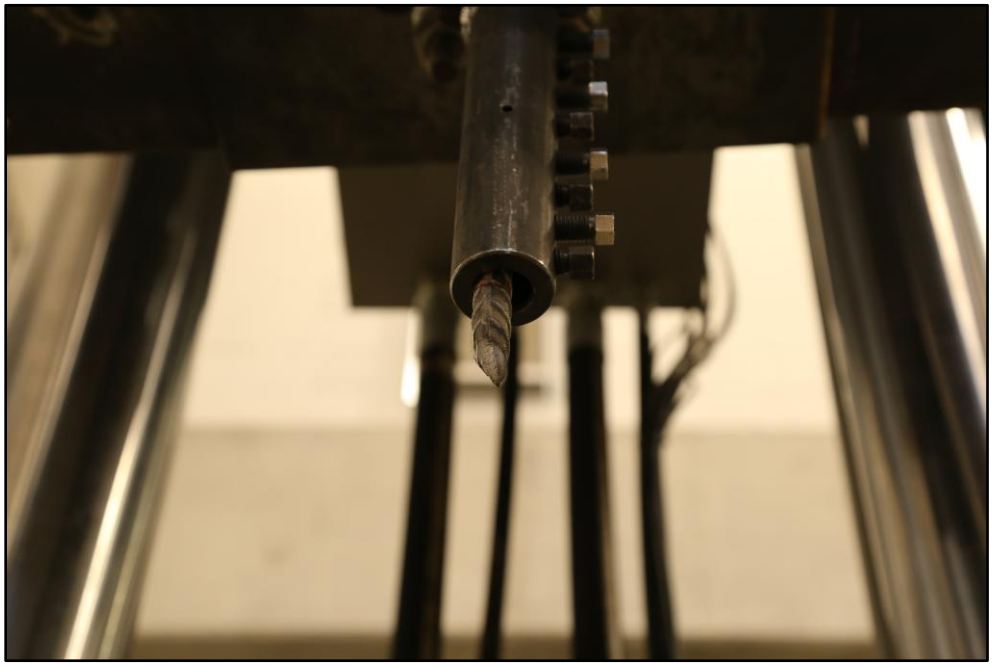

Figure 4-39: Uneven bar rupture due to bending effects.

It is important to mention the bar ruptures did not take place inside the bar lock coupler, but on the region between the end of the it and the edge of the specimens. Figure 4-39 shows one of these ruptures, which took place where the strain gauge was installed. However, the most notorious aspect is the angle inclination, which signals the presence of bending effects that induced uneven stresses. Since the load cell was placed above this

section, its readings were affected by these localized effects, which were possible due to the setup's moment rigid frame, causing the lecture of lower loads that did not match the strain levels captured by the strain gauges.

A better way to appreciate the effect and necessity of the scaling factors is by comparing the raw and scaled stress v strain curves. Figure 4-40 presents the readings coming from the strain gauges located on the loaded end of the embedded section (SG3), and the loaded end of the rebar (SG5) for the ACI-15M-170mm combination. As observed, for a 0.2% strain, where yielding starts to take place, the raw stresses are below the 400 MPa region by almost 25%, thus highlighting the presence of the bending effects as the bar area reduction (15%) does not cover the entire difference.

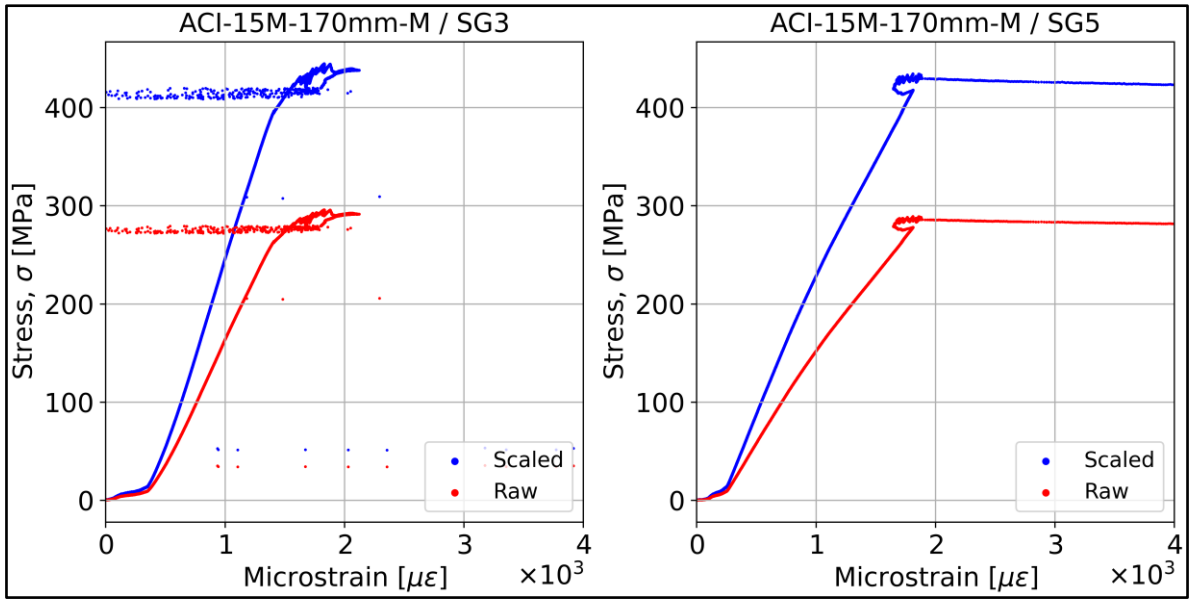

Figure 4-40: Scaled and raw stress v strain curves at yielding, ACI-15M-170mm.

Figure 4-41 presents the same analysis for the ACI-15M-320mm combination, where the bar rupture took place. As observed, at the yielding strain limit the raw stresses are still in the 300 MPa region for SG3, which does not coincide with the stress at which the rebar was yielding in the coupon tests (430 MPa). Another detail comes from the SG5 readings, where the strain progression was delayed and mostly affected by the bending of the rebar, which

in this case took place about 30 mm below where SG5 was installed. Furthermore, the raw ultimate stress recorded by the load cell was 450 MPa, which is well below the 575 MPa registered in the coupon test, and does not coincide with the required stress to generate a bar rupture under normal conditions.

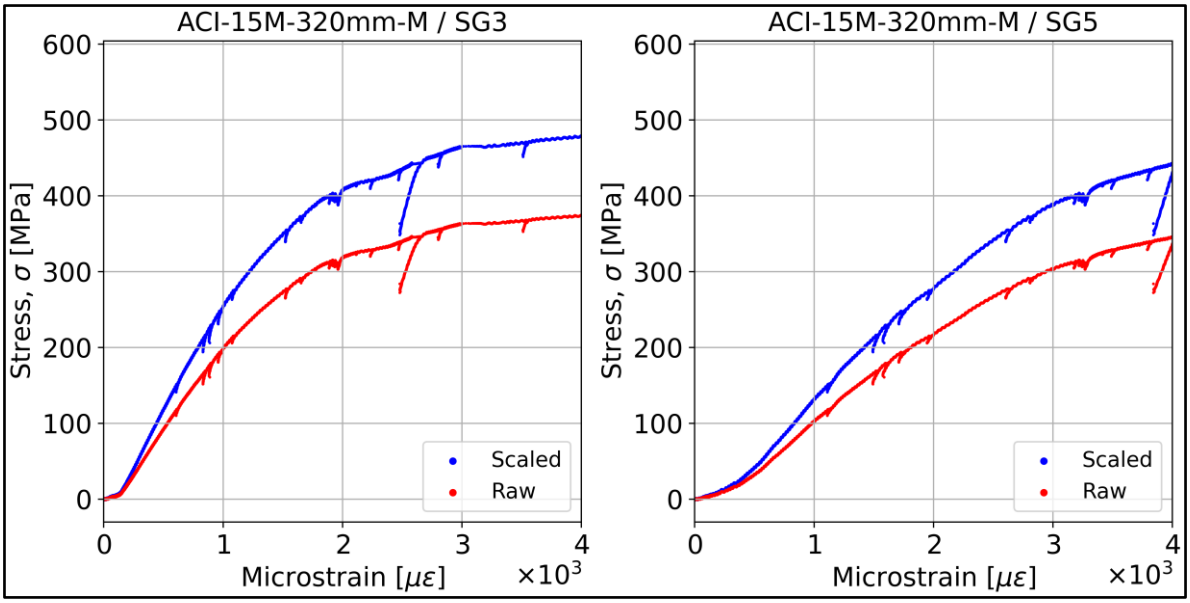

Figure 4-41: Scaled and raw stress v strain curves at yielding, ACI-15M-320mm.

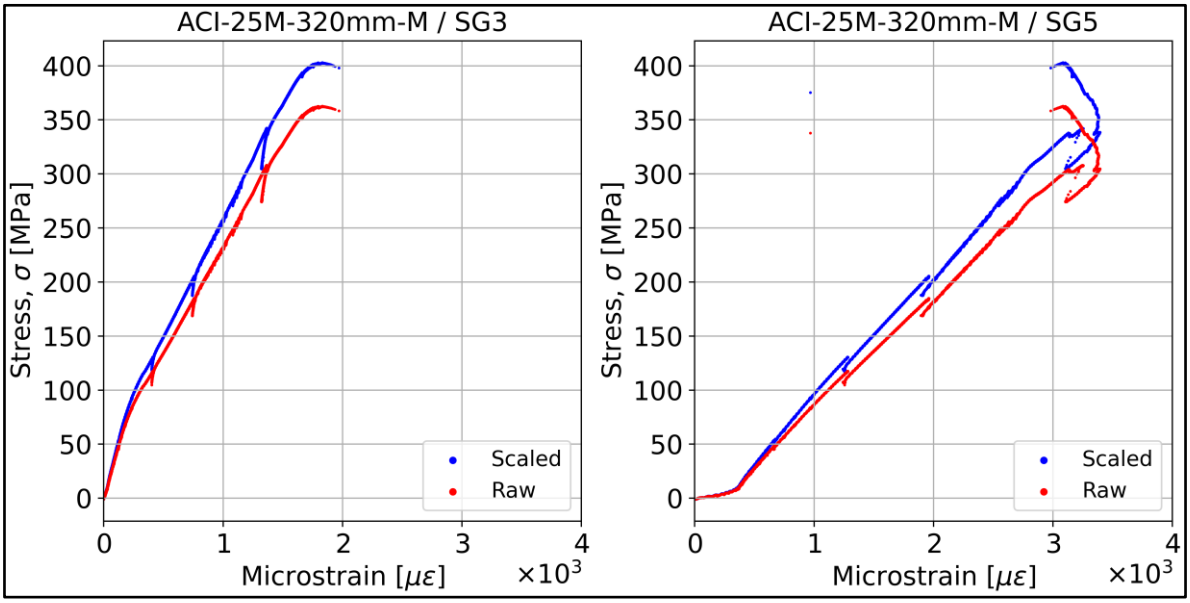

Figure 4-42: Scaled and raw stress v strain curves at yielding, ACI-25M-320mm.

Finally, Figure 4-42 presents the same comparison but for the ACI-25M-320mm specimen. As with the previous case, SG5 readings were also affected by the location of the strain gauge, which was installed above the region where the bending was taking place. However, the SG3 readings were more accurate, indicating the strain at failure was almost 0.2%, which represents the yielding point, at which the raw 350 MPa are well below the 457 MPa obtained for the coupon test.

These cases exemplify the need for the scaling factors, as the raw values coming from the load cell did not correlate with the strain readings of the strain gauges, especially those of SG3 on the embedded region. This difference was mostly caused by the local bending effect that interfered with the load cell readings but had not major effects on the strain readings of the embedded section. Therefore, once the load readings were scaled, it was possible to continue with the analysis and compute the bond stress, which was normalized using the expression given in Eq. 4.6 – 3.

$$u = \frac{T_b}{\pi d_b l_d} = \frac{f_s A_b}{\pi d_b l_d} \qquad (4.6-3)$$

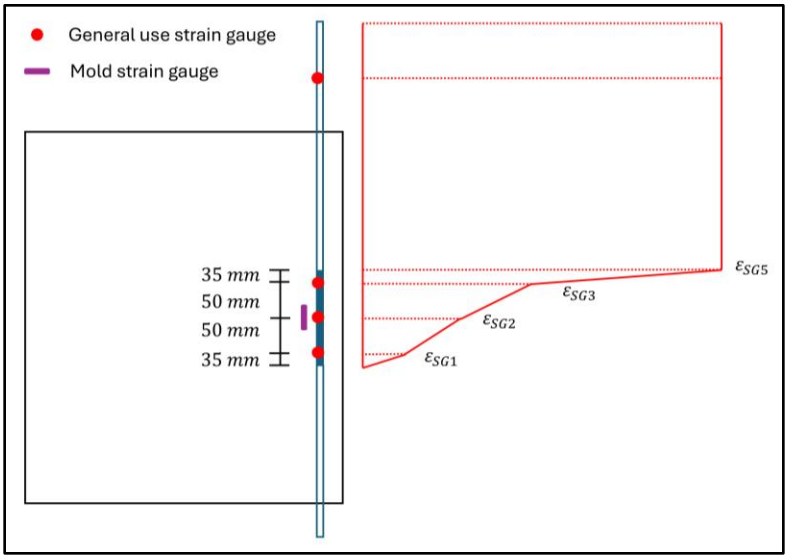

Figure 4-43: Idealized strain profile for 170 mm of embedment.

As observed, this equation allows the estimation of the average and local bond, as it depends on the values of the bar stress and embedment length. Traditionally, bond is compared against the slip of the free and loaded ends of the embedded section, respectively. The former is obtained with the measurements of the LPs, which are connected to the free end of the rebar. Meanwhile, the loaded end can be estimated by integrating the area under the strain profiles of Figure 4-43 and Figure 4-44, which represent the strain evolution in the embedded region until it meets the loaded end of the rebar.

Both strain profiles start from zero at the exact location where the embedment begins. From there, it is assumed that a linear distribution will take place between the three strain gauges placed on the rebar. The fifth gauge, installed outside the specimen, is assumed to be representative of the strain of the loaded section of rebar, which goes between the end of the embedment and the beginning of the coupler. The strain in this region is assumed to be constant; therefore, the strain in the last section of the embedment region transitions from the values of SG3 to SG5.

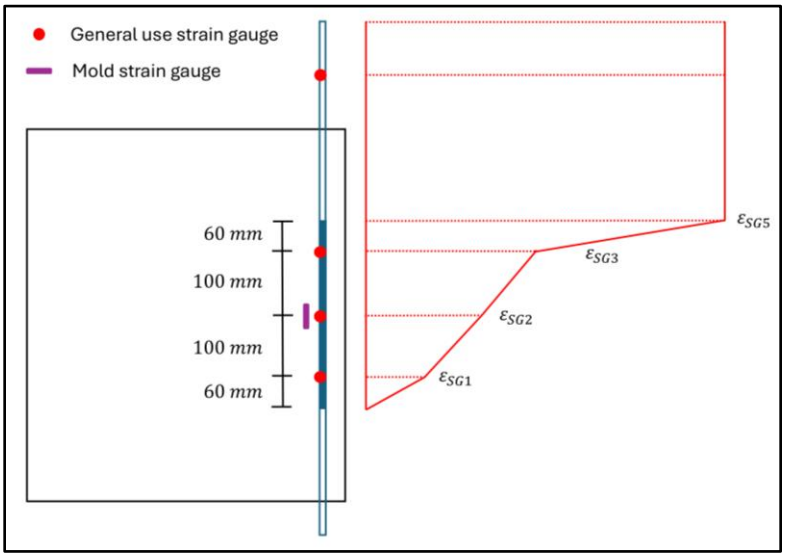

Figure 4-44: Idealized strain profile for 320 mm of embedment.

4.6.4. Test results – 15M – 170 mm

The results of all samples are presented in a 3-plot format, where the first one showcases the bond v slip evolution of the free and loaded ends of the embedded rebar. The second plot presents the strain evolution across the embedded region at different load levels and following the idealized strain profiles presented in Figure 4-43 and Figure 4-44. For this plot, the load stages at which the strain values were extracted are unscaled and represent the raw values read by the load cell in the original load v displacement curves. Finally, the third plot focuses on the strain evolution measured with the mold strain gauge. For this case, since the strains are very low, the results are plotted against the load cell displacement to allow a direct comparison with the load v displacement observations.

Figure 4-45 present the results of the ACI-15M-170 specimen tested under monotonic loading. This specimen was tested twice; the initial test run had to be stopped due to time constraints, and the specimen was unloaded before the start of the second run. As observed in the bond v slip plot, the bond region showed no residual damage since no plateau was developed. In the second test run, the load cell force readings (load v displacement results in Figure 4-32) indicated the bond failure was reached at the end of the yielding plateau and beginning of the strain hardening region, at which point the bar started to pull out as the embedded section was not able to keep up with the stress increase.

No cracking was observed outside the beam-end, suggesting a pullout failure. When analyzing the bond v slip results, the bond reached a peak and progressively started to drop as the slip increased, which is characteristic of a pullout failure. On the other hand, the strain evolution shows no yielding in the embedded region for the first run; however, the results of the second test indicate a localized yielding at SG3 because of the strain penetration coming from the loaded section of the rebar, which correlates with shape of the load v displacement curve.

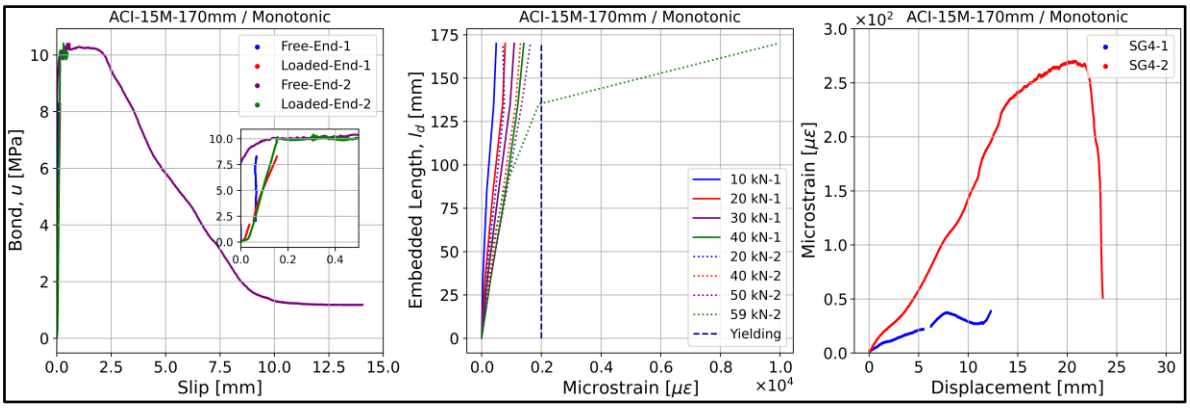

Figure 4-45: ACI-15M-170-M results.

Moreover, when considering the original load readings (as shown in the legend), it is appreciated that they do not correlate with the strain readings. For instance, 40 kN imply 1000 micro-strains, and the strain readings from SG5 at that load indicate 1430 micro-strains, which is 43% higher. When applying the computed scaling factor of Table 4-10, 0.67 for this case, the load increases to 59.7 kN, a value at which the 1430 micro-strains from SG5 are expected when using the 15M coupon stress-strain curve. In consequence, it is demonstrated the load readings coming from the actuator had to be properly scaled to reflect the actual physical behaviour of the specimens.

Finally, the third plot shows the strain evolution in the concrete at the midpoint of the embedded region. The strain profile shows an almost constant increase up to a tensile strain of 250 micro-strains followed by a more gradual increase until the bond failure occurred, resulting in a sudden drop.

The results seem to validate the failure mechanism, where the 170 mm of embedment allowed a partial bar development, which prevented a pure splitting crack development, hence the combined splitting/pullout mechanism and the lack of visible cracking. Figure 4-46 shows the bar pullout from the free end of the rebar. As observed in the red oval, the ring welded to the flat bar connecting both LPs reached the bottom of the concrete specimen, causing the LP inclination, which was a clear indicator of the bar pullout.

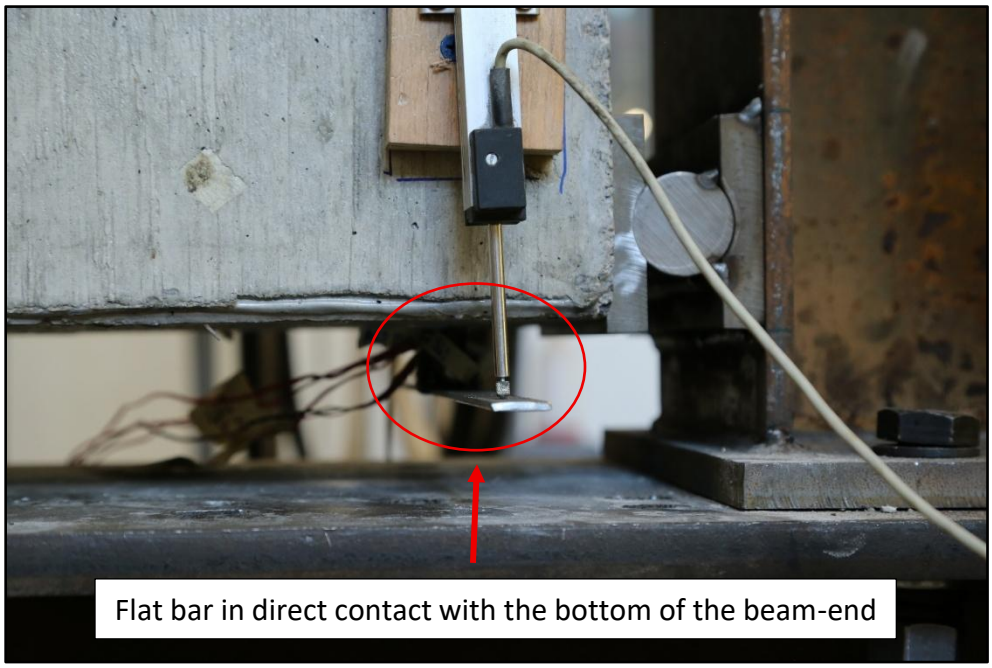

Figure 4-46: Bar pullout in ACI-15M-170-M.

Figure 4-47 presents the results of the same configuration tested under the tension cyclic loading protocol. The bond v slip results show a slightly higher bond stress than the monotonic tests, mainly due to the failure taking place past the yielding zone and with a higher peak load than its monotonic twin. The free end slip also shows the bond drop taking place at 1.7 mm, which is less than the 2 mm obtained for the monotonic test, and with a load drop that was more sudden and with less residual capacity.

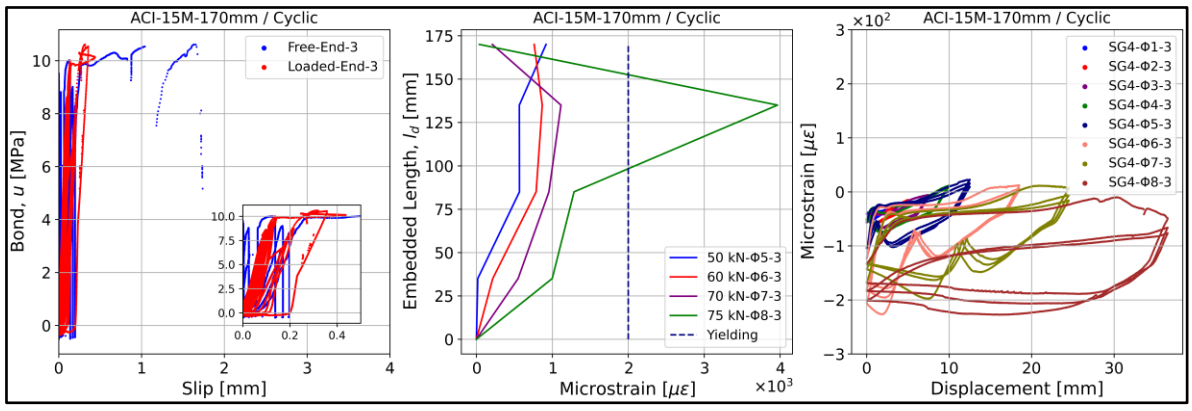

Figure 4-47: ACI-15M-170-C results.

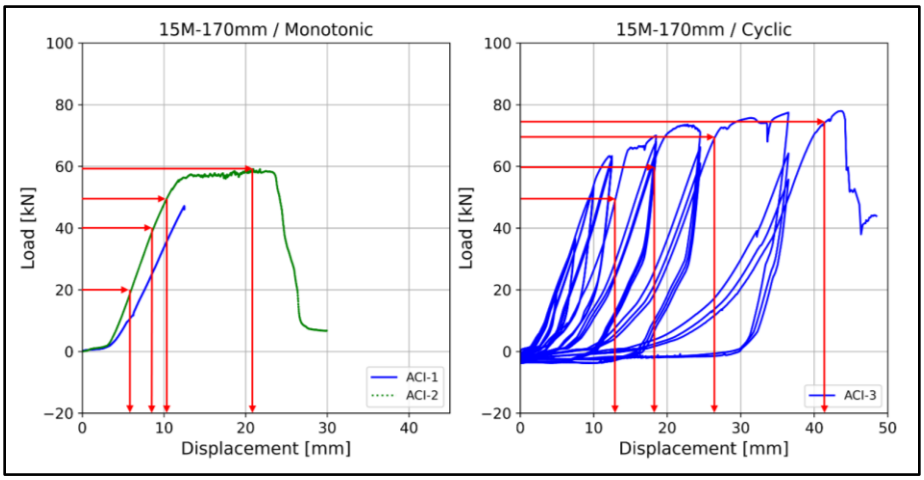

Figure 4-48: ACI-15M-170mm loading stages.

The nomenclature of the strain profile of the second and third subplots is slightly different from the monotonic tests since it includes the deformation step from which the readings were taken, and the final number represents the test run of said beam-end. In this case, this specimen was used twice for the testing of the reversed cyclic protocol, hence the 3 at the end of the nomenclature. Figure 4-48 details the chosen loading stages for both loading protocols. The values were picked according to the strain gauge data reliability and always on the ascending branch of the first cycle of a particular deformation step.

For the strain profile evolution, it is appreciated that SG1 and SG2 remained below the yielding threshold throughout the entire test run. However, localized yielding was observed for SG3 during the last deformation step (Φ_8), thus indicating a strain penetration coming from the loaded rebar. These observations, and the lack of visible cracking, can be related to a splitting-pullout bond failure. Another detail comes from the SG5 readings (located on the free length of the bar on the loaded end), which exhibited erratic values that do not correlate with the readings coming from the embedded section.

This phenomenon was recurrent and can be attributed to a gauge malfunction or to the bending effect caused by the coupler angle, since the gauge was installed close to where the bar was bending. Due to the nature of the cyclic protocol, the rebars were progressively

deformed as the test went further, and since the actuator was set to return to its original position at which the test started, it induced compression effects in cases where the rebar started yielding. Therefore, it is also possible this effect might have resulted in bending stresses in the bar that affected the strain readings during the unloading stages.

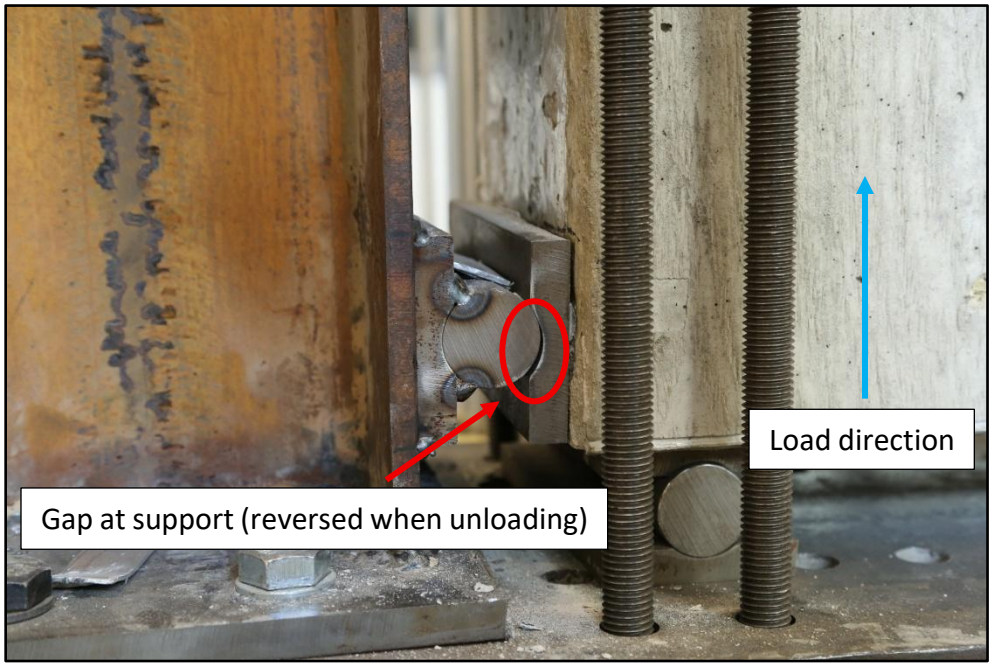

Figure 4-49: ACI-15M-170-C support movement during bar pulling.

On the other hand, the concrete strain evolution shows compression strains, which could be a result of the previous load cycles and the local bearing stresses experienced with each deformation step as part of the degradation process. Finally, Figure 4-49 shows the relative movement of the supports under the cyclic protocol as the test progressed. This movement was difficult to mitigate since it presented once the test was running and there were no gaps at the beginning.

Figure 4-50 presents the results of the EMV-15M-170 sample tested under monotonic loading. As with the previous mix design, the bond v slip plot shows a bond evolution which resembles a pullout or splitting/pullout failure. The peak bond stress is higher than the ACI

mixes, reaching almost 12 MPa, but with a bond plateau that is shorter, as the post peak region starts at a free-end slip of 1 mm.

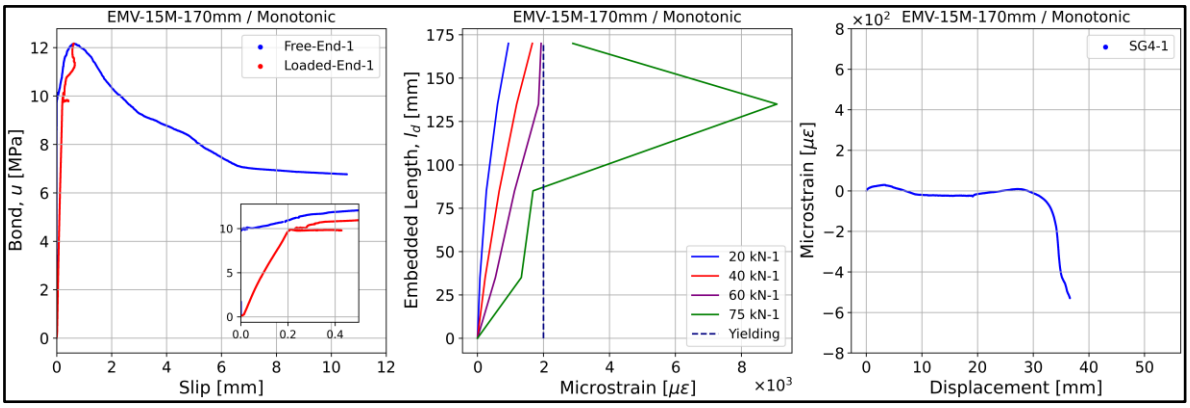

Figure 4-50: EMV-15M-170-M results.

In the case of the rebar strain evolution, the behaviour presents a similar pattern for the first three stages, where the load was still below the yielding point. In contrast, the 75 kN loading level was close to the failure point and shows how the strain picked up from SG2 to SG3, while SG5 suffered from inaccurate readings. This profile also shows the strain penetration, where the loaded end bears the highest stresses and they progressively decrease towards the free end. When compared to the ACI mix, the strain penetration was deeper since the sample was able to enter the strain hardening region. The results also indicate the embedded length was sufficient to allow a partial bar development.

Finally, the results from the concrete strain show almost zero strain for the first 30 mm of actuator displacement, followed by a sudden increase after the load reached its peak at 34 mm. This could be an indicator of when the splitting/pullout failure took take place, as it coincides with the drop observed in the load v displacement curve (Figure 4-32). Figure 4-51 shows the sample after the test, where a splitting longitudinal crack is visible on the right-hand side, thus confirming the development of a splitting/pullout failure.

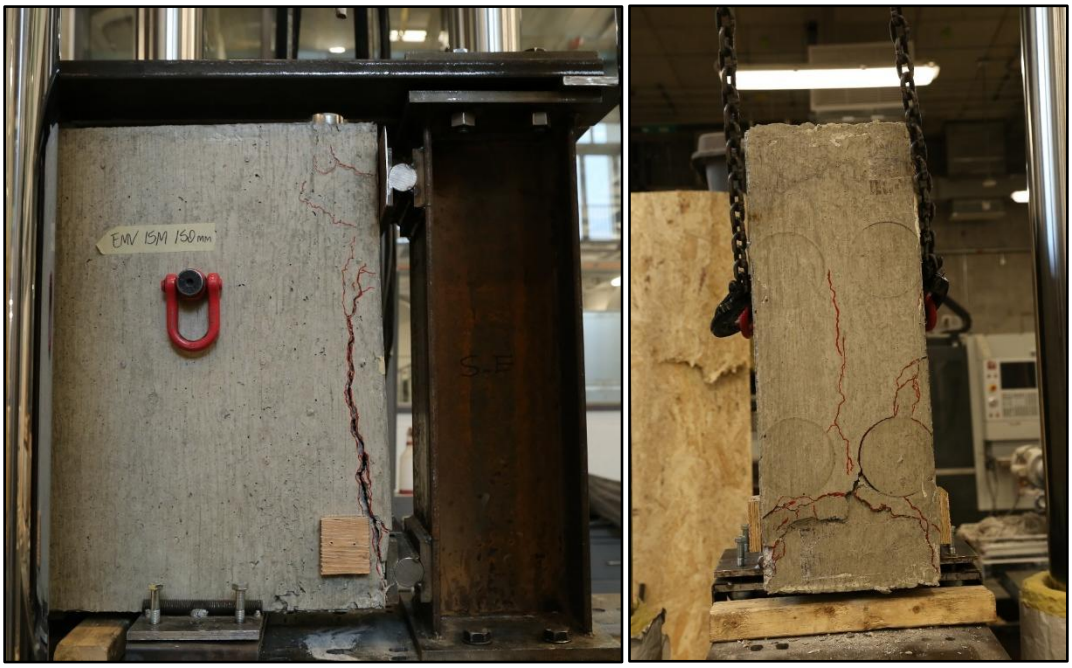

Figure 4-51: EMV-15M-170-M tested sample.

Figure 4-52 presents the results of the same configuration tested under the cyclic loading protocol. In the case of the bond v slip behaviour, the shape of the curves is similar when compared to the monotonic case but with a lower peak bond stress. The difference is mainly attributed to the lower load peak reached during the test, which could be an indication of the damage suffered by the specimen with the cyclic loads. The shape of the loaded-end bond also suggests a bond failure due to a combined splitting/pullout action.

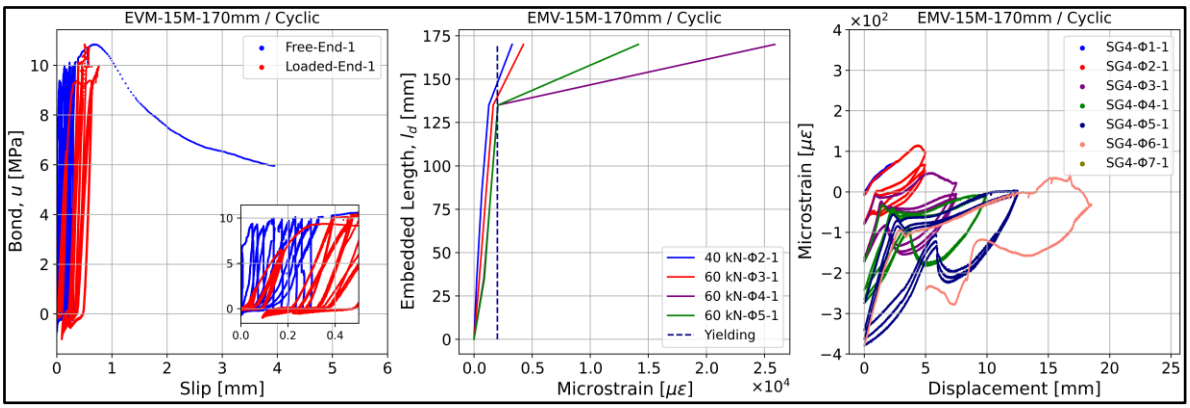

Figure 4-52: EMV-15M-170-C results.

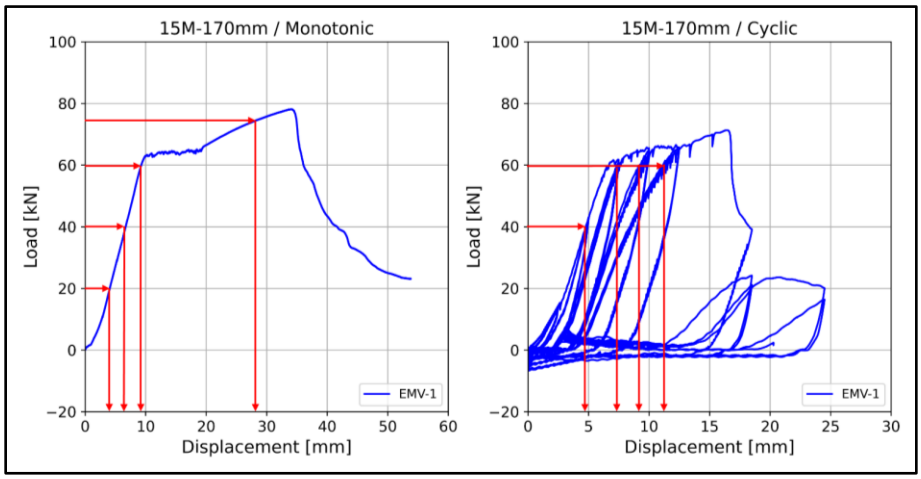

Figure 4-53: EMV-15M-170mm loading stages.

In the case of the strain profile (whose loading stages are detailed in Figure 4-53), the development follows a similar pattern between SG1 and SG3 for all loading stages. However, the readings coming from SG5 showed values well beyond the yielding limit of 2000 micro-strains. Since SG5 was placed on the rebar outside the specimen, its values indicate it was experiencing localized yielding as the test progressed, thus leading to strain penetrations as SG3 was on the yielding limit during the fourth and fifth loading stages.

On the other hand, the concrete strain measured by SG4 on the right plot shows the readings went into the compressive region with each deformation step. This profile can be attributed to the elongation the rebar was experiencing on the loaded end as the test progressed, which induced compression on the embedded section as the actuator was set to return to its original position after each cycle, thus compressing the elongated rebar. This effect will be further addressed in the discussion section as it manifested in other samples.

Figure 4-54 presents the specimen after the test. As with the monotonic twin, it is possible to observe the splitting longitudinal crack on the left side, while the right picture shows the expansion of the cracks on the sides. The development of the splitting crack is in-line with the bond v slip results, thus confirming the mixed splitting/pullout mechanism.

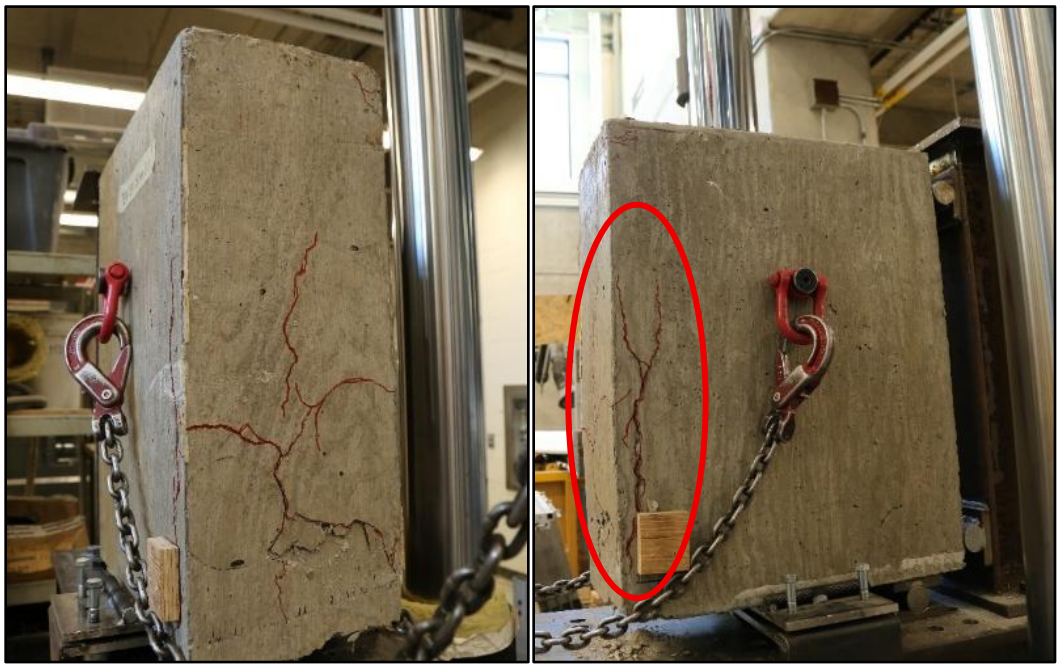

Figure 4-54: EMV-15M-170-C tested sample.

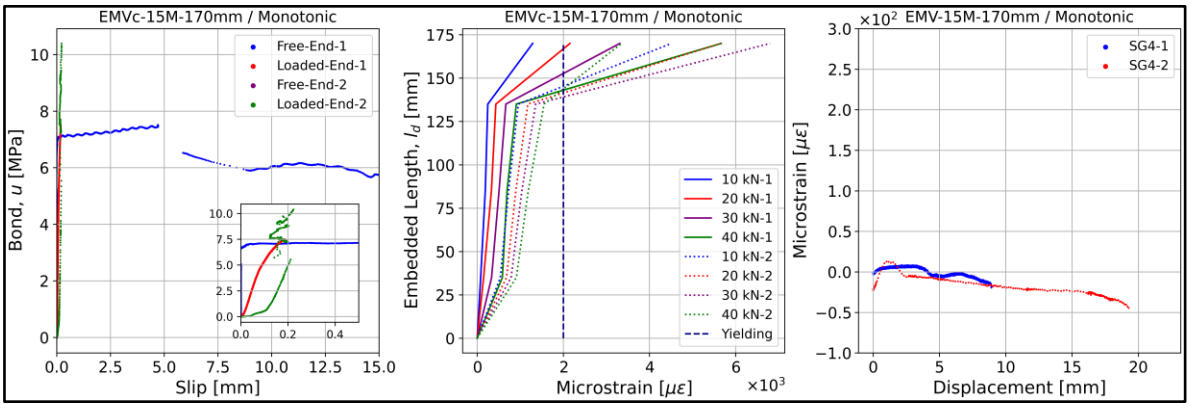

Figure 4-55: EMVc-15M-170-M results.

Figure 4-55 presents the results of the EMVc specimen tested under monotonic loading. As opposed to the previous two mix designs, the performance of the EMVc mix was severely impacted by excessive cracking in the concrete, which started at early stages of the test and developed at a much faster pace than the ACI and EMV samples. The initial test had to be stopped due to this problem, as cracks quickly developed at the bottom of the specimen (Figure 4-56). After the stoppage, the sample was checked and the embedded region did not suffer visible damage, with the strain gauges still working properly. Therefore, for the

second test, the sample was fixed and a manual loading rate with the actuator was applied to be able to pull the rebar from the beam-end and measure the bond behaviour. However, this meant the free-end slip was not captured as the LPs could not be reinstalled.

The monotonic peak bond stress was similar to the ACI sample but inferior to the EMV one. The strain profiles for the same load levels show higher strains for the second test run, which can be attributed to the possible damage sustained during the first test and the manual loading rate applied to pull the rebar on the second test. Nevertheless, the extension of the strain penetration could not be confirmed as SG3 stopped working midway through the second test run. Therefore, it is believed that a splitting/pullout failure should have taken place, but with the concrete quality playing a major role in its development.

Figure 4-56: EMVc-15M-150-M tested sample.

In the case of the concrete strain profile, the results are similar between the two test runs, with the second one following the same pattern of the first test before it was stopped However, once the load was close to the peak, the measurements became unreliable

presumably due to the crack development in the concrete (the same happened to the strain gauges placed on the rebar).

Figure 4-56 shows the specimen after the second testing run. On the left side of the picture, cracks developed and expanded near the support, with the first one taking place at the bottom support, and the second one running parallel to the area that was not confined by the longitudinal stirrups. Moreover, the right image presents the state of the concrete once the rebar was pulled. It became evident the concrete made with the "C-Crete Binder" was more brittle than the other mixes made with the traditional GUL cement, as confirmed by the splitting tensile cylinder tests presented in the previous chapter.

The results of the EMVc specimen tested under the cyclic loading protocol are presented in Figure 4-57. Contrary to the observations made in the previous samples, the calculated loaded end slip was less than the measured free-end slip. This is attributed to the development of large cracks (similar to those experienced during the monotonic test) that affected the LP readings. In terms of peak bond stress, the value is lower than its monotonic twin and the respective ACI and EMV specimens, although the same splitting/pullout failure took place, as observed in the descending branch of the free end slip.

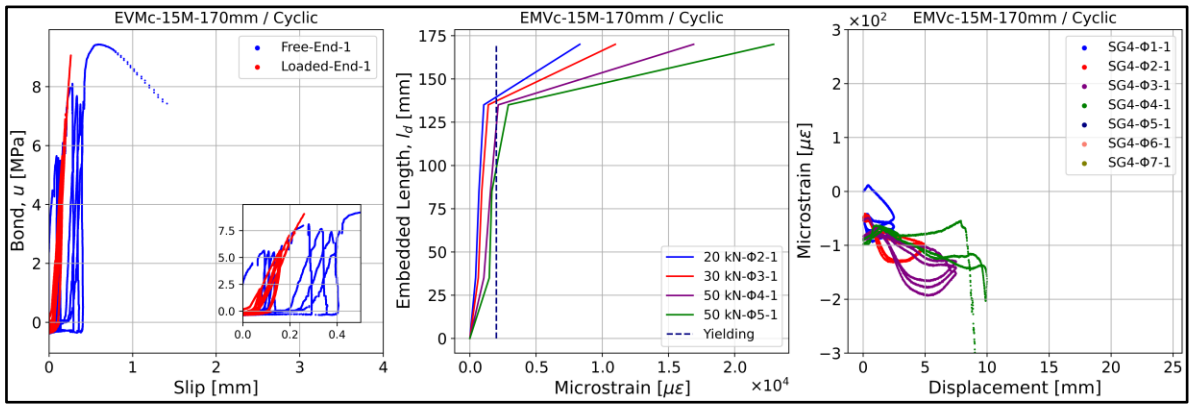

Figure 4-57: EMVc-15M-170-C results.

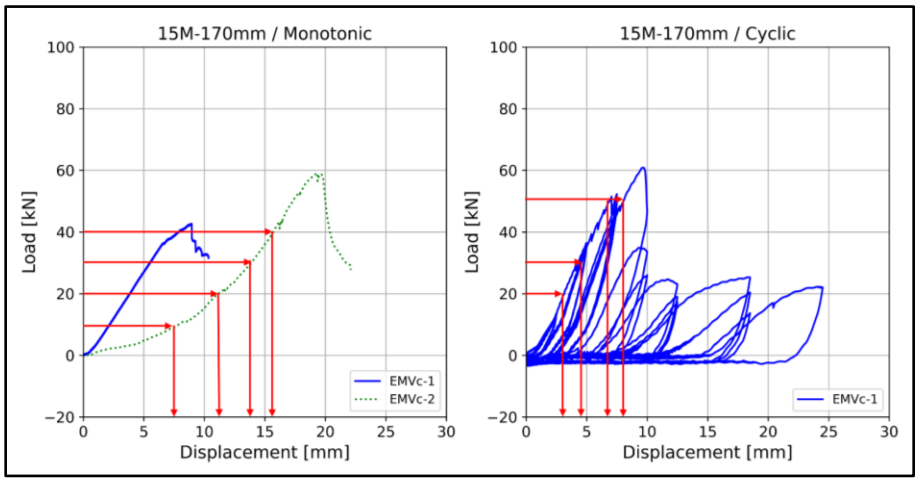

Figure 4-58: EMVc-15M-170mm loading stages.

Figure 4-59: EMVc-15M-150-C tested sample.

The strain profiles (loading stages detailed in Figure 4-58) show similar trends to those of the ACI and EMV mixes, with a strain penetration coming from the loaded end of the rebar, and with strain beyond 2000 micro-strains between SG2 and SG3 during the fifth deformation step, which indicates the rebar was locally yielding. This behaviour is believed to be like the one that could not be fully captured during the monotonic test. Furthermore,

the behaviour of the concrete strain is like the EMV sample, with compressive strains dominating as the test progressed due to the compression of the elongated rebar as the actuator returned to zero.

Figure 4-59 presents the specimen after the test. The cracking patterns and evolution are like those observed for the EMV sample, thus confirming the splitting/pullout nature of the experienced bond failure. However, the width of the cracks was bigger, and their propagation was faster like in the monotonic test. When taking a closer look at the fragments left behind, the green colour and the porous nature of the hardened paste were evident. This aspect will be revisited in the discussion section.

4.6.5. Tests results – 15M – 320 mm

Figure 4-60 presents the results of the ACI-15M-320mm specimen tested under monotonic loading. As opposed to the previous combination, the failure mechanism was due to a bar rupture on the outside of the embedded section, which means the tested embedment allowed a full bar development, which was expected given that 320 mm were slightly above the minimum 300 mm required by CSA A23.3.

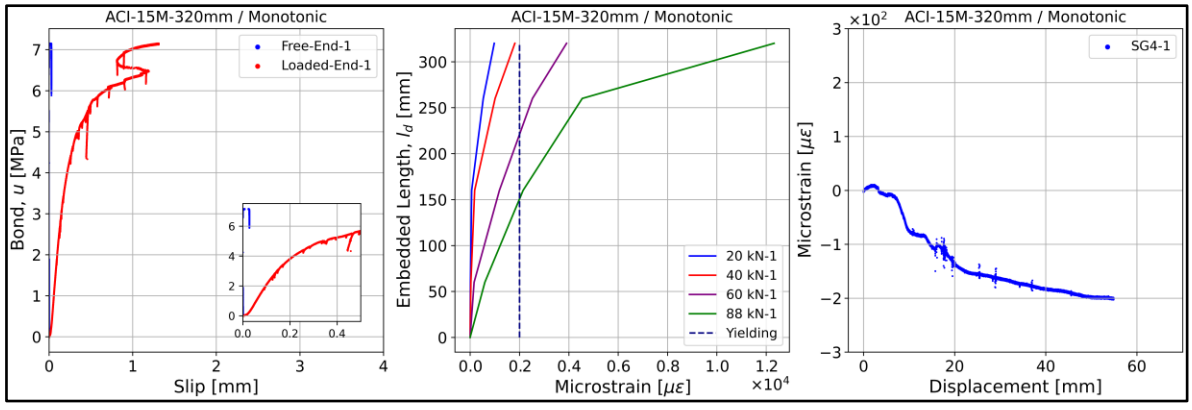

Figure 4-60: ACI-15M-320-M results.

As observed in the bond v slip plot, the free end slip is practically zero, which was expected as the rebar had enough embedment to be able to yield. Meanwhile, the loaded

end slip presented higher values than the 170 mm combination, as a result of the higher strain readings coming from the strain gauges. Moreover, the peak bond stress (close to 7 MPa) was reduced as expected because of the longer embedded section, which traduces into a lower average bond.

When analyzing the rebar strain profiles, up to 40 kN the strain was almost linear, but from 60 kN onwards the rebar was yielding inside the embedded section, signaling a deeper strain penetration with SG2 and SG3 reaching almost 2000 and 4000 micro-strains, respectively. On the other hand, the concrete strain profile was in the negative range (compression) during the test, and it continuously developed until the bar rupture, reaching a peak of almost 200 micro-strains.

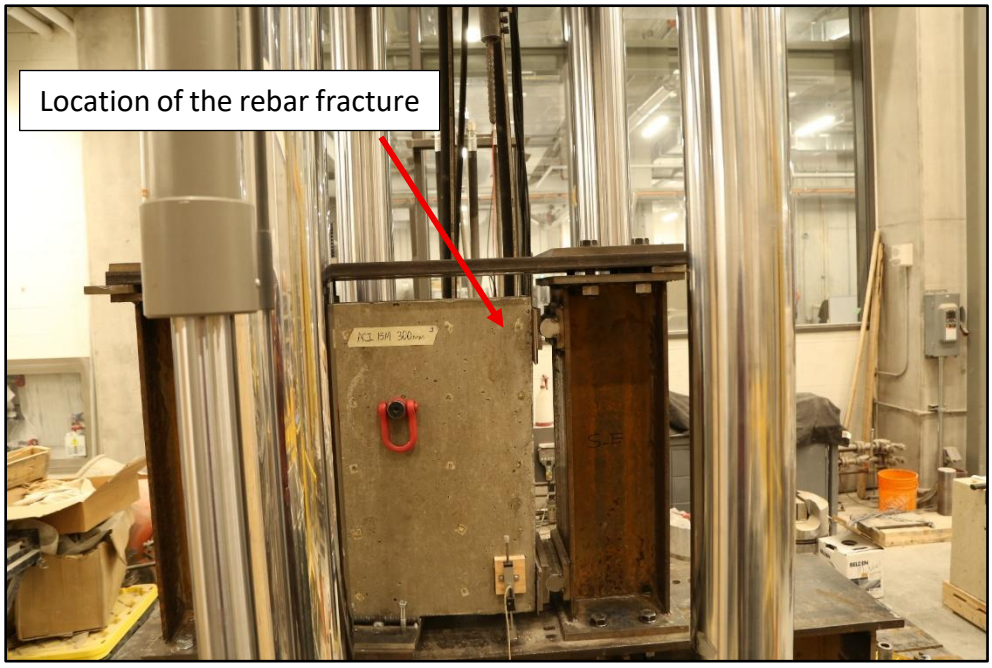

Figure 4-61: ACI-15M-320-M tested sample.

Figure 4-61 presents the specimen after the conclusion of the test. The bar failure took place inside the beam-end, more specifically in the region between the end of the embedment and the surface of the sample. Due to the failure mechanism, no minor or major splitting cracks were spotted.

Figure 4-62, on the other hand, presents the cyclic results of its twin. As observed in the bond v slip plot, the peak bond stresses and respective slips are like the monotonic case. The expected failure was a bar rupture, but the weld between the bar lock coupler and the top girder plate failed during the last deformation step and close to the point where the rebar could have ruptured.

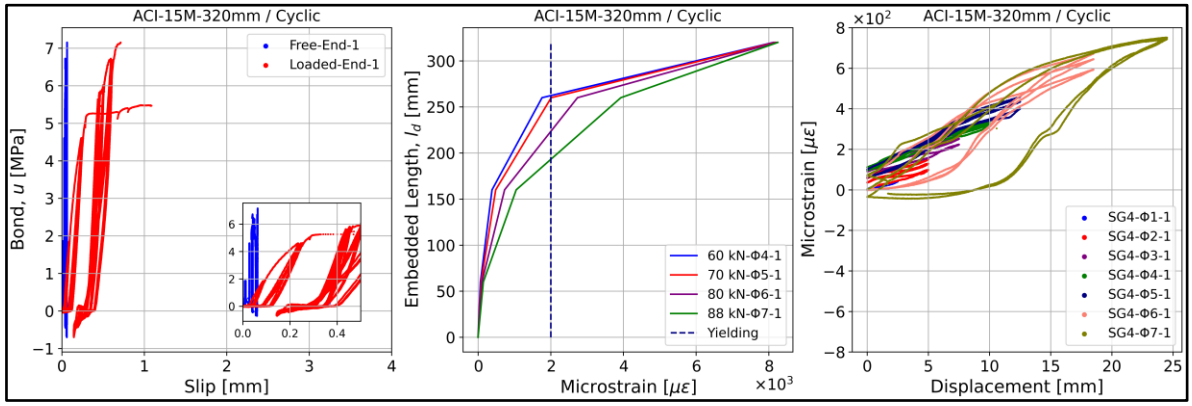

Figure 4-62: ACI-15M-320-C results.

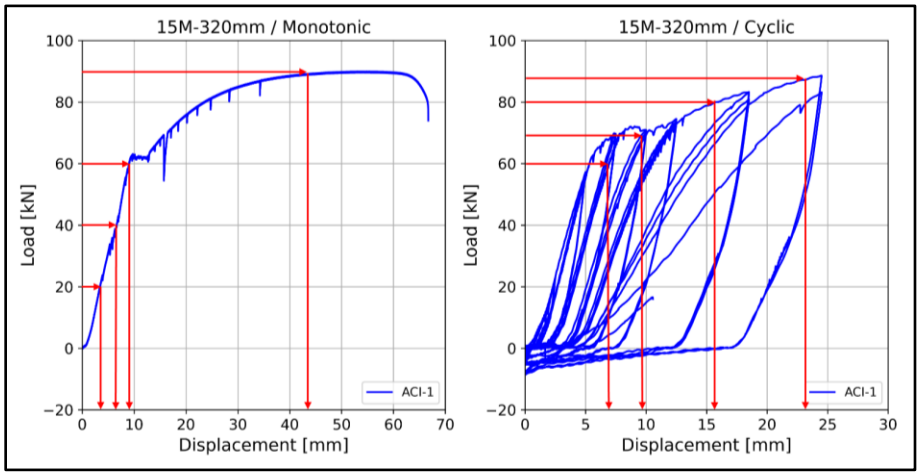

Figure 4-63: ACI-15M-320mm loading stages.

When comparing the bar strain profiles (loading stages detailed in Figure 4-63), the range between SG1 to SG3 is like those observed in the monotonic twin, which indicates the strain penetration and the yielding of the rebar in the embedded section. However, it is also observed that SG5 shows the same value for each of the considered displacement

steps, at approximately 8000 micro-strains. When analyzing the raw strain data, the readings of SG5 spiked when the actuator displacement was at approximately 7 mm and then settled at 8000 micro-strains for the rest of the test.

The strain limit of the regular strain gauges was 50,000 micro-strains, or 5% of total deformation. To rupture the rebar, the required strain was close to 18%, and SG5 was placed on the region where the rebar was deforming the most, meaning that SG5 most likely stopped working properly because it deformed beyond its limit, or because the bar bending during the unloading phase of the initial cycles caused a malfunction, as the bending was taking place close to where the gauge was placed (Figure 4-64).

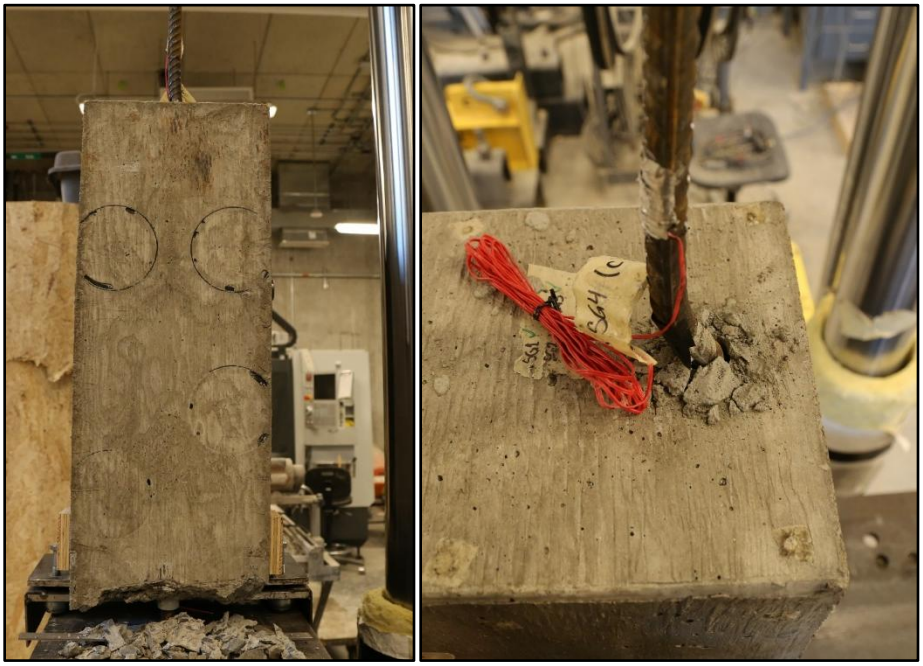

Figure 4-64: ACI-15M-320-C tested sample.

The biggest implication from this issue is that loaded end slip was most likely underestimated due to the inaccuracy of the SG5 readings. On the other hand, the concrete strain profile showed a more expected behaviour since it developed in the tensile zone. The strain increased with each deformation step showing no visible signs of significant

degradation in between the repetitions, which is in line with the rebar being able to fully develop its capacity. The peak strain in the concrete was 800 micro-strains.

Figure 4-64 shows the specimen after completing the test. On the left-hand side, it can be observed there are no splitting or longitudinal cracks, only localized cracking near the bottom support. Meanwhile, the right-hand side exemplifies the bending due to the bar elongation during the last deformation steps of the cyclic protocol. Since the rebar stretched beyond 17%, this behaviour was difficult to control as no braces were provided, and the actuator was set to return to its original position (the zero was set at start of the test with an undeformed bar) after the conclusion of each cycle.

The second mix design used for this embedment configuration was the DRM, and its monotonic results are presented in Figure 4-65. Two test runs were necessary for this specimen since coupler sliding was observed in the first run when the rebar stress was close to the maximum value of 575 MPa. This is evident in the loaded end slip and concrete strain profile, where the former shows a stagnation in the bond development and the latter presents a progressive strain release after 18 mm.

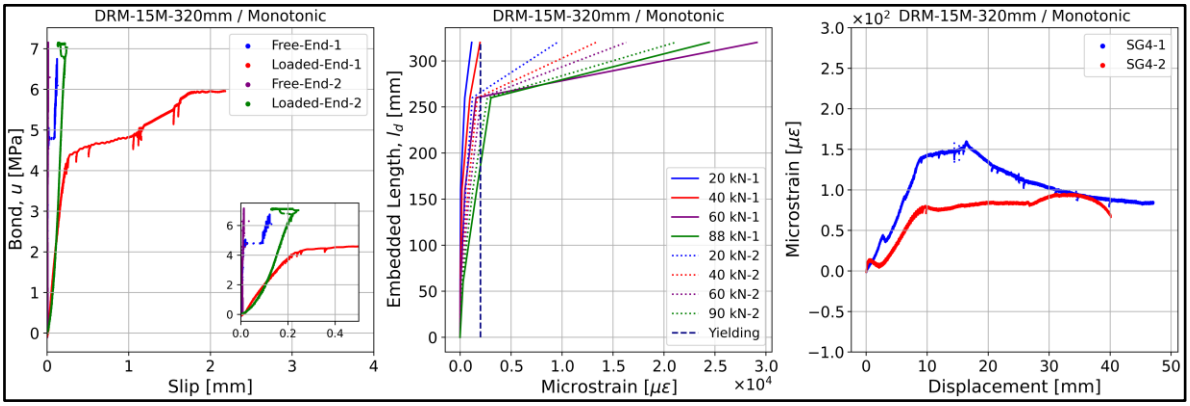

Figure 4-65: DRM-15M-320-M tested sample.

Once the sliding problem was solved, a second test was conducted and the failure occurred due to a bar rupture, as experienced with the ACI sample. The loading peaks were

the same since the rebar reached its ultimate stress, but the loaded end slip was inferior because of the deformation sustained by the strain gauges in the previous test. On the other hand, the rebar strain profile shows a similar strain penetration as the one observed for the ACI specimen, showing the rebar was indeed yielding in the embedded section.

Meanwhile, the concrete strain profile shows a linear ascent during the second test until reaching a displacement of 10 mm, which corresponds to the peak load. The strain level then remained constant until the displacement reached 28 mm, before increasing slightly to 100 micro-strains prior to the bar rupture. Figure 4-66 presents the bar rupture which occurred outside the specimen.

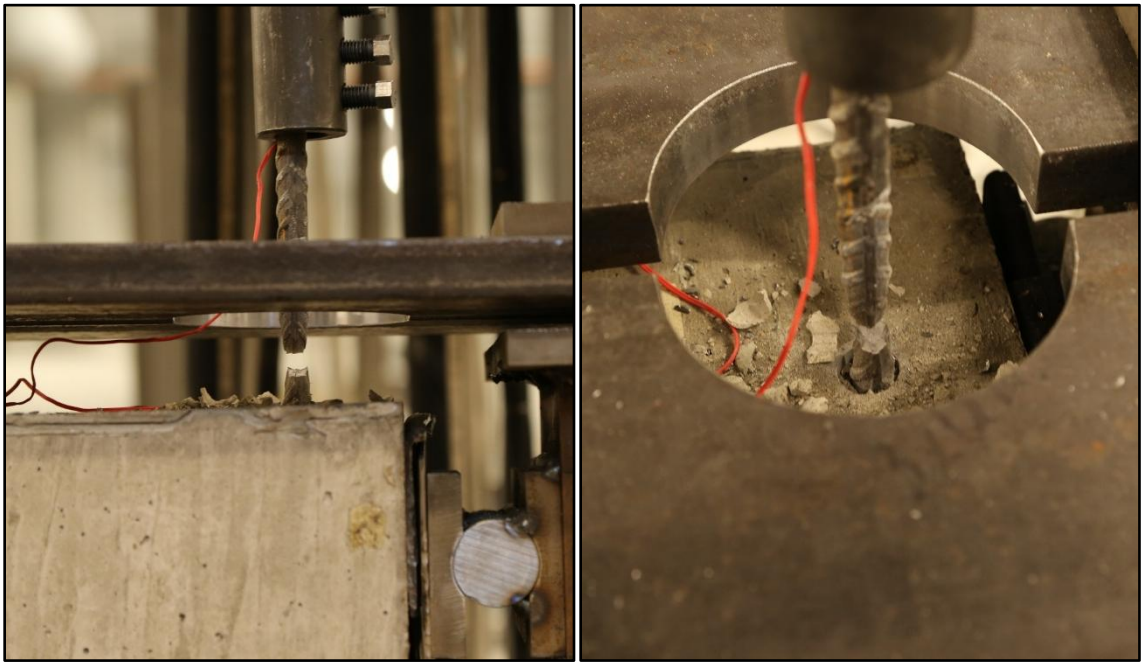

Figure 4-66: DRM-15M-320-M tested sample.

The results of the duplicate specimen tested under cyclic loading are presented in Figure 4-67. In contrast to the ACI sample, the peak bond stress was lower than the monotonic specimen, which means the failure took place in the strain hardening region of the rebar, as no rebar rupture was experienced. Moreover, the measured free end slip is higher, which is a consequence of the cracking that took place at the bottom support and interfered with

the LPs reading. However, it must be noted this sample was used in the testing of the fully reversed loading protocol, which may have introduced residual deformations. This last point will be further addressed in the discussion section.

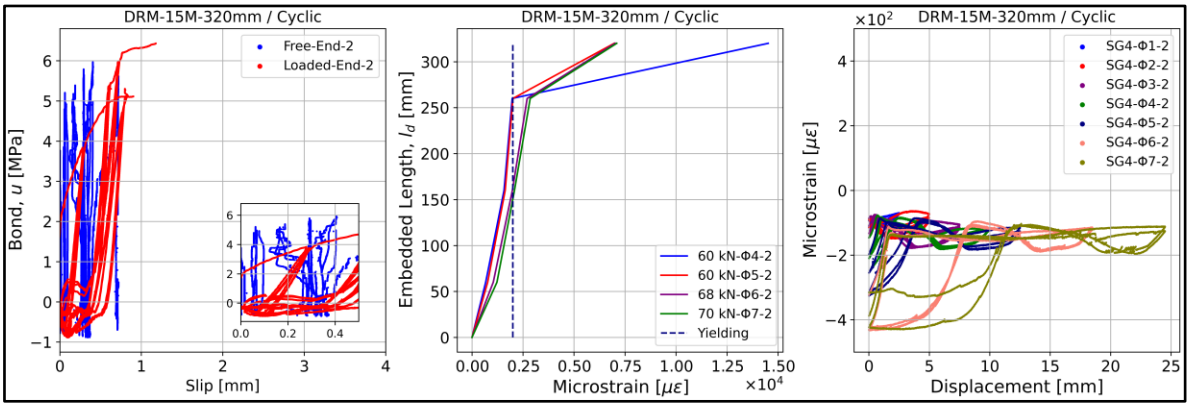

Figure 4-67: DRM-15M-320-C results.

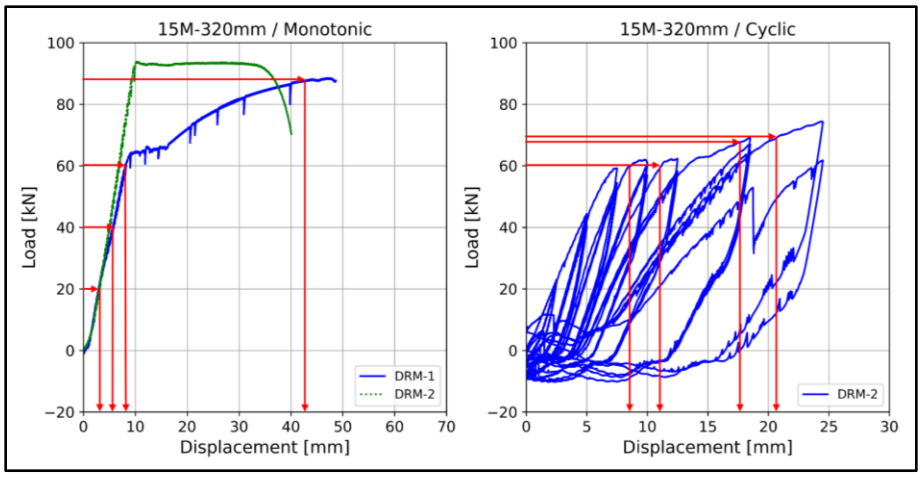

Figure 4-68: DRM-15M-320mm loading stages.

The failure mechanism that took place was most likely a combined splitting/pullout failure, as seen in the cone of Figure 4-69. When analyzing the bond v slip curves, a lower bond peak means the accumulated damage was greater than in the ACI samples, as the beam-end was not able to bear higher stresses. This is consistent with the strain profile of the rebar (loading stages detailed in Figure 4-68), which shows a deeper strain penetration in the embedded section, with SG2 and SG3 presenting similar readings between 2000 –

3000 micro-strains. In contrast, SG2 was still below the yielding limit of the ACI samples. Furthermore, the concrete strain profile shows values in the compression zone with little strain variation until the compression of the elongated rebar induced higher peaks when the actuator returned to zero.

The left-hand side of Figure 4-69 shows the cracking experienced at the bottom support. The shim plates were inserted to fill and close any gaps that could have allowed relative movement or rotation; therefore, they were hammered until a tight fit was achieved. Transverse cracks manifested once the test was started, which directly affected the readings of the free end slip since they crossed the path to which the LPs were glued. Meanwhile, the right-hand side shows the local splitting/pullout cracks that developed on the edge of the beam-end.

Figure 4-69: DRM-15M-320-C tested sample.

The last mix tested for this configuration was the EMV, and the monotonic results are presented in Figure 4-70. The peak bond stress was the same as with the ACI and DRM specimens tested under the same loading protocol. This behaviour was expected since the

failure mechanism was a bar rupture; therefore, the free end slip was almost zero as the embedment was enough to allow the development of the rebar. However, unlike the ACI sample, the loaded end slip remained below 1 mm.

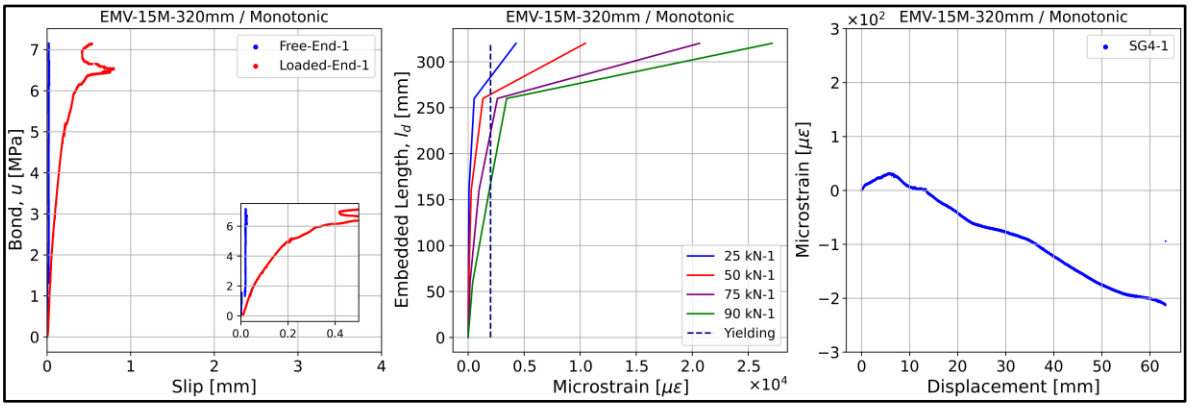

Figure 4-70: EMV-15M-320-M results.

In the case of the rebar strain profile, there is little strain penetration for the first two load levels. Nevertheless, as soon as the rebar on the loaded end went beyond its yielding stress (as seen in Figure 4-33), the strain penetration became noticeable in the region comprised by SG2 and SG3, with an evolution like the ACI sample. Therefore, as with ACI and DRM samples, the 320 mm of embedment were enough to allow a bar development when subjected to monotonic loading.

The concrete strain evolution showed a tensile strain up to a displacement of 10 mm, which corresponds to the initial yielding of the reinforcing bar (Figure 4-33). Subsequently, the strain profile transitioned to the compression zone and remained there until failure. It is possible that once the rebar yielded, the concrete surrounding the rebar started crushing during the elongation and caused the change in the strain profile. In this case, the failure mechanism was a bar rupture, which took place outside the specimen on the loaded section of the rebar. Figure 4-71 presents the failure on the right-hand side, while the left-hand side shows the area close to the bottom support, which suffered from localized cracking.

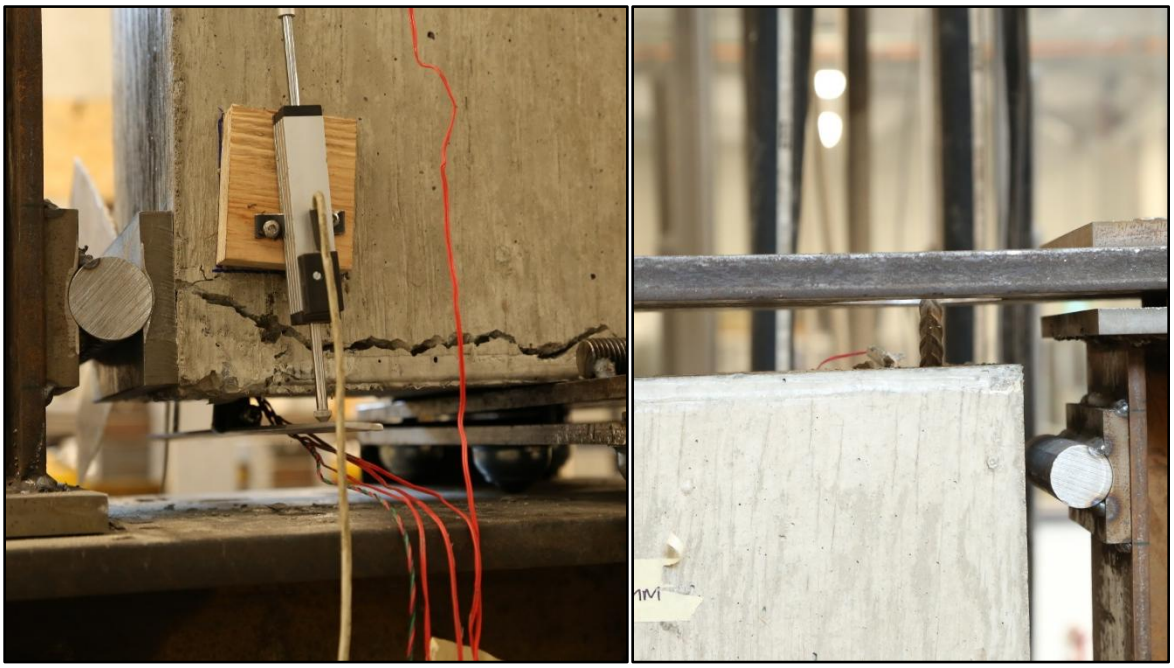

Figure 4-71: EMV-15M-320-M tested sample.

Figure 4-72 presents the results of the twin sample tested under cyclic loading. Unlike the ACI and DRM cases, this beam-end was able to reach the bar rupture, matching the monotonic results but with a lower overall displacement. The peak bond stress was the same as its twin at just over 7 MPa, though the slip readings exhibited some erratic behaviour attributed to the bottom cracks near the supports (free end slip) and the erroneous strain gauge readings, especially those coming from SG5 once the rebar went past its yielding zone on the loaded bar outside the beam-end.

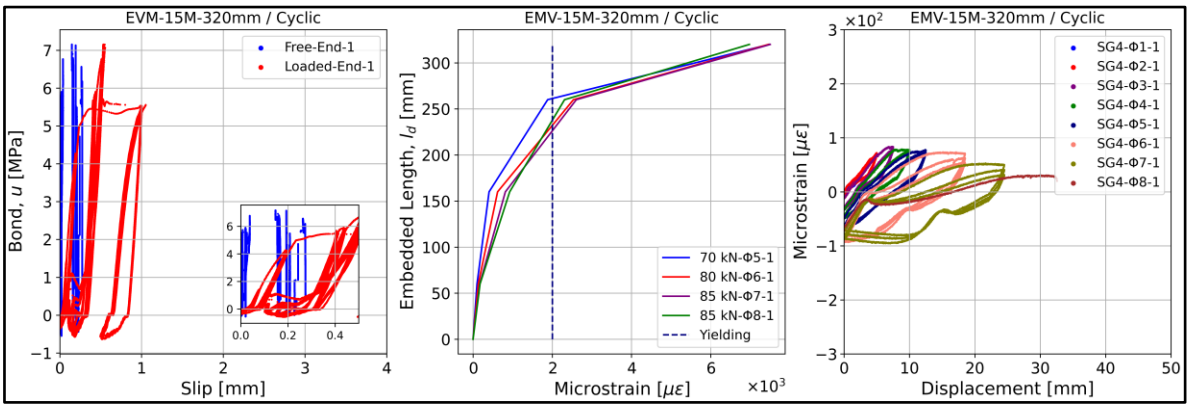

Figure 4-72: EMV-15M-320-C results.

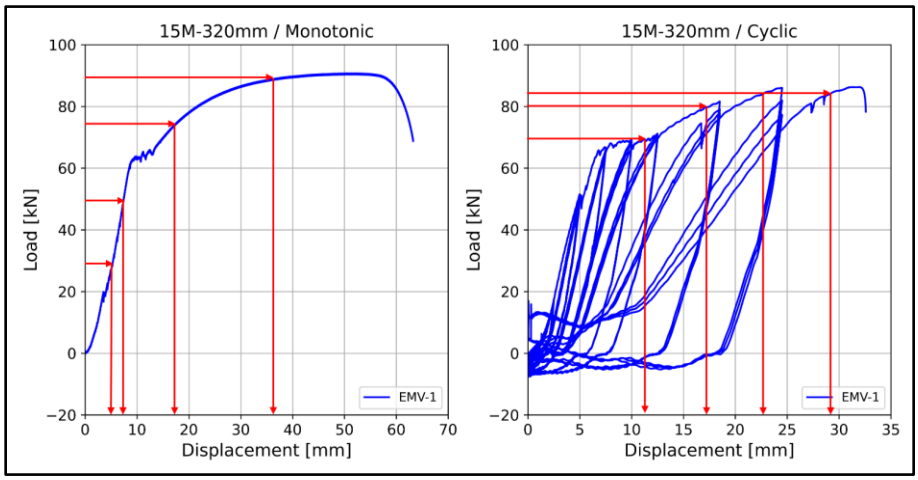

Figure 4-73: EMV-15M-320 loading stages.

When analyzing the rebar strain profile (loading stages detailed in Figure 4-73), it is possible to observe that the yield strain penetrated to a depth between SG2 and SG3, approximately 100 mm from the loaded end. Nevertheless, the SG5 measurements became unreliable at higher loads, with a constant reading of 7000 micro-strains, which might be related to the same issues experience for the monotonic ACI sample (gauge reaching its 5% strain limit or the influence of the bending on the readings since SG5 was placed exactly where the rupture took place).

On the other hand, the concrete strain profile shows the strain progressively transitioned from tension to compression as the test progressed, and it might be related to the compression of the elongated rebar as the actuator stroke came back to zero, and due to concrete keys crushing because of the stiffness degradation. The cracking suffered at bottom support is showed on the left-hand side of Figure 4-74, which caused the jumps observed in the free end slip. Meanwhile, the right-hand side shows the location of the bar rupture, which coincided with the location where SG5 was installed. Hence, the readings of this gauge were likely affected once the localized yielding started.

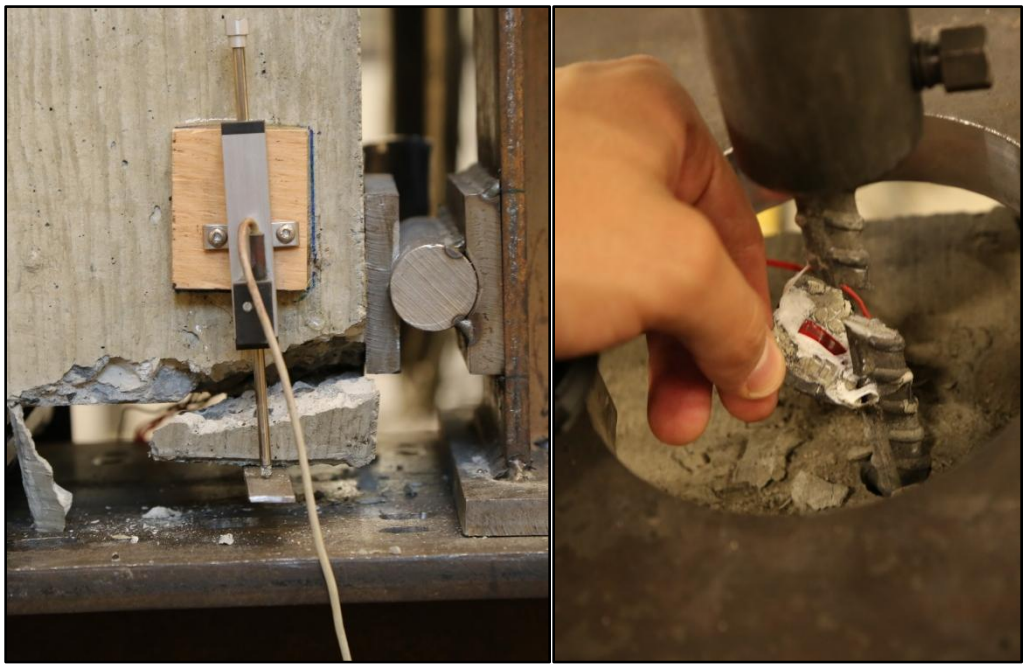

Figure 4-74: EMV-15M-320-C tested sample, Pt. I.

Figure 4-75: EMV-15M-320-C tested sample, Pt. II.

Figure 4-75 shows the specimen after being removed from the testing apparatus. No cracks are visible on the loaded side of the beam-end (left side of the figure), which was

expected due to the failure mechanism. However, cracks developed on the opposite side of the beam-end (right side of the figure), around the confined area provided by the longitudinal stirrups and similar to the pattern observed for the EMVc-15M-170-M specimen. This phenomenon manifested during the last loading cycles and might be attributed to the rotation suffered by the beam-end once the cracks at the bottom support were wide enough, causing an overload on the top left supports that induced the cracks.

4.6.6. Tests results – 25M – 320 mm

Figure 4-76 presents the monotonic results of the ACI-25M-320 specimen. Compared to the previous results, the major difference is the rebar size, which increased from 15M to 25M. Failure occurred by the expected concrete splitting along the embedded region. The bond v slip plot shows that the peak bond stress was 8 MPa, but with the free end bond showing a decrease between 0.1 mm – 0.5 mm due to cracking at the bottom support.

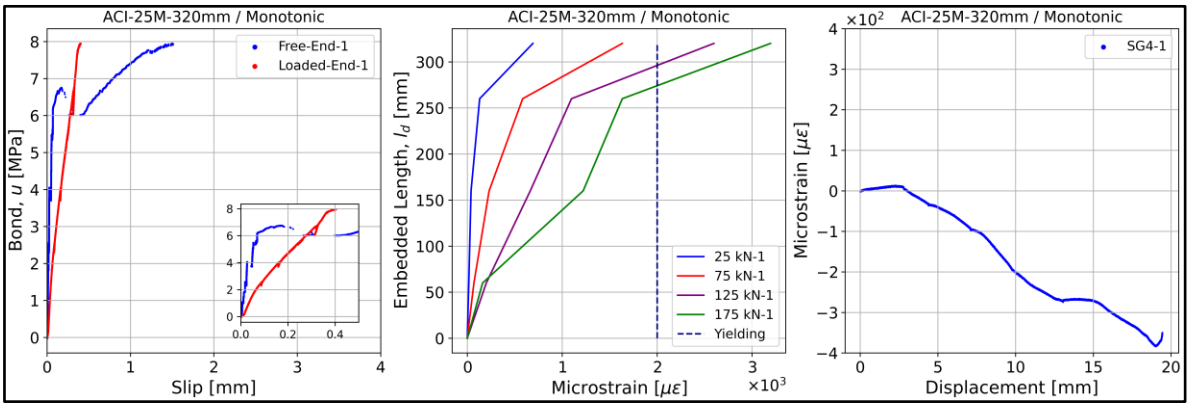

Figure 4-76: ACI-25M-320-M results.

The strain profile of the rebar shows an incremental strain development up to a load of 125 kN, while there is a substantial jump from SG1 to SG2 at 175 kN, which was close to the point where the splitting crack manifested. The strains at the loaded end exceeded 2000 micro-strains, meaning the embedded region was long enough to allow a partial yielding of the 25M rebar on the outside of the beam-end. However, the strains in the embedded section remained in the elastic region throughout the test, which is in line with the

experienced failure mechanism. On the other hand, the concrete strain profile shows a slightly linear increase in the compression zone until the failure point.

Figure 4-77: ACI-25M-320-M tested sample.

Figure 4-77 presents the specimen after the completion of the test, where the splitting longitudinal failure is evident. When compared to the splitting/pullout failures of the 15M bars, this specimen had a more sudden and explosive crack development, which is due to the 25M rebar being able to bear higher stresses, and the embedment length being 44% of the minimum required by the CSA A23.3. Therefore, the strains in the embedded section were not expected to reach the yielding limit. Furthermore, it is also possible to notice the cracking at the bottom support that provoked the jumps in the free end bond.

Figure 4-78 presents the results of the twin specimen tested under the cyclic loading protocol. This beam-end was initially subjected to the fully reversed loading protocol with a peak load of 45 kN; therefore, it is possible it might have suffered previous accumulated damage before the tension cyclic protocol run. As observed in the bond curves, the cyclic influence of each deformation step in the build-up of the curve can be appreciated upon

reaching the bond peak at almost 5 MPa. The peak bond stress was 37.5% lower than the monotonic test for the same configuration, which implies the damage accumulation due to the extended inner cracking.

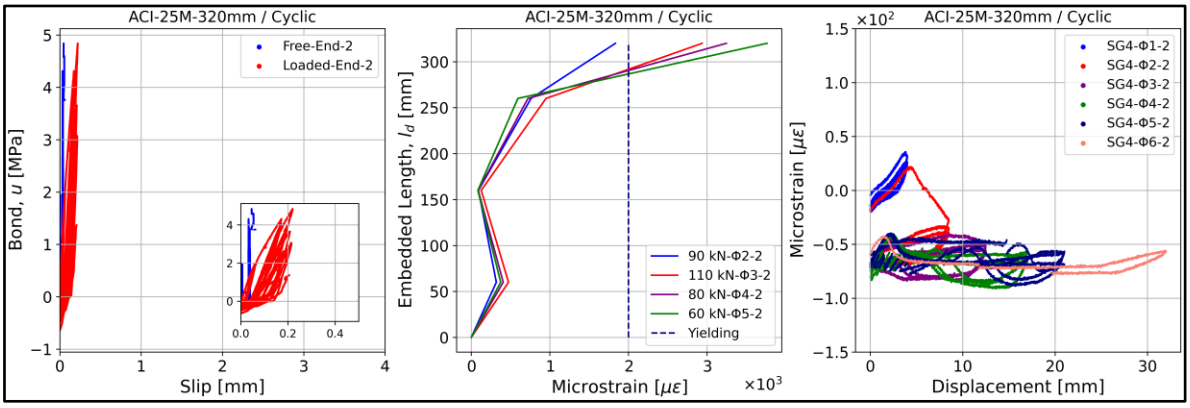

Figure 4-78: ACI-25M-320-C results.

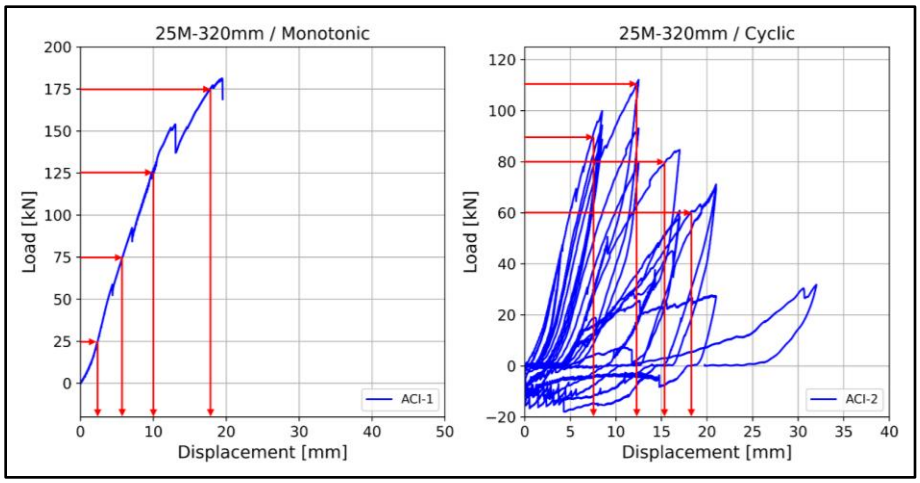

Figure 4-79: ACI-25M-320mm loading stages.

In the case of the rebar strain profile (loading stages detailed in Figure 4-79), the loads used for each deformation step are not necessarily increasing, since the peak took place at early stages; therefore, higher deformation steps had lower peaks, as shown in Figure 4-34. For this test, the strains measured by SG2 remained low throughout the test, which could be attributed to a malfunctioning in the gauge. In any case, yielding did not penetrate to the location of SG3, which was placed at 50 mm from the loaded end.

Likewise, the concrete strain profile shows that after the second deformation step, the strain rapidly went from tension to compression. Given that the position of SG4 was the same as SG2, it is possible that local damage influenced the readings at the start of the cracking process. As the test progressed, the strain remained steady with the displacement until the ultimate failure.

Figure 4-80: ACI-25M-320-C tested sample.

Figure 4-80 presents the specimen during and after the test. On the left hand-side of the picture, the crack development at the bottom support is observed, which allowed the specimen to slide and rotate, leading to an induced crack running parallel to the confined area provided by the longitudinal stirrups. However, this effect manifested near the end of the test after the loading peak and most of the stiffness degradation was recorded. No major bond-induced splitting cracks were detected when the test was stopped, though the sample may have sustained an additional cycle if the extensive cracking had not prevented the test from continuing. This is also reflected in the load drop of the last cycle when compared to the peak load obtained at early stages (Figure 4-34).

The second mix tested under this configuration was the EMV and its monotonic results are presented in Figure 4-81. The peak bond stress was lower than the ACI specimen, although this test was influenced by a coupler sliding that prevented a further load increase, as the coupler bolts were not able to secure the grip. It is presumed that without this issue, the failure load of both specimens, and consequently their bond stresses, should have been similar. When compared to the ACI results, the loaded end slip was slightly higher beyond a bond stress of 6 MPa, which suggests a deeper strain penetration.

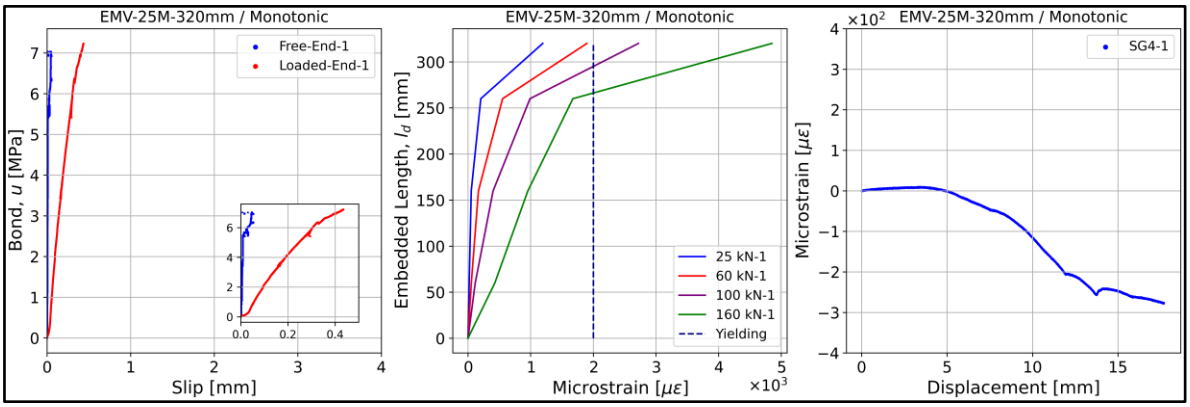

Figure 4-81: EMV-25M-320-M results.

In terms of the strain profile, the strain development of the rebar presented an almost linear behaviour up to 100 kN. However, the SG1 readings increased significantly between 100 kN and 160 kN, which was close to the failure point. For this loading stage, it is observed that the SG3 readings remained below the nominal yielding point of 2000 micro-strains, meaning the rebar inside the embedded region did not yield. Nevertheless, they are higher than the values obtained for the ACI sample. Meanwhile, the concrete strain profile shows a compressive strain development beyond a 5 mm displacement, from which it linearly increased until the 12 mm mark, where it started to flatten. This also corresponds to the onset of the coupler sliding, where the load could not keep increasing.

Figure 4-82 presents the failed specimen. At the peak load a splitting failure developed on the rebar plane, as showed on the right-hand side of the picture. The extended cracking

on the left-hand side was a consequence of the splitting crack, which caused the specimen to rotate and lift, and that accelerated the expansion of the crack at the bottom support, which propagated around the unconfined area of the longitudinal stirrups. However, due to the coupler sliding, the failure was not as explosive as with the ACI sample.

Figure 4-82: EMV-25M-320-M tested sample.

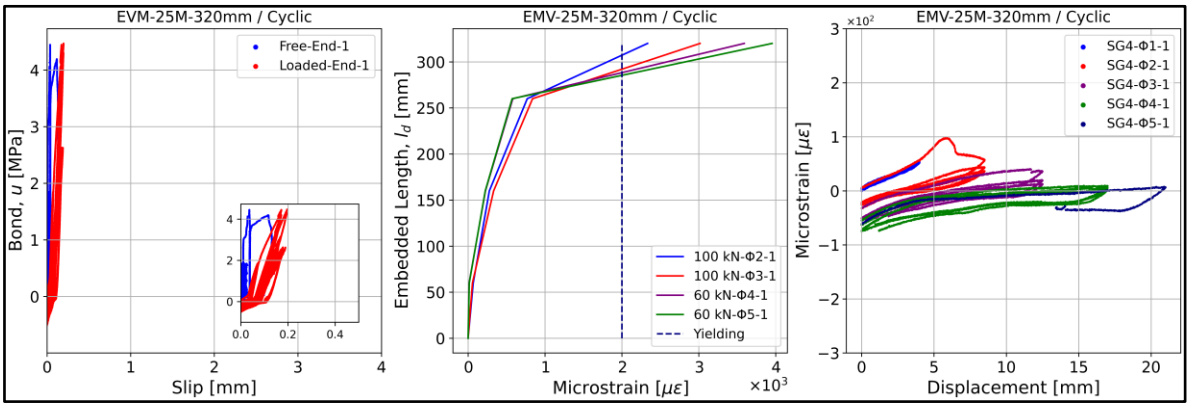

Figure 4-83: EMV-25M-320-C results.

Figure 4-83 presents the results of the twin specimen tested under the cyclic loading protocol. As with the ACI specimen, the bond peak under cyclic loading was inferior to the

monotonic one, which is attributed to the accumulated damage from the successive cycles. The bond peak was close to 4.5 MPa, which is slightly lower than the 4.8 MPa reached for the ACI combination. The bond slip of the loaded end shows the evolution throughout each deformation step, while the free end shows a jump at 0.2 mm, which can be related to the widening of the cracks at the bottom support that were interfering with the LPs readings.

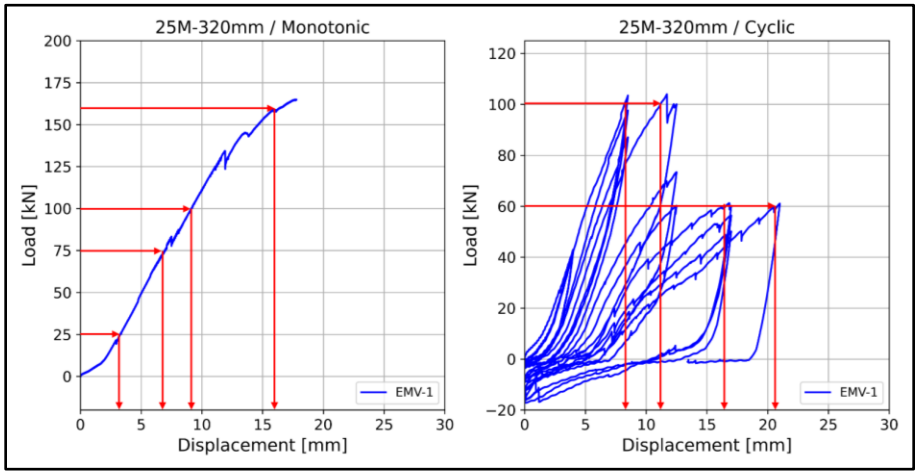

Figure 4-84: EMV-25M-320mm loading stages.

The strain profile of the rebar (loading stages detailed in Figure 4-84) indicates that neither of the strain gauges placed on the embedded section experienced localized yielding, which correlates with the shape of the load v displacement curve (Figure 4-37). As with the ACI specimen, the test was stopped when the displacement showed signs of load stabilization and not further degradation.

Visual observations indicated that the cracking at the bottom created an unstable equilibrium state at the bottom support, causing the specimen to move and rotate; hence impacting the continuation of the test, as the results were not going to be reliable anymore. It is believed the splitting failure might have completely propagated had the test completed one or two extra steps without this cracking effect.

The concrete strain profile shows a similar trend, with the first four steps taking place in the tension region. From the fifth step onwards, the strain remains almost constant with a slight compression when the displacement returned to zero, mainly due to the compression of the rebar, which suffered an elongation in the loaded end, as showed by the readings of SG5 at values above 2000 micro-strains. This concrete strain behaviour can be an indicator of the cracks developing in the embedded region of the rebar, which increased as the test progressed.

Figure 4-85 shows the specimen after the end of the test. As observed on the left-hand side, the localized crack at the bottom support interfered with the readings of the free end slip, which were reliable only until the widening of the crack made the concrete touch the flat bar connected to the rebar. On the other hand, the right-hand side shows no visible splitting cracks, similar to the ACI beam-end as the test was stopped before the splitting cracks could have expanded to the surface.

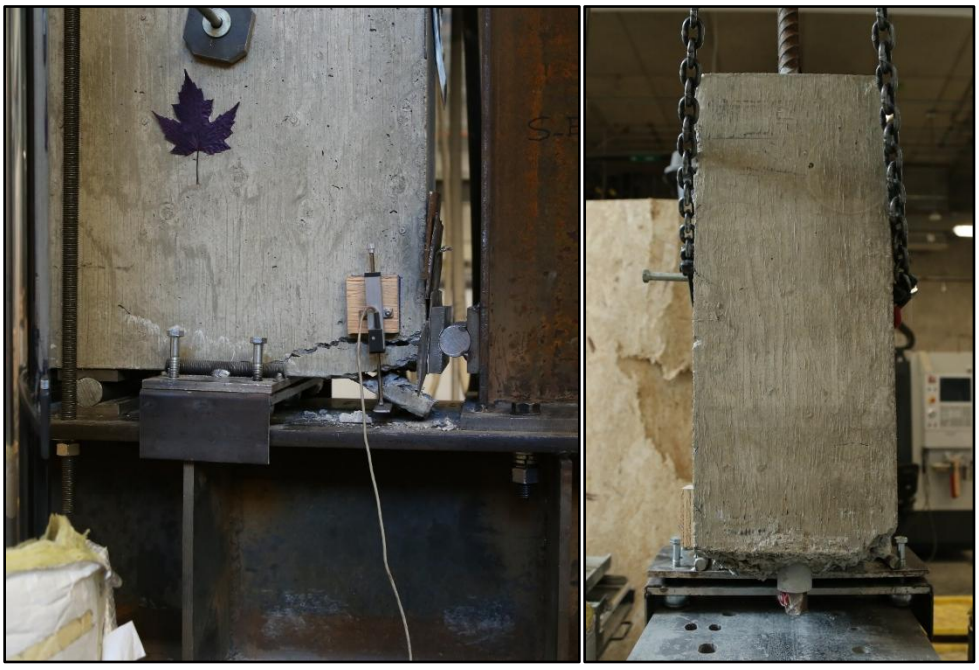

Figure 4-85: EMV-25M-320-C tested sample.

Figure 4-86 presents the monotonic results of the EMVc mix. The bond v slip plot indicates a lower bond peak than the ACI and EMV samples, just above 5 MPa. The free end slip presents a noticeable jump at almost 2 MPa due to cracking at the bottom support, which reflected on the readings coming from the LPs. The loaded end, on the other hand, indicates a more linear increase until the failure point, as the strain measurements coming from the gauges were smoother.

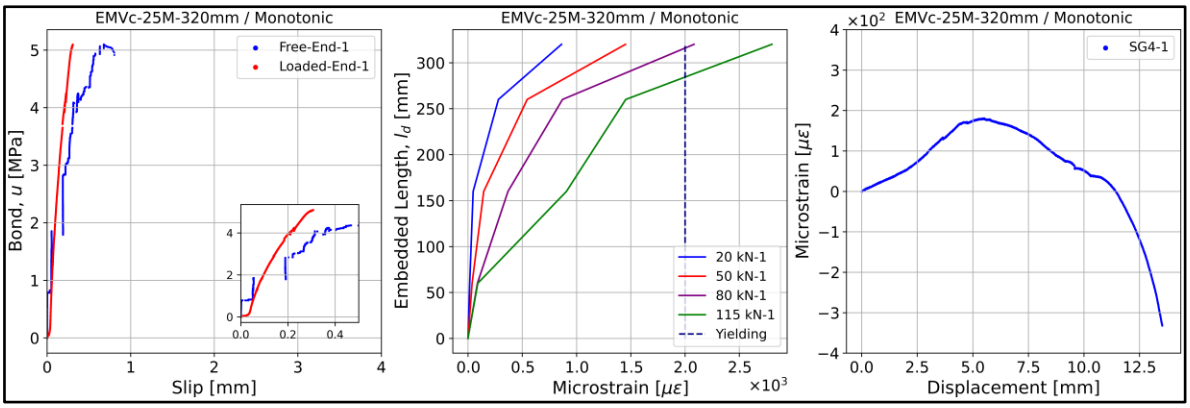

Figure 4-86: EMVc-25M-320-M results.

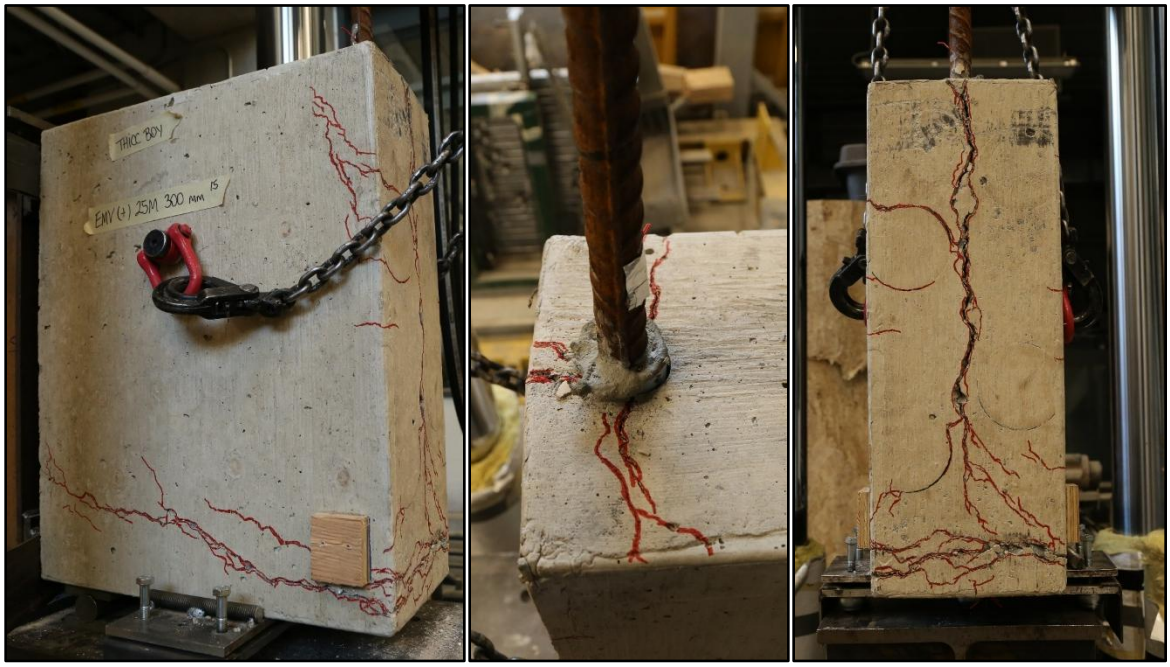

Figure 4-87: EMVc-25M-320-M tested sample.

The rebar strain profile showcases a proportional behaviour between SG1 and SG3 for the first three load stages, while a significant increase in the readings of SG2 was observed at 115 kN. As with the previous combinations, there was no yielding in the embedded region, as all strain gauges remained below the 2000 micro-strain thresholds. However, the readings from SG5 indicate the rebar was yielding outside the beam end. On the other hand, the concrete strain profile shows a constant tension increase up to a displacement of 6 mm, followed by a transition into the compression zone. This change might be an indication of the onset of internal cracking due to the constant load increase.

Figure 4-87 presents the beam-end after completing the test. As observed, the failure was due to the development of a longitudinal splitting crack, as experienced with the ACI and EMV samples. The extent of the cracking is evident in the middle and right-hand sides of the figure. Meanwhile, the cracks at the support expanded in a similar fashion to the EMV sample, and they were enhanced by the rotation sustained after the sudden splitting failure.

Finally, Figure 4-88 presents the results of the twin specimen tested under the cyclic loading protocol. As experienced with the previous cyclic beam-ends of this configuration, the bond peaks were reduced when compared to the monotonic results, in this case by around 10%. The loaded end slip presents a much more uniform behaviour since the readings were not affected by the cracking at the bottom support.

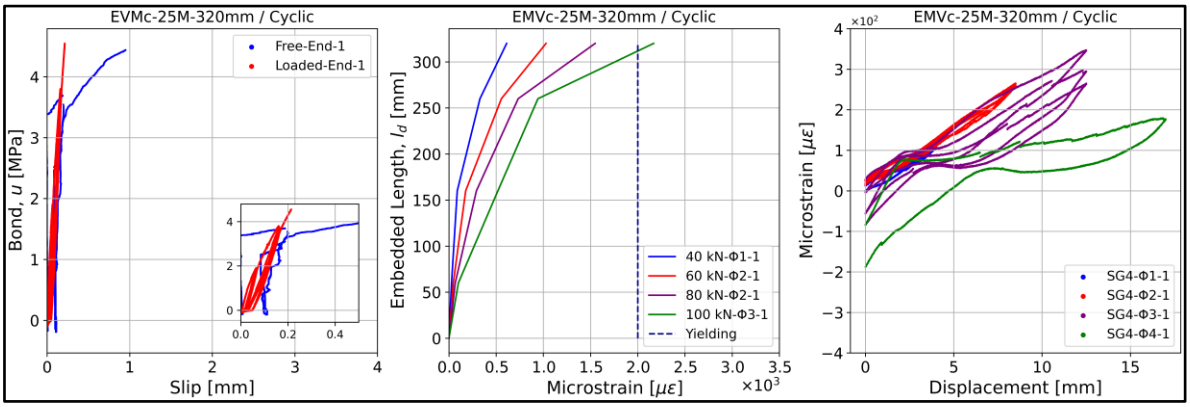

Figure 4-88: EMVc-25M-320-C results.

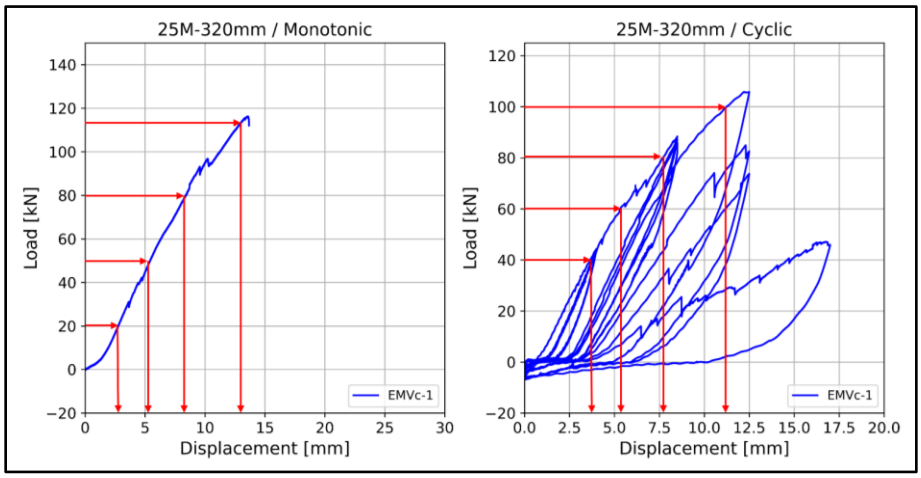

Figure 4-89: EMVc-25M-320mm loading stages.

The rebar strain profile (loading stages detailed in Figure 4-89) shows a proportional increment in the strain distribution across all gauges for the considered load stages. However, unlike the ACI and EMV mixes, the results were reliable only until the third deformation step, where the gauges started to present inaccurate readings. Therefore, the failure started to take place in the initial stage of the fourth step, which was earlier when compared to the other two combinations. The profile also shows the rebar was not yielding in the embedded region, which is aligned with the failure mechanism, a splitting failure taking place before yielding.

The concrete strain profile seems to confirm the previous assessment regarding the start of failure development. The strain starts to show degradation throughout the third deformation step, and during the fourth the strain tends to remain constant as the displacement increases, extending into the compression zone under unloading.

The final state of the beam-end is presented in Figure 4-90. As with the previous combinations, the test was influenced in the final stages by the development of the cracks at the bottom support. Nonetheless, the effects were worse in this case as the cement paste proved to be very fragile. On the right-hand side of the picture, it is possible to see how the crack developed around the aggregates, which indicates a lower tensile strength for the

cement paste. The extensive damage and strength decay after the beginning of the fourth cycle resulted in the test being stopped. However, it is possible that the splitting failure would have occurred with one extra deformation step.

Figure 4-90: EMVc-25M-320-C tested sample.

4.7. Discussion

4.7.1. Reversed cyclic loading protocol viability

Several challenges were experienced when trying to apply the fully reversed loading protocol. As observed in Figure 4-31, even for deformation steps that were below the yielding levels, the behaviour in tension and compression was highly asymmetrical. The former developed as expected with linear increments, while the latter could not generate much load resistance. For the specimen combinations containing the 15M bar, the effects became evident as soon as the deformation went onto the second step at 5 mm. Meanwhile, the 25M rebar was not able to go beyond the first step, as the load under compression was almost zero.

Figure 4-91: Clearance between PVC bond breakers and reinforcement.

The main reason behind this phenomenon was the location of the embedded section in the middle of the beam-end. The original intention of this decision was to avoid interactions close to the supports, which could have influenced the results by generating confinement stresses. However, this consequently increased the length of the free bar. For the 170 mm of embedment, this distance was approximately 227.50 mm, while the 320 mm samples had a reduced section of 152.50 mm.

The PVC conduits used to break the bond outside the embedment length were chosen to fit as tight as possible and to restrain any possible lateral movement. The 15M bar had less than 5 mm of clearance, while the 25M bar had less than 10 mm, as shown in Figure 4-91. Nevertheless, the distance between the beam-end surface and the bar lock coupler, which was 92 and 108 mm for the 15M and 25M rebars, respectively; resulted in unbraced bar lengths that exceeded the 600 mm required by CSA A23.3 as the maximum spacing for transverse reinforcement.

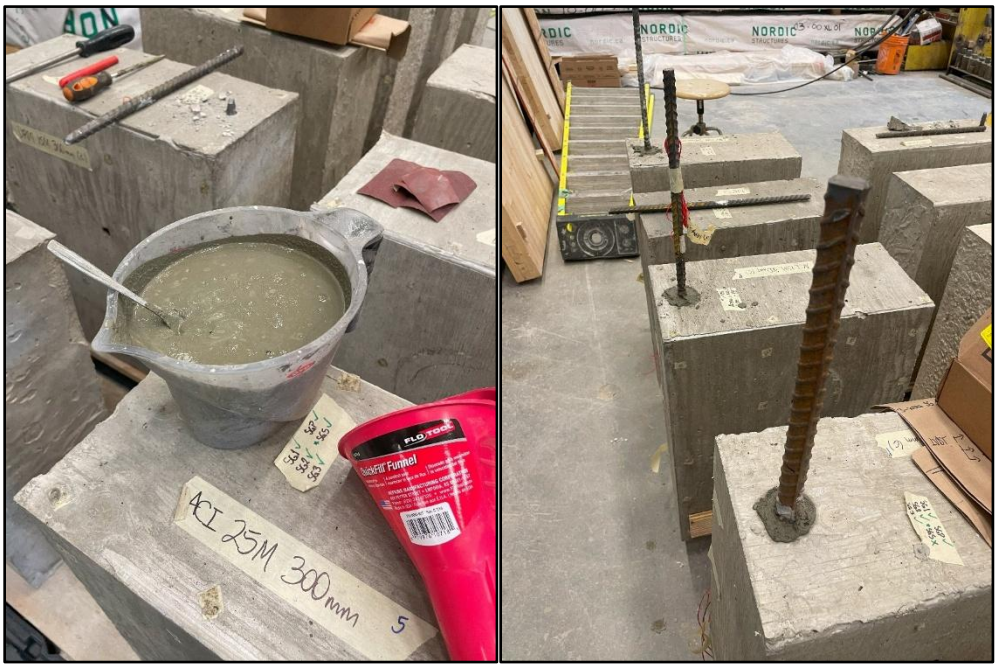

Figure 4-92: Grouting of the gaps between bond breakers and reinforcement.

As observed in Figure 4-10, the assembly of the top flat bars used to connect both columns provided minimal clearance to allow the full tightening of the coupler bolts. Therefore, during the design stages, the distance between the end of the couplers and the surface of the beam-ends was checked to comply with the elastic buckling thresholds. Additionally, the gaps between the bond breakers and the rebars were later filled with a non-shrink grout, as observed in Figure 4-92, to further reduce the free section.

Despite these preventive measures, the compression load peaks were much lower than the expected buckling limits. These thresholds were computed without the restraining effect provided by the grout; therefore, the effective length considered the unbonded section inside the beam-end, and the distance from the edge of the beam-end to the coupler. For the 25M rebar the limit was 157 kN, while for the 15M rebar the buckling loads for the 170 and 320 mm of embedment should have reached 47 kN and 58 kN, respectively.

The discrepancies between the peaks of Figure 4-31 and the buckling thresholds suggest that another mechanism was responsible for the observed behaviour, likely the P-delta

effect (or $P - \Delta$). A slight offset in the centreline of the load application point can induce additional bending moments in the bars and affect their stability in compression. As appreciated in Figure 4-93, a contributing factor for the occurrence of this phenomenon may have been the offset generated in the welding of the bar lock coupler to the plate that was bolted to the top girder, which prevented the true verticality.

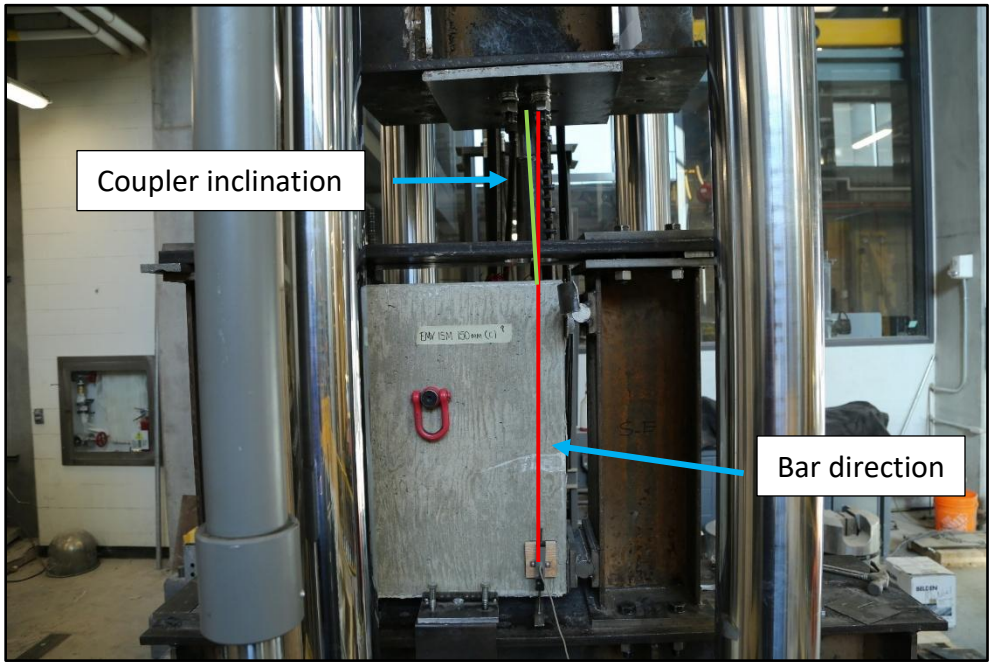

Figure 4-93: Offset between the rebar and the bar lock coupler.

When analyzing the readings coming from the strain gauges of the specimens tested under the reversed cyclic protocol, there are two indicators that signal the development of P-delta effects. The first one is related to the strain evolution of the strain gauges installed on the rebar, as seen on the central plot of Figure 4-94, Figure 4-95, and Figure 4-96. From SG1 to SG3, there is an almost mirrored strain evolution across the deformation steps, which seems to indicate the embedded section did not present any anomalies.

However, this behaviour does not apply to SG5 (installed outside the specimen). In the case of the ACI-15M-170mm (Figure 4-94), three deformation steps with displacements of 2.5, 5.0, and 7.5 mm were tested. The first step showed a normal behaviour, but the

response became different after the first tension peak at 5 mm, at which point the gauge started to exhibit an asymmetric evolution. As the test progressed, the tendency remained, and further observations confirmed the rebar was bending during the compression stages and stretching after regaining its original shape once the test went onto the tensile zone.

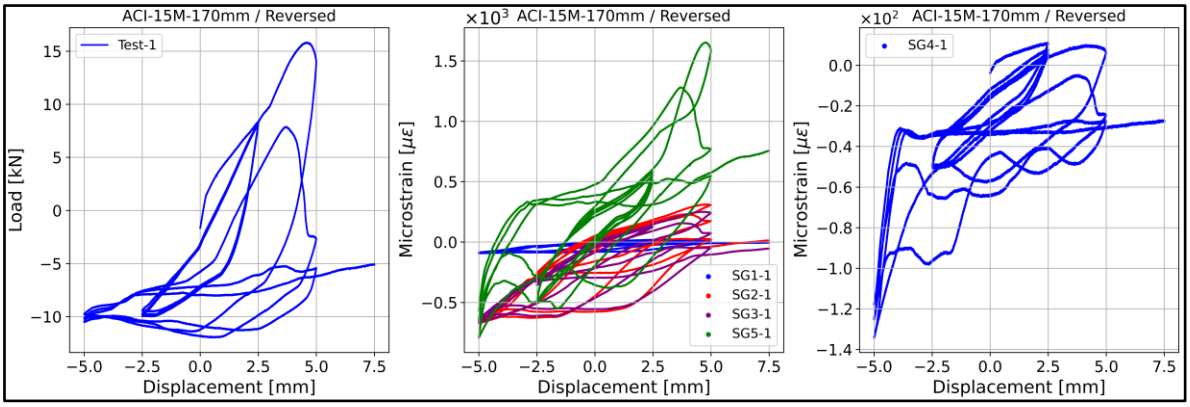

Figure 4-94: ACI-15M-170-C reversed strain gauge readings.

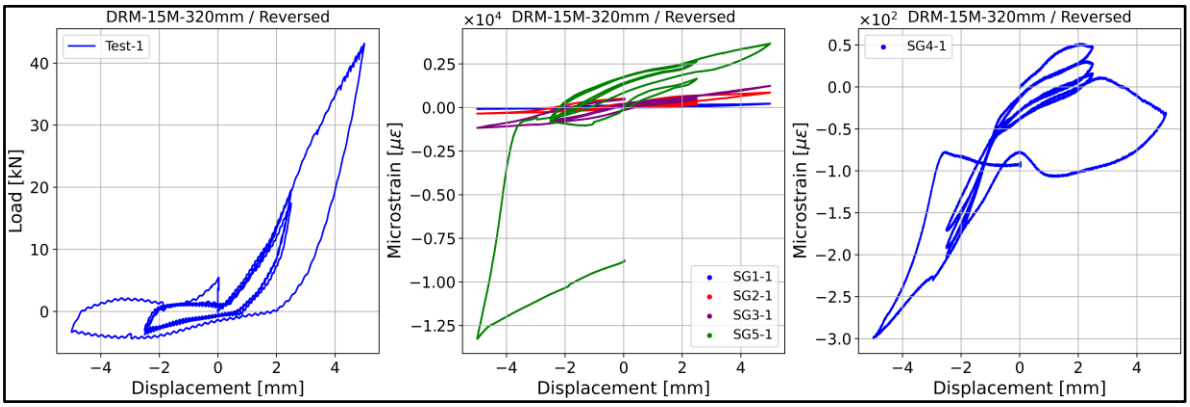

Figure 4-95: DRM-15M-320-C reversed strain profile.

In the case of the DRM-15M-320mm combination (Figure 4-95), the test was stopped upon reaching 5 mm of displacement. The first deformation step was an early indicator as the load peaks in tension and compression were different. Furthermore, it clear that the P-delta effect started to take place during the last repetition of said step, as there is a drop in the tensile peak. In the same fashion, the ascending branch of the second step (up to 5 mm) shows a proportional peak in tension, but a sudden increase as soon as it went onto the

compression field. When the bending takes place, one side of the neutral axis is exposed to compression, and the other to tension; therefore, the readings can be interpreted as the bar bending and SG5 capturing the compression strains due to its position on the rebar.

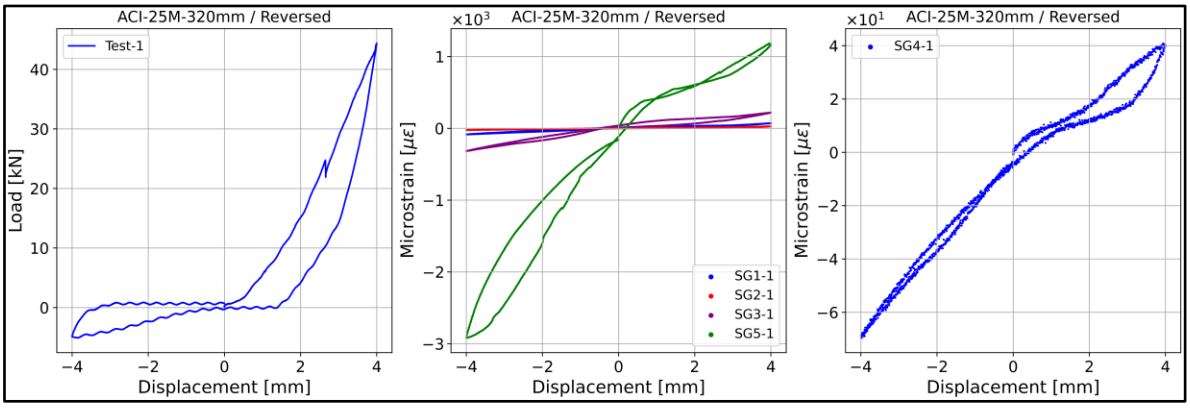

Figure 4-96: ACI-25M-320-C reversed strain profile.

The case of the ACI-25M-320mm beam-end (Figure 4-96) was almost identical to the previous case, but it manifested within the first deformation step, which reached 4 mm of displacement. The readings from SG5 indicate a higher compression strain, and when considering the load readings were below 10 kN, the rebar was suffering from a localized bending effect when applying the reversed load.

The evolution of the concrete strain measured by SG4 presents another interesting take. The location of this gauge was the same as SG2, thus measuring the strain in the middle of the beam-end. For both 15M combinations, there is a mirrored evolution throughout the first deformation steps (the 25M specimen did not experience this as it only went through one cycle), which changed as soon as the bending on the outside of the beam-end started to take place. For all three combinations, there is noticeable increment in the compression strain. This behaviour could be attributed to the bent rebar touching the specimen's edge, or to an extra internal bending in the region where the bond was broken (inside the PVC conduits between the embedded region and the beam-end surface).

Since this last phenomenon could not be physically corroborated because it took place inside the specimen, plus the clear bending on the outside of the specimen, it was determined to cancel the fully reversed loading protocol to avoid further damage. Finally, to guarantee accurate and consistent results, the consensus was to switch to the tension cyclic protocol, as the mentioned risks could be better mitigated.

4.7.2. Tension cyclic protocol assessment

The decision of transitioning from fully reversed cyclic loading to tension cyclic loading was aimed at mitigating the factors that affected the former. The advantage of this alternative was the ability to still test the cyclic bond behaviour in a consistent and reliable way, where the monotonic tests would provide the envelope curve. However, the trade-off was to miss the compression strains and pinching development, which could have provided a better understanding of the cracking patterns.

Based on the results detailed in the previous section, the general view of the loading protocol change was positive since it allowed the study of the cyclic bond behaviour, the primary objective of the research. Given the nature of its implementation, a few details need to be discussed with respect to their effects on the overall results.

As observed in the results section, the cyclic protocol induced compression on the rebar every time a cycle was finished. The protocol was run under displacement-control, meaning that each deformation step was set to return to the original position from where the actuator stroke started to pull once the test was initiated. Naturally, as the test progressed and the deformation steps increased, the development of inelastic deformations (either bar yielding or slip) resulted in the elongated section being compressed as the actuator returned to zero.

As shown in Figure 4-97, the elongation of the rebar induced bending effects on the bar section between the beam-end and the coupler. The bending increased proportionally with

the displacement, causing a drop in the load peaks of the second and third repetitions of the last deformation steps, as the bar was pulled until it was straight and ready to pick the load up again. The 15M rebar was more susceptible to this effect given its higher slenderness when compared to the 25M one.

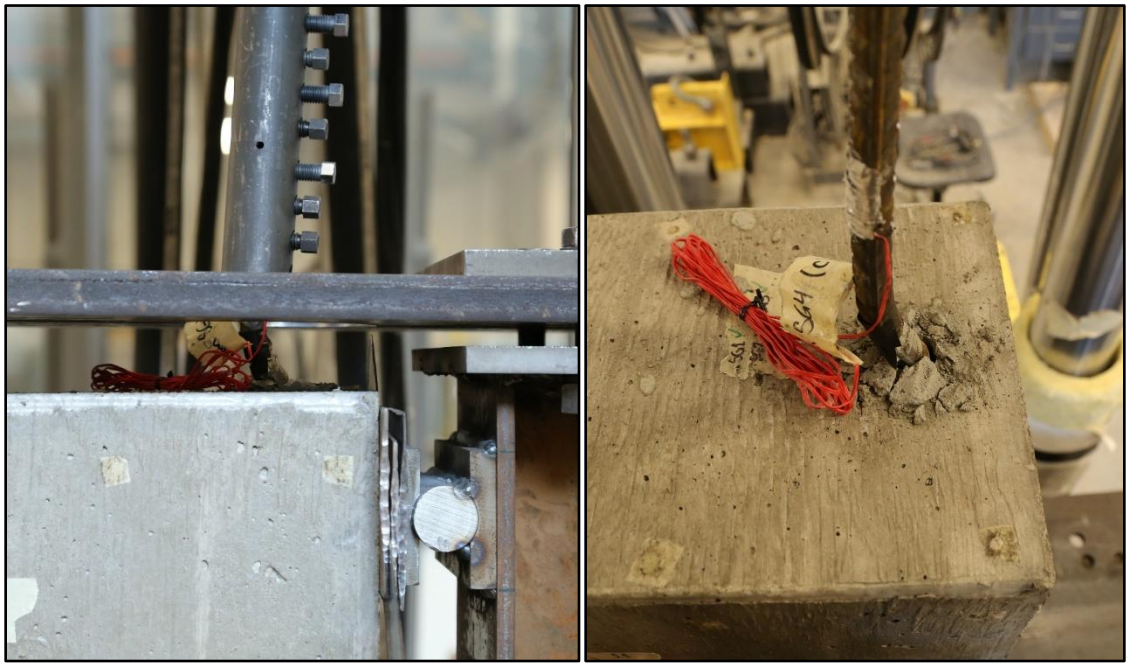

Figure 4-97: Bending due to bar elongation in cyclic tests.

The first combination, 15M – 170 mm, was not highly influenced as the failure took place just past the yielding plateau, where the strains were around 2 – 4%. On the other hand, the 15M – 320 mm combination (seen in Figure 4-97) suffered the most as the embedment allowed a full bar development until its rupture, where the strain was around 18%. It is possible that bending due to bar elongation could have accelerated the failure mechanism of the ACI and EMV mixes, which was a bar rupture (DRM combination failed prematurely due to strength degradation), by inducing local fatigue in the necking section.

In contrast, the 25M – 320 mm combination experienced minor bending effects due to the robustness of the rebar when compared to the 15M bar for the same embedment length, and because the test was run in the elastic zone. Based on the results of the previous

section, localized yielding was induced on the rebar outside the beam-end, but the strains were not high enough to cause the same bending effects observed in the 15M rebars.

Another factor that influenced the results is the cracks that developed at the bottom support and that crossed the path of the LPs. As explained in the results section, these cracks originated as an undesired side-effect of the shim plates adjustment, which were used to fill all gaps and restrain any possible movement. It is possible that an uneven concrete or plate edge might have induced a local splitting failure due to the installation process, where each plate was hammered until the gap was filled.

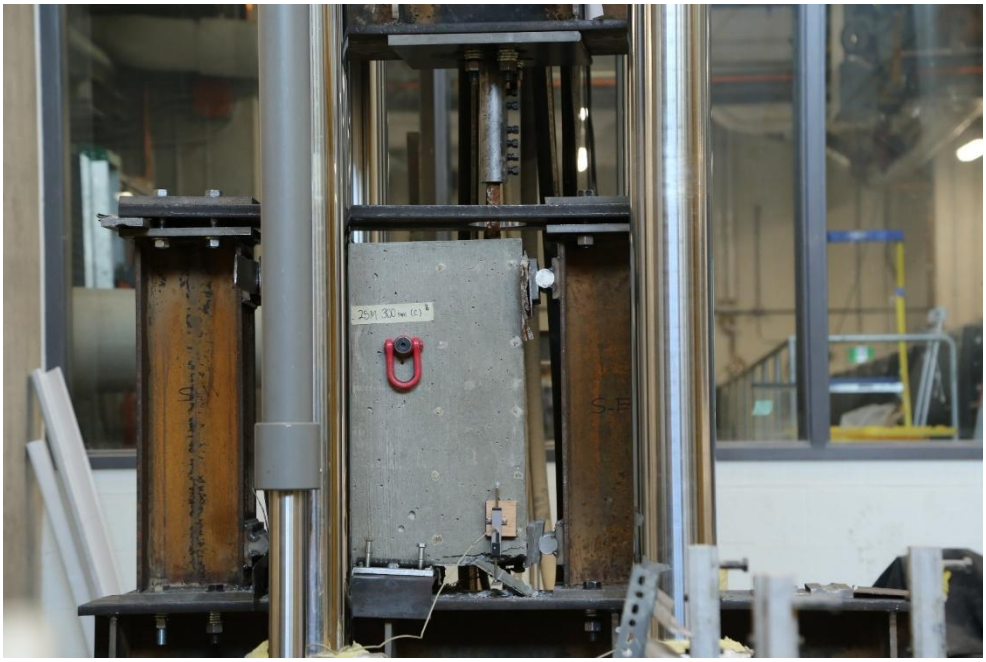

Figure 4-98: Damage sustained due to local cracking at the bottom support.

Most of the cracks manifested once the test started and all the slack was removed in the first pulling stages. The immediate consequence was the loss of reliable LP measurements as soon as the cracks were wide enough to cause local concrete spalling, although the effects were more noticeable in the cyclic tests. For those cases, once the cracks developed, they caused an unstable equilibrium state at the bottom support, which induced a rotation in the specimen as it was free to align with the inclination of the coupler.

For the 15M combinations, the effect was mitigated by realigning the shim plates as the test progressed. However, it was not possible to replicate the same measures for the 25M combination given the higher load levels.

Figure 4-98 shows the crack effects. Once they started to develop, they allowed the specimen to lift and rotate. Nevertheless, most of these effects were contained by the top supports. Only when the deformation was high enough (typically in the last deformation step), the unstable equilibrium was lost and the specimen suffered a final rotation that induced the cracks around the unconfined area, as presented in the results section.

Finally, it is important to note potential effects associated with the strain rates of the loading protocol. As the duration of each deformation step was set at 10 min, the same three repetitions had to take place before moving onto the next stage. This scenario meant that for higher displacements, the loading rate was also higher to fulfill the time requirements. As detailed in the literature review chapter, the loading rates for quasi-static tests are usually around $10^{-5}\ sec^{-1}$, while the loading rates of real dynamic seismic events are on the order of $10^{-3} - 10^{-2}\ sec^{-1}$. The monotonic tests developed in the quasi-static region as the rate was slow and uniform. Meanwhile, the maximum cyclic loading rates for the 15M specimens were on the $10^{-4}\ sec^{-1}$ region during the last deformation steps, sitting between the two spectrums.

The strain rate effects were considered through the respective dynamic increasing factors (DIF) (Malvar, 1998). As detailed in the results section, there are two factors that apply for the yielding and ultimate regions, respectively. The reasoning behind the factors is that when higher rates are applied, the material does not have enough time to relax; therefore, there is an increase in its apparent properties for the same deformation levels. The factors were considered in the scaling of the loads and were applied according to the failure mechanism. In almost all cases, the effects were below 3%, and only one case had an 8% reduction; therefore, it can be concluded their effects were minor.

4.7.3. Bond behaviour compared to previous studies

To validate the results of the tests, it is important to compare them with previous studies if available. Table 4-11 introduces a summary of the failure mechanisms for each of the beam-ends analyzed in the results section. The last number of the mix label corresponds to the test run from which the results were obtained. In most cases, only one test run was required; however, in specific cases more than one test was required since the beam-ends experienced a setup issue or were used for the testing of the reversed loading protocol. The failure mechanisms are divided into two categories: bond failure and bar rupture. The specific details of the bond failure (splitting or splitting/pullout failure) are also provided.

Table 4-11: Beam-ends' failure mechanisms summary.

Mix Label	Test Run	Failure	Notes
ACI-15M-170-M1	1	-	Stopped in the elastic region
ACI-15M-170-M2	2	Bond failure	Splitting/pullout failure
ACI-15M-170-C3	3	Bond failure	Splitting/pullout failure
ACI-15M-320-M1	1	Bar rupture	-
ACI-15M-320-C1	1	Bar rupture	Stopped before bar rupture (setup issue)
ACI-25M-320-M1	1	Bond failure	Splitting failure
ACI-25M-320-C2	2	Bond failure	Stopped before full splitting
DRM-15M-320-M1	1	-	Stopped before bar rupture (setup issue)
DRM-15M-320-M2	2	Bar rupture	-
DRM-15M-320-C2	2	Bond failure	Splitting/pullout failure
EMV-15M-170-M1	1	Bond failure	Splitting/pullout failure
EMV-15M-170-C1	1	Bond failure	Splitting/pullout failure
EMV-15M-320-M1	1	Bar rupture	-
EMV-15M-320-C1	1	Bar rupture	-
EMV-25M-320-M1	1	Bond failure	Splitting failure
EMV-25M-320-C1	1	Bond failure	Stopped before full splitting
EMVc-15M-170-M1	1	-	Stopped before bar rupture (setup issue)
EMVc-15M-170-M2	2	Bond failure	Splitting/pullout failure
EMVc-15M-170-C1	1	Bond failure	Splitting/pullout failure
EMVc-25M-320-M1	1	Bond failure	Splitting failure
EMVc-25M-320-C1	1	Bond failure	Stopped before full splitting

Since the mix designs and beam-end configurations were specifically tailored for this project, it is possible to establish a comparison with the available literature by normalizing the average bond (u) stress. This normalization is traditionally made using the square or fourth root of the compressive strength values, since they provide a better adjustment while accounting for the effect of the compressive strength.

Table 4-12: Project's normalized bond results.

Mix Label	f'_c [MPa]	Bar Size	l_d [mm]	c/d_b	T_b [kN]	u [MPa]	$\frac{u}{\sqrt{f'_c}}$	$\frac{u}{\sqrt[4]{f'_c}}$
ACI-15M-170-M1	46	15M	170	2.50	70.87	8.29	1.22	3.18
ACI-15M-170-M2	46	15M	170	2.50	88.92	10.41	1.53	4.00
ACI-15M-170-C3	46	15M	170	2.50	90.68	10.61	1.56	4.07
ACI-15M-320-M1	46	15M	320	2.50	115.07	7.15	1.05	2.75
ACI-15M-320-C1	46	15M	320	2.50	115.07	7.15	1.05	2.75
ACI-25M-320-M1	46	25M	320	1.59	201.41	7.89	1.16	3.03
ACI-25M-320-C2	46	25M	320	1.59	122.63	4.80	0.71	1.84
DRM-15M-320-M1	42	15M	320	2.50	108.56	6.75	1.04	2.65
DRM-15M-320-M2	42	15M	320	2.50	115.07	7.15	1.10	2.81
DRM-15M-320-C2	42	15M	320	2.50	103.02	6.41	0.99	2.52
EMV-15M-170-M1	45	15M	170	2.50	104.00	12.17	1.81	4.70
EMV-15M-170-C1	45	15M	170	2.50	92.60	10.84	1.62	4.18
EMV-15M-320-M1	45	15M	320	2.50	115.07	7.15	1.07	2.76
EMV-15M-320-C1	45	15M	320	2.50	115.07	7.15	1.07	2.76
EMV-25M-320-M1	45	25M	320	1.59	183.26	7.18	1.07	2.77
EMV-25M-320-C1	45	25M	320	1.59	113.28	4.44	0.66	1.71
EMVc-15M-170-M1	36	15M	170	2.50	64.18	7.51	1.25	3.07
EMVc-15M-170-M2	36	15M	170	2.50	84.96	9.94	1.66	4.06
EMVc-15M-170-C1	36	15M	170	2.50	80.62	9.43	1.57	3.85
EMVc-25M-320-M1	36	25M	320	1.59	129.16	5.06	0.84	2.07
EMVc-25M-320-C1	36	25M	320	1.59	115.22	4.51	0.75	1.84

Table 4-12 presents a summary with the normalized bond stress values obtained for this project. The compressive strength (f'_c) for each mix design is the average value at 56 days, as detailed in the previous chapter. Moreover, besides the bar size and embedment length (l_d), the cover-to-bar-diameter ratio (c/d_b) is also included as it will be helpful to understand the configurations of the upcoming references, since not all of them had the

same bar sizes or cover values. The bond loads (T_b) correspond to the scaled peak loads of each test, while the bond stresses were computed according to Eq. 4.6 – 3.

Three studies were selected to be used as references given their similarities in the mix design, compressive strength, and beam-end configuration. The details for each one are presented in Table 4-13, Table 4-14, and Table 4-15.

Table 4-13: Bond reference #1 (Rockson et al., 2020, 2021).

Mix Label	f'_c [MPa]	Bar Size	l_d [mm]	c/d_b	T_b [kN]	u [MPa]	$\frac{u}{\sqrt{f'_c}}$	$\frac{u}{\sqrt[4]{f'_c}}$
NAC-0/0-A	55.5	15M	200	1.56	90.38	8.99	1.21	3.29
NAC-0/0-B	55.5	15M	200	1.56	86.68	8.62	1.16	3.16
RAC-25/100-A	36.3	15M	200	1.56	72.21	7.18	1.19	2.93
RAC-25/100-B	36.3	15M	200	1.56	78.30	7.79	1.29	3.17
NAC-0/0-A	55.5	15M	300	1.56	104.40	6.92	0.93	2.54
NAC-0/0-B	55.5	15M	300	1.56	105.30	6.98	0.94	2.56
RAC-25/100-A	36.3	15M	300	1.56	90.30	5.99	0.99	2.44
RAC-25/100-B	36.3	15M	300	1.56	101.30	6.72	1.11	2.74
NAC-0/0-A	55.5	15M	200	2.50	107.30	10.67	1.43	3.91
NAC-0/0-B	55.5	15M	200	2.50	101.03	10.05	1.35	3.68
RAC-25/100-A	36.3	15M	200	2.50	80.53	8.01	1.33	3.26
RAC-25/100-B	36.3	15M	200	2.50	78.52	7.81	1.30	3.18

The first reference is shown in Table 4-13 and consists of 12 beam-ends, with two cover values (25 mm and 40 mm), two embedment lengths, and a 15M rebar as the bond testing bar. Two mix designs were used, the traditional ACI mix is represented in the NAC combinations. Meanwhile, the RCA was incorporated using the DRM mix and numbers between the "/" character indicate the content of recycled fine and coarse aggregates, respectively. Finally, "A" and "B" represent the primary and duplicate specimen.

The specimens with 200 mm of embedment can be compared to the 170 mm combinations of this project, while the 300 mm ones can be associated with the 320 mm samples, respectively. The first detail worth mentioning is the effect of the concrete cover,

whose increment leads to higher bond values. The second detail is the effect of increasing the embedment length from 200 mm to 300 mm, with the latter being enough to allow a full bar development.

All beam-ends failed either due to pure splitting or a pullout/splitting mechanism; therefore, the ultimate load peaks are inferior to the ones obtained in this project, where the 320 mm of embedment allowed the rebar rupture. Nevertheless, the bond peaks of the natural aggregate mix are like those obtained for the ACI and DRM mixes.

When analyzing the normalized bond of the previous study, which allows to neutralize the effect of the compressive strength, it is possible to observe that, on average, the ACI mix peaks are 10% higher when using than their reference counterparts. Nevertheless, the differences in the recycled concrete are much lower, sitting around 3%. Even though the mix design was the same (DRM mix), the composition of the reference mixes' is different since it incorporates 25% of fine RCA. However, what is clear is that the bond performance of the RCA mixes is lower than their natural aggregate counterparts, mainly due to the excess of residual mortar, whose effect was discussed in the previous chapter.

Table 4-14: Bond reference #2 (Butler et al., 2011, 2015a).

Mix Label	f'_c [MPa]	Bar Size	l_d [mm]	c/d_b	T_b [kN]	u [MPa]	$\frac{u}{\sqrt{f'_c}}$	$\frac{u}{\sqrt[4]{f'_c}}$
NAC-30-375A	34.50	25M	375	1.59	169.90	5.68	0.97	2.34
NAC-30-375B	34.50	25M	375	1.59	170.60	5.70	0.97	2.35
NAC-50-375A	49.00	25M	375	1.59	179.50	6.00	0.86	2.27
NAC-50-375B	49.00	25M	375	1.59	170.90	5.71	0.82	2.16
RAC1-30-375A	30.90	25M	375	1.59	150.80	5.04	0.91	2.14
RCA1-30-375B	30.90	25M	375	1.59	151.10	5.05	0.91	2.14
RCA1-50-375A	47.90	25M	375	1.59	161.90	5.41	0.78	2.06
RCA1-50-375B	47.90	25M	375	1.59	152.50	5.10	0.74	1.94
RCA2-30-375A	31.30	25M	375	1.59	148.80	4.97	0.89	2.10
RAC2-30-375B	31.30	25M	375	1.59	150.40	5.03	0.90	2.12
RAC2-50-375A	49.40	25M	375	1.59	164.60	5.50	0.78	2.07
RAC2-50-375B	49.40	25M	375	1.59	153.50	5.13	0.73	1.93

Table 4-14 presents the summary of the second reference. As with the previous case, 12 beam-ends made using conventional and recycled aggregate (proportioned with the DRM method) were considered. The bar size, embedment length, and concrete cover were 25M, 375 mm, and 40 mm, respectively; therefore, this reference is adequate to assess the performance of the combinations that included the 25M rebar in this project.

The key differences between these samples are the design compressive strength and mix design types. The design strength was divided between 30 MPa and 50 MPa, although the tested values presented slight variations. On the other hand, the mix design consisted of one conventional ACI concrete mix, while the two DRM mixes were made with coarse RCA coming from different sources. As detailed in the literature review chapter, RAC1 comes from crushed concrete from decommissioned regional sidewalk, curb, and gutter infrastructure. Meanwhile, RAC2 was produced from the crushing of apron and terminal structures from Pearson International Airport in Toronto, Canada (Butler et al., 2015a).

Similarly to the results of this study, all beam-ends suffered a splitting failure before reaching the yielding of the rebar. The bond peaks of the monotonic ACI and EMV specimens are 15% and 5% higher than the average of the 50 MPa beam-ends of this reference. However, the EMVc peak is 26% below the average of the conventional concrete designed for 30 MPa. Furthermore, when focusing on the mixes containing RCA and a design strength of 50 MPa, the closest to the EMV beam-end of this project in terms of configuration and performance, the peak load of the latter is on average 16% higher than its counterparts. Despite the different RMC across all RCA sources, this suggests the EMV mix is more effective at producing RCA concrete that can be closer to the performance of its conventional reference.

When comparing the average bond peaks, the results of this project are higher due to the shorter embedment length, which is 15% below the 375 mm of this reference, and the increased loading peaks as it was just mentioned. Therefore, when referring to the

normalized bond, it was expected to obtain higher contrasts. The values of the ACI and EMV specimens ended up being 38% and 27% higher than the average of the 50 MPa conventional mix of this reference.

Table 4-15: Bond reference #3 (Fathifazl et al., 2012).

Mix Label	f'_c [MPa]	Bar Size	l_d [mm]	c/d_b	T_b [kN]	u [MPa]	$\frac{u}{\sqrt{f'_c}}$	$\frac{u}{\sqrt[4]{f'_c}}$
CM-30	48.50	30M	262	1.85	145.44	6.01	0.86	2.28
EM-30	36.90	30M	250	1.85	0.00	0.00	0.00	0.00
CL-30	38.00	30M	280	1.85	179.74	6.95	1.13	2.80
CM-15	48.50	15M	279	3.25	113.59	8.10	1.16	3.07
EM-15	36.90	15M	261	3.25	140.11	10.68	1.76	4.33
CL-15	38.00	15M	320	3.25	124.82	7.76	1.26	3.13
CV-30	49.00	30M	263	1.85	152.79	6.29	0.90	2.38
EV-30	43.50	30M	260	1.85	176.75	7.36	1.12	2.87
CG-30	35.90	30M	265	1.85	174.51	7.13	1.19	2.91
CV-15	49.00	15M	287	3.25	115.70	8.02	1.15	3.03
EV-15	43.50	15M	274	3.25	142.55	10.35	1.57	4.03
CG-15	35.90	15M	291	3.25	114.24	7.81	1.30	3.19

Perhaps the most accurate reference to assess the performance of the EMV mix is presented in Table 4-15, as it was the only one that considered this mix proportioning method. As observed, three mix designs (ACI, DRM, and EMV), two bar sizes, and two concrete covers were considered. The target compressive strength was 35 MPa for all mixes, although fluctuations in the final values were due to the differences in the mix design technique, and the chosen coarse aggregate.

The failure of all 15M (but for CM-15) combinations despite the different mix designs was due to bar rupture. When analyzing the load peaks, they reached the ultimate capacity at embedment lengths that were in between the 170 mm and 320 mm used for this project. According to the rebars used in the tests, the 15M reference bars should have reached around 115 kN to reach their ultimate stress, except for CM-15, which presumably failed in the strain hardening region. Meanwhile, all 30M combinations had shorter embedment

lengths than the 320 mm used in this project and suffered from a bond splitting failure. The yielding load for this rebar was 331 kN, meaning that all of them failed in the elastic region.

When analyzing the normalized bond peaks of the 15M specimens made with the ACI (CL and CG) and EMV (EM and EV) mixes, regardless of the power used in the root, the values lie in between the range provided by the 170 mm and 320 mm specimens of this project. In the case of the ACI mixes, when averaging the normalized values of CL and CG using the square root, the value is almost the average of ACI-15M-170mm and ACI-15M-320mm (1.28 v 1.29, respectively). Meanwhile, when using the fourth root, the average of the reference (3.16) is 6.4% below the average of the ACI mixes of this project (3.37).

In the case of the EMV mixes, the average of the reference (1.66) is 15.6% higher than the average of this study (1.44) when using the square root, and 12% when using the fourth root (4.18 v 3.73, respectively). In contrast, the case of the DRM (CM and CV) mixes is different despite having a shorter embedment length. When using the square root, the average of the references (1.15) is 4.5% higher than the value of DRM-15M-320mm (1.10), and 8.5% higher when using the fourth root (3.05 v 2.81, respectively).

When applying the same criteria to the 30M bar versus the 25M – 320 mm combinations used in this study, it is not possible to make a direct comparison given the differences in the bar size, concrete cover and embedment length. However, some trends can be identified if the 30M results are considered as an upper boundary for the 25M rebars of this study. For the ACI mixes, the average of the reference (1.16) values matches the results of this study (1.16) when using the square root but is inferior with the fourth root (2.86 v 3.03, respectively). Meanwhile, the EMV results of the reference are on average 4% higher than this study regardless of the normalization root, for the square root the normalized bonds are 1.12 v 1.07, while 2.87 v 2.76 when using the fourth root, respectively.

Finally, the EMVc case requires special attention. Regardless of the bar size and embedment length, the average bond strength is lower than their counterpart EMV mixes, but the normalized values will be higher because of the lower compressive strength. When considering the brittleness of the failures observed throughout the tests, the bond values are highly influenced by the concrete's quality rather than the embedment length and concrete cover. Therefore, its normalized bond values are deceiving since this effect is not considered in the calculations.

4.7.4. Bond behaviour compared to existing equations and models

The first analytical comparison for the bond behaviour can be made using the descriptive equations of ACI 408 (ACI, 2003), which were obtained based on the results of several pullout and beam tests and do not include any safety or material factors, as is the case of the design equations of CSA A23.3 and ACI 318. As presented in the literature review, the normalized bond can be obtained using Eq. 4.7 – 1.

$$\frac{T_b}{\sqrt[4]{f_c'}} = \frac{A_b f_s}{\sqrt[4]{f_c'}} = [1.43 l_d (c_{min} + 0.5 d_b) + 57.4 A_b] \left(\frac{0.1 c_{\max}}{c_{min}} + 0.9 \right) \qquad (4.7 - 1)$$

Where:

- $c_{\max} = 40$ mm for both bar sizes.
- $c_{min} = 34.20$ mm for the 15M bar.
- $c_{min} = 27.75$ mm for the 25M bar.

Instead of using the average bond, the descriptive equation considers the bond loading peak in the normalization. The experimental and predicted values according to ACI 408 are presented in Table 4-16. Additionally, the predicted average bond and bond peak loads are included for a more detailed comparison.

As observed, the descriptive equation of ACI 408 underestimates the bond behaviour for all cases but for the cyclic 25M combinations. The values of the ACI, EMV, and EMVc mixes for this combination are 4.5%, 11.3%, and 4.6% below the prediction, respectively. In its calculation, the right leg of Eq. 4.7 – 1 does not consider the effect of the compressive strength, hence the predicted values only vary based on changes in the concrete cover, bar size or embedment length. Figure 4-99 presents a graphical comparison between the experimental and predicted bond loads. For a determined combination, the highest values come from the monotonic tests, while the lowest from their respective cyclic counterparts.

Table 4-16: Experimental v Predicted ACI 408 bond.

Mix Label	f'_c [MPa]	T_b [kN]	u [MPa]	$\frac{T_b}{\sqrt[4]{f'_c}}$	$T_{b,ACI}$ [kN]	u_{ACI} [MPa]	$\frac{T_{b,ACI}}{\sqrt[4]{f'_c}}$	$\frac{T_b}{T_{b,ACI}}$
ACI-15M-170-M1	46	70.87	8.29	27212	57.57	6.74	22107	1.23
ACI-15M-170-M2	46	88.92	10.41	34144	57.57	6.74	22107	1.54
ACI-15M-170-C3	46	90.68	10.61	34820	57.57	6.74	22107	1.58
ACI-15M-320-M1	46	115.07	7.15	44185	81.55	5.07	31313	1.41
ACI-15M-320-C1	46	115.07	7.15	44185	81.55	5.07	31313	1.41
ACI-25M-320-M1	46	201.41	7.89	77339	128.38	5.03	49294	1.57
ACI-25M-320-C2	46	122.63	4.80	47087	128.38	5.03	49294	0.96
DRM-15M-320-M1	42	108.56	6.75	42644	79.71	4.96	31313	1.36
DRM-15M-320-M2	42	115.07	7.15	45201	79.71	4.96	31313	1.44
DRM-15M-320-C2	42	103.02	6.41	40469	79.71	4.96	31313	1.29
EMV-15M-170-M1	45	104.00	12.17	40153	57.26	6.70	22107	1.82
EMV-15M-170-C1	45	92.60	10.84	35752	57.26	6.70	22107	1.62
EMV-15M-320-M1	45	115.07	7.15	44428	81.10	5.04	31313	1.42
EMV-15M-320-C1	45	115.07	7.15	44428	81.10	5.04	31313	1.42
EMV-25M-320-M1	45	183.26	7.18	70758	127.67	5.00	49294	1.44
EMV-25M-320-C1	45	113.28	4.44	43738	127.67	5.00	49294	0.89
EMVc-15M-170-M1	36	64.18	7.51	26201	54.15	6.34	22107	1.19
EMVc-15M-170-M2	36	84.96	9.94	34686	54.15	6.34	22107	1.57
EMVc-15M-170-C1	36	80.62	9.43	32912	54.15	6.34	22107	1.49
EMVc-25M-320-M1	36	129.16	5.06	52731	120.75	4.73	49294	1.07
EMVc-25M-320-C1	36	115.22	4.51	47038	120.75	4.73	49294	0.95

When comparing the differences between the monotonic and cyclic peaks with their normalized values, the drop is between 0 – 12% for all combinations except 25M – 320 mm.

For this specific case, the ACI and EMV mixes present drops of 63.5% and 61.8%, respectively. Meanwhile, the drop is less significant for the EMVc mix, with its monotonic peak being 12.6% higher than the cyclic one, much in line with the other combinations.

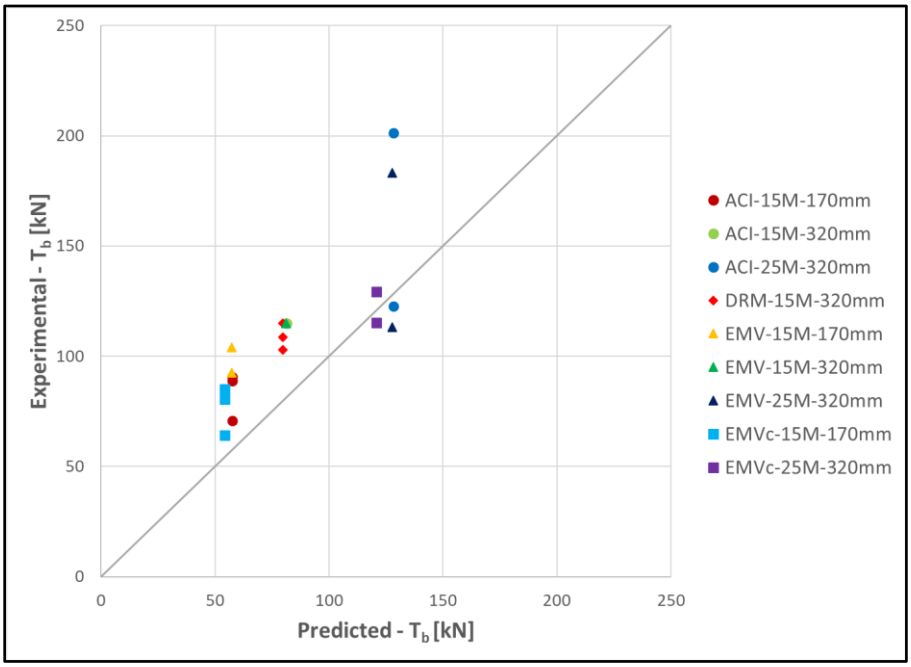

Figure 4-99: Experimental v Predicted ACI 408 bond.

Table 4-17: Statistical analysis of ACI 408 bond v experimental bond force prediction.

Value	ACI 408 Database ($T_{b,ex}/T_{b,ACI}$)	Experimental ($T_b/T_{b,ACI}$)
Max	1.288	1.816
Min	0.724	0.887
Avg	1.000	1.365
Std	0.111	0.236
CoV	0.111	0.173

According to the statistics provided in ACI 408 (ACI, 2003), the test prediction ratio for bars not confined by transverse reinforcement, or ratio of predicted to experimental data ($T_{b,ex}/T_{b,ACI}$), is below the average ratios obtained for this study ($T_b/T_{b,ACI}$ column in Table 4-16), as shown in the statistical analysis provided in Table 4-17. The biggest difference lies in the maximum prediction value, which almost 41% higher than the database of ACI 408,

thus affecting the average and standard deviation values. It is possible that these differences can be traced to the specimens used in the generation of the database, which included pullout tests, whose behaviour is different from the beam-ends used in this study given the size difference and the compression induced when pulling the rebar.

A second comparison can be made using the approach developed to compare the EMV bond performance against the normalized of the design equation of CSA A23.3 for development length (Fathifazl et al., 2012). The average bond is understood to be the stress that will allow the rebar to yield within a specific embedment, as shown in Eq. 4.7 – 2.

$$A_b f_y \leq \pi d_b u l_d \qquad (4.7-2)$$

When replacing the embedment length (l_d) with the CSA A23.3 design equation (Eq. 9.1 – 1), the bond can be normalized using the square root of the compressive strength, as shown in Eq. 4.7 – 3 and Eq. 4.7 – 4.

$$A_b f_y \leq \pi d_b u \left(0.9 \frac{k_l k_c k_d k_s k_g}{\left(\frac{d_{cs} + K_{tr}}{d_b}\right)} \frac{f_y}{\sqrt{f_c'}} \right) \qquad (4.7-3)$$

$$\frac{u}{\sqrt{f_c'}} \geq \frac{A_b d_{cs}}{0.9\pi d_b^3 k_s k_g} \qquad (4.7-4)$$

This last simplified equation for unconfined concrete ($K_{tr} = 0$) is only dependent on two of the original five reduction factors. k_s accounts for the bar size effect and k_g considers the effect of the steel when the yielding stress is greater than 400 MPa. The complete details, including the normalized bond values, as presented in Table 4-18.

As with the ACI 408 descriptive equation, the normalized bond using the CSA A23.3 expression for embedment length underestimates the bond peaks for all combinations but

DRM-15M-320mm-C2. The main differences come from the 25M – 320 mm monotonic specimens, whose bond values are twice the predicted ones. A statistical analysis for this process in presented in Table 4-19, where the experimental to predicted bond ratios (u/u_{CSA}) of Table 4-18 are compared with the equivalent ratios of Table 4-16 (u/u_{ACI}).

Table 4-18: Experimental v Predicted CSA A23.3 bond.

Mix Label	u [MPa]	$\frac{u}{\sqrt{f'_c}}$	d_{cs} [mm]	k_s	k_g	$\frac{u_{CSA}}{\sqrt{f'_c}}$	$\frac{u}{u_{CSA}}$
ACI-15M-170-M1	8.29	1.22	48.00	0.80	1.04	1.00	1.23
ACI-15M-170-M2	10.41	1.53	48.00	0.80	1.04	1.00	1.54
ACI-15M-170-C3	10.61	1.56	48.00	0.80	1.04	1.00	1.57
ACI-15M-320-M1	7.15	1.05	48.00	0.80	1.04	1.00	1.06
ACI-15M-320-C1	7.15	1.05	48.00	0.80	1.04	1.00	1.06
ACI-25M-320-M1	7.89	1.16	52.60	1.00	1.07	0.53	2.19
ACI-25M-320-C2	4.80	0.71	52.60	1.00	1.07	0.53	1.33
DRM-15M-320-M1	6.75	1.04	48.00	0.80	1.04	1.00	1.05
DRM-15M-320-M2	7.15	1.10	48.00	0.80	1.04	1.00	1.11
DRM-15M-320-C2	6.41	0.99	48.00	0.80	1.04	1.00	0.99
EMV-15M-170-M1	12.17	1.81	48.00	0.80	1.04	1.00	1.82
EMV-15M-170-C1	10.84	1.62	48.00	0.80	1.04	1.00	1.62
EMV-15M-320-M1	7.15	1.07	48.00	0.80	1.04	1.00	1.07
EMV-15M-320-C1	7.15	1.07	48.00	0.80	1.04	1.00	1.07
EMV-25M-320-M1	7.18	1.07	52.60	1.00	1.07	0.53	2.02
EMV-25M-320-C1	4.44	0.66	52.60	1.00	1.07	0.53	1.25
EMVc-15M-170-M1	7.51	1.25	48.00	0.80	1.04	1.00	1.26
EMVc-15M-170-M2	9.94	1.66	48.00	0.80	1.04	1.00	1.66
EMVc-15M-170-C1	9.43	1.57	48.00	0.80	1.04	1.00	1.58
EMVc-25M-320-M1	5.06	0.84	52.60	1.00	1.07	0.53	1.59
EMVc-25M-320-C1	4.51	0.75	52.60	1.00	1.07	0.53	1.42

Table 4-19: Statistical analysis of the CSA A23.3 v ACI 408 predicted bond.

Value	CSA A23.3 (u/u_{CSA})	Experimental (u/u_{ACI})
Max	2.192	1.816
Min	0.992	0.887
Avg	1.404	1.365
Std	0.333	0.236
CoV	0.237	0.173

When comparing the normalized bond capacities, the difference between the experimental data and the expression derived from the design equation comes from the denominator. For the former, the average bond is obtained when dividing the load by the embedment length, while the latter does not consider this variable but the bar diameter. Therefore, the 15M – 170 mm and 25M – 320 mm specimens will have a higher normalized bond capacity due to their reduced embedment lengths.

Nevertheless, there is a limit to that increased bond value, also known as ultimate bond, and any value that is higher will provoke a brittle failure as the bar will not have enough anchorage to bear the stresses to the concrete. Therefore, the underestimation for these two combinations should be interpreted as the safety range the design equation provides, as those higher bond capacities are the effective ultimate capacities at which the failure is taking place for these specific cover, bar size, and embedment length combinations; and they are not desired for real structures given the fragility of the failure mechanism.

However, the 15M – 320 mm presents a more accurate comparison due to the embedded region being within the code requirement for thar bar size. It is appreciated that, the experimental normalized bond is on average 6% higher than its theoretical design counterpart, thus highlighting the accuracy on the design equation and the safety margin it provides for the structural configuration with its safety factors, as the rebar was able to develop its yielding stresses without suffering an anchorage failure.

The third analytical tool to compare the bond results is the use of the available bond v slip models. As discussed in the literature review, these models were largely developed on the data retrieved from pullout, beam-end, and 3-point bending tests. Figure 4-100 presents the curves of two models, Pochanart and the fib MC 2010 (FIB, 2010; Pochanart & Harmon, 1989). The traditional bond curve has an ascending branch followed by a plateau where the peak bond is achieved. Soon after, the bond starts to decrease as the concrete keys shear off and ends up with a residual final capacity.

This behaviour is achieved by a pullout failure, where the bar can achieve the mentioned stresses in the elastic region when sufficient confinement is provided. If no transverse reinforcement is available, or if the concrete cover is low, the concrete will develop a splitting crack since it is not able to bear the stresses the rebar is taking. This failure mechanism means the peak will be lower than the pullout case, and after it is reached there will be no residual capacity given the brittle failure.

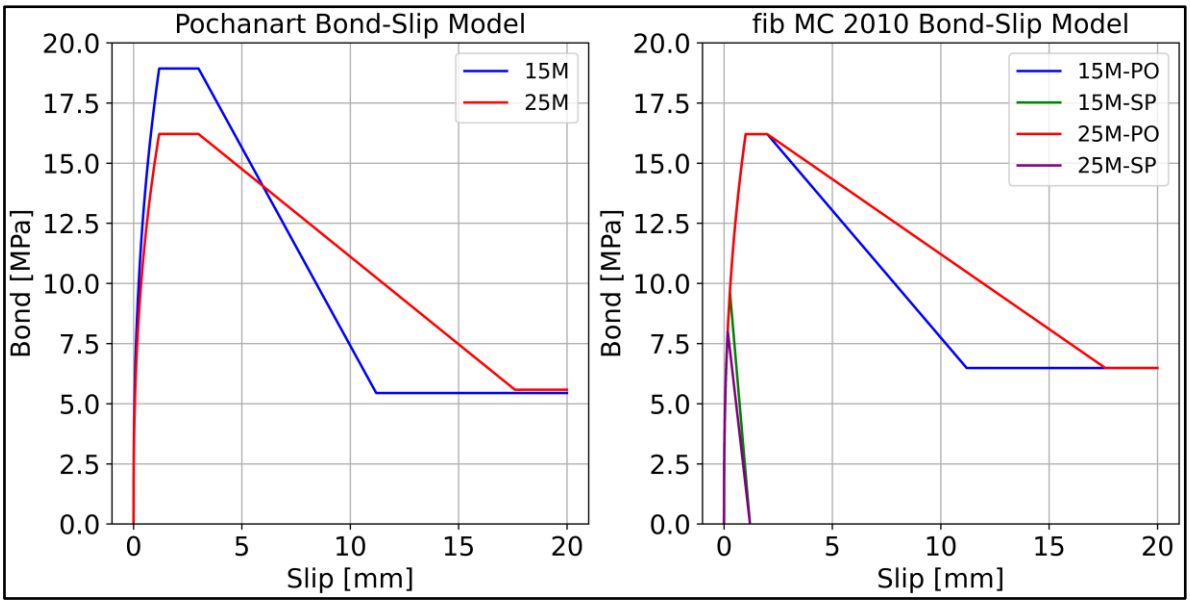

Figure 4-100: Bond v slip models calibrated for the analysis.

Although similar, the two models present a few distinctions. The first one is that the Pochanart model considers the compressive strength of the concrete and the bar size in the calculation of the bond peak, while the MC 2010 model only considers the former, hence the difference in the peaks. The second difference is that the MC 2010 model provides expressions to compute the peak bond for confined and unconfined concrete when the splitting failure governs. As seen in Figure 4-100, the splitting failure takes place on the ascending branch and has a much lower slippage than the pullout failure.

To calibrate both models, a single curve was developed for each bar size and an average concrete compressive strength of 42 MPa was considered. For the calibration of the

Pochanart model, the same equations provided in the literature review were used (Eq. 2.5 – 1 to Eq. 2.5 – 6). Meanwhile, the calibration of the MC 2010 model was based on Eq. 2.5 – 7 to Eq. 2.5 – 13, and two extra equations were needed for the calculation of the pullout and splitting bond peaks. For the former, the value only relies on the compressive strength capacity of the concrete, as shown in Eq. 4.7 – 5:

$$\tau_{max} = 2.5\sqrt{f_c'} \qquad (4.7-5)$$

On the other hand, the expression for the latter is available in Eq. 4.7 – 6:

$$\tau_{split} = \eta_2\ 6.54\left(\frac{f_c'}{20}\right)^{0.25}\left(\frac{20}{d_b}\right)^{0.2}\left(\left(\frac{c_{min}}{d_b}\right)^{0.33}\left(\frac{c_{max}}{c_{min}}\right)^{0.1} + 8K_{tr}\right) \qquad (4.7-6)$$

Since no confinement was provided, K_{tr} can be considered as zero. Meanwhile, η_2 represents the effect of the bond conditions, with 1.0 for good bond conditions, and 0.7 for all other bond conditions. The difference between them lies in the bar casting position and concrete cover. Since the rebars were parallel to the horizontal plane and had more than 25 mm of cover, the good bond conditions apply.

Table 4-20: Splitting bond stress per mix design.

Bar Size	ACI [MPa]	DRM [MPa]	EMV [MPa]	EMVc [MPa]	Avg [MPa]	Std [MPa]	CoV
15M	9.87	9.65	9.81	9.28	9.65	0.229	0.024
25M	8.21	8.02	8.16	7.72	8.03	0.191	0.024

Table 4-20 presents the values of the splitting bond peaks for each mix design and bar size. As appreciated, the 25M rebar has lower bond stresses because it requires higher embedment lengths to be able to yield. Besides the bar size effect, the fluctuations are mainly caused by the compressive strength, which was different for each mix type. The average compressive strength at 56 days for each mix type was used to compute the bond

stresses using Eq. 4.7 – 6. As appreciated in Table 4-20, the average across all batches was deemed reasonable for the construction of the bond curves of Figure 4-100 since there is little variation, as if each mix average was individually used.

The results of the empirical data of each combination and mix design against the bond behaviour given by the Pochanart model are presented in Figure 4-101, Figure 4-102, and Figure 4-103. For each combination, the free- and loaded-end bond curves were included.

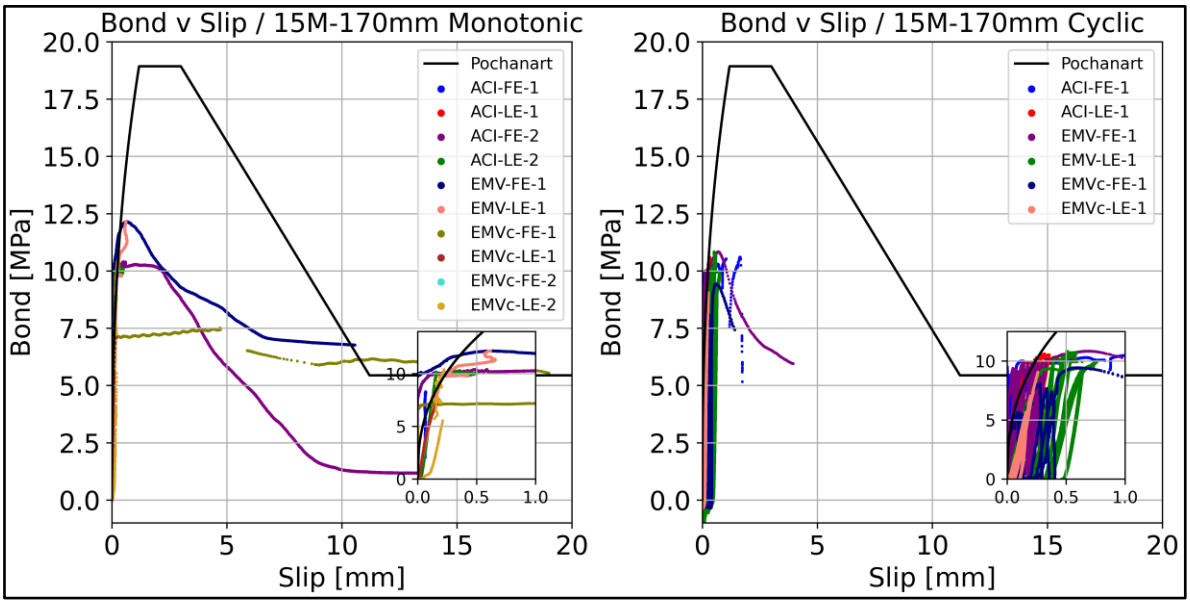

Figure 4-101: 15M – 170 mm results v Pochanart Bond-Slip Model.

In the case of the 15M – 170 mm combination (Figure 4-101), the free-end curves of the ACI and EMV mixes present a similar shape to the model curve, but with lower bond peaks and associated displacements, as the model curve is calibrated for a pullout failure condition, which is achieved either with confinement and sufficient cover. In the monotonic case, the curves presented a much better development since the data coming from the LPs was not interrupted nor disturbed after the end of the plateau. Both mixes show signs of a combined pullout/splitting failure since the bond peaks were lower than those of the model, but they did not present the sudden load decay associated to a splitting failure.

The case of the EMVc mix is different since the concrete failed before reaching the bond peak in the initial test run, hence the flat slip behaviour observed in the monotonic plot. The second monotonic and cyclic specimens presented similar results in terms of bond and displacement, although they were still lower than those of the ACI and EMV mixes. Finally, a reduction of the bond peak is also observed when comparing the monotonic and cyclic results, which is a direct consequence of the degradation induced by the latter protocol and is estimated to be 12% on average.

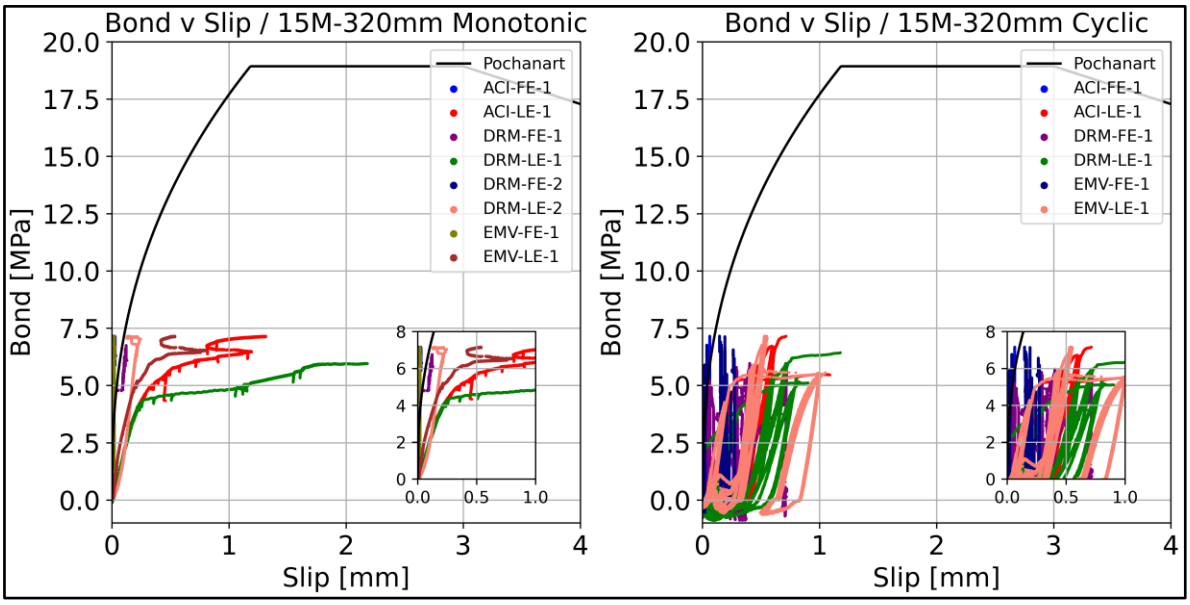

Figure 4-102: 15M – 320 mm results v Pochanart Bond-Slip Model.

The bond behaviour of the 15M – 320 mm combination presents a few interesting observations (Figure 4-102). The first one comes from the reduced average bond peaks, which can be attributed to the longer embedded section. However, the peaks could have not been higher given the rebar reached its ultimate load capacity and suffered a rupture because it met its maximum elongation. The second observation comes from the slip evolution, which was underestimated for all cases since the strain gauge placed on the loaded end of the rebar (SG5) went beyond its 5% strain limit.

Given the failure mode of the specimens, the bond v slip profile was expected to show a linear increase until the strain penetration caused the yielding of part of the embedded section. Once this phenomenon took place, the increasing rate of bond stress would decrease until the ultimate failure, where there would be no residual capacity because of the rebar fracture. In the case of the acquired data, the first phase and the start of the yielding were captured correctly until SG5 failed.

Moreover, a third observation comes from the similar behaviour of the ACI and EMV mixes in monotonic and cyclic loading. Both present an advantage over the DRM mix, since the latter was clearly affected by degradation during the cyclic protocol, which translated into a lower bond peak and a different failure mechanism (the rebar did not break). Meanwhile, for the former two mixes, the bond peaks are the same but with slightly higher slips, which can be attributed to the degradation experienced during the cyclic loading.

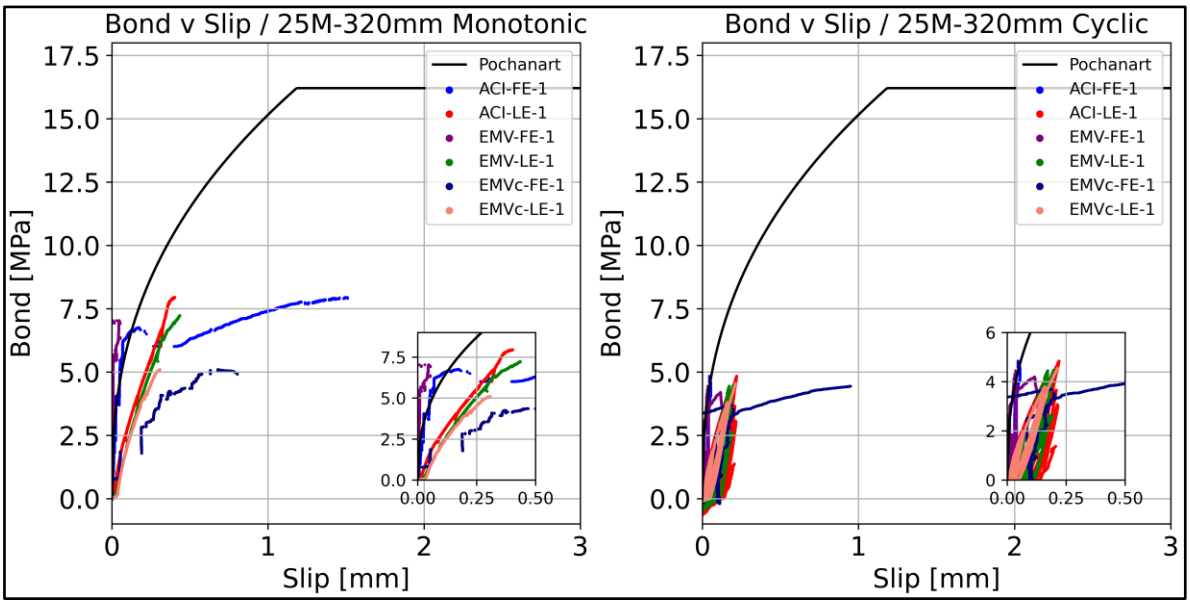

Figure 4-103: 25M – 320 mm results v Pochanart Bond-Slip Model.

On the other hand, the 25M – 320 mm combination presented a different behaviour than the previous two (Figure 4-103). Similarly to the 15M – 170 mm beam-ends, the peak bond capacity is noticeably below the model's estimation. However, no plateaus or residual

bond are appreciated after the peak, which is a direct result of the pure splitting failure. In the plots, the free-end slips of the ACI, EMV and EMVc mixes were clearly affected by the cracking at the bottom support, which resulted in the jumps and observed slip increases. Meanwhile, the loaded-end slip presents the expected linear behaviour that indicates the splitting failure took place in the elastic range.

When comparing the performance of each mix, it is possible to observe similar trends between the ACI and EMV mixes, with only minor differences in the final stages of both loading protocols. Meanwhile, the EMVc mix exhibited similar behaviour in the cyclic test, but its bond capacity was diminished in the monotonic case with almost a 30% drop. Furthermore, when comparing the same empirical results against the bond behaviour given by the fib Model Code 2010, further conclusions can be drawn. The results are presented in a similar fashion in Figure 4-104, Figure 4-105, and Figure 4-106 for each combination.

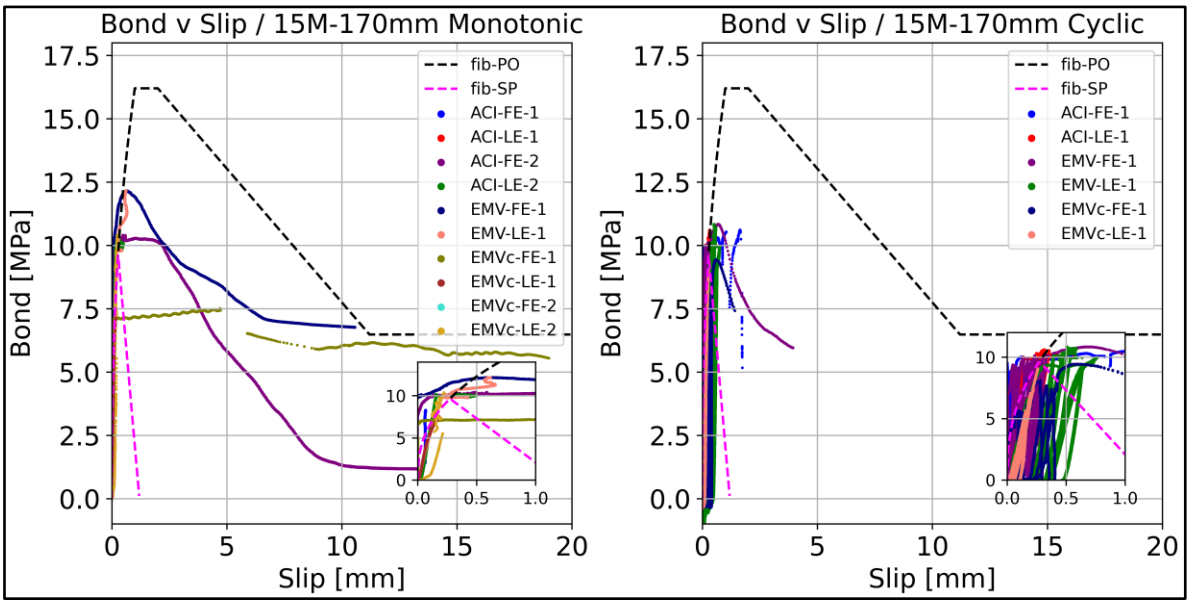

Figure 4-104: 15M – 170 mm results v fib MC 2010 Bond-Slip Model.

The advantage of the fib Model Code 2010 is that it allows the modelling of the splitting failure besides the traditional pullout bond curve. In the case of the 15M – 170 mm combination (Figure 4-104), the model confirms the failure was due to splitting/pullout

mechanism, as the bond curves of the ACI and EMV mixes sit in between the two references. Furthermore, it also shows that despite being only 55% of CSA A23.3 requirement for the 15M rebar, the 170 mm embedment length allowed the beam-ends to exceed the estimated pure splitting failure load.

When specifically comparing the ACI and EMV mixes, it is possible to observe differences in the bond peaks and plateau length, with the ACI having a better performance in the cyclic test, and the EMV in the monotonic one. Since 170 mm involve a small section of the rebar, it is possible the concrete quality in the embedded section might have varied, especially considering the congestion due to the installed instrumentation; otherwise, the performance would have likely been more similar. Furthermore, since concrete is a highly heterogeneous material and experimental variability is expected, this aspect could be assessed with replicate samples.

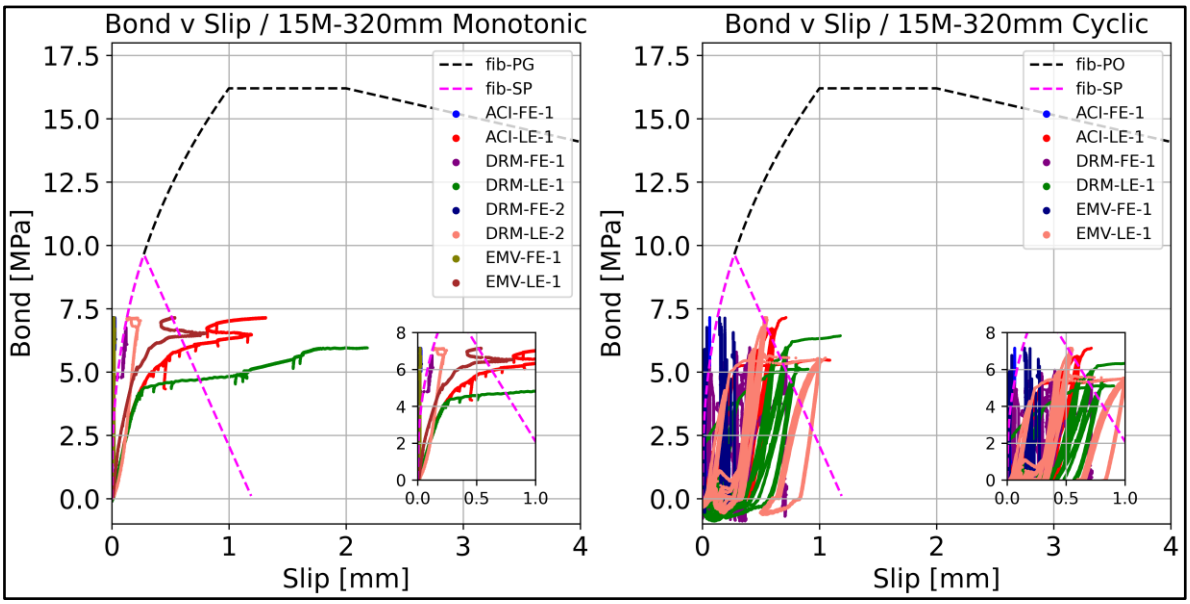

Figure 4-105: 15M – 320 mm results v fib MC 2010 Bond-Slip Model.

The situation of the 15M – 320 mm beam-ends become more interesting when comparing it to the fib Model Code 2010. As observed in Figure 4-105, the bond slips do not match any of the model curves since the failure was neither due to splitting nor pullout. In

fact, the profile is very similar to the beam-ends tested during the development of the EMV Method (Fathifazl et al., 2012). When analyzing the restrictions that apply to the curves of the model, the main constraint comes from the stress state of the rebar, since the equations are valid if the steel strain is below its yielding capacity.

In case the steel yields, the bond is significantly affected (its ultimate capacity is reduced) and the model introduces a strain-calibrated factor (Ω_y) to account for the effect (FIB, 2010). This factor can be computed according to the following equations:

$$\tau_{max,y} = \tau_{max}\Omega_y \qquad (4.7-7)$$

$$a = \frac{\varepsilon_s - \varepsilon_y}{\varepsilon_u - \varepsilon_y} \; ; b = \left(2 - \frac{f_s}{f_y}\right)^2 \qquad (4.7-8)$$

$$\Omega_y = 1.0 - \left(0.85\left(1 - e^{-5a^b}\right)\right) \qquad (4.7-9)$$

Where:

- $\tau_{max,y}$: Scaled maximum bond stress due to steel yielding
- Ω_y: Strain-calibrated factor to account for the yielding effects
- a: Coefficient that accounts for the steel strain
- b: Coefficient that accounts for the steel stress
- ε_s: Steel strain being evaluated
- ε_y: Steel yielding stress
- ε_u: Steel ultimate stress
- f_s: Steel stress being evaluated
- f_y: Steel yielding stress

For the peak strains in the embedded section (given by SG3), the values for the ACI and EMV mixes lie around 10,000 micro-strains for the monotonic case. When computing the respective coefficients, the bond reduction is approximately 23%, meaning the peak drops to 12.51 MPa. Nevertheless, even if the correction factor is applied, the bond curves will not match the model ones since no splitting nor pullouts were experienced, and because the strain penetration only caused a partial yielding inside the embedded section.

Furthermore, when considering that 320 mm of embedment length was in line with the minimum requirement given by CSA A23.3 for the 15M rebar, it is confirmed the bar was able to develop its yielding stresses before experiencing a splitting or pullout failure, which is the desired result given its implications in the structural design, where ductility is key. Nonetheless, this length is not ideal for comparing the ultimate bond strength predicted by existing models, since the traditional bond failures will not develop.

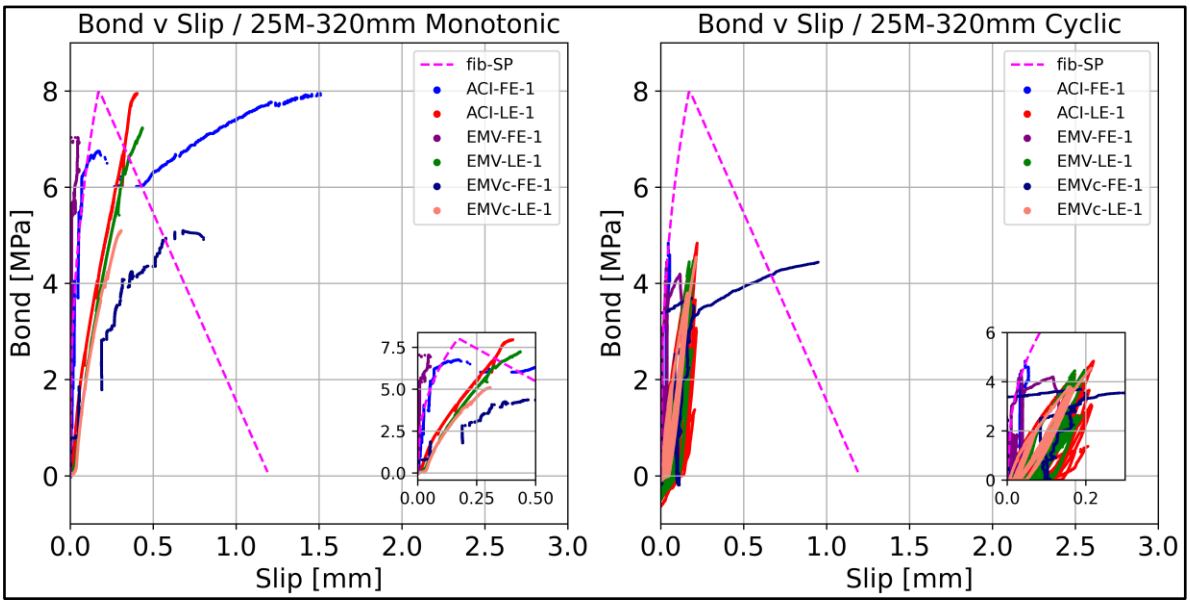

Figure 4-106: 25M – 320 mm results v fib MC 2010 Bond-Slip Model.

Finally, the 25M – 320 mm combination closely matches the prediction given by the model for a splitting failure in the elastic range (Figure 4-106). As observed for the monotonic case, the bond peaks of the ACI and EMV mixes are almost the same as the

model but with a slightly higher slip in the case of the loaded end. As with the Pochanart model, the free-end slip is not entirely reliable due to the appreciated jumps in the readings, which were caused by localized cracking in the region where the LPs were installed.

Contrary to the 15M combinations, the peak cyclic bond stress is significantly lower for the 25M rebar when compared to the monotonic case, with an average reduction of 38%. The monotonic peak is also lower than its 15M counterparts, which was expected given that for the same 320 mm of embedment length, the 15M rebars can achieve their yielding stresses, as it was previously shown. In the case of the 25M rebars, the 320 mm of embedment length meant the rebar had almost 44% of the minimum requirement of CSA A23.3, resulting in a splitting failure mechanism.

Therefore, given the nature of the failure, the higher strength degradation under cyclic loading was expected, especially when considering the lower cover-to-bar diameter ratio and the unconfined nature of the beam-end, which allowed a faster crack expansion. Moreover, another interesting detail is that the loaded end slip follows the monotonic envelope, with similar slips for the same bond readings.

Overall, the comparison of the beam-end results against the existing analytical models shows the effects of the bar size and embedment length, which led to different failure mechanisms. Additionally, the differences in the mix designs allowed a better understanding of the bond evolution under cyclic loading, where the ACI and EMV mixes were closely matching each other, despite the latter containing 74% of RCA. Therefore, the main conclusion is that the EMV mix proved to be effective by not only matching the performance of the conventional concrete when tested monotonically, but also under cyclic loads, where no severe degradation was observed across all combinations.

4.7.5. Bond behaviour on the embedded section

The final analysis required to assess the cyclic bond behaviour is by looking at the strain evolution on the embedded region between the monotonic and cyclic tests. This comparison will allow to check the strain penetration in more detail and check at which stage the degradation of the cyclic tests started to take place. To provide a more accurate analysis, the results will be divided by combination and mix design, showing the strain evolution first, to be then followed by the evolution of the cyclic tests per deformation step.

By looking at the strain evolution, it is possible to compare the monotonic and cyclic responses, where the former is expected to form the envelope of the latter. Since a few strain gauges did not work properly, or they were influenced by an external factor such as the cracking at the bottom support, the strain v stress plots presented some noise, which generally indicates the point where the gauge became faulty. For all cases, the stress values include the respective scaling factors; therefore, the stress v strain comparison should be aligned with the observed failure mechanisms.

Meanwhile, the strain v displacement plots help identify the deformation step and exact cycle where the gauges stopped working properly during the cyclic test, since the x-axis corresponds to the actuator displacement; therefore, the values are easily comparable with the previously presented load v displacement plots. The first results to be presented are those of the ACI mix, with the 15M – 170 mm combination available in Figure 4-107 and Figure 4-108, the 15M – 320 mm in Figure 4-109 and Figure 4-110, and the 25M – 320 mm in Figure 4-111 and Figure 4-112, respectively.

In the case of the 15M – 170 mm combination, the strains coming from SG3, which was the closest strain gauge to the loaded end of the rebar, show there was a strain penetration high enough to induce local yielding for both monotonic and cyclic loading, with a sudden spike that occurred during the eighth deformation step in the case of the latter. Meanwhile,

the 15M – 320 mm combination allowed the bar yielding as far as in SG2 during the monotonic test, while the cyclic loading generated localized yielding in SG3 only.

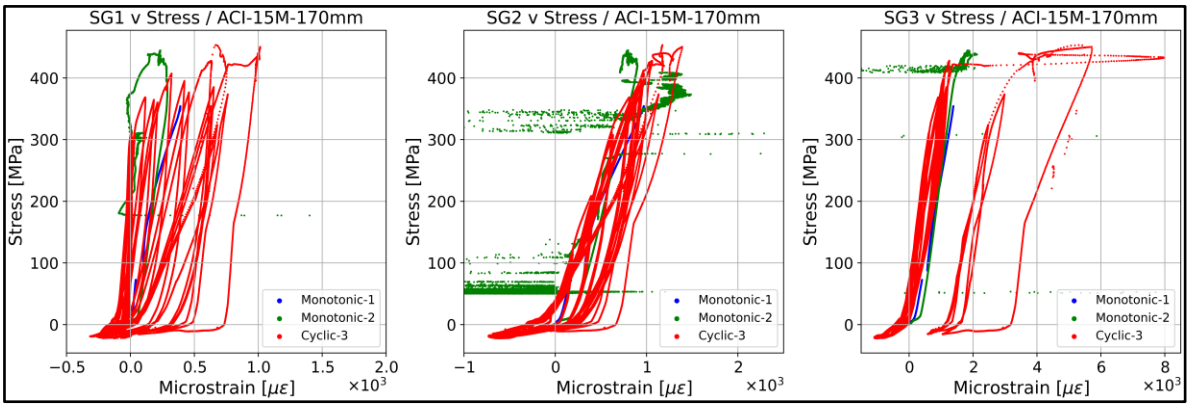

Figure 4-107: Strain v stress, ACI-15M-170mm.

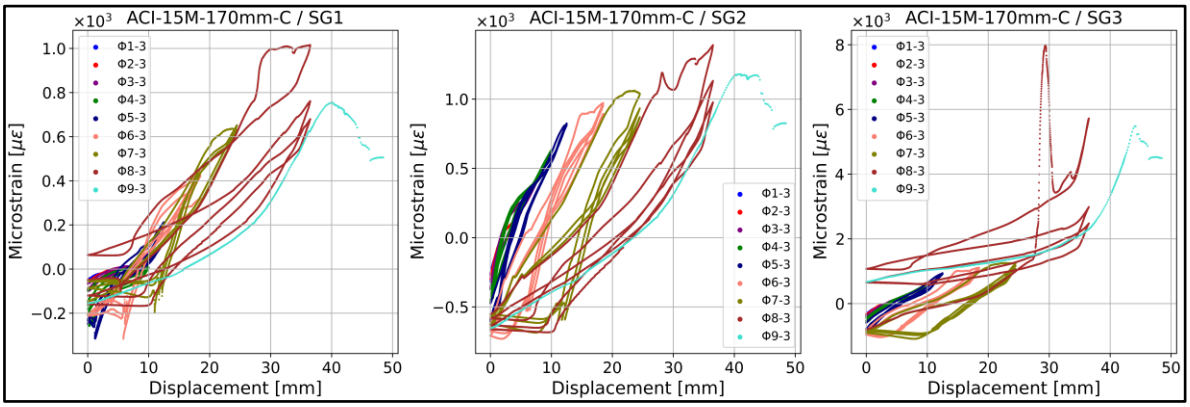

Figure 4-108: Strain per cycle v displacement, ACI-15M-170mm.

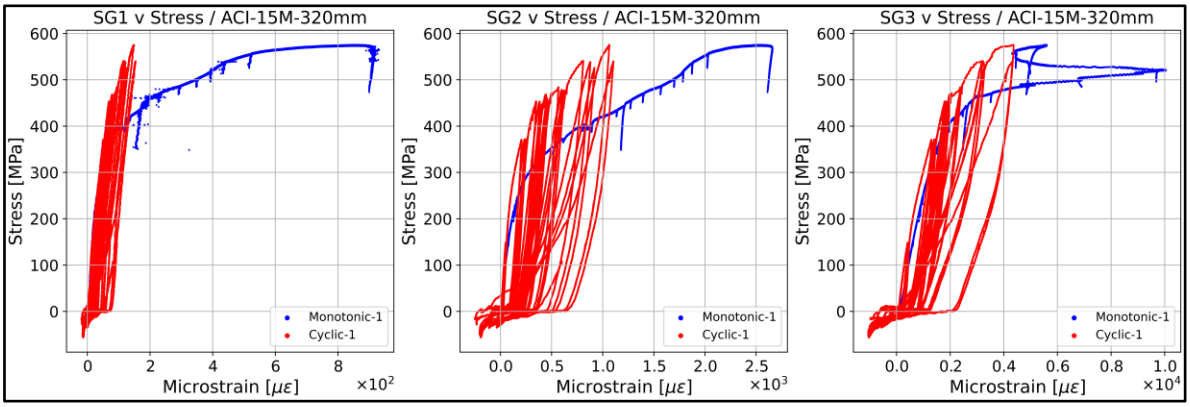

Figure 4-109: Strain v stress, ACI-15M-320mm.

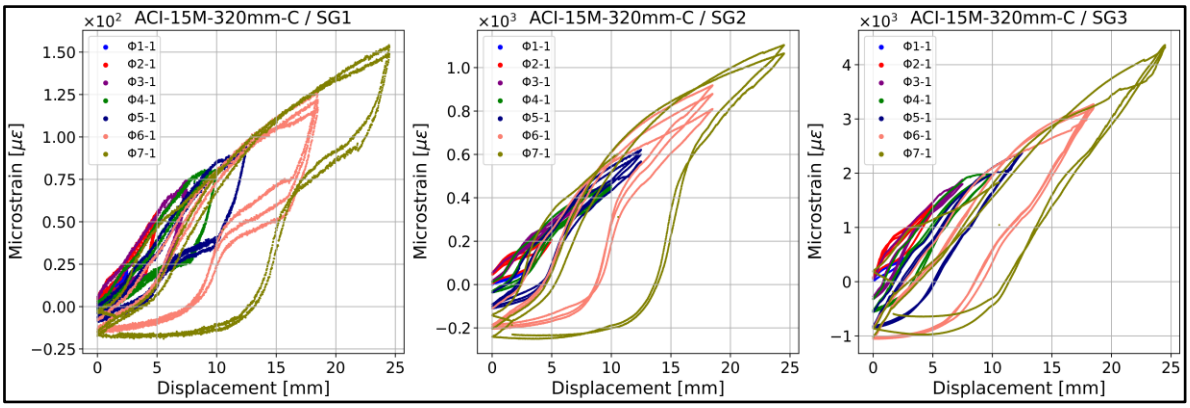

Figure 4-110: Strain per cycle v displacement, ACI-15M-320mm.

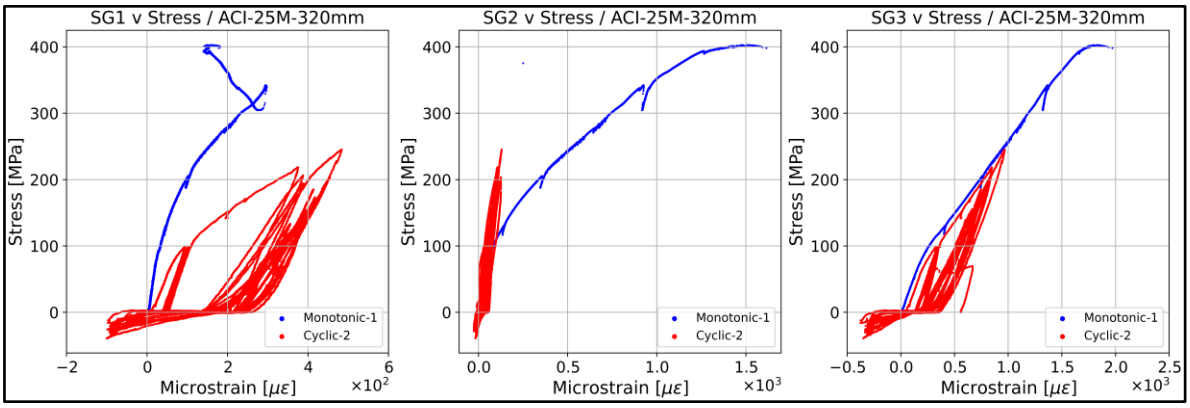

Figure 4-111: Strain v stress, ACI-25M-320mm.

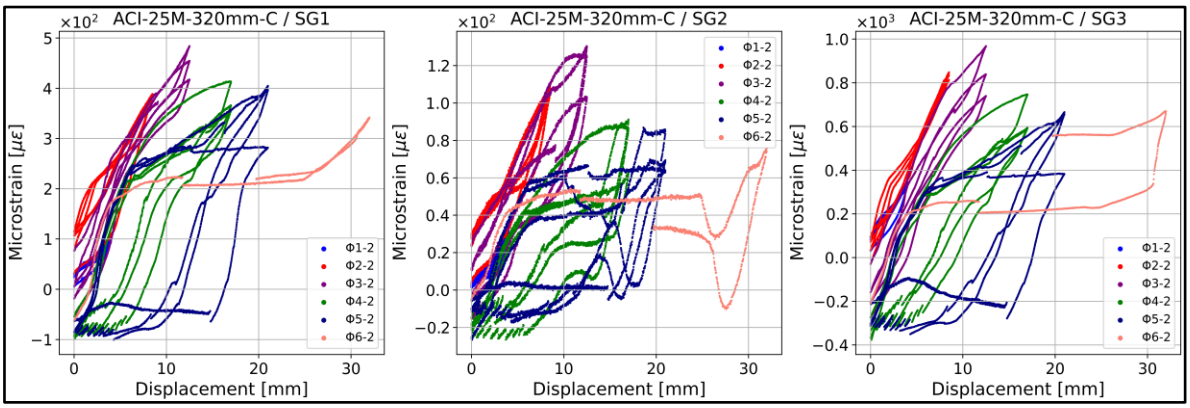

Figure 4-112: Strain per cycle v displacement, ACI-25M-320mm.

The final combination, 25M – 320 mm, further confirms the splitting failure with SG3 reaching the 2000 micro-strain mark by the time the failure took place. A special attention

to SG1 is required, since there is a noticeable degradation in both monotonic and cyclic loading, which is attributed to the bottom support cracking taking place close to the location of the gauge. Despite the degradation, the cyclic strains are aligned with their monotonic counterparts, which was the expected outcome.

The second mix to be presented is the DRM, whose only combination is the 15M – 320 mm. The strain v stress and strain v displacement results are available in Figure 4-113 and Figure 4-114, respectively.

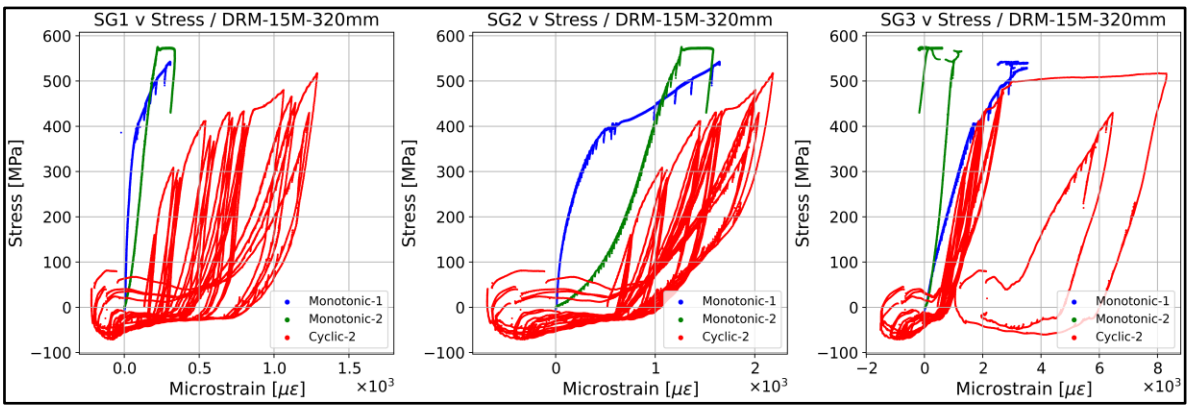

Figure 4-113: Strain v stress, DRM-15M-320mm.

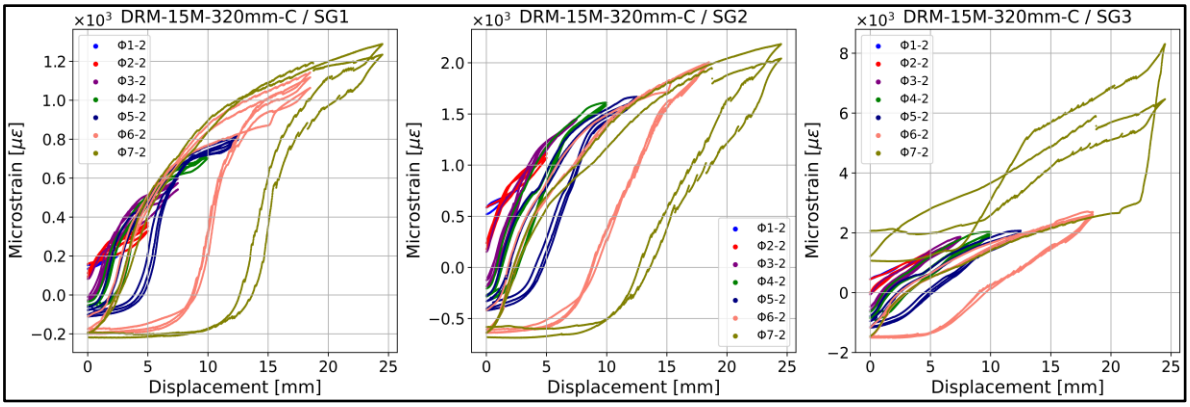

Figure 4-114: Strain per cycle v displacement, DRM-15M-320mm.

The results of this mix are similar in shape to the respective ACI combination. However, there are a couple of differences, the first one being the readings of the monotonic test.

Due to the coupler sliding, the test had to be restarted; therefore, the strain gauge readings were affected, especially at SG3 since the bar had already gone through an initial deformation. On the other hand, the cyclic results show how the degradation manifested in SG1 and SG2, where there are clear indications of softer responses with higher strains than those observed for the ACI mix.

The third mix is the EMV, which like its ACI counterpart, had three combinations. The results of the 15M – 170 mm are available in Figure 4-115 and Figure 4-116, while those of the 15M – 320 mm are available in Figure 4-117 and Figure 4-118, respectively. Finally, the 25M – 320 mm combination is presented in Figure 4-119 and Figure 4-120.

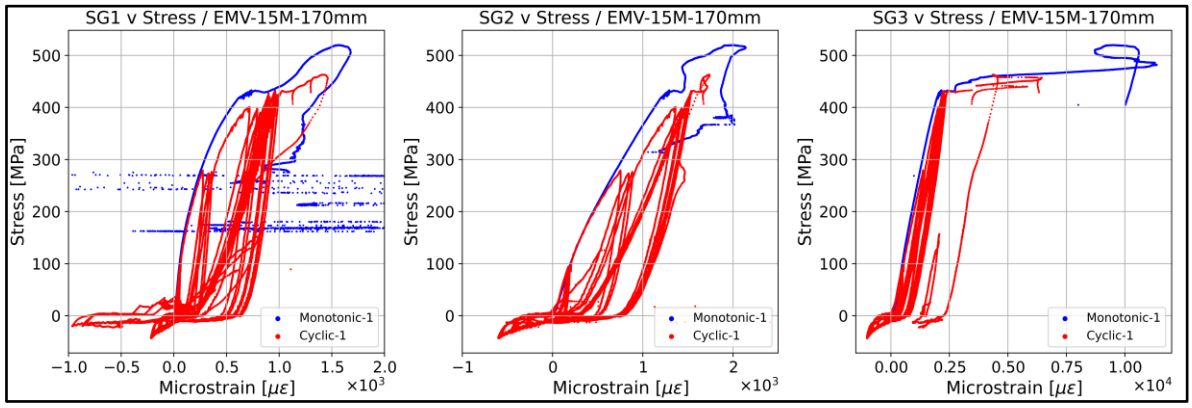

Figure 4-115: Strain v stress, EMV-15M-170mm.

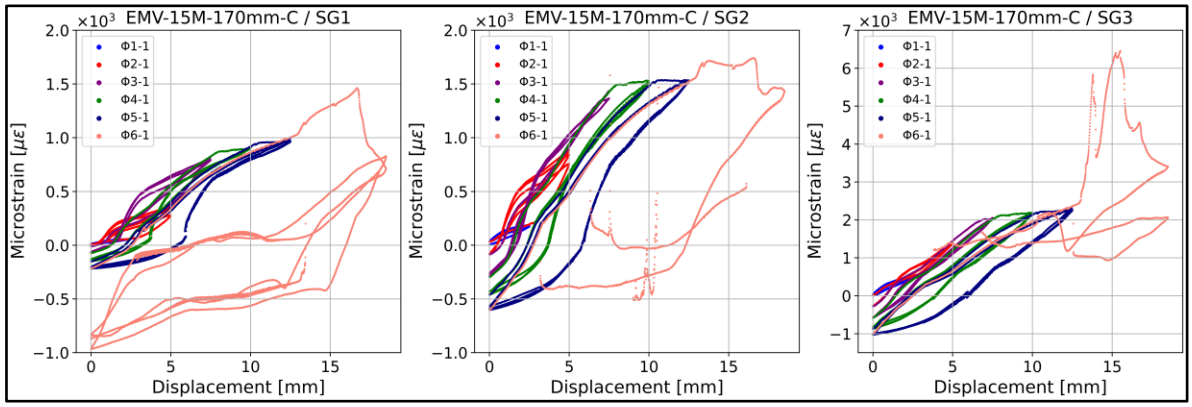

Figure 4-116: Strain per cycle v displacement, EMV-15M-170mm.

The 15M – 170 mm combination presents a similar behaviour to the one observed in the ACI mix, with a strain penetration that generated a localized yielding in the SG3 area for both monotonic and cyclic loading. Therefore, it is possible that the lower bond peak (when compared to the predictions of the bond models) might have also been affected by the yielding of a section of the embedded rebar. Moreover, the failure was clearly detected by all strain gauges during the sixth and final deformation step.

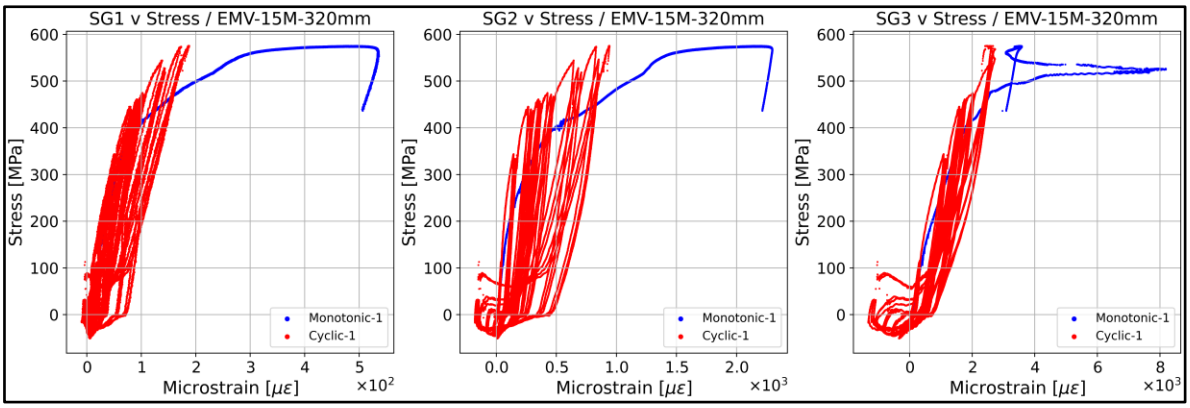

Figure 4-117: Strain v stress, EMV-15M-320mm.

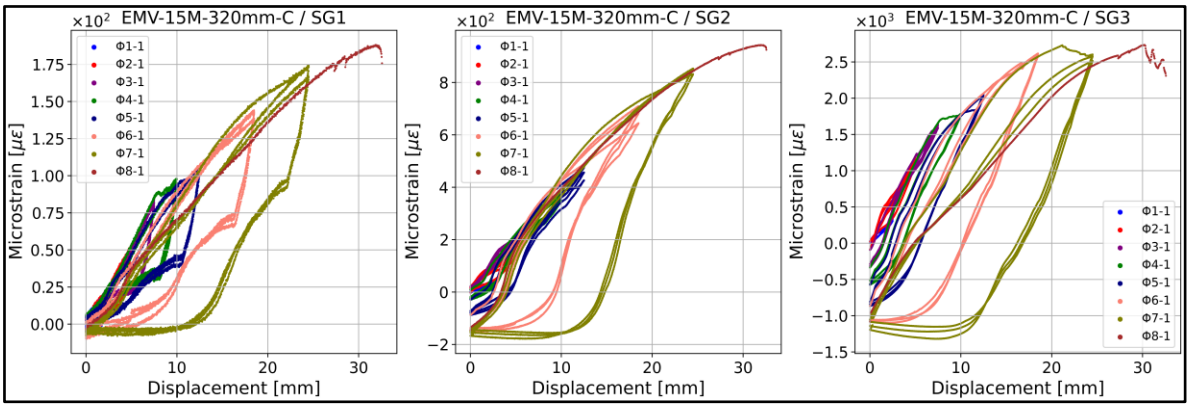

Figure 4-118: Strain per cycle v displacement, EMV-15M-320mm.

The behaviour of the 15 – 320 mm combination was also in line with the observations of the ACI mix, with the monotonic test causing a deeper strain penetration and yielding, and with the cyclic loading bearing lower strains and reaching the same stresses. There are no major signs of degradation, an effect that can be explained by the rebar having enough

embedment length to allow its yielding, which is the desired effect for reinforced concrete structures where ductility relies on the bond transfer mechanism.

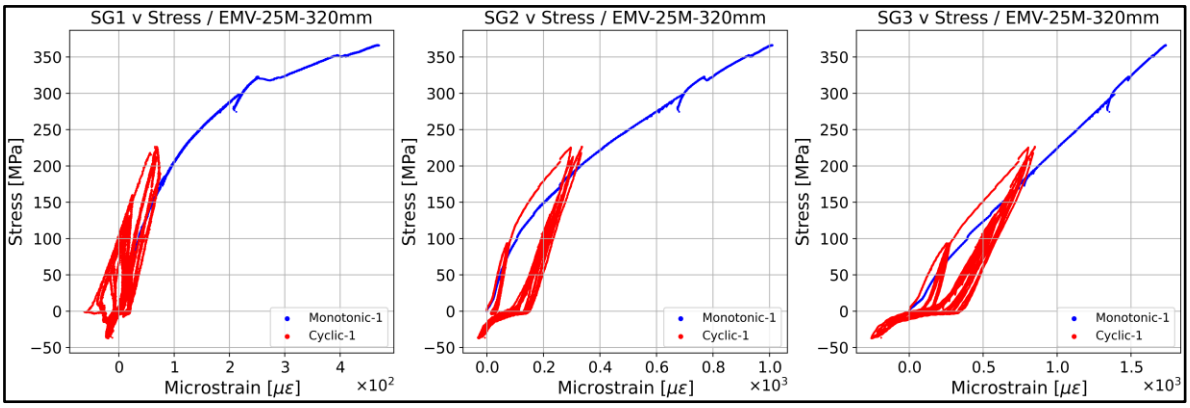

Figure 4-119: Strain v stress, EMV-25M-320mm.

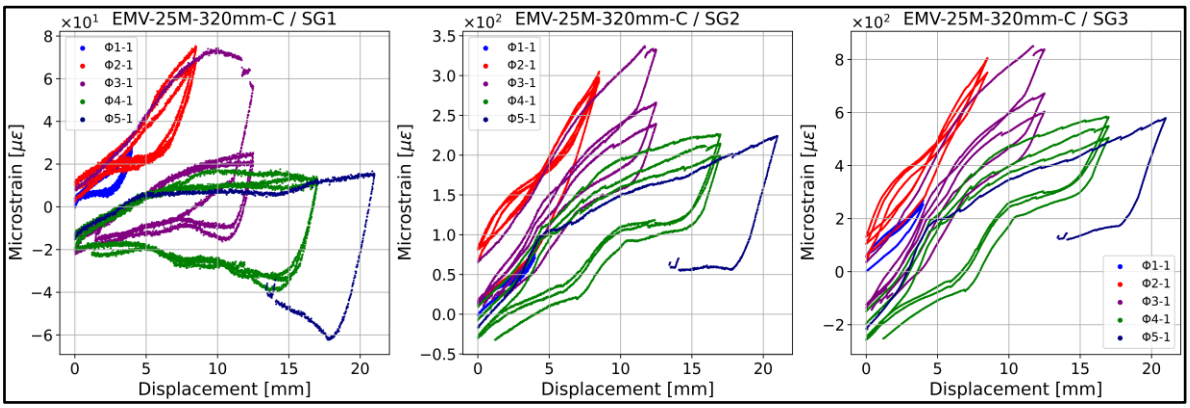

Figure 4-120: Strain per cycle v displacement, EMV-25M-320mm.

The third combination, 25M – 320 mm, follows a similar pattern to the ACI case, although the readings of SG1 are much cleaner for the monotonic case. However, there is a stress drop from the third deformation step onwards, which was evident with a softer response in all strain gauge readings. Nevertheless, the degradation stabilized in the fourth step and no further drops were observed, behaving similarly to the ACI mix.

The final round of results corresponds to the EMVc mix, which had two combinations. The results of the first one, 15M – 170 mm, are available in Figure 4-121 and Figure 4-122,

while the 25M – 320 mm combination is presented in Figure 4-123 and Figure 4-124, respectively. The results of this mix were affected by the fragility of the cement paste matrix, which severely impacted the performance of SG1.

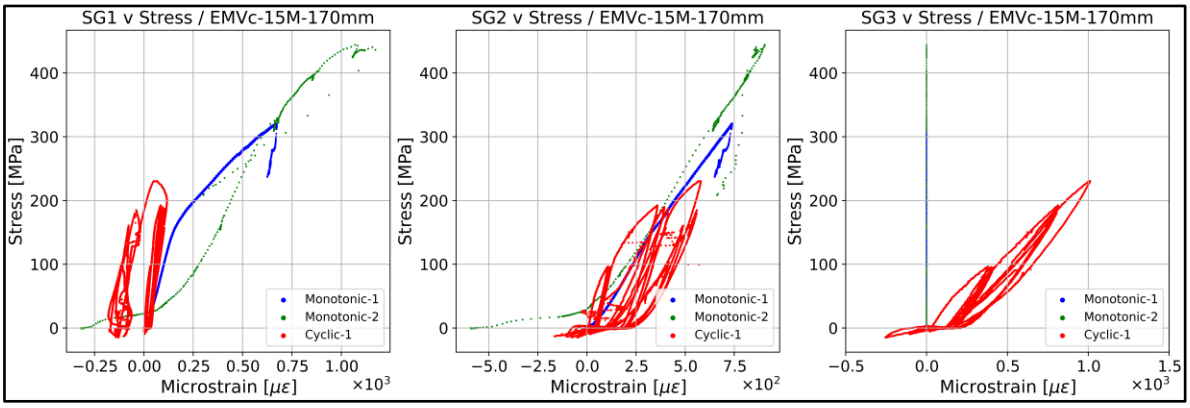

Figure 4-121: Strain v stress, EMVc-15M-170mm.

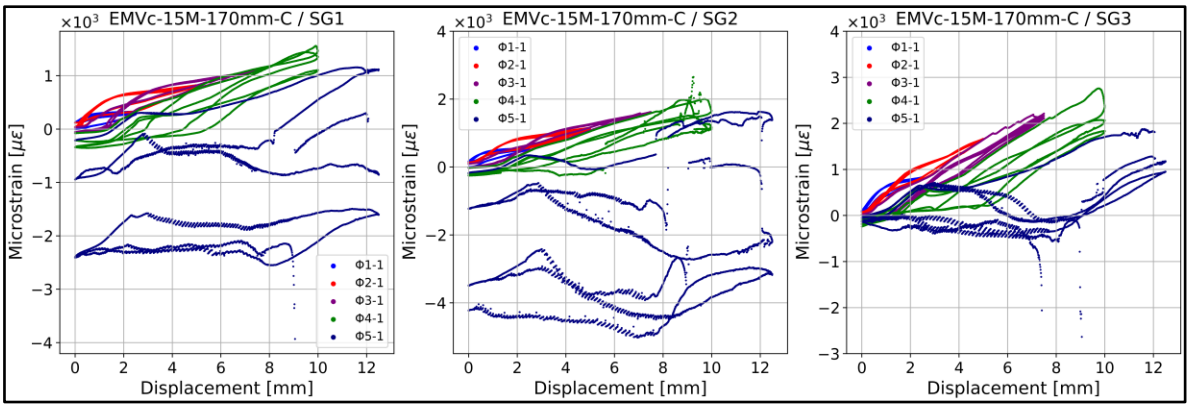

Figure 4-122: Strain per cycle v displacement, EMVc-15M-170mm.

In the case of the 15M – 170 mm combination, SG3 was damaged before the start of the test, and no data was recorded. Nonetheless, the results for this combination show a good correlation between the monotonic and cyclic loading but with lower stresses than the specimens made with the ACI and EMV mixes.

On the other hand, the case of the 25M – 320 mm combination is nearly identical, with good correlation in all gauges despite the lower stresses. The results also show a faster

degradation for both loading protocols, which is clear by looking at the slopes and stress peaks of SG1 and SG2. Therefore, when analyzing the factors that had the greatest impact on the bond performance, the quality of the cement paste is paramount, since it was the only different component when compared to the EMV mix.

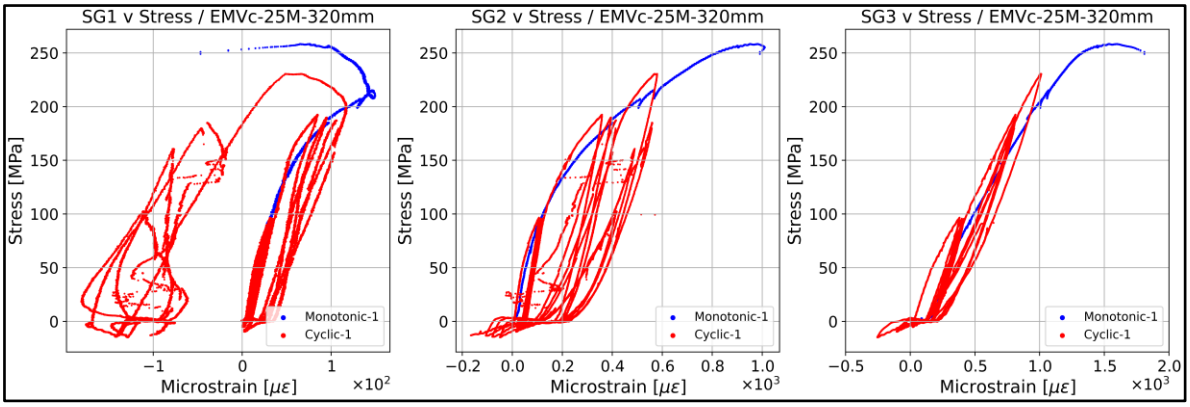

Figure 4-123: Strain v stress, EMVc-25M-320mm.

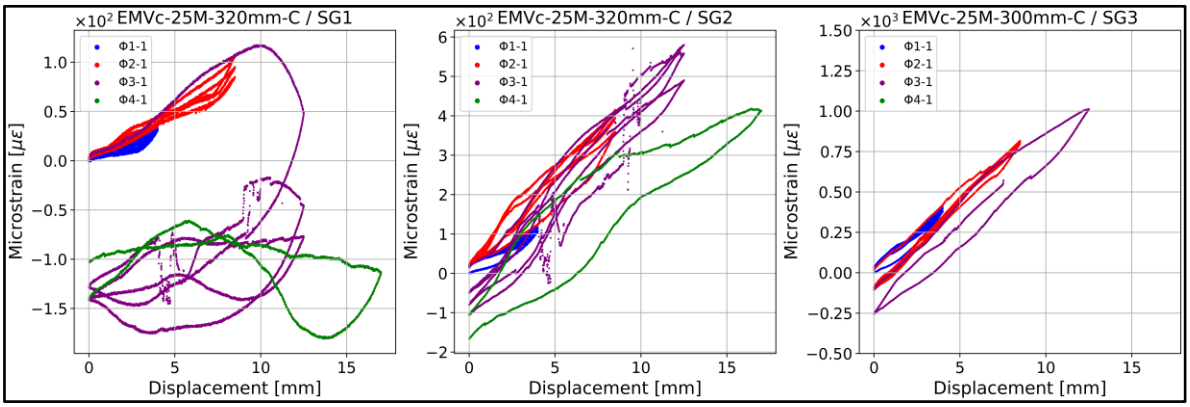

Figure 4-124: Strain per cycle v displacement, EMVc-25M-320mm.

Observations made during the test pointed to the ease of crack development, which propagated at a much higher rate than for the mixes made with GUL cement, leading to more brittle failures. These observations were validated when taking a closer look at the fragments that came loose, where there was an evident porosity on the cement paste structure, which highlights the issues mentioned in the previous chapter. Therefore, the bond behaviour was not impacted by the EMV Method, but by the used binder.

Finally, the main objective of this project was to study the bond behaviour of RCA concrete made with the EMV method. Hence, a direct comparison with the ACI mix for all three combinations is presented in Figure 4-125, Figure 4-126, and Figure 4-128. In all upcoming plots, and to facilitate a better comparison with the previous results, the strain gauge data was not completely filtered to allow a better visualization of the points or stages where they started to become unreliable.

In the case of the 15M – 170 mm combination, there are similarities in terms of bond peak and shape, especially for the readings of SG2 and SG3, although the EMV results tend to have a slightly higher degradation in the cyclic tests. It is also appreciated how the readings coming from the ACI and EMV monotonic tests present more noise than the other samples, which most likely indicates the point where the pullout/splitting failure took place.

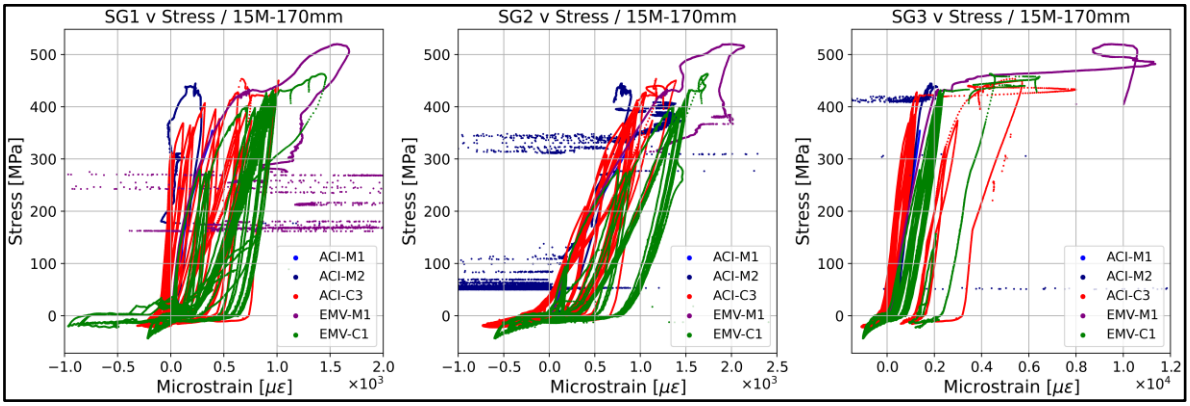

Figure 4-125: Strain v stress, ACI v EMV, 15M-170mm.

Despite being nearly 55% of the minimum embedment required by CSA A23.3 for the 15M rebar size, the 170 mm effectively allowed the development of yielding stresses, as shown in the readings coming from SG3 for both monotonic and cyclic loading. Moreover, the behaviour between both mixes seems to be similar, with the EMV presenting a slightly softer degradation during the cyclic test, which can be attributed to the ITZ cracking inherited with the coarse RCA replacement, but not on a level where the performance would suffer an evident drop when compared to the reference mix.

A different trend is observed for the 15M – 320 mm combination, where the ACI mix is the one presenting the higher degradation, although there are no significant differences in terms of peak stresses as the bars ruptured. The strain penetration profiles are also similar, with the monotonic tests confirming the yielding of the rebar starting from SG2, and the cyclic test having a reduced yielding effect affecting only the area surrounding SG3. Furthermore, the readings are noticeable less noisy than the previous case, which is linked to the failure mechanism taking place outside the specimen. It is also appreciated how the bar rupture had different strain drops, with SG3 presenting a different pattern than the readings coming from SG1 and SG2, respectively.

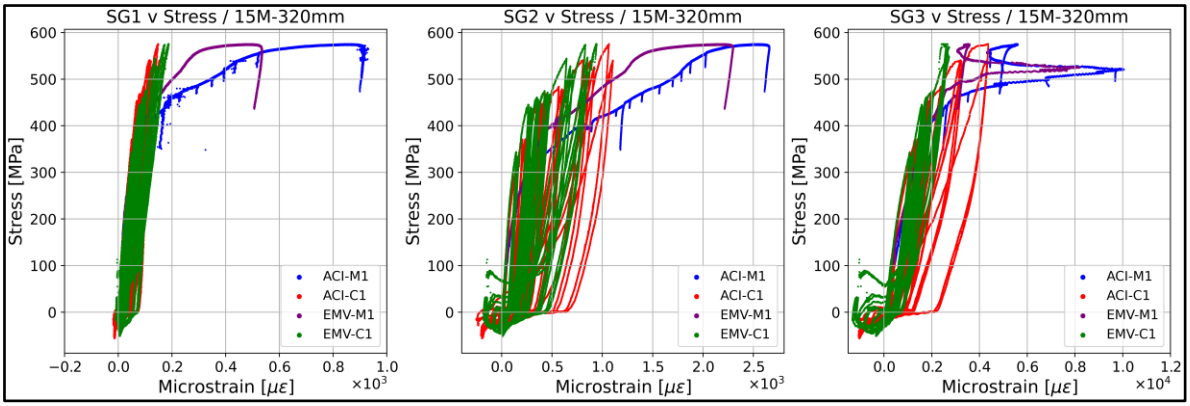

Figure 4-126: Strain v stress, ACI v EMV, 15M-320mm.

This particular combination highlights why bond is not an average property, and why it is important to understand its distribution along the embedded region. The 320 mm of embedment length are almost doubling the previous combination and are slightly above the minimum 300 mm required by CSA A23.3 and ACI 318 for all scenarios. Despite the longer section, the readings coming from SG1 are minor when compared to SG2 and SG3. The distance between these last two gauges is 160 mm, almost the same as the previous 170 mm combination, and the readings show almost identical results to those obtained for SG1 and SG3 in the previous case.

Therefore, for this particular structural combination of bar size, concrete cover and embedment length, it is implied that 170 mm are the minimum required to allow the rebar to yield. However, once the ultimate bond capacity is achieved within a limited anchorage area, the bond will break and the bar will pull out, which is undesired for structural applications. In consequence, the embedment length required by the design equations of CSA A23.3 and ACI 318 provides an anchorage length which is long enough to not only allow the rebar to yield, but to secure a safety margin that prevents the brittle failure.

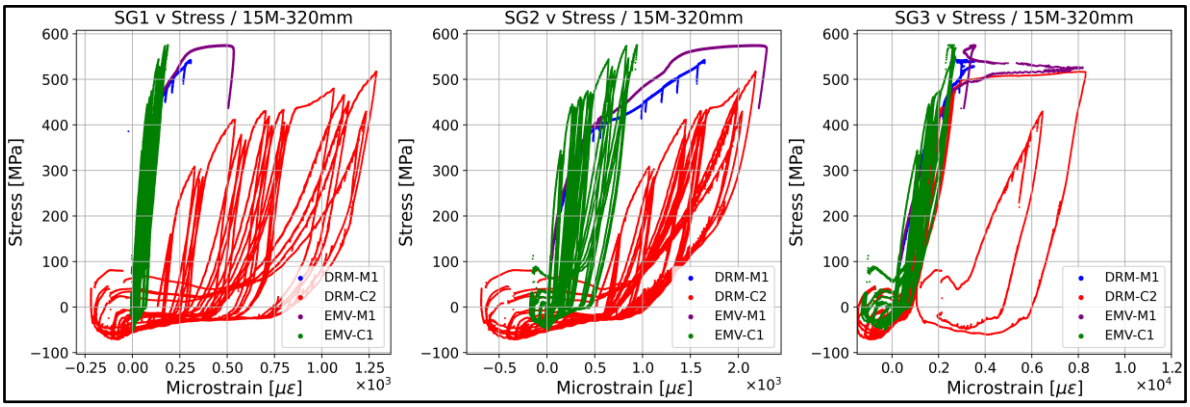

Figure 4-127: Strain v stress, DRM v EMV, 15M-320mm.

The strain distribution between the ACI and EMV mixes (as shown in Figure 4-126) presents an almost similar behaviour for both monotonic and cyclic loading, much in line with the previous 170 mm combination. Moreover, Figure 4-127 highlights the benefits of the EMV Method when compared to the traditional DRM approach used for RCA concrete. When analyzing the strain readings from all gauges, it becomes evident the DRM specimen was suffering from an accelerated degradation when compared to the EMV sample during the cyclic test, which is mainly due to the 100% coarse RCA replacement.

When using a 100% RCA replacement, the volumetric imbalance caused by the RM will lead to a new concrete mix that will have less coarse aggregates, which are concrete's skeleton. The new DRM concrete can achieve the same compressive strength as the parent ACI concrete, but the most important parameter for structural applications is the elastic

modulus, since the dynamic performance is tied to the stiffness of the composite. A lower elastic modulus indicates the concrete will degrade faster, and that is precisely the main difference between the DRM and EMV mixes, as discussed in the previous chapter. This effect is directly reflected on the strain gauge readings, where the EMV specimen is performing at the same level as the ACI mix without major degradation signs.

Lastly, the 25M – 320 mm combination presents some discrepancies in the values of SG1, which can be attributed to the moment where the crack at the bottom support started to develop. However, the readings from SG2 and SG3 also showcase a similar behaviour, which highlights the effectiveness of the EMV Method to produce RCA concrete that can match the performance of the conventional concrete under cyclic loads, even for reduced anchorage lengths as the one tested for this combination. In terms of data noise, a better cleanliness than for the 15M – 170 mm combination is observed, as the pure splitting failure induced a sudden drop with the gauges still on the elastic range.

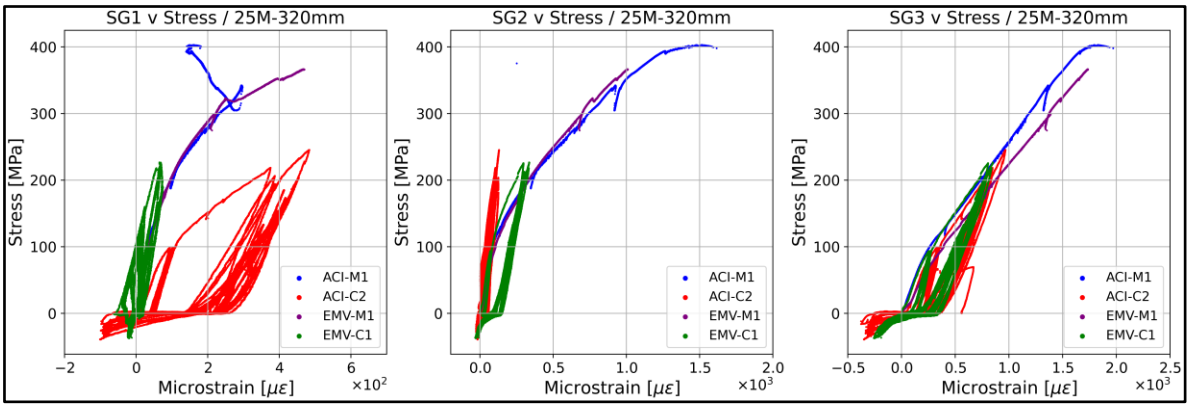

Figure 4-128: Strain v stress, ACI v EMV, 25M-320mm.

The 320 mm represent almost 45% of the minimum embedment required by CSA A23.3 for the 25M bar, and the results show it was almost enough to allow a localized yielding at SG3. This again highlights the conservative nature of the design equations, where the safety margin not only provides enough length for the rebar to yield, but also to account for any variability that can impact the bond transfer mechanism.

Therefore, when taking a global approach at the tested combinations, the 15M – 170 mm and 25M – 320 mm represent traditional bond tests configurations that aim to study the bond response with a diminished anchorage. These specimens showcase how far the bond peak can be and the actual minimum lengths that can allow the reinforcement yielding. Nevertheless, by reaching the ultimate bond capacity the failure will certainly be brittle, which is undesired for structural applications. The benefit of studying these configurations is that they allow to understand the impact of the concrete cover, confinement, embedment length, and bar size on the bond properties.

Likewise, the results also highlight why practitioners prefer to use smaller bars when possible. Since the required development length is smaller, it provides an extra safety margin and more design flexibility as more bars can be developed in a shorter distance, unless the structural member involves a congested area where less bars are preferred. For this case, larger bars can solve the structural demands, but larger sections are also needed to guarantee their anchorage and splices.

The 15M – 320 mm combination presents a better comparison for structural applications since the embedded region complies with the CSA A23.3 and ACI 318 requirements. The results show a similar performance between the ACI and EMV samples for both monotonic and cyclic loading, thus highlighting the current structural provisions could potentially be applied for RCA concrete made with the EMV Method. The data also shows the safety margin of the design equations could help offset any variability that could come from the RCA source, as the performance drops are better contained since the EMV Method helps controlling the elastic modulus, as opposed to the traditional DRM approach. Nevertheless, extra durability (for the exposure conditions) and large-scale tests with a fully reversed protocol are still required to develop a full assessment.

5. Conclusions and recommendations

The scope of this project meant that two big areas had to be developed, the concrete mix designs using the EMV Method for the RCA incorporation, and the test of the beam-ends to gain insights about their bond behaviour under cyclic loads. The main lessons and recommendations from each stage are presented in the upcoming sections.

5.1. Concrete mix development

As a general comment, the concrete fabrication process should not be underestimated since it plays a major role in the quality of the final product. When batching at an industrial scale, the automation and raw machinery power help to improve the batch consistency and to keep the properties within specified confidence levels. Nevertheless, concrete made at a laboratory scale involves more artisanal work given the diminished batch size, which adds an extra variability layer due to the workforce skillset.

Even though this topic is traditionally taken for granted, it is important to account for the labour variability early on during the initial trial batches, especially because concrete itself is a highly heterogeneous material. As seen throughout the project, small details such as presoaking or the use of a shaking table for the cylinder's compaction can play a major role in the final product quality. Therefore, an experienced and trained team is essential for a more precise assessment of the factors that might be influencing concrete's performance, especially when new materials or processes are being tested.

When it comes to the development of the concrete mixes, the overall process was considered a success as it provided the basis for the structural specimens that were discussed in Chapter 4. The series of trial batches and applied tests allowed a better understanding of the mix characteristics, and the results are in concordance with the available literature. However, a few recommendations can be laid out for future research.

The first one is the testing of the updated mixes to quantify the effects of the error in the "New-NA" properties. Besides the pool of applied tests, the inclusion of shrinkage, creep, freeze-and-thaw, and chloride tests would help expand the knowledge and long-term behaviour of the EMV mixes. The first two tests would help to corroborate whether the presoaking has a negative impact on the strength development and overall concrete quality, while the remaining two are essential to determine the concrete performance against winter conditions and the use of de-icing salts, which are severely hard in Canada. For structural applications, these tests would require increasing the concrete cover from 40 mm to 60 mm to comply with the requirements of the C-1 exposure class.

It would also be interesting to see the effects that SCMs could bring to the EMV mix performance. The cement content would be further reduced, thus leading to a lower carbon footprint but could also help enhance the workability in the fresh state, although trial batches would be needed to fine tune the admixtures content to avoid segregation and bleeding. The best way to assess their impact and combinations would be by testing one at a time, evaluate their performance in the fresh and hardened states, and build a database that could help the development of concrete mixes with multiple SCMs.

In the case of alternative binders, their potential effects on the reduction of the carbon footprint of the industry are immensely attractive since they target a full clinker replacement, by far concrete's most pollutant component. This potential benefit will keep encouraging their study and implementation in the upcoming years, especially their chemical composition and compatibility with the current generation of concrete admixtures and industry processes. A full understanding and good performance are key to incentivise their adoption, as they must guarantee confidence and safety.

For the particular case of the "C-Crete Binder", the results were inferior when compared to the same mixes made with conventional GUL cement. Given the proprietary nature of the product, it was not possible to study its full chemical composition and hydration

products; therefore, it is believed the performance drop could be linked to its hydration process in the medium- and long-term, the quality of the hydration products, or to its compatibility with admixtures, which are specifically tailored for GUL cement.

On the other hand, the EMV Method proved successful for the design of RCA mixes that can target the performance levels of conventional concrete. This phase included the use of RHC but a lack of information regarding its composition prevented a more detailed classification. Therefore, it would be interesting for future research to collect this information and determine whether mixes with different RCAs, and consequently different RMCs, could be produced and meet the current performance requirements. That would help create a better RCA integration in newer products such as structural applications and opposed to the traditional second tier filler and pavement aggregates.

Furthermore, a more tailored use of the concrete admixtures could help improve the quality and consistency of the EMV-made concrete. The biggest difference between EMV and conventional concrete mixes lies in the amount of fresh cement paste, which can be noticeably lower for the former (28% for this project). This characteristic requires enhanced dispersion and nucleation effects since the reduced cement paste must be able to coat the total coarse aggregate volume, including the RCA, and still comply with the flowability requirements (slump cone) without suffering bleeding or segregation.

The current admixtures generation has proved to be an excellent tool for conventional concrete, and it is believed that closer collaborations with industry partners can lead to the development of better suited products that can work with multiple RCA sources, binders and SCMs. The results of this project indicate that higher dosages per mass of cementitious materials can improve the fresh state, despite them being magnified due to the reduced fresh cement content that is considered for the new mix. The use of GUL cement can also help the dispersion and nucleation effects because of the limestone filler. In consequence, the major challenge is the efficiency to isolate and hydrate the reduced cement grains.

In terms of performance, once the admixtures content was defined for each mix type, the fresh state fulfilled the slump and fresh density requirements, with all mixes achieving good performance and showing no signs of bleeding or segregation. However, reliability issues with the air metre prevented a better assessment of this category, which was not mandatory for the purposes of this research, but would have been in case durability and permeability tests were applied.

In the case of the hardened state, the compressive strength evolution indicated all mixes achieved the minimum of 35 MPa at 56 days. Nevertheless, the ACI and EMV mixes were closer to the 40 MPa mark, while the DRM and EMVc mixes lagged by around 10%. The elastic modulus results showed the biggest differences, as the ACI and EMV mixes had values around the 30 GPa barrier, while the DRM and EMVc mixes were inferior at 22 GPa and 25 GPa, respectively. In consequence, this category highlights the efficiency of the EMV Method to produce reliable and good-quality RCA concrete, since the stiffness parameters are within the range of conventional concrete.

Finally, the EMV Method has the advantage of allowing the use of multiple RCA sources since the RCA replacement depends on the RM content. Therefore, it would be interesting how a blended RCA source with different origins or RM contents would perform, as the results would indicate whether the current conceptualization needs extra adjustments or not. The same would apply for an RCA source coming from RCM or CDW, which is by far the biggest RCA source available worldwide.

5.2. Cyclic bond behaviour test

In the case of the structural tests that aimed to study the bond behaviour under cyclic loading of RCA concrete made with the EMV Method, the results showed good and comparable performance to conventional concrete across all combinations. The available literature indicated the monotonic performance was already similar given the ability of the

EMV Method to improve the stiffness of the RCA mix, which is a key parameter for the seismic performance assessment.

The development of the testing phase also left valuable insights that can be applied for future research to keep expanding the actual database. The first recommendation is attached to the viability of the reversed loading protocol. To understand the full seismic performance of EMV-proportioned RCA concrete, this step still needs to be addressed since it is key for the understanding of the pinching effects and how the bond behaves during the different loading stages. However, its implementation inevitably requires changes in the current specimen and setup designs.

In the case of the specimen design, the first modification would be the inclusion of transverse reinforcement that could provide the necessary confinement to avoid bar buckling issues. For this project, this change was not considered since the beam-end design was standardized in its unconfined configuration. Likewise, a second modification would be to move the embedded region back to its original location, which is close to the edge of the beam-end. This change is recommended since it would shorten the distance of the bond breaker and its interaction with the confinement. These two modifications would require modelling and testing to verify the best configuration.

Meanwhile, when it comes to the test setup, the first recommendation would be to change the gripping system. Self-reacting machines like the MTS 311.51 can be equipped with a set of grips that can replace the bar lock couplers. These accessories can be adapted to grab the different bar sizes and would help fix the inclination issues that generated the observed bending effects. Moreover, their implementation requires less space since they do not need to be attached to the top girder, which would potentially help reduce the congestion generated when the latter was brought down to connect the rebar to the coupler, thus complicating the bolts tightening process.

Another factor comes from the geometry and surface of the beam-ends, which changed across all samples as they were not 100% perfect. This condition impacted their installation on the setup as the supports had to be complemented with shim plates once both columns were bolted to the bottom girder to account for the gaps or inclinations that came with each individual specimen. On the beam-end side, the polishing of its surfaces would allow a better contact and lock with the supports.

On the other hand, the implementation of a channel instead of a bolt pattern for the fixation of the right column of Figure 4-9 would allow a better adjustment, since the column could be directly positioned and adjusted to face the beam-end without any inclinations, and shim plates (if necessary) could also be placed before bolting the column to the bottom girder. This arrangement would not only improve the lock and setup stability during the tests but also reduce the chance of experiencing cracking at the supports.

For this project, to evaluate the bond behaviour the decision was to prioritize bond combinations over repetitions. Hence, an obvious recommendation for future research would be to test multiple repetitions of the same combination to reduce the effects of concrete variability and identify possible trends. However, the structural configuration shall be carefully designed to produce the desired failure mechanism; otherwise, the testing of multiple combinations and repetitions could have a major impact on the project timeline.

In the case of the combinations chosen for this project, only the 25M – 320 mm produced a pure splitting failure without yielding the rebar. The 15M – 170 mm samples suffered a combined splitting/pullout failure, while the 15M – 320 mm specimens sustained a bar rupture. For the 15M cases, both embedment lengths allowed a strain penetration that induced localized yielding. Even though this phenomenon is relevant for the performance study between EMV-made RCA concrete and conventional concrete, it complicates the comparison against the available bond-slip models, which were developed for splitting and pullout failures with the reinforcement still in the elastic range. Once the

reinforcement yields, the bond v slip behaviour changes and its modelling is still under investigation due to its complexity.

For the 25M rebar, future studies could consider increasing the embedment length as it was still within the elastic range. Furthermore, another aspect that can be considered is the testing of different c/d_b ratios to assess the effect of the concrete cover. In the case of the 15M rebar, the same 320 mm allowed the bar development, which was in line with the requirements of CSA A23.3 (where the minimum is 300 mm) and proved the effectiveness of the EMV Method to produce RCA concrete as the failure mechanism was the same in the monotonic and cyclic tests, and the degradation was similar to the one experienced with the conventional concrete.

Nevertheless, the failure mechanism involves a different bond-slip pattern, as the bond and slip will progressively increase until the bar rupture, which is the same phenomenon experienced during the monotonic bond tests of the EMV Method development (Fathifazl et al., 2012). To study pure splitting or pullout failures, shorter embedment lengths or different c/d_b ratios are required; however, as seen throughout this project, even 170 mm were enough to induce localized yielding on the rebar. Therefore, embedment lengths around 100 mm should provide the intended effects for the same 40 mm of cover.

If shorter embedment lengths are desired for future testing, the final recommendation would be to implement fibre-optic sensors instead of traditional strain gauges. Shorter bond lengths provide less space and given that the installation of a single gauge can take approximately 25 mm (1 in.), the surface intervention would increase along with the wire congestion. In contrast, fibre-optic sensors require less surface intervention and allow a continuous measurement, thus favouring the construction of a more accurate strain profile. Furthermore, their use may also help solve the restriction of the 5% strain limit of traditional gauges, which would improve the readings on the loaded end of the rebars.

In terms of the results obtained for this project, the three chosen bond combinations allowed the development of three different failure mechanisms. This condition favoured a broader study of the bond behaviour of all EMV-made beam-ends under monotonic and tension cyclic loading. In all cases, the performance of the EMV specimens was comparable to conventional concrete, with only minor differences in the degradation during the cyclic test, which was approximately 10%.

The 15M – 170 mm and the 25M – 320 mm specimens involved the use of shorter embedment lengths that those required by CSA A23.3 or ACI 318. However, the internal strains showed the former allowed the development of yielding stresses, while the latter was on the verge of achieving the same. When considering that they were 55% and 45% below the development length required for those bar sizes, the conservative nature of the design equations becomes clear, as they do not only provide enough length for the bar to yield, but also to account for any variability that can impact the bond behaviour and result in a brittle failure (splitting/pullout) as those observed for these combinations.

On the other hand, the 15M – 320 mm combination presented a more practical approach, as the embedded region was within the CSA A23.3 requirements (300 mm) for the 15M bar. The strain distribution once again showed that bond is not an average property and that its distribution on the embedded region is not uniform. The region where the highest strains concentrated had a length of 160 mm, almost identical to the 170 mm tested in the previous configurations.

In consequence, the results highlight two main points. The first one is the safety margin provided by the design equations, as enough length is available to yield the bar and avoid the brittle bond failure due to a lack of anchorage. On the same page, the second one is that the actual provisions could potentially be applied for structural RCA concrete made with the EMV Method, as its performance not only was comparable to the conventional concrete, but also remained well within the conservative nature of the design equations.

Now, when using the design equation of CSA A23.3 for the normalized bond prediction, the results for the 15M – 170 mm and 25M – 320 mm were underestimated by 35% on average. In contrast, the predictions for the 15M – 320 mm were accurate with only a 7% difference. As previously stated, the first two combinations involved the use of shorter embedment lengths, thus resulting in an increased bond peak since the average bond capacity is obtained by dividing the load by the embedment length. Therefore, the underestimation should be considered as the safety buffer the code provides, as those combinations represent the maximum bond capacities that can be achieved, but will not be reached in real life since the chosen embedment lengths are almost half of those mandated by the CSA A23.3 or ACI 318.

It is expected the outcomes of this project can help orient future large-scale tests, which are required for the verification of the observed behaviour but in real-life structural elements. When adding the benefit of RHC, where the RCA properties can be traced, it is believed the EMV Method could provide a reliable and effective way of producing good-quality RCA concrete that can meet the industry standards; thus helping to build and boost the confidence factor that is mandatory among practitioners, regulators, and contractors to secure its long-term adoption for structural applications.

6. Bibliography

Abbas, A., Fathifazl, G., Burkan Isgor, O., Razaqpur, A. G., Fournier, B., & Foo, S. (2008). Proposed Method for Determining the Residual Mortar Content of Recycled Concrete Aggregates. *Journal of ASTM International*, *5*(1), 1–12. https://doi.org/10.1520/JAI101087

Abbas, A., Fathifazl, G., Isgor, O. B., Razaqpur, A. G., Fournier, B., & Foo, S. (2006). Environmental Benefits of Green Concrete. *2006 IEEE EIC Climate Change Conference*, 1–8. https://doi.org/10.1109/EICCCC.2006.277204

ACI. (2001). *ACI PRC-555-01: Removal and Reuse of Hardened Concrete* (No. ACI555.1; Version 2001). American Concrete Institute. https://www.concrete.org

ACI. (2003). *ACI PRC-408-03: Bond and Development of Straight Reinforcing Bars in Tension (Reapproved 2012)* (No. ACI 408R-03; Version 1st Ed.). American Concrete Institute. https://www.concrete.org

ACI. (2013). *ACI PRC-374.2-13 Guide for Testing Reinforced Concrete Structural Elements Under Slowly Applied Simulated Seismic Loads* (No. ACI PRC-374.2; Version 1st Ed.). American Concrete Institute. https://www.concrete.org/store/productdetail.aspx?ItemID=374213&Language=English&Units=US_AND_METRIC

ACI. (2019). *ACI CODE-318-19(22): Building Code Requirements for Structural Concrete and Commentary (Reapproved 2022)* (No. ACI 318; Version 2019). American Concrete Institute. https://www.concrete.org/store/productdetail.aspx?ItemID=318U19&Language=English&Units=US_Units (Active)

ACI. (2022). *ACI PRC-211.1-22: Selecting Proportions for Normal-Density and High Density-Concrete—Guide* (No. ACI 211.1; Version 2022). American Concrete Institute. https://www.concrete.org

Adams, M. P., Fu, T., Cabrera, A. G., Morales, M., Ideker, J. H., & Isgor, O. B. (2016). Cracking susceptibility of concrete made with coarse recycled concrete aggregates.

Construction and Building Materials, *102*, 802–810. https://doi.org/10.1016/j.conbuildmat.2015.11.022

Ahimoghadam, F., Sanchez, L. F. M., De Souza, D. J., Andrade, G. P., Noël, M., & Demers, A. (2020). Influence of the Recycled Concrete Aggregate Features on the Behavior of Eco-Efficient Mixtures. *Journal of Materials in Civil Engineering*, *32*(9), 04020252. https://doi.org/10.1061/(ASCE)MT.1943-5533.0003323

Akbarnezhad, A., Ong, K. C. G., Zhang, M. H., & Tam, C. T. (2013). Acid Treatment Technique for Determining the Mortar Content of Recycled Concrete Aggregates. *Journal of Testing and Evaluation*, *41*(3), 441–450. https://doi.org/10.1520/JTE20120026

Alavi-Fard, M., & Marzouk, H. (2002). Bond behavior of high strength concrete under reversed pull-out cyclic loading. *Canadian Journal of Civil Engineering*, *29*(2), 191–200. https://doi.org/10.1139/l01-088

Al-Bayati, H. K. A., Das, P. K., Tighe, S. L., & Baaj, H. (2016). Evaluation of various treatment methods for enhancing the physical and morphological properties of coarse recycled concrete aggregate. *Construction and Building Materials*, *112*, 284–298. https://doi.org/10.1016/j.conbuildmat.2016.02.176

Arezoumandi, M., Drury, J., Volz, J. S., & Khayat, K. H. (2015a). *Effect of Recycled Concrete Aggregate Replacement Level on the Shear Strength of Reinforced Concrete Beams*. https://www.concrete.org/publications/internationalconcreteabstractsportal.aspx?m=details&i=51687766

Arezoumandi, M., Smith, A., Volz, J. S., & Khayat, K. H. (2014). An experimental study on shear strength of reinforced concrete beams with 100% recycled concrete aggregate. *Construction and Building Materials*, *53*, 612–620. https://doi.org/10.1016/j.conbuildmat.2013.12.019

Arezoumandi, M., Smith, A., Volz, J. S., & Khayat, K. H. (2015b). An experimental study on flexural strength of reinforced concrete beams with 100% recycled concrete aggregate. *Engineering Structures*, *88*, 154–162. https://doi.org/10.1016/j.engstruct.2015.01.043

Asghari Ghajari, F., & Yousefpour, H. (2023). Cyclic bond behavior in reinforced concrete flexural members exposed to elevated temperatures. *Engineering Structures*, *292*, 116520. https://doi.org/10.1016/j.engstruct.2023.116520

ASTM. (2019). *ASTM C192/C192M - Practice for Making and Curing Concrete Test Specimens in the Laboratory* (No. ASTM C192/C192M; Version 2019). ASTM International. https://doi.org/10.1520/C0192_C0192M-19 (Active)

ASTM. (2022a). *ASTM C469/469M-22—Standard Test Method for Static Modulus of Elasticity and Poisson's Ratio of Concrete in Compression* (No. C469/469M; Version 2022). ASTM International. https://doi.org/10.1520/C0469_C0469M-22 (Active)

ASTM. (2022b). *ASTM A944-22—Standard Test Method for Comparing Bond Strength of Steel Reinforcing Bars to Concrete Using Beam-End Specimens* (No. ASTM A944; Version 2022). ASTM International. https://store.astm.org/a0944-22.html

ASTM. (2023). *ASTM C29/C29M - Standard Test Method for Bulk Density ("Unit Weight") and Voids in Aggregate* (No. ASTM C29/C29M; Version 2023). ASTM International. https://doi.org/10.1520/C0029_C0029M-23

ASTM. (2024a). *ASTM C33/C33M-24a—Specification for Concrete Aggregates* (No. ASTM C33/C33M; Version 2024). ASTM International. https://doi.org/10.1520/C0033_C0033M-24A

ASTM. (2024b). *ASTM C88/C88M-24—Standard Test Method for Soundness of Aggregates by Use of Sodium Sulfate or Magnesium Sulfate* (No. ASTM C88/C88M; Version 2024). ASTM International. https://compass.astm.org/document/?contentCode=ASTM%7CC0088_C0088M-24%7Cen-US

ASTM. (2024c). *ASTM C260/C260M-24—Specification for Air-Entraining Admixtures for Concrete* (No. ASTM C260/C260M; Version 2024). ASTM International. https://doi.org/10.1520/C0260_C0260M-24

ASTM. (2024d). *ASTM C494/C494M-24—Specification for Chemical Admixtures for Concrete* (No. ASTM C494/C494M; Version 2024). ASTM International. https://doi.org/10.1520/C0494_C0494M-24

ASTM. (2024e). *ASTM C595/C595M-24—Specification for Blended Hydraulic Cements* (No. ASTM C595/C595M; Version 2024). ASTM International. https://doi.org/10.1520/C0595_C0595M-24

ASTM. (2025). *ASTM C125-25a—Terminology Relating to Concrete and Concrete Aggregates* (No. ASTM C125a; Version 2025). ASTM International. https://doi.org/10.1520/C0125-25A

Avet, F., & Scrivener, K. (2018). Investigation of the calcined kaolinite content on the hydration of Limestone Calcined Clay Cement (LC3). *Cement and Concrete Research*, *107*, 124–135. https://doi.org/10.1016/j.cemconres.2018.02.016

Baktheer, A., Spartali, H., Hegger, J., & Chudoba, R. (2021). High-cycle fatigue of bond in reinforced high-strength concrete under push-in loading characterized using the modified beam-end test. *Cement and Concrete Composites*, *118*, 103978. https://doi.org/10.1016/j.cemconcomp.2021.103978

Biernacki, J. J., Bullard, J. W., Sant, G., Brown, K., Glasser, F. P., Jones, S., Ley, T., Livingston, R., Nicoleau, L., Olek, J., Sanchez, F., Shahsavari, R., Stutzman, P. E., Sobolev, K., & Prater, T. (2017). Cements in the 21st century: Challenges, perspectives, and opportunities. *Journal of the American Ceramic Society*, *100*(7), 2746–2773. https://doi.org/10.1111/jace.14948

Bischoff, P. H., & Perry, S. H. (1991). Compressive behaviour of concrete at high strain rates. *Materials and Structures*, *24*(6), 425–450. https://doi.org/10.1007/BF02472016

Brand, A. S., Roesler, J. R., & Salas, A. (2015). Initial moisture and mixing effects on higher quality recycled coarse aggregate concrete. *Construction and Building Materials*, *79*, 83–89. https://doi.org/10.1016/j.conbuildmat.2015.01.047

Bravo, M., de Brito, J., Evangelista, L., & Pacheco, J. (2018). Durability and shrinkage of concrete with CDW as recycled aggregates: Benefits from superplasticizer's incorporation and influence of CDW composition. *Construction and Building Materials*, *168*, 818–830. https://doi.org/10.1016/j.conbuildmat.2018.02.176

Butler, L. J., West, J. S., & Tighe, S. L. (2015a). Bond of Reinforcement in Concrete Incorporating Recycled Concrete Aggregates. *Journal of Structural Engineering*, *141*(3), B4014001. https://doi.org/10.1061/(ASCE)ST.1943-541X.0000928

Butler, L. J., West, J. S., & Tighe, S. L. (2015b). Closure to "Bond of Reinforcement in Concrete Incorporating Recycled Concrete Aggregates" by Liam J. Butler, Jeffrey S. West, and Susan L. Tighe. *Journal of Structural Engineering*, *141*(2), 07014006. https://doi.org/10.1061/(ASCE)ST.1943-541X.0001233

Butler, L., Tighe, S. L., & West, J. S. (2013). Guidelines for Selection and Use of Coarse Recycled-Concrete Aggregates in Structural Concrete. *Transportation Research Record*, *2335*(1), 3–12. https://doi.org/10.3141/2335-01

Butler, L., West, J. S., & Tighe, S. L. (2011). The effect of recycled concrete aggregate properties on the bond strength between RCA concrete and steel reinforcement. *Cement and Concrete Research*, *41*(10), 1037–1049. https://doi.org/10.1016/j.cemconres.2011.06.004

Butler, L., West, J. S., & Tighe, S. L. (2012). Effect of Recycled Concrete Aggregate Properties on Mixture Proportions of Structural Concrete. *Transportation Research Record*, *2290*(1), 105–114. https://doi.org/10.3141/2290-14

Camps, B., Baktheer, A., Hegger, J., & Chudoba, R. (2018). Experimental Characterization of Bond Fatigue Using Beam-End Tests with Push-In Loading. *Proceedings*, *2*(8), Article 8. https://doi.org/10.3390/ICEM18-05270

Carrillo, J., & Alcocer, S. M. (2013). Experimental investigation on dynamic and quasi-static behavior of low-rise reinforced concrete walls. *Earthquake Engineering & Structural Dynamics*, *42*(5), 635–652. https://doi.org/10.1002/eqe.2234

C-Crete Technologies. (2023, October 31). *C-Crete Binder—Safety Data Sheet*. C-Crete Technologies. https://ccretetech.com/

Ceia, F., Raposo, J., Guerra, M., Júlio, E., & de Brito, J. (2016). Shear strength of recycled aggregate concrete to natural aggregate concrete interfaces. *Construction and Building Materials*, *109*, 139–145. https://doi.org/10.1016/j.conbuildmat.2016.02.002

Cement Association of Canada. (2022). *Design and Control of Concrete Mixtures (EB101)* (9th Edition). Cement Association of Canada. https://cement.ca

Cement Association of Canada. (2023). *Technical introduction to portland-limestone cement for municipal and provincial construction specifications* [V2.0]. Cement Association of Canada. https://cement.ca/sustainability/portland-limestone-cement/

CEN. (2011). *EN 197-1:2011—Cement—Part 1: Composition, specifications and conformity criteria for common cements* (No. EN 197-1; Version 2011). CEN. https://standards.cencenelec.eu/dyn/www/f?p=CEN:110:0::::FSP_PROJECT,FSP_ORG_ID:27250,6035&cs=175D88531A08CE46D255411A55E4E72C2

Chaouche, M., Gao, X. X., Cyr, M., Cotte, M., & Frouin, L. (2017). On the origin of the blue/green color of blast-furnace slag-based materials: Sulfur K-edge XANES investigation. *Journal of the American Ceramic Society*, *100*(4), 1707–1716. https://doi.org/10.1111/jace.14670

Cheung, J., Jeknavorian, A., Roberts, L., & Silva, D. (2011). Impact of admixtures on the hydration kinetics of Portland cement. *Cement and Concrete Research*, *41*(12), 1289–1309. https://doi.org/10.1016/j.cemconres.2011.03.005

Coffetti, D., Crotti, E., Gazzaniga, G., Carrara, M., Pastore, T., & Coppola, L. (2022). Pathways towards sustainable concrete. *Cement and Concrete Research*, *154*, 106718. https://doi.org/10.1016/j.cemconres.2022.106718

Colangelo, F., Navarro, T. G., Farina, I., & Petrillo, A. (2020). Comparative LCA of concrete with recycled aggregates: A circular economy mindset in Europe. *The International Journal of Life Cycle Assessment*, *25*(9), 1790–1804. https://doi.org/10.1007/s11367-020-01798-6

Coppola, L., Coffetti, D., Crotti, E., Gazzaniga, G., & Pastore, T. (2019). An Empathetic Added Sustainability Index (EASI) for cementitious based construction materials. *Journal of Cleaner Production*, *220*, 475–482. https://doi.org/10.1016/j.jclepro.2019.02.160

CSA Group. (2021). *CSA G30.18:21—Carbon steel bars for concrete reinforcement* (No. CSA G30.18; Version 5th Edition). CSA Group. https://www.csagroup.org/store/product/CSA%20G30.18%3A21/ (Active)

CSA Group. (2023). *CSA A3000:23—Cementitious materials compendium* (No. CSA A3000; Version 6.0). CSA Group. https://www.csagroup.org

CSA Group. (2024a). *CSA A23.1:24/CSA A23.2:24—Concrete materials and methods of concrete construction/Test Methods and Standard Practices for concrete* (No. CSA A23.1/CSA A23.2; Version 14.0). CSA Group. https://www.csagroup.org

CSA Group. (2024b). *CSA A23.3:24—Design of concrete structures* (No. CSA A23.3; Version 8.0). CSA Group. https://www.csagroup.org

Damdelen, O. (2018). Investigation of 30% recycled coarse aggregate content in sustainable concrete mixes. *Construction and Building Materials*, *184*, 408–418. https://doi.org/10.1016/j.conbuildmat.2018.06.149

Darwin, D., & Graham, E. K. (1993). Effect of Deformation Height and Spacing on Bond Strength of Reinforcing Bars. *Structural Journal*, *90*(6), 646–657. https://doi.org/10.14359/4459

Darwin, D., Zuo, J., Tholen, M. L., & Ldun, E. K. (1996). Development Length Criteria for Conventional and High Relative Rib Area Reinforcing Bars. *Structural Journal*, *93*(3), 347–359. https://doi.org/10.14359/9694

Das, S., Aguayo, M., Sant, G., Mobasher, B., & Neithalath, N. (2015). Fracture process zone and tensile behavior of blended binders containing limestone powder. *Cement and Concrete Research*, *73*, 51–62. https://doi.org/10.1016/j.cemconres.2015.03.002

de Brito, J., Ferreira, J., Pacheco, J., Soares, D., & Guerreiro, M. (2016). Structural, material, mechanical and durability properties and behaviour of recycled aggregates concrete. *Journal of Building Engineering*, *6*, 1–16. https://doi.org/10.1016/j.jobe.2016.02.003

De Souza, D. J., de Grazia, M. T., Macedo, H. F., Sanchez, L. F. M., de Andrade, G. P., Naboka, O., Fathifazl, G., & Nkinamubanzi, P.-C. (2022). Influence of the Mix Proportion and Aggregate Features on the Performance of Eco-Efficient Fine Recycled Concrete Aggregate Mixtures. *Materials*, *15*(4), Article 4. https://doi.org/10.3390/ma15041355

Deng, M., Pan, J., & Sun, H. (2019). Bond behavior of deformed bar embedded in Engineered Cementitious Composites under cyclic loading. *Construction and Building Materials*, *197*, 164–174. https://doi.org/10.1016/j.conbuildmat.2018.11.200

Deng, Z., Wang, Y., Yang, H., & Qian, J. (2018). Research on Crack Behavior of Recycled Concrete Beams under Short-term Loading. *KSCE Journal of Civil Engineering*, *22*(5), 1763–1770. https://doi.org/10.1007/s12205-017-0678-7

Diaz-Loya, I., Juenger, M., Seraj, S., & Minkara, R. (2019). Extending supplementary cementitious material resources: Reclaimed and remediated fly ash and natural pozzolans. *Cement and Concrete Composites*, *101*, 44–51. https://doi.org/10.1016/j.cemconcomp.2017.06.011

DIN. (2017). *DIN 4226-101:2017-08, Rezyklierte Gesteinskörnungen für Beton nach DIN_EN_12620_- Teil_101: Typen und geregelte gefährliche Substanzen* (Version 2017). DIN Media GmbH. https://doi.org/10.31030/2664038

DIN. (2021). *DIN EN 206:2021-06, Beton_- Festlegung, Eigenschaften, Herstellung und Konformität; Deutsche Fassung EN_206:2013+A2:2021* (Version 2021). DIN Media GmbH. https://doi.org/10.31030/3198971

DIN. (2023). *DIN 1045-2:2023-08, Tragwerke aus Beton, Stahlbeton und Spannbeton_- Teil_2: Beton* (Version 2023). DIN Media GmbH. https://doi.org/10.31030/3445766

Eguchi, K., Teranishi, K., Nakagome, A., Kishimoto, H., Shinozaki, K., & Narikawa, M. (2007). Application of recycled coarse aggregate by mixture to concrete construction. *Construction and Building Materials*, *21*(7), 1542–1551. https://doi.org/10.1016/j.conbuildmat.2005.12.023

Evangelista, L., & De Brito, J. (2014). Concrete with fine recycled aggregates: A review. *European Journal of Environmental and Civil Engineering*, *18*(2), 129–172. https://doi.org/10.1080/19648189.2013.851038

Fan, G., Song, Y., & Wang, L. (2014). Experimental study on the seismic behavior of reinforced concrete beam-column joints under various strain rates. *Journal of Reinforced Plastics and Composites*, *33*(7), 601–618. https://doi.org/10.1177/0731684413512706

Fathifazl, G., Abbas, A., Razaqpur, A. G., Isgor, O. B., Fournier, B., & Foo, S. (2009a). New Mixture Proportioning Method for Concrete Made with Coarse Recycled Concrete Aggregate. *Journal of Materials in Civil Engineering*, *21*(10), 601–611. https://doi.org/10.1061/(ASCE)0899-1561(2009)21:10(601)

Fathifazl, G., Ghani Razaqpur, A., Burkan Isgor, O., Abbas, A., Fournier, B., & Foo, S. (2011a). Creep and drying shrinkage characteristics of concrete produced with coarse recycled concrete aggregate. *Cement and Concrete Composites*, *33*(10), 1026–1037. https://doi.org/10.1016/j.cemconcomp.2011.08.004

Fathifazl, G., Razaqpur, A. G., Burka Isgor, O., Abbas, A., Fournier, B., & Foo, S. (2009b). Flexural Performance of Steel-Reinforced Recycled Concrete Beams. *ACI Structural Journal*, *106*(06). https://doi.org/10.14359/51663187

Fathifazl, G., Razaqpur, A. G., Burkan Isgor, O., Abbas, A., Fournier, B., & Foo, S. (2011b). Shear capacity evaluation of steel reinforced recycled concrete (RRC) beams. *Engineering Structures*, *33*(3), 1025–1033. https://doi.org/10.1016/j.engstruct.2010.12.025

Fathifazl, G., Razaqpur, A. g., Isgor, O. B., Abbas, A., Fournier, B., & Foo, S. (2009c). Shear strength of reinforced recycled concrete beams without stirrups. *Magazine of Concrete Research*, *61*(7), 477–490. https://doi.org/10.1680/macr.2008.61.7.477

Fathifazl, G., Razaqpur, A. g., Isgor, O. B., Abbas, A., Fournier, B., & Foo, S. (2010). Shear strength of reinforced recycled concrete beams with stirrups. *Magazine of Concrete Research*, *62*(10), 685–699. https://doi.org/10.1680/macr.2010.62.10.685

Fathifazl, G., Razaqpur, A. G., Isgor, O. B., Abbas, A., Fournier, B., & Foo, S. (2012). Bond performance of deformed steel bars in concrete produced with coarse recycled concrete aggregate. *Canadian Journal of Civil Engineering*, *39*(2), 128–139. https://doi.org/10.1139/l11-120

FIB. (2010). *Fib Model Code for Concrete Structures 2010* (No. fib Model Code 2010; Version 3th Edition). FIB-CEB-FIP. https://www.fib-international.org/publications/fib-bulletins/model-code-2010-first-complete-draft,-vol-1-pdf-146-detail.html

Flatt, R. J., & Houst, Y. F. (2001). A simplified view on chemical effects perturbing the action of superplasticizers. *Cement and Concrete Research*, *31*(8), 1169–1176. https://doi.org/10.1016/S0008-8846(01)00534-8

Garbarino, E., & Blengini, G. A. (2013). 6—The economics of construction and demolition waste (C&DW) management facilities. In F. Pacheco-Torgal, V. W. Y. Tam, J. A. Labrincha, Y. Ding, & J. de Brito (Eds.), *Handbook of Recycled Concrete and Demolition Waste* (pp. 108–138). Woodhead Publishing. https://doi.org/10.1533/9780857096906.1.108

Gartner, E., & Hirao, H. (2015). A review of alternative approaches to the reduction of CO2 emissions associated with the manufacture of the binder phase in concrete. *Cement and Concrete Research*, *78*, 126–142. https://doi.org/10.1016/j.cemconres.2015.04.012

Gartner, E. M., & Macphee, D. E. (2011). A physico-chemical basis for novel cementitious binders. *Cement and Concrete Research*, *41*(7), 736–749. https://doi.org/10.1016/j.cemconres.2011.03.006

Gartner, E., & Sui, T. (2018). Alternative cement clinkers. *Cement and Concrete Research*, *114*, 27–39. https://doi.org/10.1016/j.cemconres.2017.02.002

Gaurav, G., & Singh, B. (2021). Experimental investigation for splice strength of deformed steel bars in normal-, medium- and high-strength recycled aggregate concrete. *Construction and Building Materials*, *266*, 121185. https://doi.org/10.1016/j.conbuildmat.2020.121185

Gelardi, G., & Flatt, R. J. (2016). 11—Working mechanisms of water reducers and superplasticizers. In P.-C. Aïtcin & R. J. Flatt (Eds.), *Science and Technology of Concrete Admixtures* (pp. 257–278). Woodhead Publishing. https://doi.org/10.1016/B978-0-08-100693-1.00011-4

Government of Canada. (2022, March 29). *2030 Emissions Reduction Plan: Clean Air, Strong Economy* [Forward regulatory plan]. https://www.canada.ca/en/services/environment/weather/climatechange/climate-plan/climate-plan-overview/emissions-reduction-2030.html

Guerra, M., Ceia, F., De Brito, J., & Júlio, E. (2014). Anchorage of steel rebars to recycled aggregates concrete. *Construction and Building Materials*, *72*, 113–123. https://doi.org/10.1016/j.conbuildmat.2014.08.081

Hanehara, S., & Yamada, K. (1999). Interaction between cement and chemical admixture from the point of cement hydration, absorption behaviour of admixture, and paste rheology. *Cement and Concrete Research*, *29*(8), 1159–1165. https://doi.org/10.1016/S0008-8846(99)00004-6

Hansen, T. C. (1986). Recycled aggregates and recycled aggregate concrete second state-of-the-art report developments 1945–1985. *Materials and Structures*, *19*(3), 201–246. https://doi.org/10.1007/BF02472036

Hayles, M., Sanchez, L. F. M., & Noël, M. (2018). Eco-efficient low cement recycled concrete aggregate mixtures for structural applications. *Construction and Building Materials*, *169*, 724–732. https://doi.org/10.1016/j.conbuildmat.2018.02.127

Hover, K. (1995). Graphical Approach to Mixture Proportioning by ACI 211.1-91. *Concrete International*, *17*(9), 49–53.

Hu, X., Peng, G., Niu, D., & Wang, J. (2019). Bond properties of deformed steel bars in concrete during construction under reversed cyclic loading. *Construction and Building Materials*, *223*, 817–829. https://doi.org/10.1016/j.conbuildmat.2019.06.222

Idun, E. K., & Darwin, D. (1999). Bond of Epoxy-Coated Reinforcement: Coefficient of Friction and Rib Face Angle. *Structural Journal*, *96*(4), 609–615. https://doi.org/10.14359/698

Ignjatović, I. S., Marinković, S. B., & Tošić, N. (2017). Shear behaviour of recycled aggregate concrete beams with and without shear reinforcement. *Engineering Structures*, *141*, 386–401. https://doi.org/10.1016/j.engstruct.2017.03.026

Imbabi, M. S., Carrigan, C., & McKenna, S. (2012). Trends and developments in green cement and concrete technology. *International Journal of Sustainable Built Environment*, *1*(2), 194–216. https://doi.org/10.1016/j.ijsbe.2013.05.001

Jolicoeur, C., & Simard, M.-A. (1998). Chemical admixture-cement interactions: Phenomenology and physico-chemical concepts. *Cement and Concrete Composites*, *20*(2), 87–101. https://doi.org/10.1016/S0958-9465(97)00062-0

JSA Group. (2024a). *JIS A 5021:2024 Recycled aggregate for concrete-Class H* (No. JIS A 5021; Version 5th Edition). Japanese Standards Association. https://webdesk.jsa.or.jp

JSA Group. (2024b). *JIS A 5022:2024 Recycled aggregate concrete-Class M* (No. JIS A 5022; Version 5th Edition). Japanese Standards Association. https://webdesk.jsa.or.jp

JSA Group. (2024c). *JIS A 5023:2024 Recycled aggregate concrete-Class L* (No. JIS A 5023; Version 5th Edition). Japanese Standards Association. https://webdesk.jsa.or.jp

Ju, H., Yerzhanov, M., Serik, A., Lee, D., & Kim, J. R. (2021). Statistical and Reliability Study on Shear Strength of Recycled Coarse Aggregate Reinforced Concrete Beams. *Materials*, *14*(12), Article 12. https://doi.org/10.3390/ma14123321

Juenger, M. C. G., & Siddique, R. (2015). Recent advances in understanding the role of supplementary cementitious materials in concrete. *Cement and Concrete Research*, *78*, 71–80. https://doi.org/10.1016/j.cemconres.2015.03.018

Kachouh, N., El-Maaddawy, T., El-Hassan, H., & El-Ariss, B. (2021). Shear Behavior of Steel-Fiber-Reinforced Recycled Aggregate Concrete Deep Beams. *Buildings*, *11*(9), Article 9. https://doi.org/10.3390/buildings11090423

Kannan, S., Arunachalam, K., & Brindha, D. (2021). Performance analysis of recycled aggregate concrete with chemical admixture. *Structural Concrete*, *22*(S1), E8–E21. https://doi.org/10.1002/suco.201900380

Katkhuda, H., & Shatarat, N. (2016). Shear behavior of reinforced concrete beams using treated recycled concrete aggregate. *Construction and Building Materials*, *125*, 63–71. https://doi.org/10.1016/j.conbuildmat.2016.08.034

Kim, S.-W., Yun, H.-D., Park, W.-S., & Jang, Y.-I. (2015). Bond strength prediction for deformed steel rebar embedded in recycled coarse aggregate concrete. *Materials & Design*, *83*, 257–269. https://doi.org/10.1016/j.matdes.2015.06.008

Kisku, N., Joshi, H., Ansari, M., Panda, S. K., Nayak, S., & Dutta, S. C. (2017). A critical review and assessment for usage of recycled aggregate as sustainable construction

material. *Construction and Building Materials*, *131*, 721–740. https://doi.org/10.1016/j.conbuildmat.2016.11.029

Koga, H., Katahira, H., & Shimata, A. (2022). The introduction of recycled-aggregate concrete specifications in Japan and the research into the freezing–thawing resistance of recycled-aggregate concrete. *Journal of Material Cycles and Waste Management*, *24*(4), 1207–1215. https://doi.org/10.1007/s10163-022-01412-x

Krawinkler, H. (1996). Cyclic Loading Histories for Seismic Experimentation on Structural Components. *Earthquake Spectra*, *12*(1), 1–12. https://doi.org/10.1193/1.1585865

Lawrence, P., Cyr, M., & Ringot, E. (2003). Mineral admixtures in mortars: Effect of inert materials on short-term hydration. *Cement and Concrete Research*, *33*(12), 1939–1947. https://doi.org/10.1016/S0008-8846(03)00183-2

Leite, M. B., & Monteiro, P. J. M. (2016). Microstructural analysis of recycled concrete using X-ray microtomography. *Cement and Concrete Research*, *81*, 38–48. https://doi.org/10.1016/j.cemconres.2015.11.010

Lemcherreq, Y., Zanuy, C., Vogel, T., & Kaufmann, W. (2023). Strain-based analysis of reinforced concrete pull-out tests under monotonic and repeated loading. *Engineering Structures*, *289*, 115712. https://doi.org/10.1016/j.engstruct.2023.115712

Li, M., & Li, H. (2012). Effects of Strain Rate on Reinforced Concrete Structure under Seismic Loading. *Advances in Structural Engineering*, *15*(3), 461–475. https://doi.org/10.1260/1369-4332.15.3.461

Li, W., Xiao, J., Sun, Z., Kawashima, S., & Shah, S. P. (2012). Interfacial transition zones in recycled aggregate concrete with different mixing approaches. *Construction and Building Materials*, *35*, 1045–1055. https://doi.org/10.1016/j.conbuildmat.2012.06.022

Liew, K. M., Sojobi, A. O., & Zhang, L. W. (2017). Green concrete: Prospects and challenges. *Construction and Building Materials*, *156*, 1063–1095. https://doi.org/10.1016/j.conbuildmat.2017.09.008

Liu, J., Farzadnia, N., Shi, C., & Ma, X. (2019). Shrinkage and strength development of UHSC incorporating a hybrid system of SAP and SRA. *Cement and Concrete Composites*, *97*, 175–189. https://doi.org/10.1016/j.cemconcomp.2018.12.029

Liu, J., Shi, C., Ma, X., Khayat, K. H., Zhang, J., & Wang, D. (2017). An overview on the effect of internal curing on shrinkage of high performance cement-based materials. *Construction and Building Materials*, *146*, 702–712. https://doi.org/10.1016/j.conbuildmat.2017.04.154

Lockrey, S., Verghese, K., Crossin, E., & Nguyen, H. (2018). Concrete recycling life cycle flows and performance from construction and demolition waste in Hanoi. *Journal of Cleaner Production*, *179*, 593–604. https://doi.org/10.1016/j.jclepro.2017.12.271

Lotfi, S., Rem, P., Deja, J., & Mróz, R. (2017). An experimental study on the relation between input variables and output quality of a new concrete recycling process. *Construction and Building Materials*, *137*, 128–140. https://doi.org/10.1016/j.conbuildmat.2017.01.085

Lotfy, A., & Al-Fayez, M. (2015). Performance evaluation of structural concrete using controlled quality coarse and fine recycled concrete aggregate. *Cement and Concrete Composites*, *61*, 36–43. https://doi.org/10.1016/j.cemconcomp.2015.02.009

Lu, L., Yuan, G., Shu, Q., Huang, Z., Zhong, C., & Xu, B. (2019). Bond behaviour between early age concrete and steel bar subjected to cyclic loading after fire. *Fire Safety Journal*, *105*, 129–143. https://doi.org/10.1016/j.firesaf.2019.02.012

Lv, L., Yang, H., Zhang, T., & Deng, Z. (2018). Bond behavior between recycled aggregate concrete and deformed bars under uniaxial lateral pressure. *Construction and Building Materials*, *185*, 12–19. https://doi.org/10.1016/j.conbuildmat.2018.06.226

Maison, B., & Chao, S.-H. (2024). Test Protocols for ASCE 41 Backbones in Concrete Building Evaluation. *Journal of Structural Engineering*, *150*(9), 04024108. https://doi.org/10.1061/JSENDH.STENG-12651

Malvar, L. J. (1998). Review of Static and Dynamic Properties of Steel Reinforcing Bars. *Materials Journal*, *95*(5), 609–616. https://doi.org/10.14359/403

Marchon, D., Kawashima, S., Bessaies-Bey, H., Mantellato, S., & Ng, S. (2018). Hydration and rheology control of concrete for digital fabrication: Potential admixtures and cement chemistry. *Cement and Concrete Research*, *112*, 96–110. https://doi.org/10.1016/j.cemconres.2018.05.014

Marder, K. J., Motter, C. J., Elwood, K. J., & Clifton, G. C. (2018). Effects of variation in loading protocol on the strength and deformation capacity of ductile reinforced concrete beams. *Earthquake Engineering & Structural Dynamics*, *47*(11), 2195–2213. https://doi.org/10.1002/eqe.3064

Martí-Vargas, J. R., & García-Taengua, E. (2015). Discussion of "Bond of Reinforcement in Concrete Incorporating Recycled Concrete Aggregates" by Liam J. Butler, Jeffrey S. West, and Susan L. Tighe. *Journal of Structural Engineering*, *141*(2), 07014005. https://doi.org/10.1061/(ASCE)ST.1943-541X.0001232

McGinnis, M. J., Davis, M., De La Rosa, A., Weldon, B. D., & Kurama, Y. C. (2017). Strength and stiffness of concrete with recycled concrete aggregates. *Construction and Building Materials*, *154*, 258–269. https://doi.org/10.1016/j.conbuildmat.2017.07.015

Mechtcherine, V., Wyrzykowski, M., Schröfl, C., Snoeck, D., Lura, P., De Belie, N., Mignon, A., Van Vlierberghe, S., Klemm, A. J., Almeida, F. C. R., Tenório Filho, J. R., Boshoff, W. P., Reinhardt, H.-W., & Igarashi, S.-I. (2021). Application of super absorbent polymers (SAP) in concrete construction—Update of RILEM state-of-the-art report. *Materials and Structures*, *54*(2), 1–20. https://doi.org/10.1617/s11527-021-01668-z

Mehta, P. K., & Monteiro, P. J. M. (2014). *Concrete: Microstructure, Properties, and Materials* (4th Edition). McGraw-Hill Education. https://www.accessengineeringlibrary.com/content/book/9780071797870

Meyer, C. (2009). The greening of the concrete industry. *Cement and Concrete Composites*, *31*(8), 601–605. https://doi.org/10.1016/j.cemconcomp.2008.12.010

Miller, S. A. (2018). Supplementary cementitious materials to mitigate greenhouse gas emissions from concrete: Can there be too much of a good thing? *Journal of Cleaner Production*, *178*, 587–598. https://doi.org/10.1016/j.jclepro.2018.01.008

Miller, S. A., John, V. M., Pacca, S. A., & Horvath, A. (2018). Carbon dioxide reduction potential in the global cement industry by 2050. *Cement and Concrete Research*, *114*, 115–124. https://doi.org/10.1016/j.cemconres.2017.08.026

Moallemi Pour, S., & Alam, M. S. (2016). Investigation of Compressive Bond Behavior of Steel Rebar Embedded in Concrete With Partial Recycled Aggregate Replacement. *Structures*, *7*, 153–164. https://doi.org/10.1016/j.istruc.2016.06.010

Moehle, J. (2015). *Seismic Design of Reinforced Concrete Buildings* (1st Edition). McGraw-Hill Education. https://www.accessengineeringlibrary.com/content/book/9780071839440

Monteiro, P. J. M., Miller, S. A., & Horvath, A. (2017). Towards sustainable concrete. *Nature Materials*, *16*(7), 698–699. https://doi.org/10.1038/nmat4930

MTO. (2024). *MTO LS-614 Method of Test for Freezing and Thawing of Coarse Aggregate* (Version 38th). Ministry of Transportation Ontario. https://www.library.mto.gov.on.ca/SydneyPLUS/TechPubs/Portal/tp/tdViews.aspx?lang=en-US

Neville, A. M. (2011). *Properties Of Concrete* (5th Edition). Pearson. https://www.pearson.com/en-ca/subject-catalog/p/properties-of-concrete-properties-of-concrete/P200000005116/9780273755807

Nie, S., Zhou, J., Yang, F., Lan, M., Li, J., Zhang, Z., Chen, Z., Xu, M., Li, H., & Sanjayan, J. G. (2022). Analysis of theoretical carbon dioxide emissions from cement production: Methodology and application. *Journal of Cleaner Production*, *334*, 130270. https://doi.org/10.1016/j.jclepro.2021.130270

Nixon, P. J. (1976). The use of materials from demolition in construction. *Resources Policy*, *2*(4), 276–283. https://doi.org/10.1016/0301-4207(76)90082-9

Nixon, P. J. (1978). Recycled concrete as an aggregate for concrete—A review. *Matériaux et Construction*, *11*(5), 371–378. https://doi.org/10.1007/BF02473878

Nkinamubanzi, P.-C., Mantellato, S., & Flatt, R. J. (2016). 16—Superplasticizers in practice. In P.-C. Aïtcin & R. J. Flatt (Eds.), *Science and Technology of Concrete Admixtures* (pp. 353–377). Woodhead Publishing. https://doi.org/10.1016/B978-0-08-100693-1.00016-3

Oh, B. H., & Kim, S. H. (2007). Realistic Models for Local Bond Stress-Slip of Reinforced Concrete under Repeated Loading. *Journal of Structural Engineering*, *133*(2), 216–224. https://doi.org/10.1061/(ASCE)0733-9445(2007)133:2(216)

Oikonomou, Nik. D. (2005). Recycled concrete aggregates. *Cement and Concrete Composites*, *27*(2), 315–318. https://doi.org/10.1016/j.cemconcomp.2004.02.020

Omary, S., Ghorbel, E., & Wardeh, G. (2016). Relationships between recycled concrete aggregates characteristics and recycled aggregates concretes properties. *Construction and Building Materials*, *108*, 163–174. https://doi.org/10.1016/j.conbuildmat.2016.01.042

Paranhos, R. S., Cazacliu, B. G., Sampaio, C. H., Petter, C. O., Neto, R. O., & Huchet, F. (2016). A sorting method to value recycled concrete. *Journal of Cleaner Production*, *112*, 2249–2258. https://doi.org/10.1016/j.jclepro.2015.10.021

Park, J., Park, M., Chae, Y., & Kim, C. (2024). Dynamic cyclic loading tests for investigating the influence of loading rate and axial force on the lateral response of RC columns. *Earthquake Engineering & Structural Dynamics*, *53*(4), 1537–1551. https://doi.org/10.1002/eqe.4085

Peng, L., Zhao, Y., & Zhang, H. (2021). Flexural behavior and durability properties of recycled aggregate concrete (RAC) beams subjected to long-term loading and chloride attacks. *Construction and Building Materials*, *277*, 122277. https://doi.org/10.1016/j.conbuildmat.2021.122277

Plank, J., Sakai, E., Miao, C. W., Yu, C., & Hong, J. X. (2015). Chemical admixtures—Chemistry, applications and their impact on concrete microstructure and durability. *Cement and Concrete Research*, *78*, 81–99. https://doi.org/10.1016/j.cemconres.2015.05.016

Pochanart, S., & Harmon, T. (1989). Bond-Slip Model for Generalized Excitations Including Fatigue. *Materials Journal*, *86*(5), 465–474. https://doi.org/10.14359/2052

Poon, C. S., Shui, Z. H., & Lam, L. (2004). Effect of microstructure of ITZ on compressive strength of concrete prepared with recycled aggregates. *Construction and Building Materials*, *18*(6), 461–468. https://doi.org/10.1016/j.conbuildmat.2004.03.005

Popa, M.-M., Signorini, C., Beigh, M. A. B., Chihadeh, A., Stommel, M., Kaliske, M., Mechtcherine, V., & Scheffler, C. (2025). Bond and cracking behavior of tailored limestone calcined clay cement-based composites including bicomponent polypropylene fibers with enhanced mechanical interlocking. *Cement and Concrete Composites*, *155*, 105812. https://doi.org/10.1016/j.cemconcomp.2024.105812

Prince, M. J. R., Gaurav, G., & Singh, B. (2018). Splice strength of steel reinforcement embedded in recycled aggregate concrete. *Construction and Building Materials*, *160*, 156–168. https://doi.org/10.1016/j.conbuildmat.2017.11.007

Provis, J. L. (2018). Alkali-activated materials. *Cement and Concrete Research*, *114*, 40–48. https://doi.org/10.1016/j.cemconres.2017.02.009

Puertas, F., González-Fonteboa, B., González-Taboada, I., Alonso, M. M., Torres-Carrasco, M., Rojo, G., & Martínez-Abella, F. (2018). Alkali-activated slag concrete: Fresh and hardened behaviour. *Cement and Concrete Composites*, *85*, 22–31. https://doi.org/10.1016/j.cemconcomp.2017.10.003

Rahal, K. N., & Alrefaei, Y. T. (2017). Shear strength of longitudinally reinforced recycled aggregate concrete beams. *Engineering Structures*, *145*, 273–282. https://doi.org/10.1016/j.engstruct.2017.05.028

Rahal, K. N., & Alrefaei, Y. T. (2018). Shear strength of recycled aggregate concrete beams containing stirrups. *Construction and Building Materials*, *191*, 866–876. https://doi.org/10.1016/j.conbuildmat.2018.10.023

Rao, A., Jha, K. N., & Misra, S. (2007). Use of aggregates from recycled construction and demolition waste in concrete. *Resources, Conservation and Recycling*, *50*(1), 71–81. https://doi.org/10.1016/j.resconrec.2006.05.010

Rehm, G., & Eligehausen, R. (1979). Bond of Ribbed Bars Under High Cycle Repeated Loads. *Journal Proceedings*, *76*(2), 297–310. https://doi.org/10.14359/6948

Reineck, K.-H., Kuchma, D. A., Kim, K. S., & Marx, S. (2003). *Shear Database for Reinforced Concrete Members without Shear Reinforcement*. https://www.concrete.org/publications/internationalconcreteabstractsportal/m/details/id/12488

Rockson, C., Tamanna, K., Alam, M. S., & Rteil, A. (2020). Effect of cover on bond strength of structural concrete using commercially produced recycled coarse and fine aggregates. *Construction and Building Materials*, *255*, 119275. https://doi.org/10.1016/j.conbuildmat.2020.119275

Rockson, C., Tamanna, K., Shahria Alam, M., & Rteil, A. (2021). Effect of rebar embedment length on the bond behavior of commercially produced recycled concrete using beam-end specimens. *Construction and Building Materials*, *286*, 122957. https://doi.org/10.1016/j.conbuildmat.2021.122957

Rodríguez, J., Aldabagh, S., & Alam, M. S. (2024). Loading protocols for quasi-static cyclic testing of flexure dominated reinforced concrete circular bridge columns under crustal, subcrustal, and subduction earthquakes. *Soil Dynamics and Earthquake Engineering*, *177*, 108394. https://doi.org/10.1016/j.soildyn.2023.108394

Schiefer, C., & Plank, J. (2023). CO2 emission of polycarboxylate superplasticizers (PCEs) used in concrete. *Journal of Cleaner Production*, *427*, 138785. https://doi.org/10.1016/j.jclepro.2023.138785

Schneider, M. (2019). The cement industry on the way to a low-carbon future. *Cement and Concrete Research*, *124*, 105792. https://doi.org/10.1016/j.cemconres.2019.105792

Scrivener, K., Martirena, F., Bishnoi, S., & Maity, S. (2018). Calcined clay limestone cements (LC3). *Cement and Concrete Research*, *114*, 49–56. https://doi.org/10.1016/j.cemconres.2017.08.017

Seiler, P. H., & Duer, H. S. (2019). The future of construction. *Cement and Concrete Composites*, *101*, 2–4. https://doi.org/10.1016/j.cemconcomp.2017.09.004

Shao, Y., Tich, K. L., Boaro, S. B., & Billington, S. L. (2022). Impact of fiber distribution and cyclic loading on the bond behavior of steel-reinforced UHPC. *Cement and Concrete Composites*, *126*, 104338. https://doi.org/10.1016/j.cemconcomp.2021.104338

Shi, C., Li, Y., Zhang, J., Li, W., Chong, L., & Xie, Z. (2016). Performance enhancement of recycled concrete aggregate – A review. *Journal of Cleaner Production*, *112*, 466–472. https://doi.org/10.1016/j.jclepro.2015.08.057

Shi, C., Qu, B., & Provis, J. L. (2019). Recent progress in low-carbon binders. *Cement and Concrete Research*, *122*, 227–250. https://doi.org/10.1016/j.cemconres.2019.05.009

SIA Group. (1994). *SIA 162/4 / 1994 D - Recyclingbeton* (No. SIA 162/4; Version 1994). Swiss Society of Engineers and Architects. https://shop.sia.ch/normenwerk/ingenieur/162-4_1994_d/D/Product (Inactive)

SIA Group. (2021). *SIA 2030 / 2021 D - Beton mit rezyclierten Gesteinskörnungen* (No. SIA 2030; Version 2021). Swiss Society of Engineers and Architects. https://shop.sia.ch/normenwerk/ingenieur/2030_2021_d/D/Product (Active)

Sierens, Z., Cai, J., Van Steen, C., Verstrynge, E., & Li, J. (2021). Bond performance of deformed steel rebars in HSC incorporating industrially produced recycled concrete aggregate. *Materials and Structures*, *54*(1), 1–15. https://doi.org/10.1617/s11527-021-01639-4

Silva, F. A. N., Delgado, J. M. P. Q., Azevedo, A. C., Lima, A. G. B., & Vieira, C. S. (2021). Preliminary Analysis of the Use of Construction Waste to Replace Conventional Aggregates in Concrete. *Buildings*, *11*(3), Article 3. https://doi.org/10.3390/buildings11030081

Silva, R. V., de Brito, J., & Dhir, R. K. (2014). Properties and composition of recycled aggregates from construction and demolition waste suitable for concrete production. *Construction and Building Materials*, *65*, 201–217. https://doi.org/10.1016/j.conbuildmat.2014.04.117

Silva, R. V., de Brito, J., & Dhir, R. K. (2015a). Prediction of the shrinkage behavior of recycled aggregate concrete: A review. *Construction and Building Materials*, *77*, 327–339. https://doi.org/10.1016/j.conbuildmat.2014.12.102

Silva, R. V., de Brito, J., & Dhir, R. K. (2015b). Tensile strength behaviour of recycled aggregate concrete. *Construction and Building Materials*, *83*, 108–118. https://doi.org/10.1016/j.conbuildmat.2015.03.034

Silva, R. V., de Brito, J., & Dhir, R. K. (2015c). The influence of the use of recycled aggregates on the compressive strength of concrete: A review. *European Journal of Environmental and Civil Engineering*, *19*(7), 825–849. https://doi.org/10.1080/19648189.2014.974831

Silva, R. V., de Brito, J., & Dhir, R. K. (2017). Availability and processing of recycled aggregates within the construction and demolition supply chain: A review. *Journal of Cleaner Production*, *143*, 598–614. https://doi.org/10.1016/j.jclepro.2016.12.070

Silva, R. V., Neves, R., de Brito, J., & Dhir, R. K. (2015d). Carbonation behaviour of recycled aggregate concrete. *Cement and Concrete Composites*, *62*, 22–32. https://doi.org/10.1016/j.cemconcomp.2015.04.017

Souche, J.-C., Devillers, P., Salgues, M., & Garcia Diaz, E. (2017). Influence of recycled coarse aggregates on permeability of fresh concrete. *Cement and Concrete Composites*, *83*, 394–404. https://doi.org/10.1016/j.cemconcomp.2017.08.002

Sryh, L., & Forth, J. (2022). Long-Term Flexural Behaviour of Cracked Reinforced Concrete Beams with Recycled Aggregate. *International Journal of Concrete Structures and Materials*, *16*(1), 19. https://doi.org/10.1186/s40069-022-00512-0

Tam, V. W. Y., Gao, X. F., & Tam, C. M. (2005). Microstructural analysis of recycled aggregate concrete produced from two-stage mixing approach. *Cement and Concrete Research*, *35*(6), 1195–1203. https://doi.org/10.1016/j.cemconres.2004.10.025

Tam, V. W. Y., Soomro, M., & Evangelista, A. C. J. (2018). A review of recycled aggregate in concrete applications (2000–2017). *Construction and Building Materials*, *172*, 272–292. https://doi.org/10.1016/j.conbuildmat.2018.03.240

Tam, V. W. Y., & Tam, C. M. (2008). Diversifying two-stage mixing approach (TSMA) for recycled aggregate concrete: TSMAs and TSMAsc. *Construction and Building Materials*, *22*(10), 2068–2077. https://doi.org/10.1016/j.conbuildmat.2007.07.024

Tepfers, R., Achillides, Z., Azizinamini, A., Balázs, G., Bigaj-van-Vliet, A., Cabrera, J., Cairns, J., Cosenza, E., Den Uijl, J., Eligehausen, R., Engström, B., Erdélyi, L., Gambarova, P., Jirsa, J., Lane, S., Leon, R., Magnusson, J., Mayer, U., McCabe, S., … Vintzileou, L. (2000). *fib Bulletin 10. Bond of reinforcement in concrete* (fib. The International Federation for Structural Concrete, Ed.). fib. The International Federation for Structural Concrete. https://doi.org/10.35789/fib.BULL.0010

Topçu, İ. B., & Şengel, S. (2004). Properties of concretes produced with waste concrete aggregate. *Cement and Concrete Research*, *34*(8), 1307–1312. https://doi.org/10.1016/j.cemconres.2003.12.019

Tošić, N., Marinković, S., & Ignjatović, I. (2016). A database on flexural and shear strength of reinforced recycled aggregate concrete beams and comparison to Eurocode 2 predictions. *Construction and Building Materials*, *127*, 932–944. https://doi.org/10.1016/j.conbuildmat.2016.10.058

Trujillo Pasquale, B., Malo, R., & Jolin, M. (2018). Alternative Setup Apparatus to Test ASTM A944-10 Beam-End Specimens. *Journal of Testing and Evaluation*, *46*(4), 1741–1748. https://doi.org/10.1520/JTE20170645

U.S. Geological Survey. (2023). Mineral Commodity Summaries 2023. In *Mineral Commodity Summaries* (No. 2023). U.S. Geological Survey. https://doi.org/10.3133/mcs2023

Verian, K. P., Ashraf, W., & Cao, Y. (2018). Properties of recycled concrete aggregate and their influence in new concrete production. *Resources, Conservation and Recycling*, *133*, 30–49. https://doi.org/10.1016/j.resconrec.2018.02.005

Vieito, I., Herrador, M. F., Martínez-Abella, F., & Varela-Puga, F. (2018). Proposal and assessment of an efficient test configuration for studying lap splices in reinforced concrete. *Engineering Structures*, *165*, 1–10. https://doi.org/10.1016/j.engstruct.2018.03.004

Voglis, N., Kakali, G., Chaniotakis, E., & Tsivilis, S. (2005). Portland-limestone cements. Their properties and hydration compared to those of other composite cements. *Cement and Concrete Composites*, *27*(2), 191–196. https://doi.org/10.1016/j.cemconcomp.2004.02.006

Wang, B., Yan, L., Fu, Q., & Kasal, B. (2021). A Comprehensive Review on Recycled Aggregate and Recycled Aggregate Concrete. *Resources, Conservation and Recycling*, *171*, 105565. https://doi.org/10.1016/j.resconrec.2021.105565

Wang, C., & Xiao, J. (2018). Evaluation of the stress-strain behavior of confined recycled aggregate concrete under monotonic dynamic loadings. *Cement and Concrete Composites*, *87*, 149–163. https://doi.org/10.1016/j.cemconcomp.2017.12.012

Wang, C., Xiao, J., Qi, C., & Li, C. (2022). Rate sensitivity analysis of structural behaviors of recycled aggregate concrete frame. *Journal of Building Engineering*, *45*, 103634. https://doi.org/10.1016/j.jobe.2021.103634

Wang, D., Li, H.-N., & Li, G. (2013). Experimental study on dynamic mechanical properties of reinforced concrete column. *Journal of Reinforced Plastics and Composites*, *32*(23), 1793–1806. https://doi.org/10.1177/0731684413492451

Wight, J. K. (2021). *Reinforced Concrete: Mechanics and Design* (8th Edition). Pearson. https://www.pearson.com/en-us/subject-catalog/p/reinforced-concrete-mechanics-and-design/P200000003141/9780136834243

Wijayasundara, M., Mendis, P., Zhang, L., & Sofi, M. (2016). Financial assessment of manufacturing recycled aggregate concrete in ready-mix concrete plants. *Resources, Conservation and Recycling*, *109*, 187–201. https://doi.org/10.1016/j.resconrec.2016.02.007

Winnefeld, F., Ben Haha, M., Le Saout, G., Costoya, M., Ko, S.-C., & Lothenbach, B. (2015). Influence of slag composition on the hydration of alkali-activated slags. *Journal of Sustainable Cement-Based Materials*, *4*(2), 85–100. https://doi.org/10.1080/21650373.2014.955550

Xiao, J., Li, J., & Zhang, Ch. (2005). Mechanical properties of recycled aggregate concrete under uniaxial loading. *Cement and Concrete Research*, *35*(6), 1187–1194. https://doi.org/10.1016/j.cemconres.2004.09.020

Xiao, J., Wang, C., Li, J., & Tawana, M. M. (2012). Shake-Table Model Tests on Recycled Aggregate Concrete Frame Structure. *Structural Journal*, *109*(6), 777–786. https://doi.org/10.14359/51684121

Xiao, S., Li, J., & Mo, Y. (2020). Dynamic behaviours of reinforced concrete columns under cyclic loading with variable rates. *Advances in Structural Engineering*, *23*(4), 779–793. https://doi.org/10.1177/1369433219881753

Xiao, S., Li, J., & Mo, Y.-L. (2018). Effect of loading rate on cyclic behavior of reinforced concrete beams. *Advances in Structural Engineering*, *21*(7), 990–1001. https://doi.org/10.1177/1369433217737114

Xuan, D., Poon, C. S., & Zheng, W. (2018). Management and sustainable utilization of processing wastes from ready-mixed concrete plants in construction: A review. *Resources, Conservation and Recycling*, *136*, 238–247. https://doi.org/10.1016/j.resconrec.2018.04.007

Yang, H., Lan, W., Qin, Y., & Wang, J. (2016). Evaluation of bond performance between deformed bars and recycled aggregate concrete after high temperatures exposure. *Construction and Building Materials*, *112*, 885–891. https://doi.org/10.1016/j.conbuildmat.2016.02.220

Yang, I.-H., Park, J., Kim, K.-C., & Lee, H. (2020). Structural Behavior of Concrete Beams Containing Recycled Coarse Aggregates under Flexure. *Advances in Materials Science and Engineering*, *2020*(1), 8037131. https://doi.org/10.1155/2020/8037131

Yang, S., & Lee, H. (2017a). Mechanical properties of recycled aggregate concrete proportioned with modified equivalent mortar volume method for paving applications. *Construction and Building Materials*, *136*, 9–17. https://doi.org/10.1016/j.conbuildmat.2017.01.029

Yang, S., & Lee, H. (2017b). Structural Performance of Reinforced RCA Concrete Beams Made by a Modified EMV Method. *Sustainability*, *9*(1), Article 1. https://doi.org/10.3390/su9010131

Yang, S., & Lim, Y. (2018). Mechanical strength and drying shrinkage properties of RCA concretes produced from old railway concrete sleepers using by a modified EMV method. *Construction and Building Materials*, *185*, 499–507. https://doi.org/10.1016/j.conbuildmat.2018.07.074

Zhang, J., Tao, X., Li, X., Zhang, Y., & Liu, Y. (2022). Analytical and experimental investigation of the bond behavior of confined high-strength recycled aggregate concrete. *Construction and Building Materials*, *315*, 125636. https://doi.org/10.1016/j.conbuildmat.2021.125636

Zhou, K.-P., Yi, W.-J., Hwang, H.-J., & Zhou, Y. (2023). Influence of bond test methods on the bond performance between reinforcing bars and concrete. *Structures*, *54*, 1299–1311. https://doi.org/10.1016/j.istruc.2023.05.083

Zhu, C., Liu, C., Bai, G., & Fan, J. (2020). Study on long-term performance and flexural stiffness of recycled aggregate concrete beams. *Construction and Building Materials*, *262*, 120503. https://doi.org/10.1016/j.conbuildmat.2020.120503